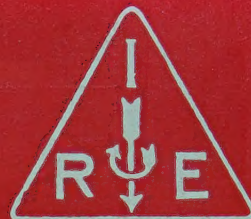


# IRE Transactions



## on Microwave Theory and Techniques

Volume MTT-8

**NOVEMBER, 1960**

Number 6

### In This Issue

Wide-Band (and Narrow-Band) Band-Pass Microwave Filters  
on Insertion Loss Basis

Radio-Frequency System of the Cambridge Electron  
Accelerator

Model Studies of a Strongly Coupled Synchrotron System

Operation of the Field Displacement Insulator in Rectangular  
Waveguide

Peak Internal Fields in Direct-Coupled-Cavity Filters

Mismatch Errors in Microwave Phase Shift Measurements

A Note on the Optimum Source Conductance of Crystal Mixers

Microwave Switching with Low-Pressure Arc Discharge

Characteristic Impedances of Broadside-Coupled Strip  
Transmission Lines

Thickness Corrections for Capacitive Obstacles and Strip  
Conductors

Inhomogeneous Quarter-Wave Transformers of Two Sections

Errors in Dielectric Measurements Due to a Sample Insertion  
Hole in a Cavity

A Pre-TR Tube for High Mean Power Duplexing

Circular Electric Mode Directional Coupler

TK7800

±23

PUBLISHED BY THE  
Professional Group on Microwave Theory and Techniques



## IRE PROFESSIONAL GROUP ON MICROWAVE THEORY AND TECHNIQUES

The Professional Group on Microwave Theory and Techniques is an association of IRE members with professional interest in the field of Microwave Theory and Techniques. All IRE members are eligible for membership and will receive all Group publications upon payment of the prescribed annual fee of \$3.00. Members of the American Physical Society and the Institution of Electrical Engineers of Great Britain may become affiliated with PGMTT and receive all Group publications upon payment of the Affiliate fee of \$7.50 per year.

### Administrative Committee

#### Chairman

K. TOMIYASU

#### Vice Chairman

T. N. ANDERSON

#### Secretary-Treasurer

H. M. ALTSCHULER

R. E. BEAM

A. C. BECK

S. B. COHN

R. C. HANSEN

W. W. MUMFORD

A. A. OLINER

R. A. RIVERS

S. W. ROSENTHAL

T. S. SAAD

R. F. SCHWARTZ

G. SHAPIRO

G. SINCLAIR

P. D. STRUM

M. C. THOMPSON

R. D. WENGENROTH

#### *Ex-Officio*

W. L. PRITCHARD

#### *Honorary Life Members*

G. C. SOUTHWORTH

A. G. CLAVIER

#### Editor

DONALD D. KING

### PGMTT Chapters

Albuquerque-Los Alamos

Baltimore

Boston

Buffalo-Niagara

Chicago

Columbus

Denver-Boulder

Long Island

Los Angeles

New York

R. L. O'Nan

J. C. Wiltse

C. E. Faflick

E. S. Schlichter

Robert Janowiak

B. Querido

G. E. Schafer

B. Aaron

R. C. Hansen

Eugene Torgow

Northern N.J.

Omaha-Lincoln

Orange Belt

Philadelphia

San Diego

San Francisco

Schenectady

Syracuse

Tokyo, Japan

Washington, D.C.

R. M. Foley

C. O. Jett

D. Sabih

T. J. Vaughan

H. O. Dickstein

E. M. T. Jones

C. C. Allen

J. C. Williamson

Kiyoshi Morita

Benjamin Bernstein

### IRE TRANSACTIONS®

#### on Microwave Theory and Techniques

Published by The Institute of Radio Engineers, Inc., for the Professional Group on Microwave Theory and Techniques, at 1 East 79 Street, New York 21, N.Y. Responsibility for the contents rests upon the authors, and not upon the IRE, the Group, or its members. Annual subscription price: IRE members, \$8.50; colleges and public libraries, \$12.75; non-members, \$17.00. Individual copies of this issue and all available back issues may be purchased at the following prices: IRE members (one copy) \$2.25, libraries and colleges \$3.25, all others \$4.50.

Address all manuscripts to Donald D. King, PGMTT Editor, Electronic Communications, Inc., 1830 York Road, Timonium, Md. Submission of three copies of manuscripts, including figures, will expedite the review.

COPYRIGHT ©1960—THE INSTITUTE OF RADIO ENGINEERS, INC.

Printed in U.S.A.

All rights, including translations, are reserved by the IRE. Requests for republication privileges should be addressed to the Institute of Radio Engineers, 1 E. 79 St., New York 21, N.Y.



# IRE Transactions

## on

# Microwave Theory and Techniques

### EDITORIAL BOARD

#### Editor

Donald D. King

#### Advertising Editor

Robert A. Rivers

D. J. Angelakos  
F. R. Arams  
W. P. Ayres  
R. W. Beatty  
A. D. Berk  
A. D. Bresler  
J. C. Cacheris  
S. B. Cohn  
R. E. Collin  
M. P. Forrer  
I. Goldstein  
R. C. Hansen  
H. Heffner  
E. T. Jaynes  
E. M. T. Jones  
R. W. Klopfenstein  
P. A. Loth  
R. V. Lowman  
T. Moreno  
S. P. Morgan  
K. S. Packard, Jr.  
M. C. Pease  
J. Reed  
J. M. Richardson  
P. A. Rizzi  
S. D. Robertson  
N. G. Sakiotis  
R. F. Schwartz  
W. Sichak  
D. C. Stinson  
E. Strumwasser  
L. Swern  
P. H. Vartanian, Jr.  
M. T. Weiss  
G. J. Wheeler  
R. F. Whitmer  
J. C. Wiltse  
L. Young  
F. J. Zucker

Volume MTT-8

NOVEMBER, 1960

Number 6

### TABLE OF CONTENTS

#### CONTRIBUTIONS

Design of Wide-Band (and Narrow-Band) Band-Pass Microwave Filters on the Insertion Loss Basis.....	<i>George L. Matthaei</i>	580
Radio-Frequency System of the Cambridge Electron Accelerator.....	<i>Kenneth W. Robinson</i>	593
Model Studies of a Strongly Coupled Synchrotron RF System.....	<i>A. E. Barrington, J. Dekleva, and J. R. Rees</i>	597
Operation of the Field Displacement Isolator in Rectangular Waveguide.....	<i>R. L. Comstock and C. E. Fay</i>	605
Peak Internal Fields in Direct-Coupled-Cavity Filters.....	<i>Leo Young</i>	612
Mismatch Errors in Microwave Phase Shift Measurements.....	<i>G. E. Schafer</i>	617
A Note on the Optimum Source Conductance of Crystal Mixers.....	<i>R. J. Mohr and S. Okwit</i>	622
Microwave Switching with Low-Pressure Arc Discharge.....	<i>R. M. Hill and S. K. Ichiki</i>	628
Characteristic Impedances of Broadside-Coupled Strip Transmission Lines.....	<i>Seymour B. Cohn</i>	633
Thickness Corrections for Capacitive Obstacles and Strip Conductors.....	<i>Seymour B. Cohn</i>	638
Inhomogeneous Quarter-Wave Transformers of Two Sections.....	<i>Leo Young</i>	645
Errors in Dielectric Measurements Due to a Sample Insertion Hole in a Cavity.....	<i>A. J. Estlin and H. E. Bussey</i>	650
Correction.....	<i>D. S. Lerner and H. A. Wheeler</i>	653
A Pre-TR Tube for High Mean Power Duplexing.....	<i>D. W. Downton and P. D. Lomer</i>	654
Circular Electric Mode Directional Coupler.....	<i>Bunichi Oguchi</i>	660

#### CORRESPONDENCE

An Equivalent Circuit of the Internal Cavity Reflex Klystron-Amplifier.....	<i>Koryu Ishii</i>	667
Some Comments on the Method of Kyhl.....	<i>L. J. Kaplan, D. J. R. Stock and R. L. Kyhl</i>	668
Scattering Matrix for an N-Port Power-Divider Junction.....	<i>O. R. Price and M. Leichter</i>	669
Lossy Resonant Slot Coupling.....	<i>R. M. Bevensee, G. S. Kino, and M. A. Allen</i>	669
Broad-Band Hybrid Junctions.....	<i>S. J. Robinson</i>	671
Lightweight Y-Junction Strip-Line Circulator.....	<i>L. Freiberg</i>	672
A Novel Broad-Band Balun.....	<i>J. H. Craven</i>	672
Contributors.....		673
Notice 1960 National Symposium Issue.....		676
Annual Index.....	<i>Follows page</i>	676



# Design of Wide-Band (and Narrow-Band) Band-Pass Microwave Filters on the Insertion Loss Basis\*

GEORGE L. MATTHAEI†, MEMBER, IRE

**Summary**—A method for design of band-pass microwave filters is described that combines the image and insertion-loss points of view to give an approximate design method having simplicity, but also high precision. This method is applicable for filter designs ranging from narrow to very wide bandwidths (2 to 1 or more). The desired insertion loss characteristic is obtained by use of a lumped-element, Tchebycheff, or maximally flat (or other) low-pass prototype. With the aid of the concept of impedance inverters, the prototype is converted into a cascade of symmetrical (but differing) sections. The image properties of symmetrical sections of the band-pass microwave filter structure are then related to those of corresponding sections of the prototype. Straightforward design equations are given for filters using short-circuited or open-circuited stubs, and also for filters using parallel-coupled lines. Mapping functions are derived that permit accurate prediction of the microwave filter cutoff characteristic from that of the prototype. The responses of a number of filter designs were computed, and a Tchebycheff filter with a 2.2 to 1 bandwidth was built and tested. The responses of all of the filter designs were in close agreement with the prescribed characteristics, and the accuracy of the mapping functions was verified.

## I. INTRODUCTION

THE TYPES of band-pass filters to be treated in this paper are shown in Figs. 1–3. Filters using some of these structures have often been designed in the past using image design methods. Although these methods are conceptually simple, the over-all filter response to be expected is known only approximately, as a result of reflections at the terminating end sections. Thus, using such methods, it takes either a great deal of trial and error or a great deal of “know how” in order to obtain precision designs with specified pass band attenuation tolerances. Design methods, such as those discussed herein, on the insertion loss basis, have the advantage that the nature of the filter response can be specified at the outset of the design process, and the final filter design will closely adhere to the specifications.

The filter in Fig. 1(a) is of the parallel-coupled type for which Cohn<sup>1</sup> has presented approximate insertion-loss-basis design equations accurate for filters of narrow or moderate bandwidth; the filter form shown in Fig. 1(d) was previously treated by Jones<sup>2</sup> on an exact

insertion-loss basis. It can be shown that exact design procedures using Richards' transformation<sup>3</sup> can be derived for all of these filters for either narrow or wide bandwidths. Examples of the use of these procedures will be found in the literature.<sup>2,4–7</sup> However, the paper by Jones,<sup>2</sup> which treats the form of filter in Fig. 1(d), is the only one of these references which deals specifically with any of the filters in Figs. 1(a) to 3 on an exact insertion-loss design basis. A serious practical disadvantage of exact methods for designing these particular filter structures is that the synthesis of special transfer functions is required<sup>8</sup> at the outset of the design process,<sup>2</sup> and, all in all, a great deal of computational labor is needed. Even though the design procedures described herein are computationally very simple and only approximate, the results, as the examples show, are satisfactory for most practical precision-design problems. Another advantage of the methods described herein is that they are quite flexible. As will be seen, the design procedure can be adapted to include changes in impedance level or special forms of structures, as required by special practical situations. These methods can also be used for other types of structures than those discussed herein.<sup>9</sup>

Easy-to-use approximate insertion-loss-basis design methods for band-pass microwave filters have existed for some time. However, these methods have in the past involved narrow-band approximations and as a result have rarely been accurate for bandwidths much

\* P. I. Richards, “Resistor-transmission-line circuits,” *PROC. IRE*, vol. 36, pp. 217–220; February, 1948.

† H. Ozaki and J. Ishii, “Synthesis of transmission-line networks and the design of UHF filters,” *IRE TRANS. ON CIRCUIT THEORY*, vol. CT-2, pp. 325–336; December, 1955.

<sup>2</sup> H. Ozaki and J. Ishii, “Synthesis of a class of strip-line filters,” *IRE TRANS. ON CIRCUIT THEORY*, vol. CT-5, pp. 104–109; June, 1958.

<sup>3</sup> A. I. Grayzel, “A synthesis procedure for transmission line networks,” *IRE TRANS. ON CIRCUIT THEORY*, vol. CT-5, pp. 172–181; September, 1958.

<sup>4</sup> N. R. Welsh and E. S. Kuh, “Synthesis of Resistor-Transmission Line Networks,” *Electronics Res. Lab., University of California, Berkeley, Rept. No. 74, ONR Contract N7-onr-29529; July 15, 1958.*

<sup>5</sup> In general, whether or not special transfer functions are required depends on the location of the frequencies of infinite attenuation inherent in the desired filter structure. By choosing certain filter structures, the more common transfer functions can be used (see footnotes 5 and 6). Such structures, however, may not always be the most convenient to fabricate.

<sup>6</sup> For example, the case of filters consisting of transmission lines coupled by series capacitors was treated in the report: G. L. Matthaei, “Research on Design Criteria for Microwave Filters,” *Stanford Res. Inst., Menlo Park, Calif., Tech. Rept. 6, SRI Project 2326, Contract DA 36-039 SC-74862; May, 1959.*

\* Received by the PGM-TT, May 8, 1960. This research was supported by the Signal Corps under Contract DA 36-039 SC-74862.

† Stanford Res. Inst., Menlo Park, Calif.

<sup>1</sup> S. B. Cohn, *et al.*, “Research on Design Criteria for Microwave Filters,” *Stanford Res. Inst., Menlo Park, Calif., Final Rept., SRI Project 1331, Contract DA 36-039 SC-64625, ch. 4; June, 1957.* Also S. B. Cohn, “Parallel-coupled transmission line-resonator filters,” *IRE TRANS. ON MICROWAVE THEORY AND TECHNIQUES*, vol. MTT-6, pp. 223–231; April, 1958.

<sup>2</sup> *Ibid.* (SRI Rept.), ch. 3. Also, E. M. T. Jones, “Synthesis of wide-band microwave filters to have prescribed insertion loss,” 1956 *IRE CONVENTION RECORD*, pt. 5, pp. 119–128.



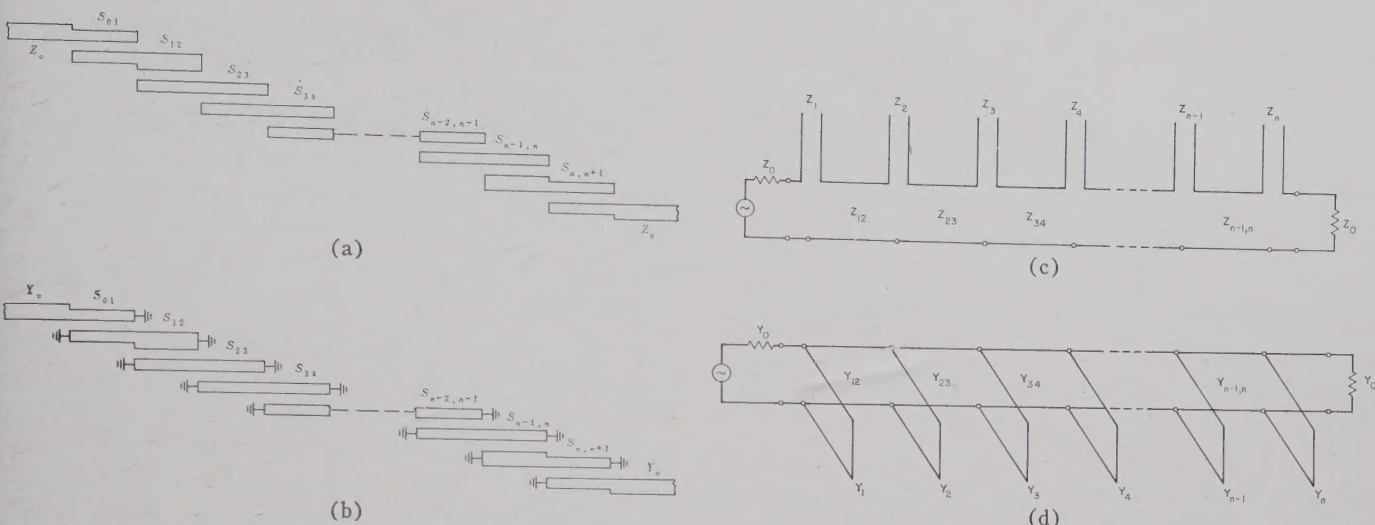


Fig. 1—(a) Parallel-coupled, strip-transmission-line filter with open-circuited sections. Each section is one-quarter wavelength long where the reference wavelength is that at the midband frequency,  $\omega_0$ . Each section  $S_{k,k+1}$  is characterized by even and odd mode impedances  $(Z_{oe})_{k,k+1}$  and  $(Z_{oo})_{k,k+1}$ , respectively.<sup>1,11,16</sup> (b) Parallel-coupled, strip-transmission-line filter with short-circuited sections. This filter is the dual of that in (a). Each section  $S_{k,k+1}$  is one-quarter wavelength long where the reference wavelength is the propagation wavelength at the midband frequency,  $\omega_0$ . Each section  $S_{k,k+1}$  is characterized by even and odd mode admittances  $(Y_{oe})_{k,k+1}$  and  $(Y_{oo})_{k,k+1}$ , respectively.<sup>1,16</sup> (c) Band-pass filter using quarter-wavelength series stubs and quarter-wavelength connecting lines. Filters of the form in (a) can always be converted to this form. (d) Band-pass filter using quarter-wavelength shunt stubs and quarter-wavelength connecting lines. This filter is the dual of that in (c). The reference wavelength is the propagation wavelength at the midband frequency,  $\omega_0$ .

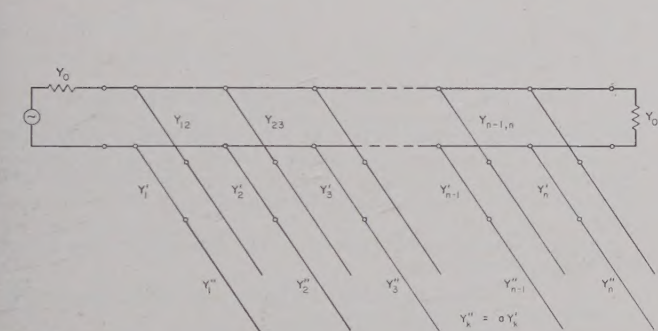


Fig. 2—Band-pass filter with half-wavelength shunt stubs and quarter-wavelength connecting lines. The reference wavelength is the propagation wavelength at the midband frequency,  $\omega_0$ .

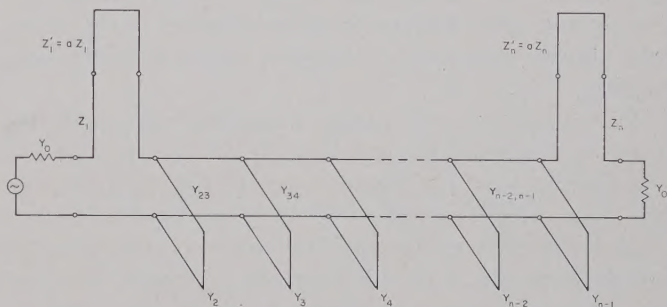


Fig. 3—Band-pass filter with quarter-wavelength shunt stubs, quarter-wavelength connecting lines, and half-wavelength series stubs at the ends. The reference wavelength is that at the midband frequency,  $\omega_0$ .

over 20 per cent. The design approach used herein has the advantage that it does not involve approximations of a narrow-band sort; hence, it gives good accuracy for narrow bandwidths on out to bandwidths of 2 to 1 or more.

In Section II, the use of the design equations and the results of design examples will be discussed. To make routine use of the design equations more convenient, their derivation will be treated separately in Section III.

## II. PRACTICAL APPLICATION OF THE DESIGN EQUATIONS

### A. Equivalence of the Networks in Figs. 1(a)–(d)

The filter in Fig. 1(b) is simply the dual of that in Fig. 1(a). It can be obtained directly from the circuit in Fig. 1(a) by replacing the open circuits by short circuits and by replacing each even- or odd-mode im-

pedance,  $(Z_{oe})_{k,k+1}$  and  $(Z_{oo})_{k,k+1}$ , respectively, by corresponding *odd*- and *even*-mode admittances.

$$\begin{aligned} (Y_{oe})_{k,k+1} &= Y_0^2 (Z_{oe})_{k,k+1}, \\ (Y_{oe})_{k,k+1} &= Y_0^2 (Z_{oo})_{k,k+1}, \end{aligned} \quad (1)$$

where  $Y_0 = 1/Z_0$  is the characteristic admittance of the input and output lines. By use of the equivalences shown in Fig. 4,<sup>10,11</sup> it is seen that the circuit in Fig. 1(c) is

<sup>10</sup> The correctness of these equivalences can be verified with the aid of the impedance and admittance matrices for parallel-coupled strips given by Jones and Bolljahn (see footnote 11) or by using Richards' viewpoint to map the elements in Equivalent Circuits (5) and (6) of Table II of Ozaki and Ishii's work (see footnote 5) into the corresponding transmission line form.

<sup>11</sup> Cohn, *et al.*, *op. cit.*, (SRI Rept.), ch. 4. Also, E. M. T. Jones and J. T. Bolljahn, "Coupled-strip-transmission-line filters and directional couplers," IRE TRANS. ON MICROWAVE THEORY AND TECHNIQUES, vol. MTT-4, pp. 75–81; April, 1956.



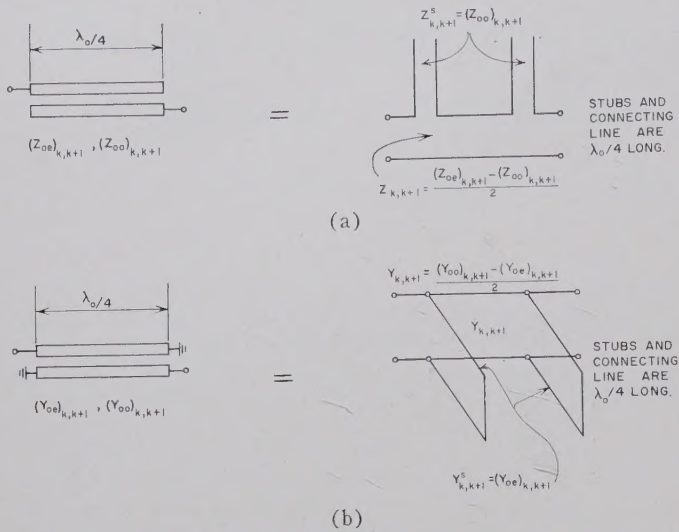


Fig. 4—Equivalence between parallel-coupled strip-line sections and sections consisting of stubs with connecting lines.

exactly equivalent to that in Fig. 1(a), while the circuit in Fig. 1(d) is exactly equivalent to that in Fig. 1(b). Thus, any of these four circuits can be derived from any other, by use of duality and the equivalences in Fig. 4; and when derived from one another in this manner, all will yield exactly the same transmission characteristic.

For simplicity, the design equations applicable for these four filter structures (Fig. 1) will be expressed in the specific form for the structure in Fig. 1(a). Any of the other forms may then be obtained by duality and Fig. 4. In converting from the form in Fig. 1(a) to the form in Fig. 1(d), for example, it should be noted that the characteristic admittance of the shunt stub at each end is determined solely by the end sections of the filter in Fig. 1(a); however, the characteristic admittance of each of the shunt stubs in the interior of the filter in Fig. 1(d) is determined by the corresponding two adjacent sections in Fig. 1(a) so that

$$\begin{aligned} Y_k &= Y_{k-1,k}^s + Y_{k,k+1}^s \\ &= Y_0^2 [Z_{k-1,k}^s + Z_{k,k+1}^s] \\ &= Y_0^2 [(Z_{00})_{k-1,k} + (Z_{00})_{k,k+1}], \end{aligned} \quad (2)$$

where  $Y_0 = 1/Z_0$  is again the characteristic admittance of the input and output lines, and the  $Y_{k,k+1}^s$  and  $Z_{k,k+1}^s$  are defined in Fig. 4. It is helpful to note that in the case of Fig. 1(d), the characteristic admittances of the connecting lines are given by

$$Y_{k,k+1} = Y_0^2 \left[ \frac{(Z_{0e})_{k,k+1} - (Z_{0o})_{k,k+1}}{2} \right] = Y_0^2 K_{k,k+1}, \quad (3)$$

where the  $K_{k,k+1}$  are impedance inverter parameters to be discussed later. (They are defined numerically in Tables I and II, p. 592.)

The filter structures in Figs. 2 and 3 are not equivalent to those in Fig. 1; however, they are closely related structures which can readily be treated using many of the same concepts and equations.

### B. Use of Mapping Functions, and Selection of Appropriate Lumped-Element Prototypes

In the design procedure described herein, the band-pass microwave filter derives characteristic properties of its response from a lumped-element prototype filter having analogous low-pass filter response properties. Fig. 5 shows a typical low-pass prototype and defines the prototype parameters  $g_0, g_1, \dots, g_n, g_{n+1}$ . The design equations in Tables I–III (p. 592) assume that the prototype filter is either symmetric or antimetric<sup>12</sup>—a condition satisfied by the common maximally flat or Tchebycheff lossless filter designs (which have one or more frequencies at which zero reflection occurs).

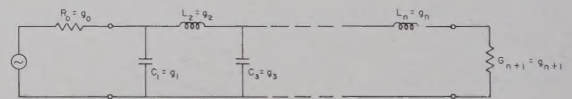


Fig. 5—Definition of the low-pass prototype parameters  $g_0, g_1, \dots, g_n, g_{n+1}$ . The symmetry about the middle of the filter indicated in the equations of Tables I–III results from the use of symmetric or antimetric prototypes. The common maximally flat or Tchebycheff prototypes, which have one or more frequencies where zero reflection occurs, always satisfy this symmetry or antimetry condition.

A typical low-pass prototype is shown. The dual of this circuit would also be satisfactory.

$$g_k |_{k=1 \text{ to } n} = \begin{cases} \text{The inductance of a series coil, or the capacitance of a shunt capacitor.} \\ \text{The generator resistance } R_0 \text{ if } g_1 = C_1, \text{ but is defined as the generator conductance } G_0 \text{ if } g_1 = L_1. \\ \text{The load resistance } R_{n+1} \text{ if } g_n = C_n, \text{ but is defined as the load conductance } G_{n+1} \text{ if } g_n = L_n. \end{cases}$$

Note: An additional prototype parameter  $\omega_1'$  is defined in Figs. 6 and 7.

Weinberg<sup>13</sup> and Technical Report 4 of this project<sup>14</sup> give tables of element values for such filters. (Weinberg<sup>13</sup> also includes tables for filters which are not symmetric or antimetric.) The use of symmetric or antimetric prototypes along with equal terminations in the final microwave filter (as depicted in Figs. 1–3) is usually desirable, and so has been made implicit in the equations in Tables I–III. However, these conditions are not

<sup>12</sup> E. A. Guillemin, "Synthesis of Passive Networks," John Wiley and Sons, Inc., New York, N. Y., p. 371; 1957.

<sup>13</sup> L. Weinberg, "Network Design by Use of Modern Synthesis Techniques and Tables," Res. Labs., Hughes Aircraft Co., Culver City, Calif., Tech. Memo. 427; April, 1956. Also, in *Proc. NEC*, vol. 12; 1956.

<sup>14</sup> W. J. Getsinger, *et al.*, "Research on Design Criteria for Microwave Filters," Stanford Res. Inst., Menlo Park, Calif., Tech. Rept. 4, SRI Project 2326, Contract DA 36-039 SC-74862; December, 1958.



necessary, and equations for other cases may be derived by the theory in Section III.

Fig. 6 shows a typical lossless low-pass-filter maximally flat response along with the equation for this response. The frequency  $\omega_1'$  establishes the pass-band edge, while  $A_m$  is the db attenuation which is permissible within the pass band. The frequency  $\omega_a'$  is a frequency at which a stated attenuation,  $A_a$  db, is required. An analogous maximally flat band-pass response, such as might be obtained by the filters in Fig. 1, is also shown. Note that this response has arithmetic symmetry about  $\omega_0$ , so that the essential parameters of the response may be specified simply as  $\omega_1/\omega_0$ ,  $A_m$ ,  $A_a$ , and  $\omega_a/\omega_0$ . The response of the band-pass filter may be predicted directly from that of the low-pass filter by mapping the  $\omega'$  frequency scale of the low-pass filter to the  $\omega$  frequency scale of the band-pass filter, as indicated in the figure. For the circuits in

Fig. 1, and the design equations in Tables I and II, the proper function  $F_n(\omega/\omega_0)$  to use is

$$F_n\left(\frac{\omega}{\omega_0}\right) = \frac{-\cos\left(\frac{\pi}{2} \frac{\omega}{\omega_0}\right)}{\sqrt[n]{\left|\sin\left(\frac{\pi\omega}{2\omega_0}\right)\right|}} \quad (4a)$$

For narrow or moderate bandwidths, the simpler function

$$F_n\left(\frac{\omega}{\omega_0}\right) = \left(\frac{\omega}{\omega_0} - 1\right) \quad (4b)$$

will also give good accuracy.<sup>1</sup> As will be shown, the accuracy of (4b) is fair even for wide bandwidths. For the circuit in Fig. 3 and the equations in Table III, the proper function to use is

$$F_n\left(\frac{\omega}{\omega_0}\right) = \frac{-\cos\left(\frac{\pi\omega}{2\omega_0}\right)}{\sqrt[n]{\left|\sin\left(\frac{\pi\omega}{2\omega_0}\right)\right| \left[\sin\left(\frac{\pi}{2} \frac{(\omega - \omega_\infty)}{(\omega_0)}\right)\right]^2 \left[\sin\left(\frac{\pi}{2} \frac{(\omega - 2\omega_0 + \omega_\infty)}{(\omega_0)}\right)\right]^2}}, \quad (5)$$

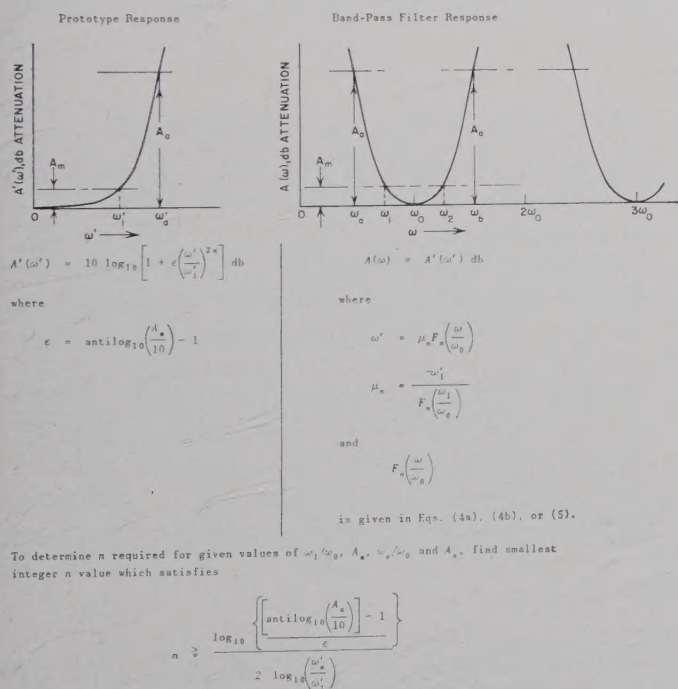


Fig. 6—Equations and parameters for maximally flat response.

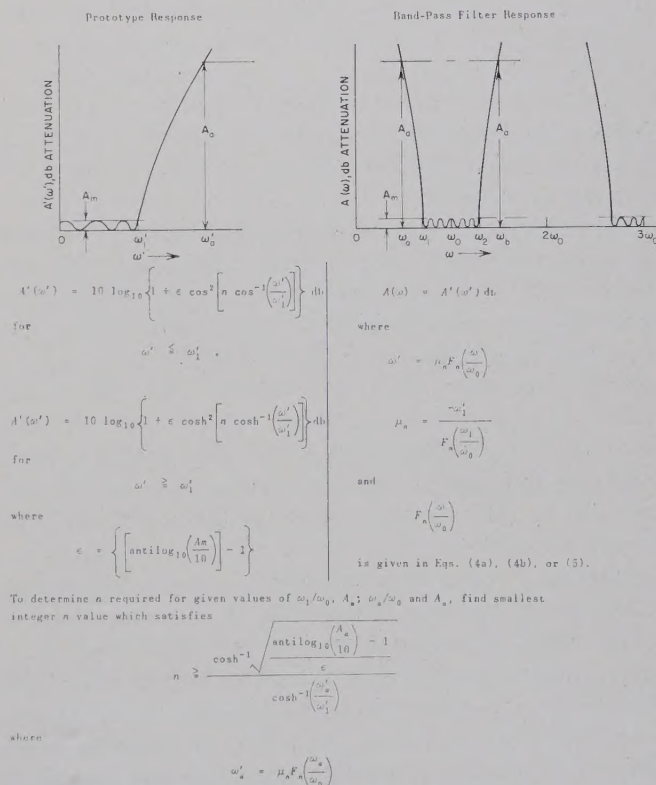


Fig. 7—Equations and parameters for Tchebycheff response.



where  $\omega_\infty$  is a frequency of infinite attenuation, to be specified. An accurate general mapping for the circuit in Fig. 2 has not been determined.

Fig. 7 shows corresponding curves and equations for the case of filters having Tchebycheff responses. Since the choice of mappings is determined by the type of filter structure, rather than by the type of response, the functions in (4) and (5) apply as before. For both the maximally flat and Tchebycheff cases, the number of reactive elements  $n$  required in the low-pass prototype is fixed by the parameters  $\omega_1/\omega_0$ ,  $A_m$ ,  $\omega_a/\omega_0$ , and  $A_a$ . In Figs. 6 and 7, equations are given for solving for  $n$  in terms of these parameters. Since the  $F_n(\omega_a/\omega_0)$  in (4a) and (5) are also functions of  $n$ , one must estimate a value of  $n$  to use in these functions, solve for  $n$  to get an improved value, and then repeat the process. However, since the  $F_n(\omega_a/\omega_0)$  are only weak functions of  $n$ , the process will converge very quickly. In the case of (4a) and (4b), the latter equation may be easily used to obtain  $n$  accurately for narrow-band cases, and this equation will also give a fairly accurate value of  $n$  in wide-band cases. In wide-band cases, the value of  $n$  obtained using (4b) can be inserted in (4a), and the equation for  $n$  can then be used again to obtain a more accurate verification of the  $n$  value.

### C. A Design Procedure Especially Suited to Filters Realized in the Forms in Fig. 1(a) and (b)

Table I summarizes a design procedure which gives good impedance levels for filter structures such as those in Fig. 1(a) and (b). After an appropriate prototype is selected, as described above, the parameters  $g_0$ ,  $g_1$ ,  $\dots$ ,  $g_n$ ,  $g_{n+1}$ , and  $\omega_1'$  from the low-pass prototype are used along with the band-pass-filter lower-band-edge ratio,  $\omega_1/\omega_0$ , to obtain the filter design in a straightforward manner as outlined.

Fig. 8 shows the results of some trial designs obtained by using a Tchebycheff prototype having 0.10-db pass band ripple and  $n=6$  reactive elements. The curves show the response, computed by a digital computer, from the circuit element values. For Fig. 8(a),  $\omega_1/\omega_0 = 0.975$  was used, which calls for a 5 per cent bandwidth. As is seen from the figure, there is no noticeable deviation from the design objective, and points mapped from the low-pass prototype response by use of (4a) and also by (4b) are all in excellent agreement with the computed response. Fig. 8(b) shows the computed response for a design obtained using  $\omega_1/\omega_0 = 0.850$ , which calls for a 30 per cent bandwidth. In this case, there is a very slight deviation from perfect Tchebycheff character, inasmuch as two of the peaks of the pass band ripples do not quite reach the 0.10-db level. In this case, points mapped from the prototype response using (4a) are in practically perfect agreement with the filter response, while points mapped using (4b) show some noticeable error at the higher attenuation levels.

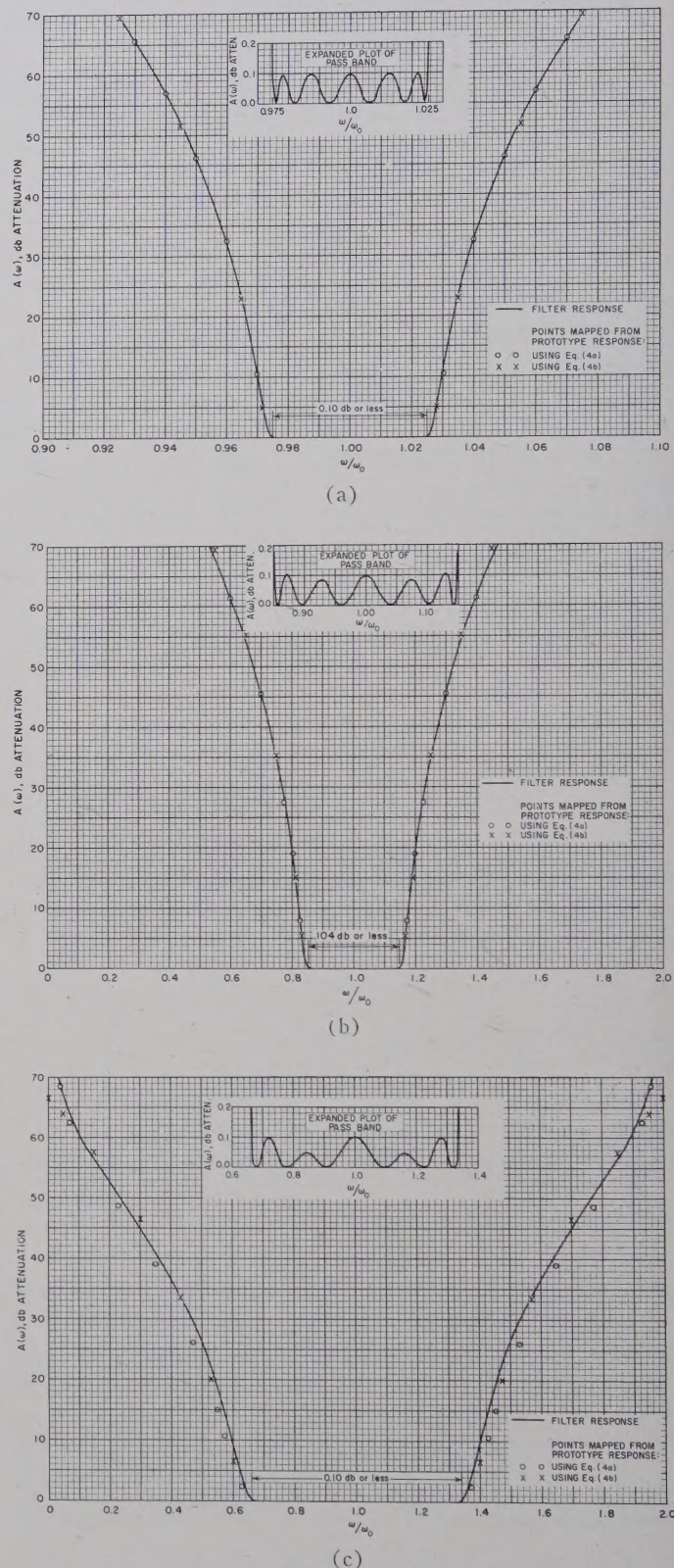


Fig. 8—(a) Computed response of filter designed as in Table I to have 5 per cent bandwidth. Design value for  $\omega_1/\omega_0$  was 0.975. Prototype had 0.10-db Tchebycheff pass band ripple with  $n=6$  reactive elements. (b) Computed response of filter designed as in Table I to have 30 per cent bandwidth. Design value of  $\omega_1/\omega_0$  was 0.850. Prototype same as (a). (c) Computed response of filter designed as in Table I to have approximately 2 to 1 bandwidth. Design value for  $\omega_1/\omega_0$  was 0.650, which calls for  $\omega_2/\omega_1 = 2.077$ . Prototype same as for (a).



Fig. 8(c) shows the computed response for a design obtained using  $\omega_1/\omega_0 = 0.650$ , which calls for a band-edge ratio of  $\omega_2/\omega_1 = 2.077$ . In this case, the deviation from a perfect response is more noticeable, the most important deviation being that the frequency ratio of the 0.10-db band-edge points is about  $\omega_2/\omega_1 = 1.96$ , instead of 2.077. All of the expected pass band ripples are present, although in this case two of the ripple peaks are reduced to half size. Points mapped from the prototype response by use of (4a) appear to fall almost exactly where the response curve would have been if the slight shrinkage in the pass band width had not occurred. Points mapped by use of (4b) weave across the computed response somewhat, but follow it surprisingly closely.

Table IV (p. 593) gives the odd- and even-mode impedances<sup>11</sup> for these filters realized in the form in Fig. 1(a). Using construction methods to be outlined later, all three of these designs should be quite practical. Filters designed by use of Table I and realized in the form in Fig. 1(a) or (b), are of special practical interest for applications where bandwidths of perhaps 50 per cent or less are desired. Although the forms in Fig. 1(a) and (b) are also practical for larger bandwidths, filters designed by Table II and realized in the form in Fig. 1(d) will have reasonable element values for large bandwidth designs and become attractive because they require two less sections to achieve a given response.

A corresponding filter designed by Cohn's equations<sup>1</sup> was compared with the 5 per cent bandwidth filter described herein, in order to compare the two design methods. The designs were found to be basically similar, except that Cohn's equations yielded slightly different end sections and a 7 per cent higher impedance level in the interior sections of the filter. For filters of about 10 per cent bandwidth or less, either method should give good designs, but Cohn's design method has an advantage of being computationally even simpler than that described herein. For bandwidths greater than about 10 or 15 per cent, the accuracy of Cohn's equations begins to deteriorate noticeably and the design equations described herein are preferable.

#### D. A Design Procedure Especially Suited to Filters Realized in the Forms in Figs. 1(c) and (d)

In the design procedure of Table I, the end sections  $S_{01}$  and  $S_{n,n+1}$  are, in a sense, primarily impedance-transforming sections. Using that design procedure, moderate impedance levels are maintained in the interior sections of filters realized in the forms in Figs. 1(a) or (b), regardless of the bandwidth of the filter, but this is achieved by not making full use of all of the natural modes of oscillation of which the circuit is capable. Using the design procedure in Table II, the end sections  $S_{01}$  and  $S_{n,n+1}$  are eliminated, and the remaining network makes full use of all possible natural modes. Table II is thus seen to call for  $n-1$  band-pass filter

sections to realize a response mapped from an  $n$ -reactive-element prototype, while the design method in Table I calls for  $n+1$  band-pass filter sections to achieve the same response. Designs obtained by Table II will usually yield impractical impedance levels for filters of the forms in Fig. 1(a) and (b), but the impedance levels are moderate for wide-band filters of the forms in Fig. 1(c) and (d). The form in Fig. 1(d), which is quite practical for wide-band designs, becomes less practical for narrow-band designs since the characteristic admittances of the shunt stubs then become quite large.

Fig. 9 shows the response of a filter designed using Table II from a 0.10-db ripple,  $n=8$ , Tchebycheff prototype with  $\omega_1/\omega_0 = 0.650$ . Table V (p. 593) shows the element values for a realization as in Fig. 1(d). In this case, the pass band ripples are more uneven than in the previous examples; however, the bandwidth suffered less shrinkage than in the previous 2 to 1 bandwidth design, whose response was shown in Fig. 8(c). In both the case of Fig. 8(c) and the case of Fig. 9, the filter has seven sections; however, it should be noted that the latter response has a steeper cutoff, since it was designed from an  $n=8$  instead of an  $n=6$  prototype. It is thus seen that points mapped from the prototype response by use of (4a) are again quite accurate, but those using (4b) show appreciable error at high attenuation levels.

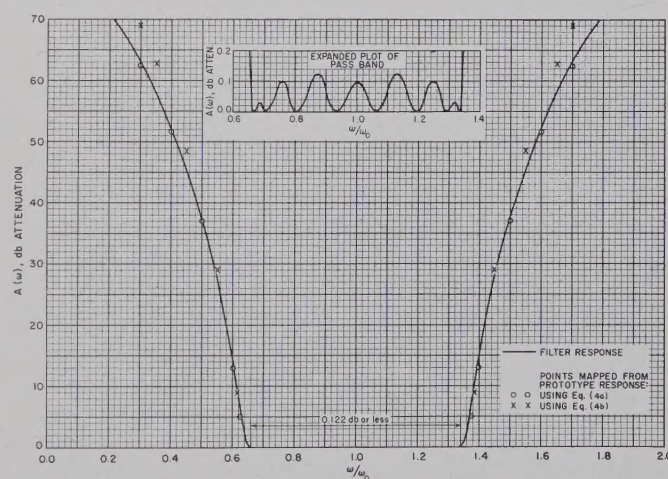


Fig. 9—Computed response of a filter designed as in Table II to have approximately 2 to 1 bandwidth. Design value for  $\omega_1/\omega_0$  was 0.650. Prototype had 0.10-db Tchebycheff pass band ripple with  $n=8$  reactive elements.

If filters in the form of Fig. 1(c) or 1(d) are desired, but with a somewhat different impedance level for their interior sections, they can be achieved by using a modified form of the calculation procedure in Table III, as is described in Section III-D.

#### E. Design of Filters in the Form in Fig. 2

Filters of the form shown in Fig. 2 can be readily designed by a modified use of Table II. The design is



carried out to first give a filter in the form in Fig. 1(d), with the desired pass band characteristic and bandwidth. Then each shunt, quarter-wavelength,<sup>15</sup> short-circuited stub of characteristic admittance  $Y_k$  is replaced, as shown in Fig. 2, by a shunt, half-wavelength, open-circuited stub having an inner quarter-wavelength portion with a characteristic admittance,

$$Y_k' = \frac{Y_k(a \tan^2 \theta_1 - 1)}{(a + 1) \tan^2 \theta_1}, \quad (6)$$

and an outer quarter-wavelength portion with a characteristic admittance,

$$Y_k'' = a Y_k'. \quad (7)$$

The parameter  $a$  is fixed by

$$a = \cot^2 \left( \frac{\pi \omega_\infty}{2\omega_0} \right) \bigg|_{(\omega_\infty/\omega_0) < (\omega_1/\omega_0)}, \quad (8)$$

where  $\theta_1 = \pi \omega_1 / 2\omega_0$ , and  $\omega_\infty$  is a frequency at which the shunt lines present short circuits to the main line and cause infinite attenuation. The principle upon which the above substitution is made is that (6) to (8) are constrained to yield half-wavelength open-circuited stubs, which have exactly the same susceptance at the band-edge frequency  $\omega_1$ , as did the quarter-wavelength short-circuited stubs that they replace, while both kinds of stubs have zero admittance at  $\omega_0$ .

To test out this procedure, a filter was designed as in Table II to give 30 per cent bandwidth ( $\omega_1/\omega_0 = 0.850$ ) using a 0.10-db Tchebycheff prototype with  $n=8$ . Then, choosing  $\omega_\infty/\omega_0 = 0.500$ , which gives  $a=1$ , the quarter-wavelength stubs were replaced by half-wavelength stubs as described above, and the resulting computed response is shown in Fig. 10. Note that the pass band is almost exactly as prescribed, and that there are low attenuation regions in the vicinity of  $\omega=0$  and  $\omega=2\omega_0$ , which are to be expected. The element values for this filter are shown in Table VI (p. 593).

The 2 to 1 bandwidth filter design (Fig. 9 and Table V) was also converted to this form using  $\omega_\infty/\omega_0 = 0.500$ , and its response was computed. The features of the pass band looked much the same as those in the expanded plot in Fig. 9, while the stop bands consisted of very sharp attenuation spikes surrounding  $\omega/\omega_0 = 0.500$ , in a manner similar to that in Fig. 10, except that the attenuation bands were much narrower.

Filters of the form in Fig. 2 should be particularly useful where the pass bands around  $\omega=0$  and  $\omega=2\omega_0$  are not objectionable, and where there is a relatively narrow band of signals to be rejected. By the proper choice of  $\omega_\infty$ , the infinite attenuation point can be placed so as to give maximum effectiveness against the

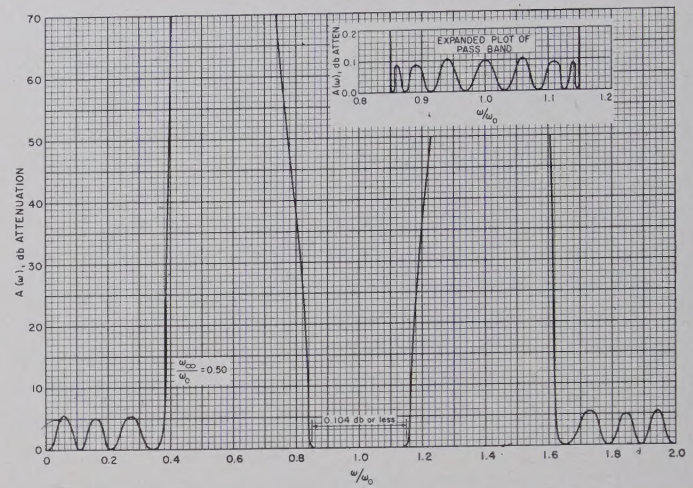


Fig. 10—Computed response of a 30 per cent band-pass filter designed in the form in Fig. 2. Design value for  $\omega_1/\omega_0 = 0.850$ . Prototype had 0.10-db Tchebycheff ripple with  $n=8$  reactive elements.

unwanted signals. Filters of the form in Fig. 2 are more practical for narrower bandwidths than are those in the form in Fig. 1(d), because of the larger susceptance slope of half-wavelength stubs for a given characteristic admittance. For example, in the case of Fig. 10, the shunt stubs for this filter as shown in Fig. 2 have characteristic admittances  $Y_k' = Y_k''$ , which are 0.471 times the characteristic admittances of the shunt stubs of the analogous filter in the form in Fig. 1(d), from which it was designed. Thus narrower bandwidths can be achieved without having the characteristic admittances of the shunt stubs become excessive.

#### F. Design of Filters in the Form in Fig. 3

For filters of the form in Fig. 3, the mapping function in (5) should be used along with the equations in Table III. In this case  $\omega_\infty$  is the frequency of infinite attenuation created by the half-wavelength series stubs at the ends. The parameter  $d$  may be chosen to adjust the impedances of the interior of the filter to a convenient level.

This type of filter gives a cross between the type of response obtained using a filter as in Fig. 1(d), and that obtained by a filter as in Fig. 2. At first, a design of the form in Fig. 1(d) was tried, but with the end stubs (only) replaced with shunt half-wavelength open-circuited stubs. This gave infinite attenuation at  $\omega=0$  and  $\omega_\infty$  as expected, but yielded a point of very low attenuation (around 10 db) between these two frequencies (and between other corresponding frequencies). It was then found that by using an altered design procedure which yields series half-wavelength short-circuited stubs at the ends, the desired type of response could be obtained without excessive drop in attenuation between  $\omega=0$  and  $\omega_\infty$ .

<sup>15</sup> The reference wavelength is that at the mid-band frequency  $\omega_0$



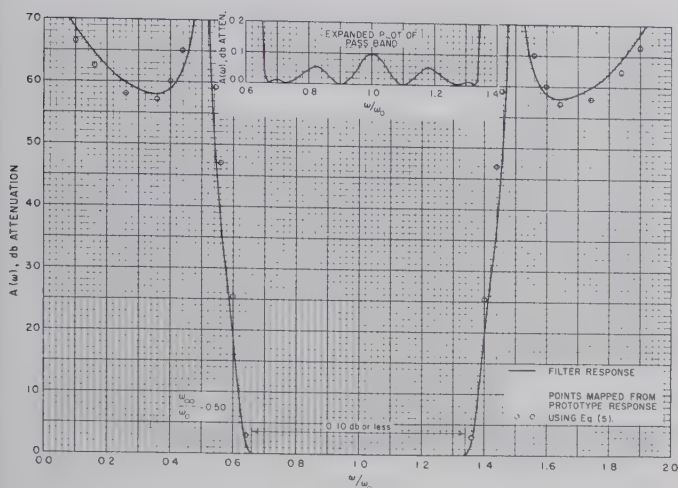


Fig. 11—Computed response of a filter as in Fig. 3, with approximately 2 to 1 bandwidth. Design value for  $\omega_1/\omega_0$  was 0.650. Prototype had 0.10-db Tchebycheff ripple with  $n=8$  reactive elements. Parameters  $d$  and  $\omega_\infty/\omega_0$  were both chosen as 0.500.

Fig. 11 shows the computed response of a filter designed using Table III to give approximately 2 to 1 bandwidth. The prototype, again, had 0.10-db Tchebycheff ripple, and  $n=8$ . The remaining design parameters were  $\omega_1/\omega_0=0.650$ ,  $\omega_\infty/\omega_0=0.500$ , and  $d=0.500$ . In this case the pass band ripples are not as well developed as in the previous examples. It has been found that the design theory used herein works best if all of the sections are of the same basic form; since the end sections are different from the other sections in this case, the larger deviation from a 0.10-db equal-ripple response is not surprising. (From a practical standpoint, this deviation may be good, since the ripples are small at the band edges, where incidental dissipation will tend to increase the pass band loss most.) Points mapped from the prototype response using (5) are seen to come fairly close to the computed response, although not as close as (4a) did where it was applicable. Both (4a) and (5) were derived on the same basis and should probably yield similar accuracy. The larger deviations in this case are probably due at least in part to the fact that the pass band response itself deviates more from the design objective. The element values for this filter design are given in Table VII (p. 593).

### G. Suggested Ways for Fabricating the Filters Under Consideration

For bandwidths of perhaps around 20 per cent or less, filters of the form in Fig. 1(a) are readily realized in printed-circuit form by use of Cohn's data for zero-thickness parallel-coupled strips.<sup>1,16</sup> Larger bandwidths

are difficult using this construction, because the gaps between the conductors must become extremely small. A suggested way for getting around this problem while still using printed circuit construction is shown in Fig. 12. Instead of just two slabs of dielectric, four slabs are used, two of which are relatively thin. Then alternate conductors are printed to form a double layer, as shown in the cross-sectional view, so that the adjacent conductors can be interleaved. This gives a relatively large odd-mode capacitance without the need for extremely close spacings. The cross section of the conductors is no longer balanced geometrically; however, by proper design, the even- and odd-mode impedances for both the single- and double-layer conductors can be made the same.

Fig. 13 shows a suggested way for realizing filters of the type in Fig. 1(b). In this case, the conductors are rectangular bars supported mechanically by the short circuits at their ends. This construction can be used for either narrow- or wide-band filters and has the advantages of not requiring dielectric material (hence having no dielectric loss), and, with rounded corners on the conductors, of having relatively high power-handling capability.

Fig. 14(a) shows a possible way for building filters of the type in Fig. 1(d). This filter uses mostly double stubs instead of single stubs, so that the cross-sectional dimensions of the stubs (and the junction discontinuities) can be made smaller. It was designed in thick bar strip-line construction, in order to reduce the junction discontinuity effects and to make these effects less frequency-sensitive.<sup>17</sup> This filter was designed for a 2.2 to 1 bandwidth from a 0.10-db Tchebycheff ripple ten-reactive-element prototype. Three additional sections identical with the middle sections of the  $n=10$  design were added in order to increase the rate of cutoff. This gave a resulting design which is not quite the same as a true  $n=13$ , 0.10-db-ripple Tchebycheff design, but the difference is small. As can be seen from the measured results in Fig. 14(b), the response is close to the theoretical.

It has been observed that any of the types of filters in Figs. 1, 2, or 3 may have narrow spurious pass bands, at frequencies in the vicinity of  $f=2f_0$ , if there is deviation from perfect tuning in one part of a filter with respect to the rest of the filter. Since small deviations from perfect tuning are difficult to avoid, some measures should be taken to suppress these spurious pass bands if they are objectionable for the application

<sup>16</sup> S. B. Cohn, *et al.*, "Strip Transmission Lines and Components," Stanford Res. Inst., Menlo Park, Calif., Final Rept., SRI Project 1114, Contract DA-36-039 SC-63232, ch. 3; February, 1957. Also, S. B. Cohn, "Shielded coupled-strip transmission line," IRE TRANS. ON MICROWAVE THEORY AND TECHNIQUES, vol. MTT-3, pp. 29-38; October, 1955.

<sup>17</sup> P. S. Carter, Jr., G. L. Matthaei, and W. J. Getsinger, "Design Criteria for Microwave Filters and Coupling Structures," Stanford Res. Inst., Menlo Park, Calif., Tech. Rept. 8, pt. 3, SRI Project 2326, Contract DA 36-039 SC-7462. This reference discusses reasons why this bar construction is expected to have less junction discontinuity effect than either thin strip transmission line or coaxial line construction of equivalent size. It also discusses other practical matters with respect to the design of this type of filter.



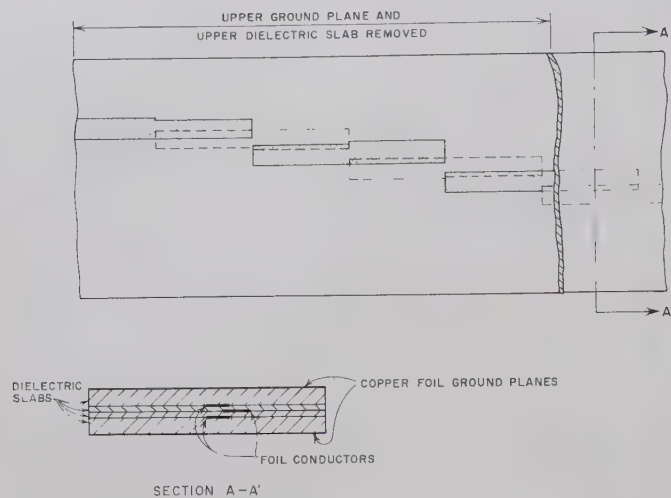


Fig. 12—Possible means for fabricating wide-band filters of the type in Fig. 1(a), using printed circuit techniques. (In order to achieve tight coupling with reasonably large conductor spacings, alternate conductor strips are made to be double so that conductor strips can be interleaved. This construction is electrically balanced with respect to the ground planes and will not excite ground plane modes, as would overlapped strips which did not interleave.)

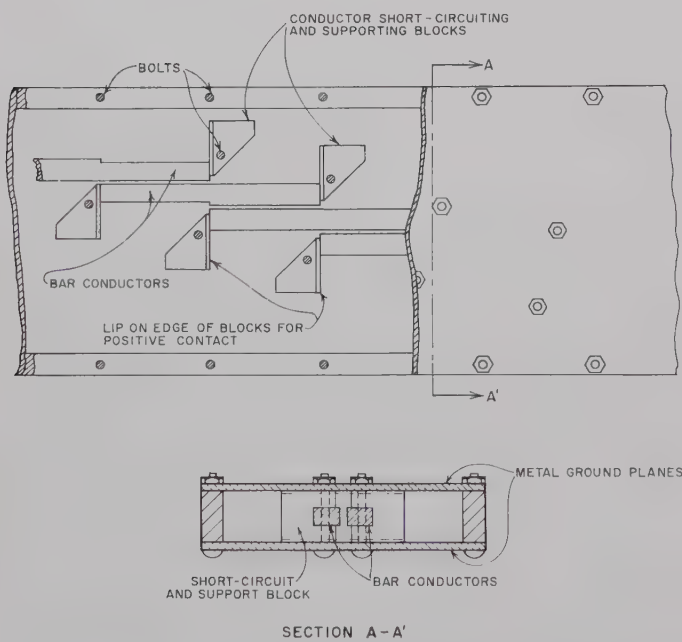
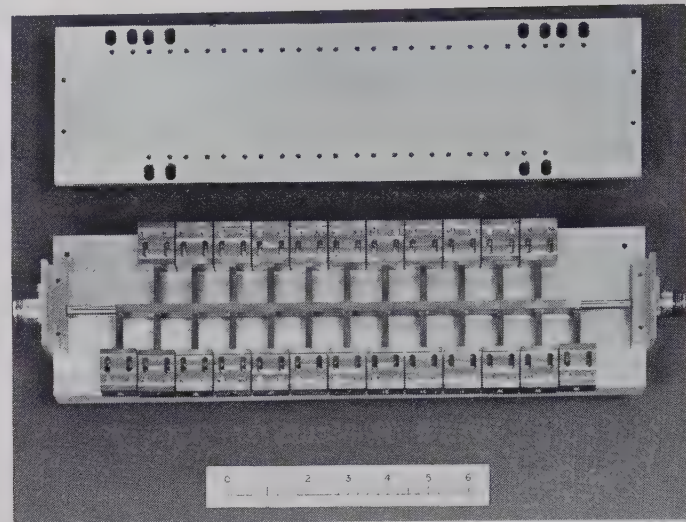
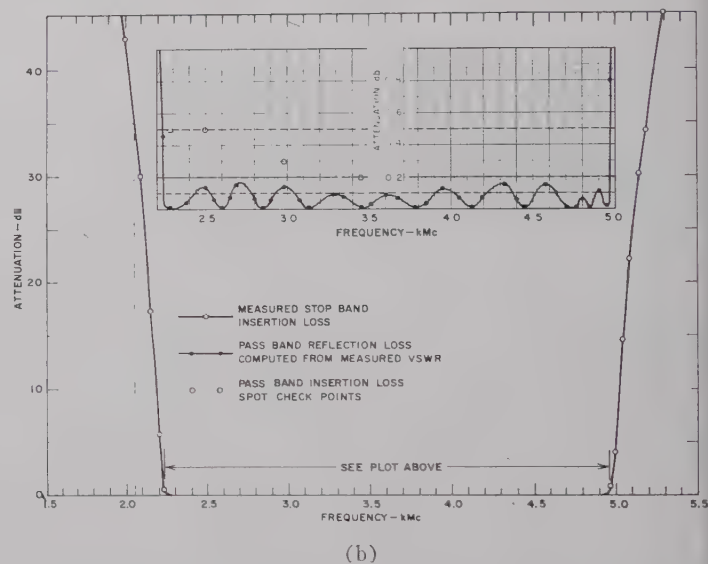


Fig. 13—Possible means for fabricating wide-band filters of the type in Fig. 1(b), in bar-transmission-line construction. (The short-circuiting blocks support the bar conductors so that no dielectric material is required.)

at hand. A possible way of suppressing such responses is to use a filter of the form in Fig. 3, with  $a = \infty$ , so that the series stubs become open-circuited stubs one-quarter-wavelength long at  $f_0$ . Although this has not been tested as yet, it appears reasonable that series stubs of this sort can be used to maintain high attenuation in the vicinity of  $2f_0$ , since they present large series reactances at frequencies in the vicinity of  $2f_0$ , while the spurious responses in the shunt-stub portion of the



(a)



(b)

Fig. 14—(a) Filter of the type in Fig. 1(d) with cover plate removed. Rectangular bar strip transmission line construction is used. The blocks along the sides of the filter short circuit the stubs and support the center-conductor structure. (b) Measured response of the filter in Fig. 14(a). The dissipation loss can be reduced by silver plating since the filter as tested used a brass inner structure with aluminum cover plates.

filter are due to large shunt susceptances of opposite signs cancelling each other. Quarter-wavelength or half-wavelength series stubs, such as those in Fig. 3, can be realized as coaxial structures within the center conductor of the filter.<sup>6</sup>

### III. THEORETICAL BASIS FOR THE FILTER EQUATIONS AND MAPPING FUNCTIONS

#### A. Modified Prototypes as a Basis for Design

The first step in deriving the design equations used herein is to convert the low-pass prototype (Fig. 5) to a modified form that involves impedance inverters or admittance inverters. The concept of impedance inverters has previously been discussed in detail by



Cohn;<sup>18</sup> admittance inverters are simply the dual representations of impedance inverters, and are introduced only for convenience. Fig. 15 summarizes the basic properties of these two types of inverters.

Using methods similar to those of Cohn,<sup>18</sup> any circuit like that in Fig. 5 may be converted into either of the dual forms in Fig. 16. In Fig. 16(a), which uses impedance inverters, all of the elements  $R_g, L_{a1}, L_{a2}, \dots, L_{an}, R_L$  may be chosen arbitrarily; the inverter parameters  $K_{k,k+1}$  are then computed as indicated.

Analogous conditions hold for the dual circuit at (b) in Fig. 16. In the discussion to follow, the impedance (or admittance) inverters will be assumed to be idealized so that their electrical behavior is exactly as indicated in Fig. 15. They will be used merely as an aid to mathematical reasoning, and no direct attempt will be made to find a circuit which approximates their idealized performance. Instead, as indicated below, the approximations will be based upon the impedance inverters plus part of each adjacent element.

B. Procedure for Deriving the Equations in Table I

The design equations in Table I are based on the modified prototype shown at (a) in Fig. 16, while Fig. 17 shows the manner in which the element values are specified, and the manner in which the prototype is broken into sections. The image impedance,  $Z_{k,k+1}^i(\omega')$ , and phase,  $\beta_{k,k+1}$  (in the pass band) for each of the prototype interior sections ( $S_{12}'$  to  $S_{n-1,n}'$ ) are readily shown to be

$$Z_{k,k+1}^i(\omega') = K_{k,k+1} \sqrt{1 - \left( \frac{\omega' (L_a/2)}{K_{k,k+1}} \right)^2} \quad (9)$$

and

$$\beta_{k,k+1} = \left|_{\omega' \leq (K_{k,k+1}) / (L_a/2)} \right. = \sin^{-1} \left[ \frac{\omega' (L_a/2)}{K_{k,k+1}} \right] \pm \frac{\pi}{2}, \quad (10)$$

where, as before,  $\omega_1'$  is the cutoff frequency for the low-pass prototype. The choice of  $\pm \pi/2$  in (10) depends on whether the inverter is taken to have  $\pm 90$  degrees phase shift. The work of Jones and Bolljhan shows<sup>11</sup> that the image impedance and pass band image phase for a parallel-coupled section as shown in Fig. 4(a) are given by

$$Z_I = \frac{\sqrt{(Z_{oe} - Z_{oo})^2 + (Z_{oe} + Z_{oo})^2 \cos^2 \theta}}{2 \sin \theta} \quad (11)$$

and

$$\beta = \cos^{-1} \left[ \left( \frac{Z_{oe} + Z_{oo}}{Z_{oe} - Z_{oo}} \right) \cos \theta \right], \quad (12)$$

where  $\theta = \pi\omega/2\omega_0$ , and where  $Z_{oe}$  and  $Z_{oo}$  are the even- and odd-mode line impedances, respectively. The

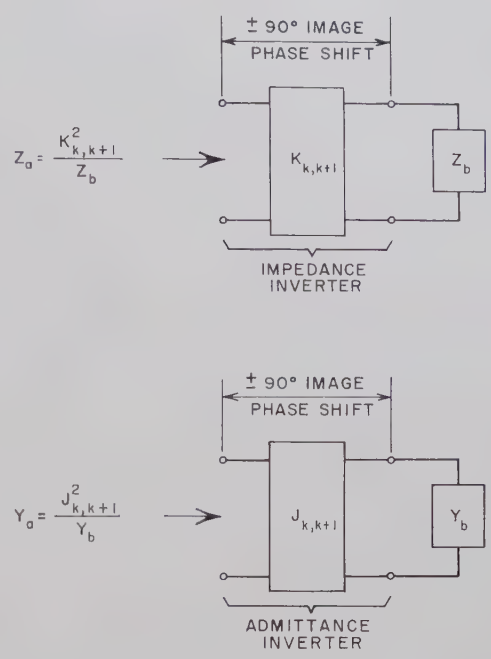


Fig. 15—Definition of impedance inverters and admittance inverters.

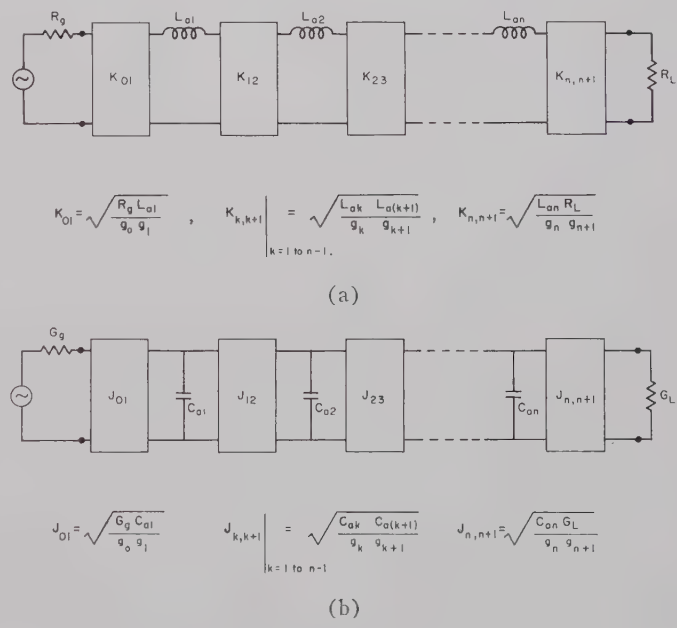


Fig. 16—Low-pass prototypes modified to include impedance inverters or admittance inverters. (The  $g_0, g_1, \dots, g_n, g_{n+1}$  are obtained from the original prototype as in Fig. 5, while the  $R_g, L_{a1}, \dots, L_{an}$ , and  $R_L$  or the  $G_g, C_{a1}, \dots, C_{an}$ , and  $G_L$  may be chosen as desired.) (a) modified prototype using impedance inverters. (b) Modified prototype using admittance inverters.

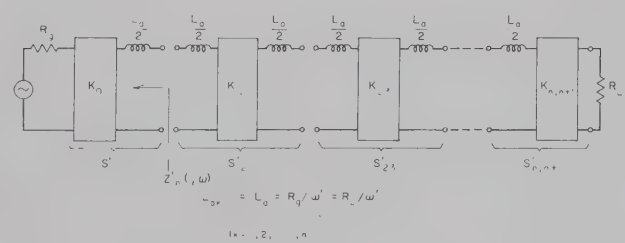


Fig. 17—Modified prototype for deriving the design equations in Table I.

<sup>18</sup> Cohn, *et al.*, *op. cit.*, footnote 1 (SRI Rept.), ch. 2. Also, S. B. Cohn, "Direct-coupled-resonator filters," *Proc. IRE*, vol. 45, pp. 187-196; February, 1957.



parameters of the parallel-coupled sections  $S_{12}$  to  $S_{n-1,n}$  in Fig. 1(a) are related to the prototype sections  $S_{12}'$  to  $S_{n-1,n}'$  of the prototype by forcing the following correspondences between the two structures:

- (a) The image phase of the parallel-coupled sections when  $\omega = \omega_0$  must be the same as the image phase of the prototype sections when  $\omega' = 0$ .
- (b) The image impedances of the parallel-coupled sections when  $\omega = \omega_0$  must be the same (within a scale factor  $s$ )<sup>19</sup> as the image impedances of the corresponding prototype sections when  $\omega' = 0$ .
- (c) The image impedance of the parallel-coupled sections when  $\omega = \omega_1$  must be the same (within a scale factor  $s$ )<sup>19</sup> as the image impedances of the corresponding prototype sections when  $\omega' = \omega_1'$ .

(13)

Correspondence (a) is fulfilled in this case by choosing the  $+$  sign in (10). Equating (9) and (11) and evaluating each side at the appropriate frequencies indicated above, two equations are obtained from which the equations in part (b) of Table I may be derived (with the help of the information in Figs. 16 and 17) by solving for  $Z_{oe}$  and  $Z_{oo}$ .

The end sections,  $S_{01}$  and  $S_{n,n+1}$ , must be treated as a special case. Defining  $Z_{in}(j\omega)$  as the impedance seen looking in the right end of the parallel-coupled section  $S_{01}$  in Fig. 1(a), with the left end connected to the input line of impedance  $Z_0$ , the following correspondences are forced with respect to  $Z_{in}'(j\omega)$  indicated in Fig. 17:

- (a)  $\text{Re } Z_{in}(j\omega_0) = \text{Re } Z_{in}(j\omega_1)$  for the parallel-coupled terminating circuit, just as  $\text{Re } Z_{in}'(j0) = \text{Re } Z_{in}'(-\omega_1')$  for the terminating circuit of the prototype.
- (b)  $\text{Im } Z_{in}(j\omega_1) / \text{Re } Z_{in}(j\omega_1)$  must equal  $X'/R' = \text{Im } Z_{in}'(-j\omega_1') / \text{Re } Z_{in}'(-j\omega_1')$  computed from the prototype.

Defining

$$P = \frac{(Z_{oe})_{01} - (Z_{oo})_{01}}{R_0 2 \sin \theta_1}, \quad (15)$$

and

$$Q = \frac{(Z_{oe})_{01} + (Z_{oo})_{01}}{R_0 2 \tan \theta_1}, \quad (16)$$

it can be shown that correspondence (a) in (14) will be obtained if

$$Q = \cot \theta_1 \quad (17)$$

<sup>19</sup> Taking  $R_0 = R_L = Z_0$ .

is satisfied, where  $\theta = \pi\omega_1/2\omega_0$ . Further, correspondence (b) requires that

$$Q^3 + Q(1 - P^2) + \frac{X'}{R'} P^2 = 0 \quad (18)$$

be satisfied. Substituting (17) in (18), and solving for  $(Z_{oe})_{01}$  and  $(Z_{oo})_{01}$  yields the results in part (a) of Table I. Even if  $R_0 = Z_0$ , the above conditions will generally result in an impedance level for  $Z_{in}(j\omega)$  of the band-pass filter, which is different than that of  $Z_{in}'(j\omega')$  for the prototype. The impedances of the interior sections must therefore be corrected by multiplying by the scale factor  $s$  indicated in Table I.

### C. Procedure for Deriving the Equations in Table II

Fig. 18 shows the manner in which the modified prototype at (a) in Fig. 16 is broken into sections and the elements specified for deriving the equations in Table II. Note that in this case the end impedance inverters,  $K_{01}$  and  $K_{n,n+1}$ , are both made equal to the terminating resistances  $R_0 = R_L$ . For the end inductances,  $L_{a1} = L_{an} = R_0 g_0 g_1$ ; however,  $L_{a2} = L_{a3} = \dots = L_{a,n-1}$  are made equal to  $2L_{a1}$  so that the structure can be broken into symmetrical sections without the need for end sections. Using the indicated values for the  $L_{ak}$ , the  $K_{k,k+1}$  are obtained by use of Fig. 16. Then all of the sections are designed by use of (9)–(12) and the correspondences given in (13).

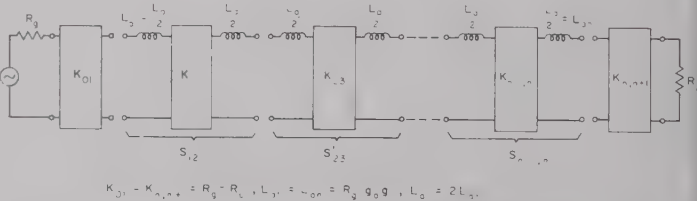


Fig. 18—Modified prototype for deriving the equations in Table II.

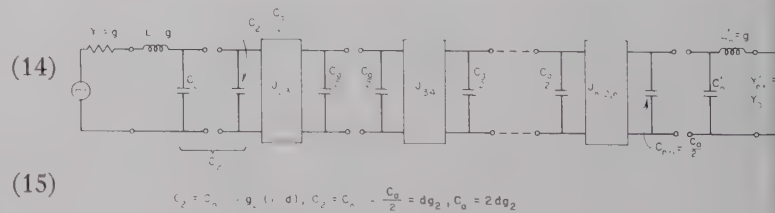


Fig. 19—Modified prototype for deriving the equations in Table III. Parameter  $d$  may be used to adjust the impedance level in the center part of the filter. In the example of Fig. 11,  $d$  was chosen as one-half, to split  $C_2 = C_2' + C_2''$  in half.

### D. Procedure for Deriving the Equations in Table III

Fig. 19 shows the modified prototype used for deriving the equations in Table III. In this case, most of the structure is in the form shown in Fig. 16(b). However, inverters  $J_{01}$ ,  $J_{12}$ ,  $J_{n-1,n}$ , and  $J_{n,n+1}$  have been omitted. Here,  $L_1$  and  $C_2$  have the same values that they had in



their original prototype form in Fig. 5. Capacitor  $C_2$  is split into two parts,  $C_2'$  and  $C_2''$ , and the parameter  $d$  is used to establish what fraction of  $C_2$  becomes  $C_2''$ . Then the capacitance values  $C_{a3}=C_{a4}=\dots=C_{a,n-2}$  are established, so that all of the interior sections can be broken into symmetrical sections. The interior sections are then related to parallel-coupled sections, as in Fig. 4(b) by dual procedures to those used for the interior sections for Tables I and II. The parallel-coupled sections are then converted to stub form by the equivalence in Fig. 4(b). The end sections are designed by forcing the stubs to have reactances at  $\omega=\omega_0$  and  $\omega=\omega_1$  (on a normalized basis) which are the same as those of the corresponding prototype elements  $L_1$  and  $C_2'$ , at  $\omega'=0$  and  $\omega'=-\omega_1'$ , respectively.

This same general viewpoint should be useful for designing filters in the form in Fig. 1(c) and (d) to give some desired impedance level in the interior part of the filter. To accomplish this, the prototype in Fig. 18 should be converted to its dual form analogous to that shown in Fig. 16(a). Then, the capacitor  $C_1$  is split, just as  $C_2$  is split in Fig. 19. The resulting design equations are

$$C_a = 2dg_1, \quad \frac{J_{12}}{Y_0} = \frac{J_{n-1,n}}{Y_0} = \frac{g_0\sqrt{g_1C_a}}{\sqrt{g_1g_2}},$$

$$\left. \frac{J_{k,k+1}}{Y_0} \right|_{k=2 \text{ to } n-2} = \frac{g_0C_a}{\sqrt{g_kg_{k+1}}},$$

$$M_{k,k+1} = \sqrt{\left(\frac{J_{k,k+1}}{Y_0}\right)^2 + \left(\frac{g_0\omega_1' C_a \tan \theta_1}{2}\right)^2},$$

$$Y_{k,k+1}^{\circ} \Big|_{k=1 \text{ to } n-1} = Y_0 \left( M_{k,k+1} - \frac{J_{k,k+1}}{Y_0} \right),$$

$$Y_1 = Y_n = g_0 Y_0 \omega_1' (1-d) g_1 \tan \theta_1 + Y_{12}^{\circ},$$

$$Y_k \Big|_{k=2 \text{ to } n-1} = Y_{n-k+1} = Y_{k-1,k}^{\circ} + Y_{k,k+1}^{\circ},$$

$$Y_{k,k+1} \Big|_{k=1 \text{ to } n-1} = Y_{n-k,n-k+1} = J_{k,k+1}.$$

Although this technique has been used successfully for achieving small adjustments in impedance level within a filter, the filter-response accuracy resulting when this technique is used to achieve large changes in impedance level has not been tested.

### E. Selection of Mapping Functions

Previous work of Cohn,<sup>1</sup> and also the plots presented herein, show that when the function in (4b) is used as indicated in Fig. 6 or 7 to map the response of a low-pass prototype, it will predict quite accurately the response of band-pass filters of the form in Fig. 1(a) having narrow or moderate bandwidth. Although the function in (4b) is very useful, it should not be expected to give high accuracy for wide-band cases because it is not periodic (which the filter response is), nor does it go to infinity for  $\omega=0, 2\omega_0, 4\omega_0$ , etc., which is necessary in

order to predict the infinite attenuation frequencies in the response of the band-pass filter structure. It might at first seem that

$$F_n\left(\frac{\omega}{\omega_0}\right) = -\cot\left(\frac{\pi\omega}{2\omega_0}\right) \quad (19)$$

would solve this problem nicely, since it is periodic as desired, it varies similarly to (4b) in the vicinity of  $\omega_0$ , and it has poles at the desired frequencies  $\omega=0, 2\omega_0, 4\omega_0$ , etc. However, if the structures in Fig. 1 are analyzed, it will be seen that no matter what value of  $n$  is used, the poles of attenuation at  $\omega=0, 2\omega_0, 4\omega_0$ , etc., are always first-order poles.<sup>20</sup> Meanwhile, an  $n$ -reactive-element prototype as in Fig. 5 (which will have an  $n$ th-order pole at  $\omega'=\infty$ ) will map so as to give  $n$ th order poles at  $\omega=0, 2\omega_0$ , etc., if the function in (19) is used. This important source of error is corrected in the case of (4a) by replacing  $\cot(\pi\omega/2\omega_0)$  by  $\cos(\pi\omega/2\omega_0)/|\sin(\pi\omega/2\omega_0)|$ , and then taking the  $n$ th root of the denominator. In this manner, the poles generated by the zeros of  $|\sin(\pi\omega/2\omega_0)|$  become of  $1/n$  order, which causes the  $n$ th-order pole at  $\omega'=\infty$  for the prototype response to map into first-order poles of the band-pass filter response at the desired frequencies.

In the case of the circuit in Fig. 3, the poles of attenuation at  $\omega=0, 2\omega_0, 4\omega_0$ , etc., will again always be of first order regardless of the value of  $n$  used. However, the series stubs at each end produce second-order poles at the frequency  $\omega_{\infty}$  and at other corresponding points in the periodic response.<sup>21</sup> Thus, the

$$\sqrt[n]{|\sin(\pi\omega/2\omega_0)|}$$

factor in the denominator of (5) assures that the  $n$ th-order poles at  $\omega'=\infty$  in the prototype response will always map to first-order poles at  $\omega=0, 2\omega_0$ , etc., for the band-pass filter response. In addition, the factor

$$\sqrt[n]{\left[\sin\left(\frac{\pi}{2}\frac{(\omega-\omega_{\infty})}{\omega_0}\right)\right]^2\left[\sin\left(\frac{\pi}{2}\frac{(\omega-2\omega_0+\omega_{\infty})}{\omega_0}\right)\right]^2}$$

is introduced to cause the  $n$ th-order pole at infinity in the prototype response to map to second-order poles at  $\omega_{\infty}$  (and other periodic points) for the band-pass filter

<sup>20</sup> For example, for the filter form in Fig. 1(d), as  $\omega \rightarrow 0$  the effect of all of the shunt stubs can be reduced to that of a single shunt zero-impedance branch which would produce a first-order pole of attenuation  $\omega=0$ . (One way in which higher-order poles can be generated is to produce shunt zero-impedance branches alternating with series branches having infinite impedance.)

<sup>21</sup> This can be seen as follows: For  $\omega=\omega_{\infty}$ , each of the series stubs represents an infinite-impedance series branch. For this single frequency, the interior part of the filter can be replaced by an equivalent T-section with a finite shunt impedance. Thus, the structure can be reduced (for the frequency  $\omega_{\infty}$ ) to two series infinite-impedance branches separated by a finite shunt-impedance branch. This can be seen to result in a second-order pole of attenuation. (If the impedance of the equivalent shunt branch had been zero, the pole of attenuation would have been raised to third order.)



response. In this manner, all of the proper poles of attenuation are introduced with their proper order.

These principles can also be applied to the structure in Fig. 2, but this structure presents some new difficulties. It can be seen that this structure will develop  $n$ th-order poles of attenuation at  $\omega_\infty$  and corresponding periodic points, but the half-wavelength stubs also introduce additional natural modes of oscillation which create, in addition to the desired pass band, a low-pass pass band (and corresponding periodic pass bands) as shown in the response in Fig. 10. This additional low-pass pass band approaches  $\omega_\infty$  quite closely, with the result that, although the pole at  $\omega_\infty$  is of relatively high order, its effectiveness is weakened by the close proximity of this low-pass pass band. The function

$$F_n\left(\frac{\omega}{\omega_0}\right) = \tan\left(\frac{\pi\omega}{\omega_0}\right) \quad (20)$$

for the case of  $\omega_\infty/\omega_0 = 0.50$  would map the prototype response to give a low-pass pass band, an  $n$ th-order pole at  $\omega_\infty$ , and the desired pass band centered at  $\omega_0$ . However, it would not properly predict how close the low-pass pass band comes to  $\omega_\infty$ , nor could it account for the oversize attenuation ripples which occur in this band (Fig. 10). As a result, the function in (20) predicts an overly optimistic rate of cutoff at the edges of the pass band centered at  $\omega_0$ . It is probable that a useful approximation could be obtained by using a mapping function, such as that in (20), with additional factors

TABLE I

DESIGN EQUATIONS ESPECIALLY SUITED FOR FILTERS OF THE FORM IN FIG. 1(a) AND (b)

Use mapping (4a) or (4b) and Fig. 6 or 7 to select prototype having required value of  $n$ . Equations below are for filters in the form of Fig. 1(a). There are  $n+1$  parallel-coupled sections for an  $n$ -reactive-element prototype when using the design procedure below.

(a) Sections  $S_{01}$  and  $S_{n,n+1}$

$$\begin{aligned} \frac{K_{01}}{Z_0} &= \frac{1}{\sqrt{g_0 g_1 \omega_1'}} = \frac{K_{n,n+1}}{Z_0}, & \theta_1 &= \frac{\pi \omega_1}{2 \omega_0} \\ Q &= \cot \theta_1, & P &= \sqrt{\frac{Q(Q^2 + 1)}{Q + \frac{1}{2(K_{01}/Z_0)^2}}} \\ s &= Z_0 \left( \frac{P \sin \theta_1}{K_{01}/Z_0} \right)^2 \\ (Z_{oe})_{01} &= (Z_{oe})_{n,n+1} = Z_0(1 + P \sin \theta_1) \\ (Z_{oo})_{01} &= (Z_{oo})_{n,n+1} = Z_0(1 - P \sin \theta_1) \end{aligned}$$

(b) Sections  $S_{12}$  to  $S_{n-1,n}$

$$\begin{aligned} \frac{K_{k,k+1}}{Z_0} &= \frac{1}{\omega_1' \sqrt{g_k g_{k+1}}}, & N_{k,k+1} &= \sqrt{\left( \frac{K_{k,k+1}}{Z_0} \right)^2 + \frac{\tan^2 \theta_1}{4}} \\ (Z_{oe})_{k,k+1} &= (Z_{oe})_{n-k,n-k+1} = s \left( N_{k,k+1} + \frac{K_{k,k+1}}{Z_0} \right) \\ (Z_{oo})_{k,k+1} &= (Z_{oo})_{n-k,n-k+1} = s \left( N_{k,k+1} - \frac{K_{k,k+1}}{Z_0} \right) \end{aligned}$$

where  $\theta_1$  and  $s$  are defined as in (a) above and  $k=1, 2, \dots, n-1$ .

added which create zeros in  $F_n(\omega/\omega_0)$ , close to, but somewhat off, the  $j\omega$  axis (regarded from the complex-frequency point of view). Proper location of these zeros could then be used to extend the low-pass pass band upwards toward  $\omega_\infty$ , which should give the proper effect.

TABLE II

DESIGN EQUATIONS FOR FILTERS ESPECIALLY SUITED FOR REALIZATION IN THE FORM IN FIG. 1(c) AND (d)

Use mapping (4a) or (4b) and Figs. 6 or 7 to select prototype. Equations below are for filters in the form of Fig. 1(a), but they are readily converted to the form in Fig. 1(c) or (d) by use of Fig. 4. Using these equations, sections  $S_{01}$  and  $S_{n,n+1}$  are omitted, and there will be  $n-1$  parallel-coupled sections for an  $n$ -reactive-element prototype.

Sections  $S_{12}$  to  $S_{n-1,n}$

$$\begin{aligned} \frac{K_{12}}{Z_0} &= \frac{K_{n-1,n}}{Z_0} = \frac{\sqrt{2g_0 g_1}}{\sqrt{g_1 g_2}}, \\ \frac{K_{k,k+1}}{Z_0} \Big|_{k=2 \text{ to } n-2} &= \frac{K_{n-k,n-k+1}}{Z_0} = \frac{2g_0 g_1}{\sqrt{g_k g_{k+1}}}, \\ \theta_1 &= \frac{\pi}{2} \frac{\omega_1}{\omega_0}, & N_{k,k+1} &= \sqrt{\left( \frac{K_{k,k+1}}{Z_0} \right)^2 + (\omega_1' g_0 g_1 \tan \theta_1)^2} \\ (Z_{oe})_{k,k+1} &= (Z_{oe})_{n-k,n-k+1} = Z_0 \left( N_{k,k+1} + \frac{K_{k,k+1}}{Z_0} \right) \\ (Z_{oo})_{k,k+1} &= (Z_{oo})_{n-k,n-k+1} = Z_0 \left( N_{k,k+1} - \frac{K_{k,k+1}}{Z_0} \right) \end{aligned}$$

where  $k=1, 2, \dots, n-1$ .

TABLE III

DESIGN EQUATIONS FOR FILTERS OF THE FORM IN FIG. 3

Use mapping (5) and Fig. 6 or 7 to select prototype.

$$\theta_1 = \frac{\pi \omega_1}{2 \omega_0}, \quad \theta_\infty = \frac{\pi \omega_\infty}{2 \omega_0},$$

where  $\omega_\infty$  is a frequency of infinite attenuation as indicated in Fig. 11. Referring to Fig. 3:

$$\begin{aligned} a &= \cot^2 \theta_\infty, & Z_1 &= Z_n = \frac{[a(\tan \theta_1)^2 - 1] \omega_1' g_0 g_1}{Y_0(a+1) \tan \theta_1}, \\ Z_1' &= Z_n' = a Z_1, & C_a &= 2d g_2, \end{aligned}$$

where  $d \leq 1$  is a constant (typically one-half or somewhat larger), which may be chosen to give a desired impedance level in the interior of the filter.

$$\begin{aligned} \frac{J_{23}}{Y_0} &= \frac{J_{n-2,n-1}}{Y_0} = \frac{\sqrt{g_2 C_a}}{g_0 \sqrt{g_2 g_3}}, & \frac{J_{k,k+1}}{Y_0} \Big|_{k=3 \text{ to } n-3} &= \frac{C_a}{g_0 \sqrt{g_k g_{k+1}}}, \\ M_{k,k+1} &= \sqrt{\left( \frac{J_{k,k+1}}{Y_0} \right)^2 + \left( \frac{\omega_1' C_a \tan \theta_1}{2g_0} \right)^2}, \\ Y_{k,k+1}^s \Big|_{k=2 \text{ to } n-2} &= Y_{n-k,n-k+1}^s = Y_0 \left( M_{k,k+1} - \frac{J_{k,k+1}}{Y_0} \right). \end{aligned}$$

Then for the shunt stubs:

$$Y_2 = Y_{n-1} = \frac{Y_0 \omega_1' (1-d) g_2}{g_0} \tan \theta_1 + Y_{23}^s,$$

$$Y_k \Big|_{k=3 \text{ to } n-2} = Y_{n-k+1} = Y_{k-1,k}^s + Y_{k,k+1}^s.$$

And for the connecting lines:

$$Y_{k,k+1} \Big|_{k=2 \text{ to } n-1} = Y_{n-k,n-k+1} = J_{k,k+1}.$$



TABLE IV

SUMMARY OF EVEN-MODE AND ODD-MODE IMPEDANCE VALUES FOR THE FILTERS OF FIG. 8(a)-(c) DESIGNED BY USE OF TABLE I AND REALIZED IN THE FORM IN FIG. 1(a)

	Fig. 8(a) (5% Band- width)	Fig. 8(b) (30% Band- width)	Fig. 8(c) (2 to 1 Band- width)
$(Z_{oe})_{01} = (Z_{oe})_{67}$	1.251	1.540	1.716
$(Z_{oe})_{12} = (Z_{oe})_{56}$	0.996	1.023	1.142
$(Z_{oe})_{23} = (Z_{oe})_{45}$	0.981	0.937	0.954
$(Z_{oe})_{34}$	0.980	0.927	0.933
$(Z_{oo})_{01} = (Z_{oo})_{67}$	0.749	0.460	0.284
$(Z_{oo})_{12} = (Z_{oo})_{56}$	0.881	0.491	0.208
$(Z_{oo})_{23} = (Z_{oo})_{45}$	0.895	0.536	0.250
$(Z_{oo})_{34}$	0.896	0.542	0.255

All values normalized so that  $Z_0 = 1$ .

TABLE V

ELEMENT VALUES FOR THE FILTER OF FIG. 9  
REALIZED AS SHOWN IN FIG. 1(d)

Filter designed using Table II from a 0.10-db ripple,  $n=8$ , Tchebycheff prototype using  $\omega_1/\omega_0=0.650$ .

$Y_1 = Y_8 = 1.042$	$Y_3 = Y_6 = 2.049$
$Y_{12} = Y_{78} = 1.288$	$Y_{34} = Y_{56} = 1.292$
$Y_2 = Y_7 = 2.050$	$Y_4 = Y_5 = 2.087$
$Y_{23} = Y_{67} = 1.364$	$Y_{45} = 1.277$

All values normalized so  $Y_0 = 1$ .

TABLE VI

ELEMENT VALUES FOR THE FILTER OF FIG. 10  
REALIZED AS SHOWN IN FIG. 2

Filter designed from a 0.10-db ripple,  $n=8$ , Tchebycheff prototype using  $\omega_1/\omega_0=0.850$  and  $\omega_\infty/\omega_0=0.500$ . This, then, calls for  $a=1$  so that  $Y_k' = Y_k''$  throughout.

$Y_1' = Y_8' = 1.806$	$Y_3' = Y_6' = 3.584$
$Y_{12} = Y_{78} = 1.288$	$Y_{34} = Y_{56} = 1.292$
$Y_2' = Y_7' = 3.585$	$Y_4' = Y_5' = 3.614$
$Y_{23} = Y_{67} = 1.364$	$Y_{45} = 1.277$

All values normalized so that  $Y_0 = 1$ .

TABLE VII

ELEMENT VALUES FOR THE FILTER OF FIG. 11  
REALIZED AS SHOWN IN FIG. 3

Filter designed using Table III from a 0.10-db ripple,  $n=8$ , Tchebycheff prototype using  $\omega/\omega_0=0.650$  and  $\omega_\infty/\omega_0=0.500$ .

$Z_1 = Z_8 = 0.606$	$Y_3 = Y_6 = 1.235$
$Z_1' = Z_8' = 0.606$	$Y_{34} = Y_{56} = 0.779$
$Y_2' = Y_7' = 1.779$	$Y_4 = Y_5 = 1.258$
$Y_{23} = Y_{67} = 0.823$	$Y_{45} = 0.770$

# Radio-Frequency System of the Cambridge Electron Accelerator\*

KENNETH W. ROBINSON†, MEMBER, IRE

**Summary**—The requirements for the RF system of the Cambridge Electron Accelerator are investigated and the choice of the major parameters of the system is discussed. The strongly coupled waveguide cavity system is analyzed and the performance of the system with various types of imperfections is calculated.

## INTRODUCTION

THE Cambridge Electron Accelerator is a project to design and construct a 6-billion-volt electron synchrotron at Harvard University to be used for high energy physics research.<sup>1</sup>

The Cambridge accelerator has two important differences from most synchrotrons which require the design of the RF system to be very different from that of other circular accelerators. The electrons radiate electromagnetic energy due to the curvature of their orbits in

the magnetic guide field. At 6 bev, the radiation loss is 4.5 mev per turn. This radiation loss occurs as discrete quanta which are typically 15-kv X rays at 6 bev. The emission of these discrete quanta produces synchronous oscillations of the individual electrons in energy and phase position about the equilibrium values, and requires the RF voltage to be substantially larger than the radiation loss, in order to prevent the particles being lost from the phase stable region.<sup>2</sup> The other characteristic is the initial injection of electrons at an energy of 20 mev or higher which eliminates the need to modulate the frequency, and makes it possible to use high  $Q$  cavities for the system.

The problem of the RF system is, then, to design a system capable of developing the large accelerating voltage required to make up the peak radiation loss of 4.5 mev per turn and contain the quantum induced phase oscillations. During the acceleration cycle the radiation

\* Received by the PGMTT, April 14, 1960; revised manuscript received July 13, 1960.

† Cambridge Electron Accelerator, Harvard University, Cambridge, Mass.

<sup>1</sup> *Proc. Internatl. Conf. on High-Energy Accelerators and Instrumentation*, CERN, Geneva, Swiz., pp. 335-338; 1959.

<sup>2</sup> M. Sands, "Synchrotron oscillations induced by radiation fluctuations," *Phys. Rev.*, vol. 97, pp. 470-473; 1955.



loss is proportional to the fourth power of the electron energy, so the RF power required during the early portion of the acceleration cycle will be much less than the peak RF power. The ratio of average to peak RF power required is estimated to be about 15 per cent.

The magnet structure of the Cambridge accelerator has 48 magnets with 48 equal-length straight sections. The number of RF cavities is chosen to be 16, as the largest number of symmetrically located cavities which can be put into the 48 straight sections, due to other requirements for use of the straight sections.

The choice of the frequency of the RF system is determined by several factors. The general range of the frequency is chosen so as to approximately minimize the RF power required. In a cavity of fixed total length, the number of cavity sections may be increased proportionally to the frequency, and the total shunt impedance will then increase proportionally to the square root of the frequency. However, as the frequency is increased and the wavelength is decreased, the allowable longitudinal displacement in a phase oscillation is reduced, and a higher RF accelerating voltage is required to prevent the electrons from being lost due to the quantum induced synchronous oscillations. Quantitative evaluation of these two factors gives an optimum frequency of about 600 mc. Other considerations, such as the aperture required in the cavity for the electrons, and the desire to synchronize the RF system with the linear accelerator used for injection, lead to a choice of 475 mc as the operating frequency.

The calculated losses of electrons due to the quantum induced synchronous oscillations are shown in Fig. 1. With a peak RF voltage of 6 mev per turn, less than 10 per cent of the electrons will be lost before reaching 6 bev. If the peak RF voltage is only 5 mev per turn, most of the electrons will be lost before reaching 6 bev.

The design of the RF cavity is shown in Fig. 2. The cavity consists of two half-wave sections partially loaded with re-entrant drift tubes to reduce the transit time factor of the electrons traversing the cavity. Each cavity has an inductive aperture with a ceramic window for coupling to waveguide. There is also an inductive slot in the center wall for coupling the two half-sections of a single cavity. The shunt impedance of a single cavity is about 7.5 megohms and the  $Q$  is about 25,000. The peak power dissipated in the cavity is about 15 kw and the average power is about 2.2 kw.

In order to supply the RF power to the separate cavities, it is proposed to couple the 16 cavities together by means of waveguide so as to form a closed ring. The dimensions of the waveguide are 9 inches  $\times$  18 inches, and the length of waveguide between adjacent cavities is about 50 feet.

The waveguide-cavity system will be a standing wave system with many separate modes. By operating at the frequency of the proper mode, the fields in the individual cavities will have the correct phase relationship to accelerate particles.

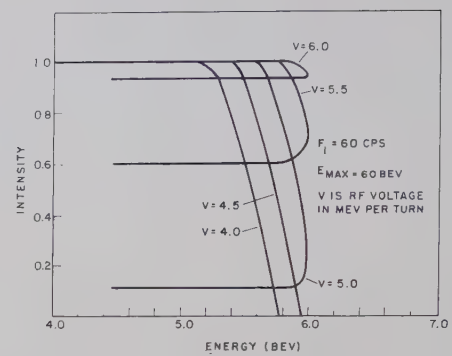


Fig. 1—Loss of particles due to quantum induced synchronous oscillations.

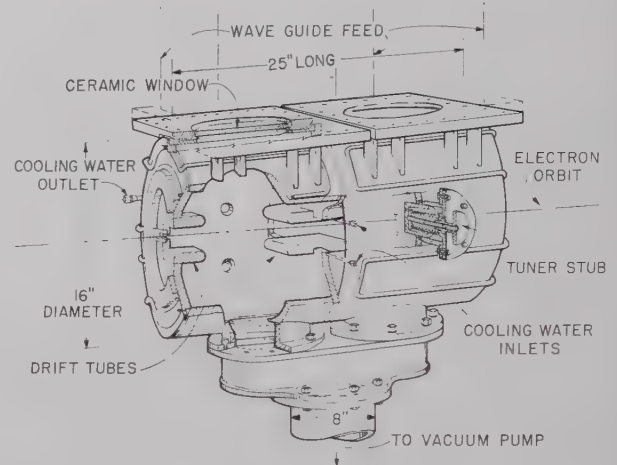


Fig. 2—RF cavity.

The alternative to the strongly coupled system would be to supply the RF power individually to each cavity by means of a transmission line which is matched by the cavity. Since the  $Q$  of the cavity is about 25,000, it would be necessary to maintain the tuning of each individual cavity correct to an accuracy of about one part in 100,000. This accuracy would probably require an automatic system on each cavity to maintain the tuning by monitoring the reflected power. The automatic tuning system would be complicated by the effect of the circulating electron beam in the synchrotron, which would cause the reflected power to vary during the acceleration cycle. With the strongly coupled RF system, the tolerance on the accuracy of tuning of each cavity becomes much larger and it is not necessary to control the tuning of each cavity independently; but only to control the tuning of the system as a whole, which may be easily done by controlling the frequency.

#### ANALYSIS OF STRONGLY COUPLED SYSTEM

In order to analyze the performance of the strongly coupled system, the system is represented by a closed loop of transmission line, coupled to equally spaced resonant cavities as shown in Fig. 3. We assume that the coupling between the two sections of a single cavity is sufficiently large so that in the frequency region of



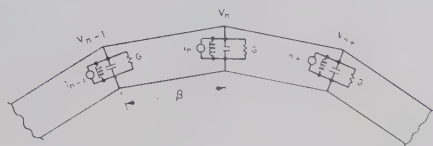


Fig. 3—Schematic representation of strongly coupled RF system.

interest the cavity may be represented by a simple resonant circuit. The length of the transmission line is defined from the principal planes of the cavity.  $G$  is the normalized conductance of the cavity.  $\gamma = \alpha + i\beta$  is the complex phase angle of the length of transmission line between cavities.

In order to analyze the operation of the strongly coupled system, it is convenient to choose a number of normal spatial modes for the system equal to the number of resonant cavities. The modes are defined so that

$$v_{p,n+1} = v_{p,n} e^{i\theta_p}$$

$$\theta_p = \frac{2\pi p}{N}$$

or

$$i_{p,n+1} = i_{p,n} e^{i\theta_p}.$$

$v_{p,n}$ ,  $i_{p,n}$  is the voltage or current generator at the  $n$ th cavity due to mode  $p$ .  $N=16$  is the total number of cavities or modes. Only one mode will be effective in accelerating electrons. The voltages in the other modes result in increased power dissipation, as compared with an ideal system.

A characteristic admittance may be defined for each mode for the ideal system.

$$Y_p = \frac{i_{p,n}}{v_{p,n}}.$$

From the definition of the normal modes and the representation of the strongly coupled system, the characteristic admittance of the modes is calculated to be

$$Y_p = G + 2iGQ \frac{\Delta\omega}{\omega_0} + 2 \coth \gamma - (e^{-i\theta_p} + e^{i\theta_p}) \operatorname{csch} \gamma.$$

For good performance of the system, it is desirable that the admittance of all the undesired modes be large compared with that of the proper mode, so that imperfections in the system will not cause large voltages and power dissipation in the undesired modes. For this reason, the proper mode is chosen to be a nondegenerate mode with  $\cos \theta_p = \pm 1$ . For other modes there would be a degenerate mode with  $\theta_{p2} = -\theta_{p1}$ , with equal admittance. We take the fundamental mode to be  $\theta_p = 0$  in this analysis. By using the relation  $\alpha \ll 1$ , the admittance of the fundamental mode becomes

$$Y_0 = G + \frac{2\alpha}{1 + \cos \beta} + i2GQ \frac{\Delta\omega}{\omega_0} + i \frac{2 \sin \beta}{1 + \cos \beta}.$$

In order to make the admittance of the undesired modes large,  $\beta \ll 1$ . Then the admittance of the fundamental mode when the system is tuned to resonance becomes

$$Y_0 = G_0 = G + \alpha.$$

The ratio  $\alpha/G$  then represents the fractional increase in power required for the perfect strongly coupled system.

The admittance of the undesired modes with the assumptions  $\alpha \ll 1$ ,  $\beta \ll 1$ , becomes

$$Y_p = Y_0 + \frac{4 \sin^2 \frac{\theta_p}{2}}{\alpha^2 + \sin^2 \beta} (\alpha - i \sin \beta).$$

In order to determine the effect of imperfections on the strongly coupled system we analyze the effect of detuning a single cavity. If the changes in cavity voltages produced by the imperfection are small compared with the fundamental mode voltage, the result of the imperfection may be calculated as a first-order effect. The detuning of a single cavity may be considered equivalent to adding a current generator of  $I = iV_0 \cdot 2GQ(\Delta\omega/\omega_0)$  at that cavity. This current generator at one cavity may be expressed as a combination of the normal modes of current generators applied to all cavities.

The fundamental mode component of this current is  $i(V_0/N) \cdot 2GQ(\Delta\omega/\omega_0)$ . The effect of the detuning on the admittance of the fundamental mode can be eliminated by changing the resonant frequency of all the cavities by an amount  $-\Delta\omega/N$ , or by changing the frequency by an amount  $\Delta\omega/N$ .

The change in tuning of a single cavity also produces current generators in every undesired mode with a magnitude equal to  $(V_0/N) \cdot 2GQ(\Delta\omega/\omega_0)$ . The magnitude of the voltage produced in an undesired mode is then

$$V_p = 2 \frac{V_0}{N} \frac{GQ}{Y_p} \frac{\Delta\omega}{\omega_0}.$$

The power dissipated in an undesired mode is

$$P_p = V_0^2 \left( \frac{1}{N} 2Q \frac{\Delta\omega}{\omega_0} \right)^2 \frac{G^2}{Y_p^2} G_p.$$

We make the assumption that  $\alpha \ll \beta \ll 1$ . Then

$$Y_p \approx i4 \frac{\sin^2 \frac{\theta_p}{2}}{\sin \beta} + G_0 \approx i4 \frac{\sin^2 \frac{\theta_p}{2}}{\sin \beta} \quad \text{for } G \ll 1$$

$$G_p \approx 4 \frac{\sin^2 \frac{\theta_p}{2}}{\sin^2 \beta} \alpha + G_0.$$

The ratio of power dissipated in all the undesired modes, due to detuning of a single cavity, to the power dissipated in an ideal system is given by



$$\frac{\Delta P}{P} = \left(2Q \frac{\Delta\omega}{\omega_0}\right)^2 \frac{G}{16N^2} \left\{ 4\alpha \sum_{p=1}^{15} \frac{1}{\sin^2 \frac{\theta_p}{2}} + G_0 \sin^2 \beta \sum_{p=1}^{15} \frac{1}{\sin^4 \frac{\theta_p}{2}} \right\}.$$

The summation over  $p$  from 1 to 15 includes all the modes, except the fundamental mode with  $p=0$ . The summations are evaluated to be

$$\sum_{p=1}^{15} \frac{1}{\sin^2 \frac{\theta_p}{2}} = 84.6 \quad \text{and} \quad \sum_{p=1}^{15} \frac{1}{\sin^4 \frac{\theta_p}{2}} = 1499.$$

If all the cavities are detuned in a random manner by a rms amount  $\Delta\omega/\omega_0$ , the power dissipated in the spurious modes will be increased by a factor of  $N$ . The fractional total increase in power dissipated in the strongly coupled system, including the power dissipated in the transmission line in the fundamental mode, is then given by

$$\frac{\Delta P_T}{P} = \frac{\alpha}{G} + \left(2 \frac{\Delta\omega}{\omega_0} Q\right)^2 \frac{G}{256} \{345\alpha + 1499G \sin^2 \beta\}.$$

The value of  $\alpha$  for the waveguide transmission line between adjacent cavities is about 0.004. Then

$$\frac{\Delta P_T}{P} = \frac{0.004}{G} + [0.0054G + 5.86(\sin^2 \beta)G^2] \left(2Q \frac{\Delta\omega}{\omega_0}\right)^2.$$

If we assume that we want to allow a rms detuning of the individual cavities by 10 half-bandwidths, and take  $\sin \beta = 0.1$ , then the minimum increased power dissipation occurs for  $G=0.06$  and is equal to  $\Delta P_T/P=0.12$ . The fractional power dissipation in the transmission lines for an ideal system with no cavity detunings is then 0.066.

There will also be a possible mode in which the fields are zero in the cavities and all the energy is stored in the transmission lines. This mode will not be excited by detuning of the individual cavities, but may be excited by imperfections in the transmission lines. The worst possible case would be if an imperfection occurred at a point midway between a voltage maximum and current maximum for the fundamental mode on every transmission line. The admittance of this waveguide mode at this point is given approximately by  $Y_w \approx i2\beta$ . An imperfection in the form of a susceptance of  $iS$  at this point can be considered a current generator of magnitude  $(V_0/\sqrt{2})S$ , which will produce a voltage in the waveguide mode of  $V_0 S/2\beta$ . The power dissipated due to this mode will be

$$\Delta P_w = V_0^2 \frac{S^2}{4\beta^2} \alpha$$

and, when expressed as a fraction of the power dissipated in the fundamental modes, is:

$$\frac{\Delta P_w}{P} = \frac{S^2}{4\beta^2} \frac{\alpha}{G}.$$

If we allow an imperfection which will produce a VSWR of 1.1 for the transmission line ( $S=0.1$ ), and take  $\beta=0.1$  as before, then

$$\frac{\Delta P_w}{P} = \frac{1}{4} \frac{\alpha}{G} = 0.016 \quad \text{for } \alpha = 0.004, G = 0.06.$$

The RF power is supplied to the standing-wave ring system from a power source in a central location by means of a transmission line which makes a matched junction with the ring at one point. For optimum operation of the system, the junction should be at a cavity or approximately an integral number of half wavelengths from a cavity; which, in the strongly coupled system, is almost electrically equivalent to having the junction at the cavity. The effect of introducing power into the system at only one point may be analyzed in terms of power dissipation in the undesired modes, in a manner similar to the effect of detuning of cavities. With the junction at the optimum position, the waveguide mode will not be excited. The junction may be taken equivalent to a current generator of magnitude  $NGV$  at that point. This is equivalent to detuning a single cavity by an amount  $2Q(\Delta\omega/\omega_0)=N$ , and will then produce an increased power dissipation equal to that produced by detuning all the cavities by a rms amount  $2Q(\Delta\omega/\omega_0)=N^{1/2}$ . Since  $N=16$ , this will then result in an increased power dissipation of 16 per cent of that produced by the random detuning of all the cavities by a rms amount of  $2Q(\Delta\omega/\omega_0)=10$ , which is about 1 per cent of the power dissipated in the fundamental mode.

The power level in the waveguide transmission line may be calculated from the ratio of power dissipated in the waveguide to the power dissipated in the cavities. This ratio is given by

$$\frac{\Delta P}{P} = \frac{0.004}{G} + 0.0054 \left(2Q \frac{\Delta\omega}{\omega_0}\right)^2 \quad \text{and} \quad \frac{\Delta P}{P} \approx 0.10.$$

Since the voltage attenuation in the waveguide is 0.004 nepers, this corresponds to a power flow in one direction of about 12.5 times the power dissipated in one cavity. From the previous values of 15 kw peak and 2.2 kw average for the power dissipated in a single cavity, the corresponding power flow in the waveguide becomes 187 kw peak and 27.5 kw average. Since the fields in the waveguide are more like standing wave fields, the maximum fields in the waveguide will correspond to power levels of twice the above values. These power levels in the waveguide will be somewhat further increased, due to the effect of the circulating electron beam in the synchrotron.



# Model Studies of a Strongly Coupled Synchrotron RF System\*

A. E. BARRINGTON†, J. DEKLEVA†, AND J. R. REES†

**Summary**—The strongly coupled multicavity synchrotron RF system proposed for the 6-bev Cambridge Electron Accelerator operates at 475 Mc and, because of its large size, presents complex problems of assembly and tuning. To achieve a better understanding of the characteristics of the system, a scaled model operating at 9000 Mc was constructed. The work was undertaken in two stages; first a simple single-cavity ring was studied and later a more complicated double-cavity ring. An account is given of the design of cavities and waveguide links of variable electrical length, and instrumentation devised for various measurements is described. This is followed by experimental data which were in good agreement with theoretical predictions. Recommendations arising from the model study for the assembly and tuning of the 475-Mc system are put forward.

## I. INTRODUCTION

IN ORDER TO gain practical experience on various problems arising from Robinson's<sup>1</sup> proposal of the strongly coupled multicavity synchrotron RF system for the 6-bev Cambridge Electron Accelerator, it was decided to construct an X-band model.

The behavior of a ring structure consisting of 16 strongly coupled double cavities depends on 48 tuning adjustments: the resonant frequencies of each individual half-cavity and the electrical length of the waveguide links joining the double cavities. In order to obtain the desired mode of operation, a systematic tuning method must be established. The desired mode must be identified by cavity voltage measurements, and observations may then be made of the frequency separation between neighboring modes and of the effects on the mode spectrum due to the deliberate detuning of individual components. It was considered feasible to obtain this information with a greatly reduced number of components; for geometrical simplicity a six-cavity structure, intended solely for radio-frequency studies and not suitable for the acceleration of electrons, was chosen. It consisted of a hexagon whose sides were formed by waveguide sections of variable electrical length, with resonant cavities at the vertices. Power was fed to the structure though either a three-port cavity at one of the vertices or a T-junction in one of the waveguide links. The work was undertaken in two stages, first a simple single-cavity ring was studied and later a more complicated double-cavity ring. A diagram of the model assembly is shown in Fig. 1.

\* Received by the PGMTT, April 14, 1960; revised manuscript received, June 22, 1960. This work was carried out under AEC Contract AT(30-1)-1909.

† Cambridge Electron Accelerator, Harvard University, Cambridge, Mass.

<sup>1</sup> K. W. Robinson, "Radio-frequency system of the Cambridge Electron Accelerator," this issue, p. 593.

## II. DESIGN OF COMPONENTS AND MEASURING EQUIPMENT

In order to obtain an axial accelerating field in the synchrotron cavities, the  $TM_{010}$  mode is excited and this was also the mode chosen for the individual model cavities. Fig. 2 shows a single cavity. The height of the cavity was chosen to avoid excitation of the unwanted  $TE_{111}$  mode. For tuning, a polystyrene rod, mounted on a micrometer head, was inserted through a  $\frac{1}{8}$  inch diameter central hole in the top of each cavity. This resulted in a linear tuning range of about  $\pm 1\frac{1}{2}$  per cent around the center frequency. The cavities were constructed of triangular blocks of brass. Unloaded  $Q$ -

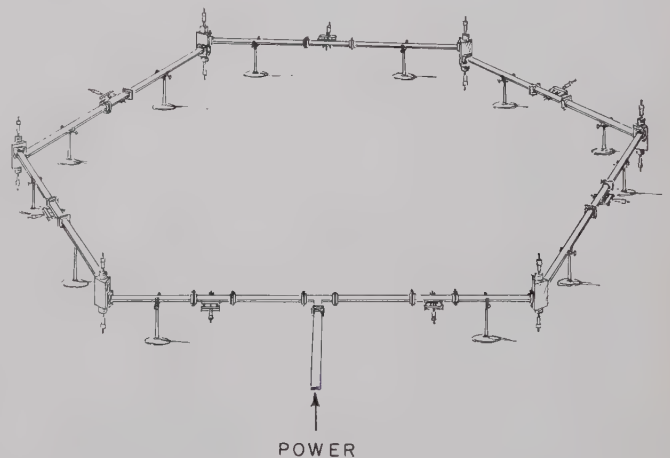


Fig. 1—Model assembly.

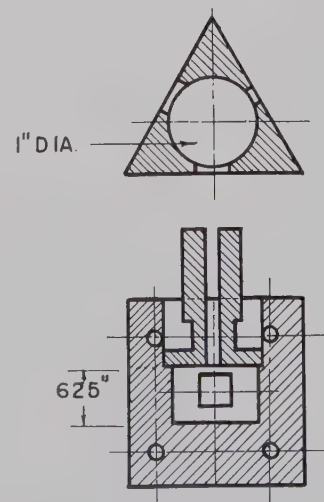


Fig. 2—Single cavity, construction.



values of more than 3000 were obtained with the single cavities and of nearly 4000 with the double cavities as shown in Fig. 3, where the dividing diaphragm between the chambers was made of copper.

An overcoupled double cavity is characterized by two resonant modes which occur at frequencies where the individual cavity voltages are either in phase or in anti-phase; *i.e.*, the 0 mode and  $\pi$  mode. For scaling purposes a coupling factor  $f_{\pi}/\Delta f$  was defined where  $f_{\pi}$  is the  $\pi$ -mode resonant frequency and  $\Delta f$  is the frequency separation between the 0 mode and the  $\pi$  mode. For the coupling factor to be equal to that in the 475-Mc synchrotron cavities, namely 200,  $\Delta f$  equaled 44 Mc in the X-band model. Owing to manufacturing difficulties it was not possible to reproduce this coupling factor consistently with two magnetic coupling slots; however, good reproducibility was obtained by changing from magnetic to electric coupling through a central  $\frac{1}{4}$  inch-diameter coupling hole, and this coupling scheme was adopted. The change from magnetic to electric intracavity coupling caused a frequency reversal of the 0 mode and the  $\pi$  mode, the  $\pi$  mode being the higher frequency resonance of the electrically coupled pair.

In order to obtain a satisfactory frequency separation between the desired and adjacent modes of the synchrotron ring, a quantity  $1/GZ_0$  equal to 17 was specified by

Robinson,<sup>1</sup> where  $G$  is the shunt conductance of a cavity represented as a parallel resonant circuit shunted across a waveguide of characteristic impedance  $Z_0$ . For a cavity with two matched waveguide terminations, this corresponds to a ratio of unloaded to loaded  $Q$ -values equal to 35. In view of the difficulties involved in measuring  $Q$ -values less than 300 to a reasonable degree of accuracy with the available test equipment, 300 was accepted for the loaded  $Q$ -value of both single and double cavities. This corresponds to a value of  $1/GZ_0$  approximately equal to 5.

The single cavities were tuned by terminating both coupling holes by matched waveguides and observing the resonant frequency as a function of the depth of penetration of the dielectric tuning rods. This tuning method was not sufficiently accurate for the double cavities, since the frequency response of the cavities loaded by matched waveguides was much broader than in the ring structure where the cavities operate under essentially unloaded conditions. A different tuning technique had to be devised in which the cavities were terminated in shorted quarter-wave waveguides so that they were unloaded and their sharpness of tuning was preserved. The details of this procedure are discussed in Section III.

For maximum flexibility the electrical length of the waveguide links joining adjacent cavities was designed for a possible variation exceeding one guide wavelength. For this purpose, a phase shifter was scaled from a Radiation Laboratory design,<sup>2</sup> where a polystyrene vane supported by three correctly spaced metal rods, to achieve cancellation of reflections, could be moved laterally across the interior of the waveguide. At the desired frequency, a vane length of 8 inches gave a phase shift of more than  $360^\circ$ ; the voltage standing wave ratio as a function of vane position over the frequency band from 8500 Mc to 9500 Mc did not exceed 1.13. The  $Q$ -value of the dielectric loaded section was of the order of 6000 and, within the limits of accuracy of the  $Q$ -measuring apparatus, was the same as that of empty copper waveguide.

The frequency response of all components as well as of the assembled resonant ring was measured by means of a reflectometer where the incident power from a frequency-modulated klystron and the power reflected by the component under test were displayed simultaneously on an oscilloscope.

An important feature in studying the behavior of the double cavities and the ring structure was the measurement of RF phase. The scheme adopted is shown in Fig. 4, where two signals whose relative phase is to be measured are introduced into a calibrated slotted line which is terminated by matched attenuators. The superposition of the signals results in a standing wave

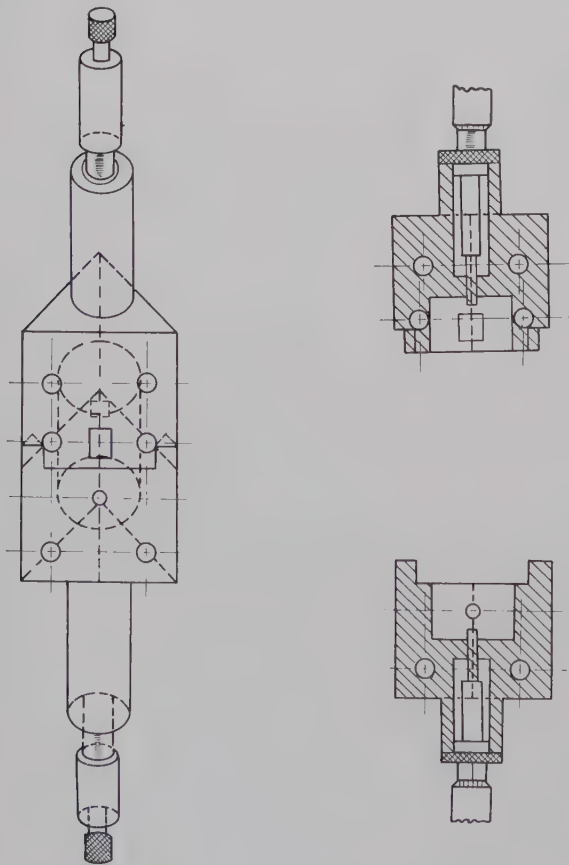


Fig. 3—Double cavity, construction.

<sup>2</sup> G. L. Ragan, "Microwave Transmission Circuits," McGraw-Hill Book Co., Inc., New York N. Y., p. 516; 1948.



pattern, the position of which depends on the relative phase angle. If the position of the standing wave minimum for in-phase signals is taken as the reference phase, then for a phase angle  $\phi$ , the minimum will move to a new position at a distance  $(\lambda g/2) (\phi/360)$ . The slotted line with its flexible cable connections was calibrated by establishing a minimum position corresponding to a relative phase of  $0^\circ$  with two identical signals obtained from a single cavity with three identical coupling holes as shown. Although the accuracy of the method was greatest with signals of equal amplitude where the position of a standing wave minimum could be measured with great precision, it was possible to make measurements with signals of arbitrary magnitude.

### III. TUNING PROCEDURE OF THE RING STRUCTURE

In order to establish the correct electrical length of the waveguide links, a precise determination of the cavity planes is required. Near the resonant frequency, a two-port cavity may be represented by a four-terminal network as shown in Fig. 5, where the effect of the coupling holes is represented by lumped reactances  $X$ . If the cavity is excited through one port and connected to an adjustable short-circuited waveguide through the other port, it is possible to determine the equivalent electrical length of the combination of lumped reactance  $X$  and shorted line by monitoring the cavity voltage as the line length is varied. For constant input power the cavity voltage will change from a maximum to a minimum as the equivalent line length is changed. In practice, it was difficult to observe the maximum where the cavity voltage was not sensitive to changes of line length, but deep minima were obtained. If  $X$  is small, the effective cavity plane  $a-b$  may then be taken to be one-half guide wavelength from the face of the shorting plunger.

It was first required to ascertain the distance between the effective plane of the shorting plunger and its flange from a slotted-line measurement. The cavity whose effective plane was to be measured was then connected as shown in Fig. 6. The minimum cavity voltage corresponded to a position of the shorting plunger approximately one-half guide wavelength from the inner cavity wall. This result was confirmed with a slotted-line measurement. The data obtained were in good agreement for the two sets of six cavities.

Regarding the tuning of the double cavities, it can be shown that in the desired mode of operation of the ring structure, a voltage minimum exists in the ring at a distance of approximately one-quarter of a guide wavelength from the plane where a half-cavity may be represented by an equivalent lumped parallel resonant circuit. If the circuit is considered to be lossless, the standing wave pattern in the ring remains theoretically undisturbed by inserting a metal wall into the waveguide at this point. If the position of the effective cavity plane is known, this condition may be simulated by means of two adjustable shorting plungers in waveguide arms connected to the coupling holes of the individual half-cavities. In the experiment, the plungers were adjusted to one-quarter guide wavelength from the effective cavity planes; each half-cavity was provided with two small coupling holes such that power could be fed through one and the cavity voltage could be monitored through the other. The tuning procedure consisted of feeding power at the desired frequency into one of the half-cavities, displaying both half-cavity voltages simultaneously and recording the position of the tuning rods for equal voltage maxima.

The electrical length of the waveguide links joining

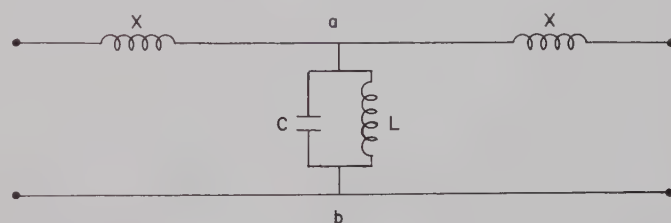


Fig. 5—Equivalent circuit of two-port cavity.

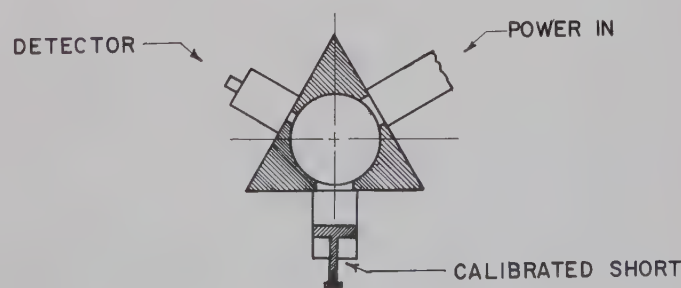


Fig. 6—Determination of cavity plane.

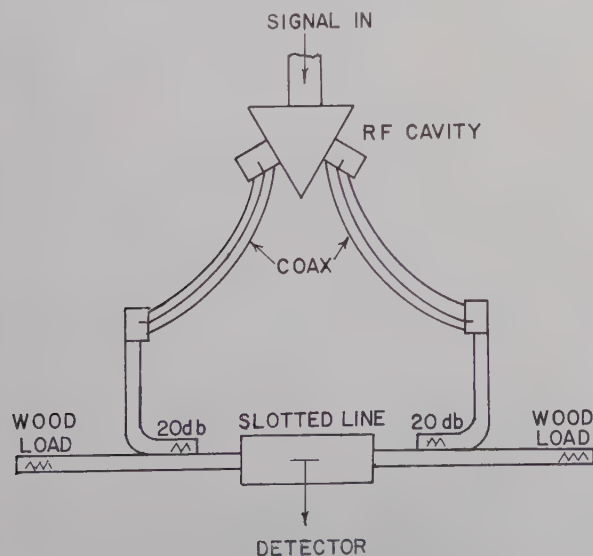


Fig. 4—Calibration of slotted-line phasometer.



adjacent cavities was chosen to be about  $18\frac{1}{2}$  guide wavelengths, approximately the same as the electrical distance between cavities in the synchrotron ring. By means of the phase shifters described previously, this quantity could be varied over a range of over  $360^\circ$ . In order to obtain the optimum frequency spacing between the desired fundamental mode and the resonant frequencies of the other, nonaccelerating modes, an electrical length of the waveguide links was specified differing from an integral number of half wavelengths by a small angle  $\delta$ . The method used for adjusting the links to the required electrical length was as follows: A typical link consisted of two empty sections, 14.42 inches long, mounted on either side of a phase shifter, 8.5 inches long, giving a total length of 37.34 inches, corresponding to  $18\frac{1}{2}$  guide wavelengths in empty guide at 8700 Mc. The link was terminated at one end with a thin copper diaphragm containing a small coupling hole and at the other with an adjustable short circuit. The position of the shorting plunger, when it produced an electrical short circuit at its flange face, was designated the "0" position. For a positive angle  $\delta$  and a distance  $d$  of the effective cavity plane from the face of the cavity, the plunger was set at  $"0" + 2d + \delta\lambda_g/360$  inches. The resonant frequency of the structure fed as a resonator through the small coupling hole was adjusted to the ring operating frequency.

For a phase shift range over  $360^\circ$ , resonant positions were found corresponding to phase shifts from flange to flange of approximately  $0^\circ$  or  $180^\circ$ . The link was then connected between two cavities, one of which was terminated by a matched load and the other was driven by the generator. The desired position of the phase shifter was identified by a phase measurement of the cavity voltages. This procedure was adequate for the single-cavity ring. In the double-cavity case where cavity tuning was more sensitive and complicated, the following scheme was adopted: Each cavity was tuned individually by means of quarter-wave plungers, a link was then tuned to the desired length and connected between two cavities. The frequency at which the correct phase relation between cavities obtained was now different from the resonant frequency of individual cavities. All other links, when terminated by two tuned cavities and adjusted to this new frequency, were then of the correct electrical length. The two frequencies were identical only when  $\delta$  was equal to zero.

Regarding the tuning of the input link, a T-junction may be represented at a fixed frequency by the equivalent circuit shown in Fig. 7. If phase shifters are included in arms I and II of the T and these are terminated by a diaphragm containing a small coupling hole and an adjustable short circuit, respectively, at a given frequency the phase shifters can be adjusted such that maximum power may be coupled into arm I while essentially no power is coupled into arm III. Under this

condition the link is an integral number of half-wave-lengths long and, of course, power fed through arm III then divides symmetrically into arms I and II, if these are terminated identically. In order to simulate the cavity planes, arm I was lengthened by a shim of the appropriate thickness and arm II was suitably compensated by adjusting the micrometer setting of the adjustable short. Two cases were of interest, 1) where arms I and II were equal and 2) where their electrical lengths differed by one-half guide wavelength, corresponding to  $0^\circ$  and  $180^\circ$  excitation, respectively. Resonance of the link in the desired mode pattern was then indicated by a deep null on the detector output meter in arm III and by minimum reflection from arm I.

#### IV. EXPERIMENTAL RESULTS

The characteristics of the ring structure can be computed by means of a matrix formulation (see Appendix).

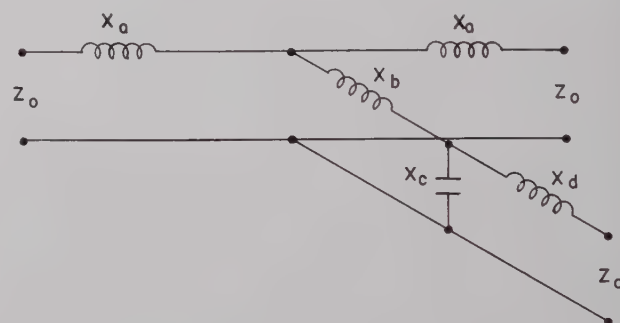


Fig. 7—Equivalent circuit of T junction.

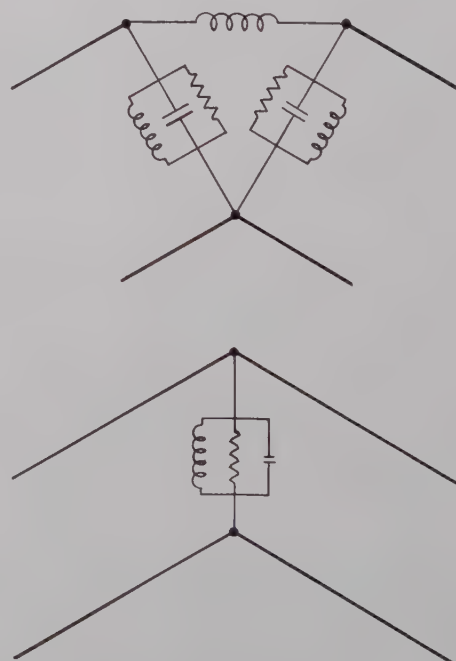


Fig. 8—Equivalent circuit of double cavity (upper diagram), and single cavity representation at either resonance (lower diagram).

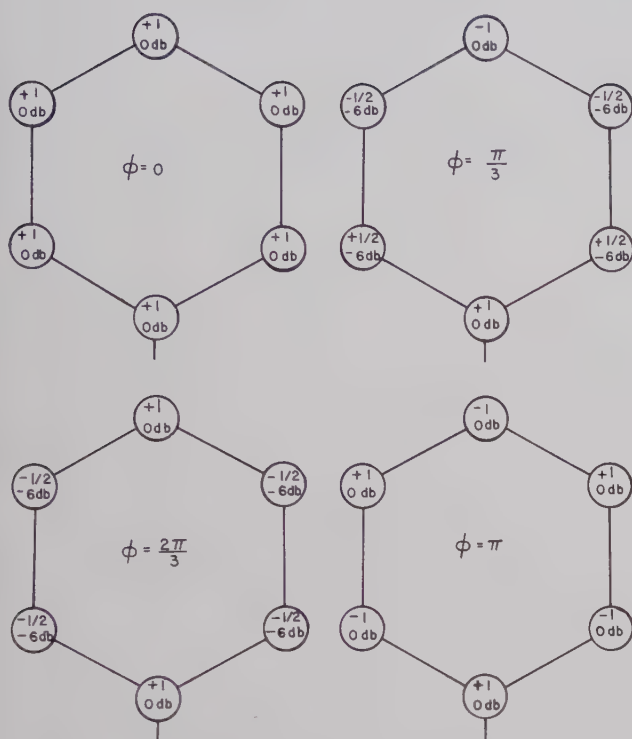


Fig. 9—Amplitude distribution of modal cavity voltages (cavity-fed single-cavity ring).

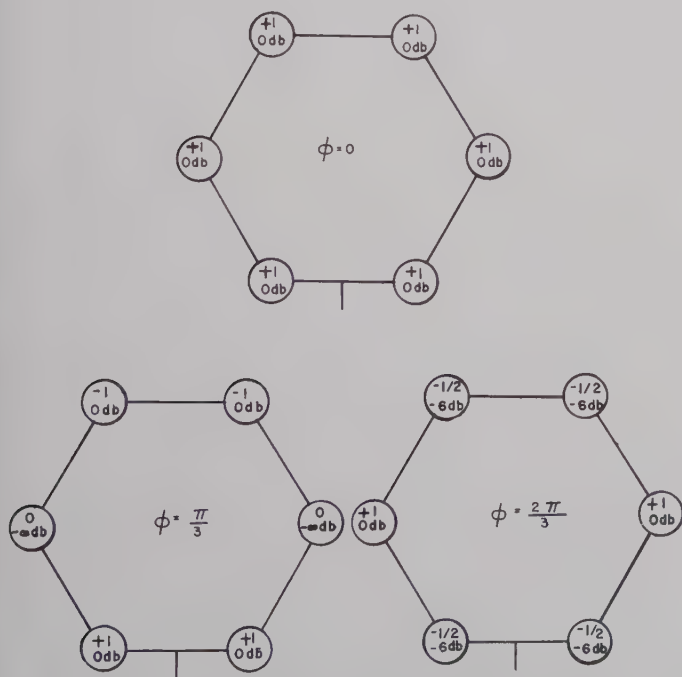


Fig. 10—Amplitude distribution of modal cavity voltages (T-fed single-cavity ring).

Since the cavities are strongly coupled, a double cavity at either of its resonances may be represented by a single cavity (Fig. 8). This simplifies the analysis considerably and enables one to obtain the characteristics of the system by means of a hand calculation. For this reason, the first set of experiments was carried out with a system consisting of single cavities. In order to reduce the number of variables, the ring was initially fed through a three-port cavity with identical coupling holes.

At resonance, the phase shift,  $\phi$ , between adjacent cavities is limited to values of  $\phi$  equal to  $0, \pi/3, 2\pi/3, \pi, 4\pi/3, 5\pi/3$  radians. Pairs of degenerate modes occur at some frequencies and their amplitudes add. The amplitude distribution of the modal voltages depends on the location where power is fed into the system. For the cavity-fed ring, the theoretical amplitude distribution of the cavity voltages is shown in Fig. 9. For convenience, the mode with  $\phi=0$ , where all cavities oscillate in phase, was chosen as the operating mode. Similarly, for the T-fed ring the cavity voltages vary according to Fig. 10, where it is seen from symmetry considerations that the mode with  $\phi=\pi$  cannot be excited.

A typical mode-pattern obtained in terms of power reflected from the input of the ring as a function of frequency is shown in Fig. 11(a); two sets of modes appear on either side of the operating mode ( $\phi=0$ ) resonance. For comparison, the theoretical modal frequencies are indicated in terms of frequency separation from the desired  $\phi=0$  mode in Fig. 11(b).

A mode corresponding to the resonant frequency of the waveguide link, the "waveguide-mode" (WG), was calculated to be separated from the operating mode by 6 Mc. This was confirmed experimentally; this mode was unaffected by a detuning of the cavities but was greatly influenced by the individual phase shifters.

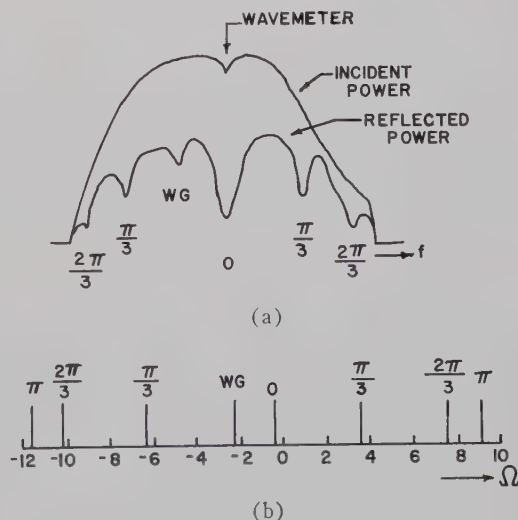


Fig. 11—(a) Experimental resonance pattern of single-cavity ring. (b) Theoretical modal resonances of single-cavity ring.  $\Omega$ =frequency separation in cavity bandwidths from the operating ( $\phi=0$ ) mode.



The calculated and measured modal resonant frequencies are shown in Table I; the amplitude distribution of cavity voltages in decibels for both cavity-fed and T-fed rings is given in Table II, the maximum deviation from the mean being 0.73 db for the cavity-fed ring and 0.75 db for the T-fed ring in the desired  $\phi=0$  resonance. In view of the fact that the position of the dielectric vane in the phase shifters was not the same in the six links, resulting in a variation of the dispersion from link to link, the discrepancy between experimental and theoretical data regarding the other modes was surprisingly small.

A change of the resonant frequency  $\Delta f$  of a single cavity was shown by Robinson<sup>1</sup> to produce a corresponding change  $\Delta f/N$  in the resonant frequency of a ring consisting of  $N$  cavities. This was confirmed experimentally for the operating mode of the T-fed ring, where cavity no. 1 was detuned in three steps to a

TABLE I  
FREQUENCIES OF MODAL RESONANCES

Modal resonance $\phi$	Resonant frequency (Mc)	
	Calculated 8698.8	Measured 8700
0		
$\pi/3$	8710.4, 8681.7	8711, 8684
$2\pi/3$	8722.0, 8670.4	8722, 8675
$\pi$	8726.4, 8666.4	8726, 8670

TABLE II  
AMPLITUDE DISTRIBUTION OF CAVITY VOLTAGES

Cavity No.	Modal resonances				
	$\phi=0$		$\phi=\pi/3$		$\phi=2\pi/3$
	Cavity-fed*	Tee-fed	Cavity-fed*	Tee-fed	Tee-fed
1	—	0	—	0 (0)	-6.0 (-6)
2	0	-2.0	-4.5 (-6)	-10.3 (-∞)	0 (0)
3	-1.45	-1.0	-9.0 (-6)	-1.2 (0)	-4.0 (-6)
4	-0.60	-1.5	0 (0)	-0.6 (0)	-5.6 (-6)
5	-0.95	-1.0	-4.0 (-6)	-9.8 (-∞)	-1.0 (0)
6	-0.60	-1.0	-5.0 (-6)	-2.8 (0)	-3.5 (-6)
Cavity voltages in decibels—reference level 0 decibels					

\* No provision for voltage monitoring of feed-cavity. Bracketed figures are theoretical values.

TABLE III  
AMPLITUDE DISTRIBUTION OF OPERATING-MODE CAVITY VOLTAGES  
(RESONANT FREQUENCY OF CAVITY NO. 1 DECREASING)

Cavity No.	Resonant frequency of cavity no. 1 decreased by			
	0 Mc	14.6 Mc	29.2 Mc	44 Mc
1	0	0.1	-1.8	-3.9
2	-2.2	-2.2	-3.7	-4.8
3	-1.2	-1.4	-2.8	-3.0
4	-1.6	-2.0	-2.8	-3.0
5	-1.2	-1.5	-1.4	-3.0
6	-0.6	-0.4	-1.5	-2.7
Cavity voltages in decibels—reference level 0 decibel				

maximum of 44 Mc. The change of the operating mode frequency under this condition was 7 Mc. The amplitude distribution of the cavity voltages for the three changes of no. 1 cavity resonant frequency is shown in Table III.

Since the synchrotron ring is required to operate in the  $\pi$ - $\pi$  mode ( $180^\circ$  phase difference between successive half-cavities), this was the mode most thoroughly investigated with the double-cavity ring. As in the single-cavity experiments, power was fed into the ring through either a cavity or a T-junction. The results of amplitude-distribution measurements and detuning experiments are summarized in Tables IV and V, from which it is seen that the behavior of the ring was essentially the same as that of the single-cavity structure. Apart from the desired fundamental mode, it was not possible to identify the resonant modes by their amplitude distributions. This was probably due to mechanical imperfections of the double cavities, particularly to ran-

TABLE IV  
AMPLITUDE DISTRIBUTION OF  $\pi$ - $\pi$  MODE CAVITY VOLTAGES,  
INITIAL CAVITY TUNING 8852 Mc

Double Cavity No.	Resonant frequency of cavity no. 5					
			Decreased by 17 Mc		Increased by 6.5 Mc	
	Upper	Lower	Upper	Lower	Upper	Lower
1*	—	—	—	—	—	—
2	-2.0	-1.2	-3.3	-4.2	-2.3	-1.2
3	-1.6	-1.8	-2.5	-4.0	-1.4	-1.8
4	-1.7	-2.4	0	-2.0	0	-2.0
5	-2.6	-2.2	-0.2	0	-1.4	-0.8
6	-1.9	-2.8	-3.3	-0.2	-1.4	-0.4
Modal resonant frequency	8851 Mc		decreased by 2 Mc		increased by approx. $\frac{1}{2}$ Mc	
Maximum deviation from mean, db	0.8		2.2		1.15	

\* Cavity-fed ring, no provision for voltage monitoring of feed cavity. Surplus electrical length of waveguide link  $\delta=0$ . Cavity voltages in decibels, reference level 0 decibels.

TABLE V  
AMPLITUDE DISTRIBUTION OF  $\pi$ - $\pi$  MODE CAVITY VOLTAGES FOR  
TWO VALUES OF SURPLUS ELECTRICAL LENGTH  $\delta$   
OF WAVEGUIDE LINK

Double Cavity No.	Surplus electrical length of waveguide link			
	$\delta = -15^\circ$		$\delta = +15^\circ$	
	Upper	Lower	Upper	Lower
1*	—	—	—	—
2	-0.2	0.5	-1.0	-2.4
3	0	0	-0.8	-1.6
4	0	-0.4	0	-1.6
5	-0.8	0	-1.6	-1.7
6	0.5	0	-0.6	-1.7
Maximum deviation from mean, db	0.65		1.2	

\* Cavity-fed ring, no provision for voltage monitoring of feed cavity. Cavity voltages in decibels, reference level 0 decibels.

dom distortions of the copper diaphragm forming the separating wall. It was possible, however, to compare experimental results with theoretical predictions of the mode spectrum by means of phase measurements. The computation of the modal resonances in this case was carried out on a digital computer. Both experimental and theoretical data are shown in Fig. 12. The results are plotted in terms of frequency separation from the desired  $\phi=180^\circ$  mode as a function of the electrical length of the waveguide links around an odd integral number of half wavelengths. As in the single cavity case, the waveguide mode was identified by its sensitivity to changes in phase shifter setting. It was not possible to detune any double cavity by more than 5 bandwidths without seriously disturbing the mode pattern.

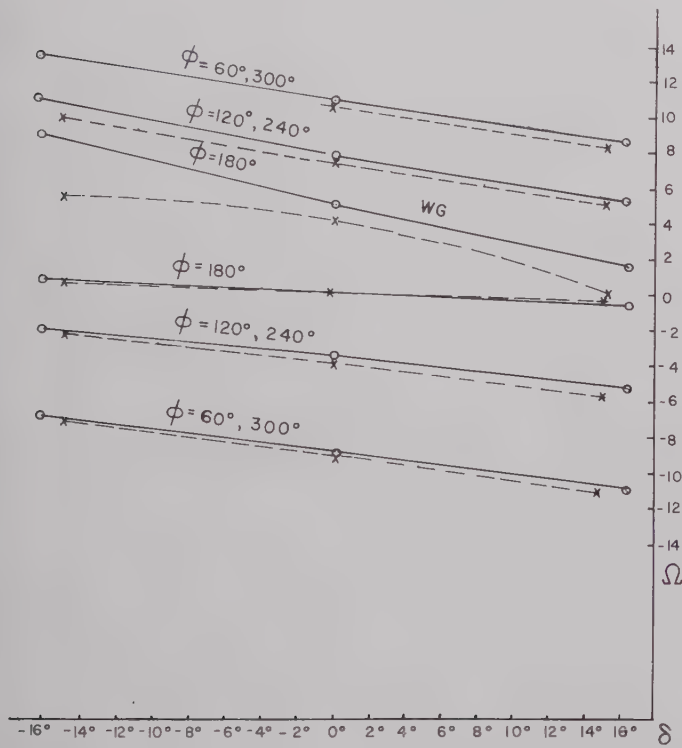


Fig. 12—Experimental and theoretical modal resonances of double-cavity ring.  $\Omega$  = frequency separation in cavity bandwidths from the operating ( $\phi = 180^\circ$ ) mode;  $\delta$  = excess electrical length of waveguide links over nearest integral number of half-wavelengths.

### V. CONCLUSIONS

The experiments described essentially confirm the theoretical predictions regarding the ring structure and demonstrate its feasibility for accelerating purposes.

However, considering the mechanical complexity of the synchrotron ring whose average radius is 118 feet, it is desirable that individual components can be tuned without removal from the ring. From the model investigation of the double-cavity tuning which required quarter wavelength shorts to simulate the unloaded conditions of the cavities, a method has been devised to accomplish this.

The scheme involves shorting the waveguide link

joining two cavities, which is approximately 50 feet long, at appropriate positions by means of resonant posts and it depends ultimately on the reflection coefficient of the posts. An experimental post has been built for operation in 18-inch  $\times$  9-inch waveguide at 475 Mc, and a VSWR of better than 40 db was obtained. For tuning of the cavities or of the waveguide links, the posts will be placed at an odd-integral number of quarter wavelengths from the effective cavity planes; the cavities and waveguide links will then be adjusted as required with a low-power signal. Once the components are tuned, the posts are withdrawn from the guide.

It is proposed to equip all waveguide sections with such posts, mounted on sliding carriages in order to adjust their position. The tuning procedure will otherwise be identical with that outlined in the paper.

### APPENDIX

One of the most important sets of parameters characterizing the strongly coupled multicavity RF system is its group of resonant frequencies in the desired frequency range. These frequencies are intimately related to the circuit parameters in theory, and they are readily available as experimental data.

Since the RF system under investigation is a high- $Q$  circuit, the resonant frequencies will not be affected greatly by circuit losses. Consequently, the frequency spectrum may be calculated from an eigenvalue formulation.<sup>3</sup>

Consider the resonant ring circuit from which the losses and the input junction have been deleted. The circuit has no terminals. Suppose, now, that the ring is broken at some point in the circuit so that a two-terminal-pair network is produced. This circuit is described by a matrix of general circuit parameters<sup>4</sup> relating the voltage and current at the terminals on one side of the network to the voltage and current at the terminals on the other side. The matrix elements are functions of the frequency and the resonances occur at frequencies where the voltage and current at one port are reproduced at the other port.

If the ring consists of  $n$  identical cells, each of which is itself symmetrical, then the matrix for a cell may be written,

$$m = \begin{pmatrix} \cos \phi & b \\ c & \cos \phi \end{pmatrix},$$

and the matrix of the opened ring,

$$m^N = \begin{pmatrix} \cos N\phi & b \sin N\phi / \sin \phi \\ c \sin N\phi / \sin \phi & \cos N\phi \end{pmatrix} = M;$$

the elements  $b$  and  $c$  are imaginary because of conservation of energy.

<sup>3</sup> G. B. Collins, "Microwave Magnetrons," McGraw-Hill Book Co., Inc., New York, N. Y., p. 123; 1948.

<sup>4</sup> "Reference Data for Radio Engineers," International Telephone and Telegraph Corp., New York, N. Y., 4th ed., p. 143; 1956.



The general eigenvalue problem may be expressed as  $M\psi = \lambda\psi$ , where  $\psi$  is the voltage-current eigenvector and  $\lambda$  is the eigenvalue. For resonance,  $\lambda = 1$  and hence  $\cos N\phi = 1$ , from which  $\phi = 2\pi(n/N)$  ( $n = 0, 1, 2, \dots, N-1$ ).

The elementary cell for the single-cavity ring may be chosen in two ways, as shown in Fig. 13.

With either choice,

$$\cos \beta - GZ_0 \Omega \sin \beta = \cos \phi$$

yields the resonant frequencies. A graphical solution using the parameters of the model:

$$\omega = 2\pi \times 8.7 \times 10^9 \text{ radians/sec,}$$

$$\Omega = Q\Delta\omega/\omega,$$

$$1/GZ_0 = 5,$$

$$\beta(\omega_0) = 36\pi + 0.2 \text{ radians,}$$

yields the spectrum in the neighborhood of the fundamental mode as shown in Fig. 11(b).

The elementary cell network for the double-cavity ring is shown in Fig. 14.

The equation for the resonant frequencies in this case is:

$$\cos \beta \left( 1 + \frac{GZ_0}{SZ_0} \Omega \right) - \sin \beta \left( \frac{G^2 Z_0^2}{2SZ_0} \Omega + GZ_0 \Omega - \frac{1}{2SZ_0} \right) = \cos \phi,$$

where

$$\phi = 2\pi n/N \quad (n = 0, 1, 2, \dots, N-1),$$

$$\Omega = Q\Delta\omega/\omega,$$

$$\beta(\Omega) = \beta_0(1 + \Omega\Delta/Q),$$

$$\Delta = 1 + (\lambda_{g0}/\lambda_c)^2 = (\lambda_{g0}/\lambda)^2,$$

$$\lambda_{g0} = \text{guide wavelength at } \omega_0,$$

$$\lambda_c = \text{cutoff wavelength,}$$

$$S = 1/2X, \text{ where } X \text{ is the coupling reactance.}$$

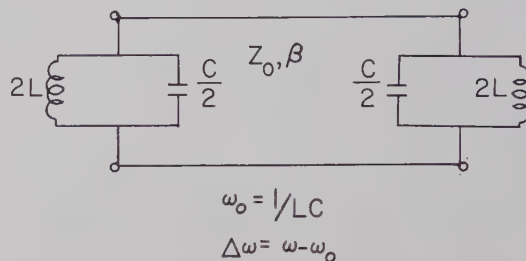
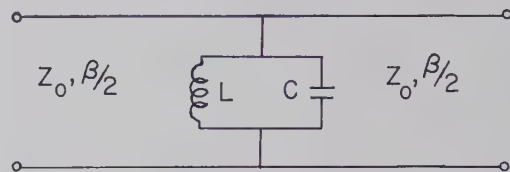


Fig. 13—Elementary cell representations of single-cavity ring.

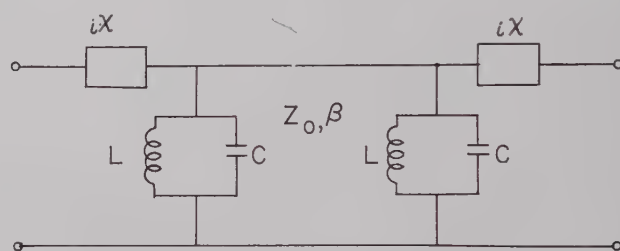


Fig. 14—Elementary cell representation of double-cavity ring.

This equation was solved on the Harvard Univac Electronic Computer and the results are plotted in Fig. 12 for the parameters of the model:

$$1/GZ_0 = 4.87,$$

$$SZ_0 = 2.5,$$

$$Q = 4033,$$

$$\beta_0 = 37\pi + \delta,$$

$$\Delta/Q = 0.000563.$$

# Operation of the Field Displacement Isolator in Rectangular Waveguide\*

R. L. COMSTOCK<sup>†</sup>, STUDENT MEMBER, IRE, AND C. E. FAY<sup>‡</sup>, FELLOW, IRE

**Summary**—A field displacement isolator in WR-159 rectangular waveguide consisting of a full height ferrite slab having a resistive film on one face is treated analytically. The resultant transcendental equation was programmed for a computer and values of the propagation constant found in the frequency range 5.90 to 6.45 kMc for various film resistivities. Two TE modes are found to exist whose relative behavior depends on the resistivity of the film.

Reasonably close experimental verification of the results was obtained for the total attenuation and for the predicted *E*-field distributions by *E*-field probe tests. Additional attenuation above that predicted by the theory for a single mode is observed as a result of an interference at the end of the ferrite.

A partial height ferrite slab isolator was subjected to *E*-field probe tests. The field distributions were found to be similar to the full height case. Here, also, additional attenuation is obtained at some frequencies as a result of an interference.

## INTRODUCTION

THE field displacement isolator has proved to be a valuable device in microwave transmission systems where low attenuation in the forward direction of transmission and high attenuation in the reverse direction are desired. In rectangular waveguide it has usually taken the form of an off-center slab of ferrite having a resistance sheet on the side nearer the center of the waveguide as shown in Fig. 1(a). The best performance so far has been obtained with "partial height" ferrites, where there is an air gap between all faces of the ferrite and the waveguide walls [Fig. 1(b)].

This type of isolator has been made to have reverse to forward attenuation ratios as high as 150 to 1 db over an 8 per cent bandwidth at 6 kMc. Such a device was first described by Fox, Miller, and Weiss.<sup>1</sup> A more complete treatment was given by Weisbaum and Seidel.<sup>2</sup> More recently, Button<sup>3</sup> has given an analysis which is quite useful in a preliminary determination of the thickness of the ferrite slab and its spacing from the sidewall for the "full height" case of Fig. 1(a). Other authors have treated the problem of propagation in ferrite-loaded waveguide but none has, to the best of our knowledge, considered the case of the field displacement isolator with resistance sheet, or the case of the

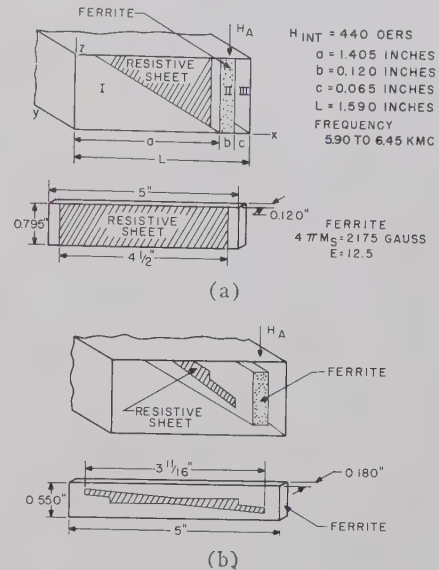


Fig. 1—Field displacement isolator configurations and dimensions. (a) Full height isolator. (b) Partial height isolator.

"partial height" ferrite. The "partial height" case would be very difficult to treat analytically.

W. J. Crowe<sup>4</sup> has calculated modes in ferrite-loaded rectangular waveguide with consideration of the effect of magnetic losses in the ferrite. We have treated a similar problem in which magnetic loss is neglected and a resistive sheet is introduced on the face of the ferrite.

Analysis of the "full height" case in WR-159 waveguide has been carried out for different loss film resistivities over the 500-Mc frequency band centered at 6.175 kMc.

The experimental work has consisted of measurement of attenuation and electric field patterns of isolators of both "full height" and "partial height" configurations. A quite powerful experimental tool for this work is the *E*-field probe. One of the authors<sup>5</sup> had considerable experience in its use prior to this work. More recently, other papers dealing with field probe experiments on ferrite-loaded waveguide have appeared.<sup>6,7</sup> One of these<sup>7</sup>

\* Received by the PGMTT, March 11, 1960; revised manuscript received, July 8, 1960.

<sup>†</sup> Microwave Laboratory, Stanford University, Stanford, Calif. Formerly with Bell Telephone Labs., Murray Hill, N. J.

<sup>‡</sup> Bell Telephone Labs., Murray Hill, N. J.

<sup>1</sup> A. G. Fox, S. E. Miller and M. T. Weiss, "Behavior and applications of ferrites in the microwave region," *Bell Syst. Tech. J.*, vol. 34, pp. 5-103; January, 1955.

<sup>2</sup> S. Weisbaum and H. Seidel, "The field displacement isolator," *Bell Syst. Tech. J.*, vol. 35, pp. 877-898; July, 1956.

<sup>3</sup> K. J. Button, "Theoretical analysis of the operation of the field displacement ferrite isolator," *IRE TRANS. ON MICROWAVE THEORY AND TECHNIQUES*, vol. MTT-6, pp. 303-308; July, 1958.

<sup>4</sup> W. J. Crowe, "Behavior of TE modes in ferrite loaded rectangular waveguide in the region of ferromagnetic resonance," *J. Appl. Phys.*, vol. 29, pp. 397-398; March, 1958.

<sup>5</sup> R. L. Comstock, D. J. Angelakos and A. Johnson, "Determination of Fields in Ferrite Loaded Waveguide," University of California, Berkeley, Engrg. Res. Ser. No. 60, Issue No. 186; July 16, 1957.

<sup>6</sup> D. J. Angelakos, "Transverse electric field distributions in ferrite loaded waveguides," *IRE TRANS. ON MICROWAVE THEORY AND TECHNIQUES*, vol. MTT-7, pp. 390-391; July, 1959.

<sup>7</sup> T. M. Straus, "Field Displacement Effect in Dielectric and Ferrite Loaded Waveguides," 1958 IRE WESCON CONVENTION RECORD, pt. I; pp. 135-145.



gives some data on a field displacement isolator which are qualitatively consistent with some of our results.

The ferrite used in this experimental work was General Ceramics Corporation's Ferramic R1, a magnesium manganese ferrite having a saturation magnetization of 2175 gauss. This had been found to make good isolators at 6 kMc. In preliminary experiments the thickness of the ferrite slab and its position in the waveguide had been varied until a situation was achieved where the minimum forward loss and a reasonably high reverse loss occurred at the same applied biasing field at a frequency of 6.175 kMc. This was done to provide a starting point for theoretical and experimental work which would be near a useful operating condition. The dimensions chosen for the ferrite bar were: length 5 inches, width 0.795 inch (equal to the narrow dimension of the waveguide), thickness 0.120 inch.

The waveguide used was WR-159 rectangular waveguide having transverse internal dimensions 1.590 inches by 0.795 inch, and the spacing of the ferrite from the waveguide sidewall was 0.065 inch.

### THEORETICAL CONSIDERATIONS

#### The Boundary Value Problem

It is desired to find the solution to the boundary value problem of a lossless ferrite slab, with a resistance sheet on one face, in rectangular TE mode waveguide [Fig. 1(a)]. The electric fields in the three regions shown in the figure are given by the following expressions:

Region	Electric Field
I	$E_z = \mathcal{A} \sin(k_a x) e^{-\Gamma y}$
II	$E_z = [\mathcal{B} e^{jk_m x} + \mathcal{C} e^{-jk_m x}] e^{-\Gamma y}$
III	$E_z = \mathcal{D} \sin[k_a(L - x)] e^{-\Gamma y}$

where  $\Gamma = \alpha + j\beta$  is the complex propagation constant. The transverse wave numbers are:

Region	Transverse Wave Number
I, III	$k_a = \sqrt{\frac{\omega^2}{c^2} + \Gamma^2}$
II	$k_m = \sqrt{\frac{\omega^2}{c^2} \epsilon \mu_e + \Gamma^2}$

where  $\epsilon$  is the relative dielectric constant and  $\mu_e$  is the effective permeability, or  $\mu_e = (\mu^2 - k^2)/\mu$ , in which  $\mu$  and  $k$  are the diagonal and off-diagonal components of the Polder tensor<sup>8</sup> which describes the ferrite permeability. To evaluate  $\Gamma$  it is not necessary to solve the boundary value problem completely and evaluate the constants  $\mathcal{A}$ ,  $\mathcal{B}$ ,  $\mathcal{C}$  and  $\mathcal{D}$ . H. Seidel<sup>9</sup> has developed a

method for the determination of  $\Gamma$  for structures of this type. Briefly, the method consists in representing the ferrite slab, resistance sheet, empty waveguide and any other region in the laminated waveguide cross-section by a transverse matrix operator. The particular operator chosen was the  $ABCD$  matrix which transfers the vector

$$\begin{bmatrix} E_z \\ H_y \end{bmatrix}$$

from one vertical longitudinal plane to another, i.e.,

$$\begin{bmatrix} E_z \\ H_y \end{bmatrix}_1 = \begin{bmatrix} A & B \\ C & D \end{bmatrix} \begin{bmatrix} E_z \\ H_y \end{bmatrix}_2$$

where subscripts 1 and 2 denote longitudinal planes in the waveguide.

Once the operators for each region are determined, they are multiplied to give an over-all matrix for the structure. From the above relation we obtain  $E_{z1} = AE_{z2} + BH_{y2}$ . If we choose planes 1 and 2 to be the waveguide sidewalls, then  $E_{z1} = E_{z2} = 0$ . This requires that  $B \equiv 0$ . Putting  $B = 0$  results in a transcendental equation from which the propagation constant  $\Gamma$  can be found as will be shown.

The relation involving the individual operators is as follows:

$$\begin{aligned} \begin{bmatrix} E_z \\ H_y \end{bmatrix}_1 &= \begin{bmatrix} \cos \Phi & j \sin \Phi \\ j \sin \Phi & \cos \Phi \end{bmatrix} \begin{bmatrix} 1 & 0 \\ \frac{1}{Z'} & 1 \end{bmatrix} \\ &\quad \text{(region I)} \quad \left( \begin{array}{c} \text{resistance} \\ \text{sheet} \end{array} \right) \\ &\quad \cdot \begin{bmatrix} \cos \theta - \nu \sin \theta & j \zeta \sin \theta \\ \frac{j}{\zeta} (1 + \nu^2) \sin \theta & \cos \theta + \nu \sin \theta \end{bmatrix} \\ &\quad \text{(ferrite—region II)} \\ &\quad \cdot \begin{bmatrix} \cos \psi & j \sin \psi \\ j \sin \psi & \cos \psi \end{bmatrix} \begin{bmatrix} E_z \\ H_y \end{bmatrix}_2, \\ &\quad \text{(region III)} \end{aligned} \quad (1)$$

where:

$$\Phi = k_a a$$

$$\theta = k_m b$$

$$\psi = k_a c$$

$$\nu = \frac{-jk\Gamma}{\mu k_m}$$

$$\zeta = \frac{k_a}{k_m} \frac{\mu^2 - k^2}{\mu}$$

$$Z' = \frac{R_s k_a}{\omega \mu_0}$$

<sup>8</sup> D. Polder, "On the theory of ferromagnetic resonance," *Phil. Mag.*, vol. 40, pp. 99-115; January, 1949.

<sup>9</sup> H. Seidel, "Ferrite slabs in transverse electric mode waveguide," *J. Appl. Phys.*, vol. 28, pp. 218-226; February, 1957.

Performing the indicated multiplication and setting the  $B$  term of the over-all matrix equal to zero results in the following equation:

$$\sin(\psi + \Phi) + \frac{j \sin \Psi \sin \Phi}{Z'} + \nu \tan \theta \left[ \sin(\Phi - \psi) - \frac{j}{Z'} \sin \psi \sin \Phi \right] + \tan \theta \left[ \zeta \cos \psi \cos \Phi + \frac{j \zeta}{Z'} \cos \psi \sin \Phi - \frac{\sin \Phi \sin \psi}{\zeta} (1 + \nu^2) \right] = 0. \quad (2)$$

An IBM 704 electronic data processing machine was used to find the roots of (2).

### Solutions of the Characteristic Equation

The first set of solutions of (2) was obtained for the case studied by Button,<sup>3</sup> that is, with no resistance sheet ( $R_S = \infty$ ). The ferrite and its position in the waveguide used in the calculations are described in the introduction and all calculations use the parameters given there. The solutions for this case are shown by the solid curves in Fig. 2. The propagation constants  $\beta_+$  and  $\beta_-$  are given as functions of the internal applied biasing field,  $H_A$ , for a frequency of 6.175 kMc. It is seen that there are two propagating modes. The one labeled "TE<sub>10</sub>" is the dominant mode and is the one discussed by Button and others. When  $H_A$  is less than 215 oersteds, another mode labeled "TE<sub>20</sub>" can propagate. These modes have the general properties of their empty waveguide equivalents but are in this case distorted by the asymmetrically placed ferrite slab. The quotation marks are used to indicate the distorted modes in the ferrite-loaded waveguide as distinguished from the empty waveguide modes of similar designation. It should be noted that the problem of determining the proportion of the energy scattered into each of these modes was not attempted. However, experimental work has shown that generally both will be excited in significant amounts. As soon as appreciable loss is introduced, the situation in regard to TE<sub>20</sub> changes markedly. The dotted curve of Fig. 2 shows that with  $R_S$  of 5000 ohms per square, a relatively high value, the TE<sub>20</sub> mode can now propagate over the entire range of applied field shown. The solutions for the "forward" direction ( $\beta_+$ ) are seen to remain essentially independent of  $H_A$  over the interval shown, a conclusion also reached by Weisbaum and Seidel.<sup>2</sup> These solutions correspond closely to the value of  $\beta$  (and hence  $k_a$ ) required by  $k_a a = \pi$  for the condition that the electric field is zero at the face of the ferrite. The computed value of  $H_A$  which results in a true null at the face of the ferrite for this frequency is 440 oersteds (internal biasing field).

Fig. 3 is a plot of solutions to (2) for a large range of

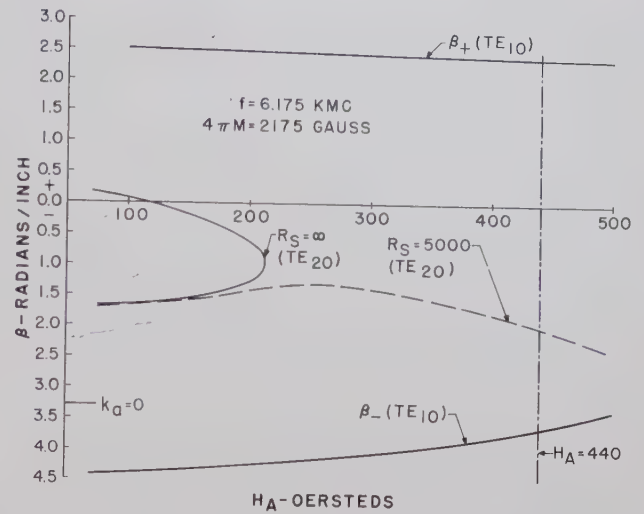


Fig. 2—Propagation constants for ferrite slab-loaded waveguide of Fig. 1(a).

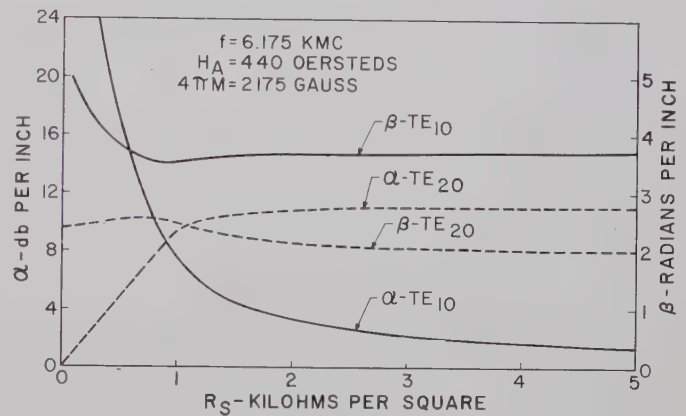


Fig. 3—Propagation constants for "reverse" direction with resistive sheet of the configuration shown in Fig. 1(a).

resistivities of the loss film. Values of  $\alpha$  and  $\beta$  are shown for a biasing field of 440 oersteds and a frequency of 6.175 kMc. These are for the "reverse" or high attenuation direction of propagation under the same conditions that produced the null at the face of the ferrite and hence theoretically no loss for the "forward" direction. For extremely low values of  $R_S$  the TE<sub>10</sub> mode is highly attenuated and all propagation is in the TE<sub>20</sub> mode or possibly higher modes. For  $R_S = 0$  the system is just a waveguide of width  $a$  (Fig. 1), and is reciprocal. For all values of  $R_S$ , at least one of the modes propagates with a value of  $\alpha \leq 8.6$  db per inch (Fig. 3). This then represents the maximum attenuation to be expected for this bias and frequency since, as will be shown in the experimental results, the energy seems to propagate principally in the mode with the lowest loss.

Fig. 4 is a plot in the complex  $\Gamma$  plane of solution curves with frequency as a parameter. The solutions are given for three representative values of resistivity:  $R_S = 670, 1000$  and  $2500$  ohms per square. Several things should be noted about the character of these solutions.



First, in contrast to unloaded waveguide solutions, it is difficult to determine when a given mode is truly cut off. The reason for this is inherent in problems involving waveguides loaded with ferromagnetic media—the non-reciprocity of the medium is manifested in the characteristic equations by a linear term in  $\Gamma$ . Because of the presence of this term, the propagation constants of the modes, which in the absence of loss would be cut off, are complex. However, if a given mode has a large value of  $\alpha$ , e.g.,  $\alpha > 15$  db per inch, the mode can be regarded as nonpropagating regardless of the value of  $\beta$ .

A second point of interest regarding these curves is the ambiguity in labeling them consistently. For example, if the resistivity of the loss sheet were increased from 670 ohms per square, at the lower frequencies the  $TE_{20}$  mode would change into a  $TE_{10}$  mode, while at the higher frequencies it would remain a  $TE_{20}$  mode. W. J. Crowe<sup>4</sup> has discussed this problem in relation to the TE mode solutions in magnetically lossy slabs in waveguides and has shown that it results from the existence of singular points at which the left side of the characteristic equation, e.g., (2), and its partial derivative with respect to  $\Gamma$ , are zero simultaneously. Such a point is observed in Fig. 4 and is labeled "A". At this point the two modes become degenerate at one frequency and changes in resistivity near this critical point result in the  $TE_{10}$  mode becoming a  $TE_{20}$  mode and vice versa.

The case of the double slab isolator having two ferrite slabs symmetrically disposed with respect to the center of the waveguide but having oppositely polarized biasing fields was not considered. One can see intuitively that the field distribution for this case must be either even or odd with respect to the center plane of the waveguide. Advantage of this could be taken in the analysis in that it would only be necessary to use the half-circuit transverse matrix operator. Lax, Button and Roth<sup>10</sup> have considered this structure without resistive sheets on the ferrites and have found the expected symmetries in the field configurations. Weisbaum and Boyet<sup>11</sup> have shown results on a partial height isolator of this type built for a commercial application.

## EXPERIMENTAL RESULTS

### Apparatus and Procedure

The  $E$ -field probe used in these experiments was a transverse traveling probe inserted in a broad face of a length of WR-159 waveguide. The probe itself was a fine wire extending about 3/32 inch into the waveguide. The wire passed through a copper sleeve and terminated on a type  $N$  coaxial fitting to which a tuned crystal detector mount was attached. A reference level of out-

put of this crystal was established, usually the reading at the center of empty waveguide. All fields were measured by adjusting a precision attenuator to bring the crystal output to this reference level. Total attenuation of the isolator is given in db with respect to the same length of empty waveguide. Transverse field distributions were taken by varying the position of the probe, usually in 0.1 inch increments across the waveguide. Unfortunately it was not possible to probe closer than about 0.1 inch from the ferrite as capacitance loading of the probe when in close proximity to the ferrite caused inaccuracies. Variation of longitudinal position was obtained by sliding the ferrite, along with its biasing magnet, past the probe.

### The Full Height Isolator

The first arrangement investigated was the full height slab of Fig. 1(a). The loss sheet was a coating of Aquadag covering the full width of the flat face of the slab leaving a 1/4 inch uncoated margin at each end. Thus the coated area was 4.5 inches by 0.795 inch.

A series of measurements of attenuation in the "reverse" direction over the frequency band was made at a constant applied biasing field using three different re-

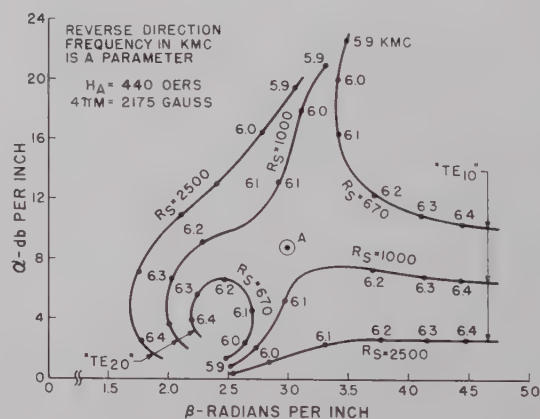


Fig. 4—Complex propagation constants of the full height isolator in the "reverse" direction with frequency and resistivity of the sheet as parameters.

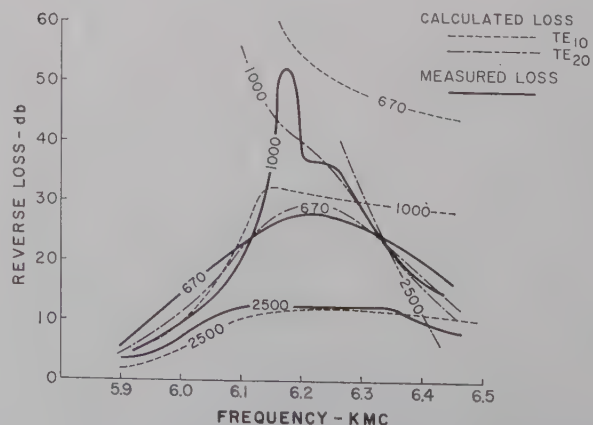


Fig. 5—Calculated and measured attenuations of the full height isolator for the "reverse" direction of transmission with sheet resistivities of 670, 1000 and 2500 ohms per square, respectively.

<sup>10</sup> B. Lax, K. J. Button and L. M. Roth, "Ferrite phase shifters in rectangular waveguide," *J. Appl. Phys.*, vol. 25, pp. 1413-1421; November, 1954.

<sup>11</sup> S. Weisbaum and H. Boyet, "Field displacement isolators for 4, 6, 11, and 24 kMc," *IRE TRANS. ON MICROWAVE THEORY AND TECHNIQUES*, pp. 194-198; July, 1957.

sistivities of the loss sheet; namely, 670, 1000 and 2500 ohms per square. The results of these measurements are compared with the calculated attenuations for these cases in Fig. 5. In addition, transverse field distributions at the center of the slab are plotted along with calculated distributions in Fig. 6. Here transverse distributions were measured at both the low and high frequency ends of the band for each loss sheet. The comparisons are made on a relative shape basis, zero db being taken as the peak value in each case. In general, good agreement with the calculated distribution is obtained. With the lowest sheet resistivity, 670 ohms per square, the

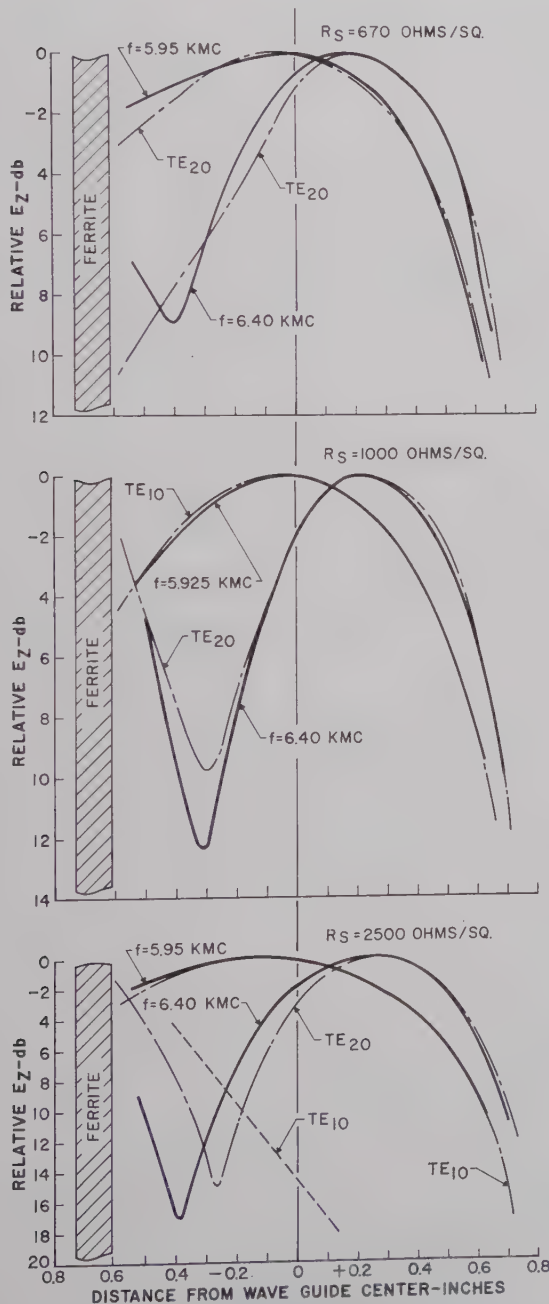


Fig. 6—Calculated and measured transverse distributions of the  $E$  field for the full height isolator with sheet resistivities of 670, 1000, and 2500 ohms per square. Solid lines indicate measured values.

$TE_{20}$  mode predominates throughout the frequency band, while with the two higher resistivities the  $TE_{10}$  mode predominates at the low frequencies and the  $TE_{20}$  mode at the high frequencies.

Longitudinal variations of the  $E$  field are shown in Fig. 7 at the midband frequency of 6.175 kMc for the resistivity of 1000 ohms per square. Four transverse positions of the probe are represented in these curves. The curve marked 0 represents the probe at the center of the waveguide,  $-0.3$  inch and  $-0.5$  inch represent distance toward the ferrite and  $+0.3$  inch represents distance away from the ferrite measured from the center of the waveguide. The signal level at the center of empty waveguide before it reaches the ferrite is the reference level, 0 db. In empty waveguide the  $+0.3$  inch and  $-0.3$  inch positions are normally 1.6 db down and the  $-0.5$  inch position is 5.1 db down. In Fig. 5, we see that at this frequency the attenuations of  $TE_{10}$  and  $TE_{20}$  are comparable so that no matter which mode is favored, the attenuation will be high. There is also the possibility of an interference of fields due to each at some points in the waveguide. If one of these points comes near the center of the waveguide and near the end of the ferrite, there usually results an increased attenuation. This is probably due to a difficulty in scattering back into the  $TE_{10}$  empty waveguide mode from such a field configuration. Although this interference condition would be reactive, the wave reflected in the "forward" direction is evidently highly attenuated since no pronounced ripple in the longitudinal distribution is found.

The sharp peak of attenuation of Fig. 5 for the 1000 ohms per square case is thus explained in Fig. 7, where we see an interference which produces a low field spot at the center of the waveguide near the end of the ferrite. Without this interference we would expect an attenuation of about 31 db for this case if the  $TE_{10}$  mode carried most of the energy. The transverse distribution for the

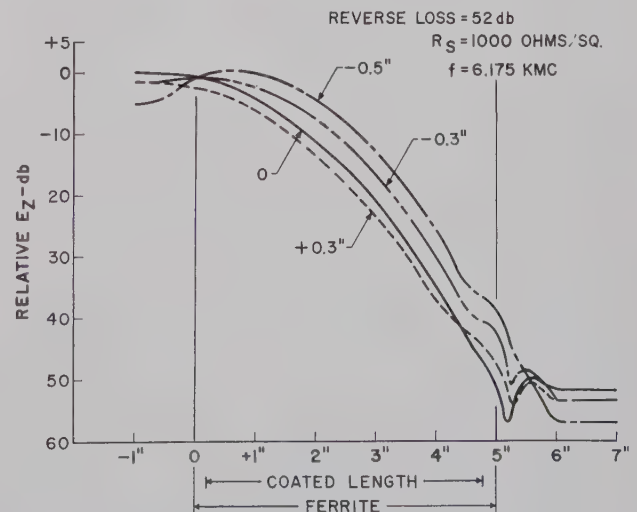


Fig. 7—Measured longitudinal distributions of the  $E$  field for the full height isolator at a frequency of 6.175 kMc for a sheet resistivity of 1000 ohms per square. Four transverse positions of the probe are used.



first four inches of the ferrite in Fig. 7 is seen to be exponential-like, that is, high field nearest the ferrite and dropping rapidly away. This is most indicative of a predominant  $TE_{10}$  mode, with the presence of the other mode being apparent only near the output end of the isolator.

### The Partial Height Isolator

A partial height isolator of a design developed for a commercial application was subjected to a field probe test. The dimensional arrangement was maintained as in the regular isolator, but some mechanical details had to be changed to allow use of the probe. The attenuation of this isolator across the frequency band is shown in Fig. 8. This curve shows two peaks of attenuation. Probe measurements were made at five frequencies: one at the low frequency end of the band, 5.925 kMc; one at the first peak of attenuation, 5.958 kMc; one in the low center region at 6.10 kMc; one at the second peak 6.25 kMc; and one near the high frequency end of the band at 6.40 kMc. The results are shown on the longitudinal plots of Fig. 9.

The 5.925-kMc plot, Fig. 9(a), shows a fairly uniform attenuation with a transverse field distribution indicative of a  $TE_{10}$  type mode. The 5.958-kMc plot, Fig. 9(b), shows much the same type distribution, as might be expected since the frequency is little changed. However, at the end of the ferrite a peculiar situation exists and a sudden increase in attenuation is found. This is probably a result of an interference taking place at a position such that scatter into the normal  $TE_{10}$  mode is difficult. The 6.10-kMc plot, Fig. 9(c), shows an interference taking place before the end of the ferrite such that it has little effect on the total attenuation. The 6.25-kMc curves, Fig. 9(d), show two interferences. One in the middle of the ferrite-loaded section has little net effect, but another at the end results again in increased attenuation. The 6.40-kMc plot, Fig. 9(e), also shows two interferences, both within the ferrite-loaded portion, and the start of another at the end but the total attenuation is the least of the five cases. The first four of these field curves start out with  $TE_{10}$  type distributions at the 1-inch transverse plane for example. How-

ever, Fig. 9(e) does not show this distribution, indicating that some other mode is of magnitude comparable to  $TE_{10}$  from the beginning.

### DISCUSSION AND CONCLUSIONS

It is apparent from Fig. 4 that not much attenuation is possible at the low frequencies if both  $TE_{10}$  and  $TE_{20}$  can be excited since one of these modes will have fairly low attenuation no matter what the resistivity of the loss sheet. The transverse distributions for the low frequencies in Fig. 6 are all not markedly different from the empty waveguide  $TE_{10}$  sinusoid and hence should be

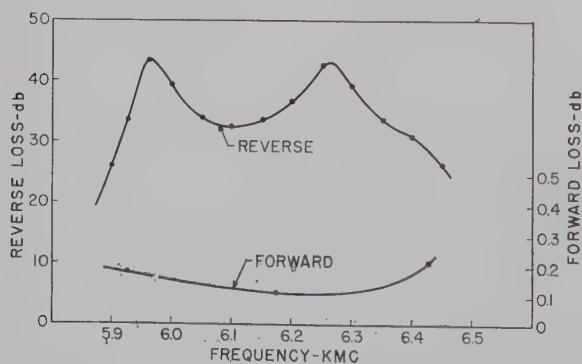


Fig. 8—Attenuation of the partial height isolator as a function of frequency.

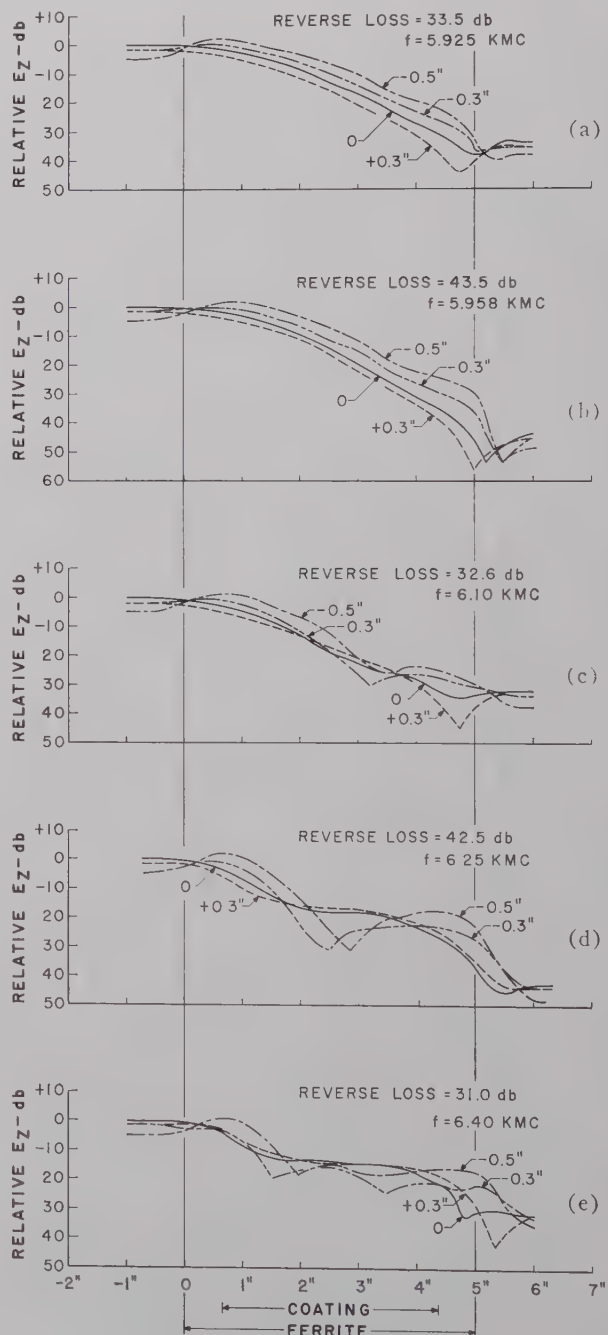


Fig. 9—Longitudinal distributions of the  $E$  field in the partial height isolator for the "reverse" direction of propagation at five representative frequencies. Four transverse positions of the probe are used.

easily excited. It would seem, therefore, that the most useful isolator would have its lowest frequency and resistivity corresponding to the region of point *A* in Fig. 4. Going from this point to higher frequencies, the attenuation of  $TE_{10}$  holds up well. However, that of  $TE_{20}$  drops so it appears the device is not inherently very broadband. An interference arranged to occur at a suitable frequency would help to increase the bandwidth somewhat. If some means could be found to discourage the excitation of  $TE_{20}$  without increasing the reciprocal loss appreciably, the bandwidth could be improved. The optimum resistivity of the loss sheet for the case considered here seems, from Fig. 3, to be about 900 ohms per square. The nearest to optimum performance was obtained in the case of the resistivity of 1000 ohms per square as shown in Fig. 5. Here the agreement between theory and experiment is quite good except in the region of the interference which the calculations do not take into account.

A single-mode concept of operation seems obviously inadequate to account for the observed performance. The effect of the resistance sheet in the case for optimum attenuation is a critical factor in determining the field distributions and cannot be regarded as a small perturbation of the field. The role of the interference in providing peaks of attenuation seems to be well established. This was first noted and discussed by H. Seidel.<sup>12</sup>

Although the partial height isolator has not been treated analytically, the behavior is sufficiently similar to that of the full height isolator that a general understanding of its operation is obtainable. Since fairly good attenuations are obtained at the low frequency end of its band it would seem that this corresponds to operation in the vicinity of the equivalent of point *A* of Fig. 4. It is also possible that the  $TE_{20}$  mode is not propagated as

easily in this structure and that its attenuation does not drop so rapidly with frequency. The field configurations obtained seem consistent with the hypothesis that basically the  $TE_{10}$  mixes with enough of another mode to cause two useful interferences in its operating frequency band. Here, of course, the narrower coating of lower resistivity, approximately 150 ohms per square, is used. The effect of the peculiar changes in width of the pattern is not understood, but it is known they have an effect on the position of the interferences in the frequency response curve. The partial height of the ferrite and the resistive coating would permit *z*-dependent modes such as described by Seidel<sup>12</sup> and by Seidel and Fletcher<sup>13</sup> to be excited in this structure. These may indeed provide some of the attenuation. If they were responsible for the major part of the total attenuation, one would expect that the  $TE$  fields, particularly those away from the ferrite, would practically disappear near the beginning of the ferrite-loaded waveguide and then reappear suitably attenuated at the end, but this is not observed.

The combination of an analytical approach and experimental verification involving field mapping has provided an insight into the operation of a field displacement isolator in one rather narrow frequency range. We believe this has resulted in a sufficient knowledge of the device to provide a qualitative guide to the design of similar devices at other frequencies.

#### ACKNOWLEDGMENT

The authors wish to acknowledge the valuable suggestions of W. J. Crowe and his assistance in programming the problem for the computer. They are also indebted to J. A. Weiss for helpful comments and suggestions in the preparation of the manuscript.

<sup>12</sup> H. Seidel, "Anomalous propagation in ferrite loaded waveguide," *PROC. IRE*, vol. 44, pp. 1410-1414; October, 1956.

<sup>13</sup> H. Seidel and R. C. Fletcher, "Gyromagnetic modes in waveguide partially loaded with ferrite," *Bell Syst. Tech. J.*, vol. 38, pp. 1427-1456; November, 1959.



# Peak Internal Fields in Direct-Coupled-Cavity Filters\*

LEO YOUNG†, SENIOR MEMBER, IRE

**Summary**—Microwave filters are limited in their power-handling capacity by high fields generated inside the filter.

Simple formulas are derived here for the peak fields inside each cavity of a direct-coupled-cavity filter at any frequency. The computed peak fields in each cavity of a three-cavity, a four-cavity, and a six-cavity filter as a function of frequency are reproduced up to several harmonics. Inside the pass band, the internal fields are generally minimum at center frequency, rising to sharp peaks just outside the pass band.

Phase characteristics were also computed, and their relation to the internal field amplitudes is explained.

## INTRODUCTION

HIGH-POWER applications of microwave filters are becoming more numerous,<sup>1-4</sup> as the transmitter power of radars is increased. Commonly used are microwave band-pass filters, which generally take the form of direct-coupled-cavity filters. Cohn has obtained formulas for designing such filters to meet a specified maximum insertion loss over a given pass band,<sup>5</sup> and has also discussed general design considerations for such high-power filters.<sup>6</sup>

A more detailed analysis of the power-handling capacity of direct-coupled-cavity filters is presented here. Several filters were analyzed numerically, and results for a three-cavity, a four-cavity, and a six-cavity filter are presented.

## DEFINITIONS

All transmission lines and all obstacles in them will be considered to have no dissipation losses. One can therefore associate a power flow with each traveling wave, the net forward power flow being simply the difference in the powers carried by the forward and backward waves. The amplitude  $a_i$  of a forward traveling wave

(traveling towards the load) is defined in magnitude by<sup>7,8</sup>

$$|a_i|^2 = \text{power flow due to the forward traveling wave,} \quad (1)$$

and a similar definition holds for the amplitude,  $b_i$ , say, of a backward-traveling wave (traveling towards the generator).

The same peak amplitude as is produced inside a cavity by internal reflections would occur in a properly terminated transmission line without obstacles, if sufficient power were fed into it. Thus, if  $a_i$  and  $b_i$  are the forward- and backward-wave amplitudes in the  $i$ th cavity, and if  $a_{in}$  is the amplitude of the forward traveling wave at the filter input, then the *equivalent power ratio* is defined by

$$\left( \frac{|a_i| + |b_i|}{|a_{in}|} \right)^2 \quad (2)$$

provided that a maximum of the standing wave occurs inside the cavity.

## EQUIVALENT POWER RATIOS IN THE CAVITIES

A direct-coupled-cavity filter is shown schematically in Fig. 1. To find the peak amplitude inside the  $i$ th section, let  $a_i$  be the forward-wave amplitude (Fig. 2) and  $r_i$  the reflection coefficient, in that cavity. Then, if unit power emerges from the filter,

$$|a_i|^2 - |a_i r_i|^2 = 1. \quad (3)$$

Therefore

$$|a_i| = (1 - |r_i|^2)^{-1/2}. \quad (4)$$

Therefore, the peak internal amplitude is

$$|a_i| (1 + |r_i|) = \left( \frac{1 + |r_i|}{1 - |r_i|} \right)^{1/2} = S_i^{1/2} \quad (5)$$

times the magnitude of the wave amplitude *emerging* from the filter, where  $S_i$  is the VSWR seen in the  $i$ th section. The "equivalent power ratio" was defined by (2) in terms of the incident power. It is thus given by

$$\left. \begin{aligned} &\text{Equivalent power ratio in the } i\text{th cavity} \\ &= (\text{VSWR seen in the } i\text{th cavity, } S_i) \\ &\times (\text{fraction of power transmitter by the filter}) \end{aligned} \right\} \quad (6)$$

\* Received by the PGM-TT, April 18, 1960; revised manuscript received, July 13, 1960.

† Stanford Res. Inst., Menlo Park, Calif. Formerly with Electronics Div., Westinghouse Electric Corp., Baltimore, Md.

<sup>1</sup> H. A. Wheeler and H. L. Bachman, "Evacuated waveguide filter for suppressing spurious transmission from high-power S-band radar," IRE TRANS. ON MICROWAVE THEORY AND TECHNIQUES, vol. MTT-7, pp. 154-162; January, 1959.

<sup>2</sup> E. N. Torgow, "Hybrid junction-cutoff waveguide filters," IRE TRANS. ON MICROWAVE THEORY AND TECHNIQUES, vol. MTT-7, pp. 163-167; January, 1959.

<sup>3</sup> L. Young and J. Q. Owen, "A high power diplexing filter," IRE TRANS. ON MICROWAVE THEORY AND TECHNIQUES, vol. MTT-7, pp. 384-387; July, 1959.

<sup>4</sup> J. H. Vogelmann, "High-power microwave rejection filter using higher-order modes," IRE TRANS. ON MICROWAVE THEORY AND TECHNIQUES, vol. MTT-7, pp. 461-465; October, 1959.

<sup>5</sup> S. B. Cohn, "Direct-coupled-resonator filters," PROC. IRE, vol. 45, pp. 187-196; February, 1957.

<sup>6</sup> S. B. Cohn, "Design considerations for high-power microwave filters," IRE TRANS. ON MICROWAVE THEORY AND TECHNIQUES, vol. MTT-7, pp. 149-153; January, 1959.

<sup>7</sup> L. Young, "Transformation matrices," IRE TRANS. ON CIRCUIT THEORY, vol. CT-5, p. 147; June, 1958.

<sup>8</sup> L. Young, "Analysis of a transmission cavity wavemeter," IRE TRANS. ON MICROWAVE THEORY AND TECHNIQUES, vol. MTT-8, pp. 436-439; July, 1960.

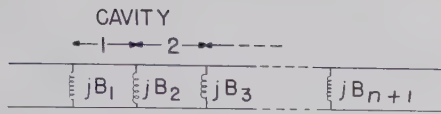


Fig. 1—Direct-coupled-cavity filter with shunt-inductive elements.  $jB_1, jB_2, \dots, jB_{n+1}$  are the normalized susceptances at band-center of the  $N$ -cavity filter.

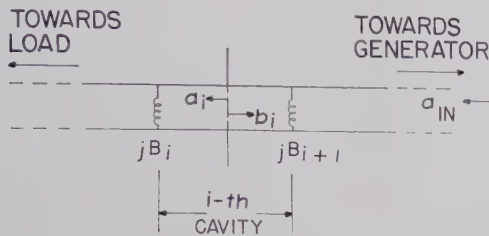


Fig. 2—Showing wave amplitudes inside the filter.

One has to be sure, of course, that the maximum of the standing wave in each cavity occurs at a real position inside the cavity, and not at a virtual position beyond the cavity in question. In the case of cavities a half-wavelength long or longer, this is always true. It also holds at least near band-center for quarter-wave transformers, and for the electric field in shunt-inductively coupled cavities.

For waveguide filters with shunt-inductive irises, and for coaxial line filters with shunt-inductive posts, the reactance of the shunt-coupling element is approximately proportional to frequency, *i.e.*, it behaves as an inductor. A digital computer program for computing the VSWR of such filters was available. By feeding in (for instance) only the first four cavities of a six-cavity filter, the VSWR in the fifth cavity was computed. The fraction of power transmitted by the whole filter was also computed by the same program applied to the whole filter; and the equivalent power ratio in the fifth (or any other) cavity was then determined from (6).

#### RELATION BETWEEN EQUIVALENT POWER RATIO AND PHASE

A direct-coupled-cavity filter resembles a periodic transmission system,<sup>9,10</sup> in which the group velocity  $v_g$  is given by

$$v_g = \frac{d\omega}{d\beta}, \quad (7)$$

where  $\omega$  = radian frequency, and  $\beta$  is the phase constant. The phase change  $\phi$  through a long section of length  $L$  is then  $\phi = \beta L$ . For our present purposes, we may write

$$v_g \propto \frac{1}{\left(\frac{d\phi}{d\omega}\right)} \quad (8)$$

Since  $v_g$  is also the velocity of propagation of energy, one may write in a pass band,

$$(\text{average energy density}) \times v_g = \text{const}, \quad (9)$$

or,

$$\text{Average energy density} \propto \frac{1}{v_g} \propto \frac{d\phi}{d\omega}, \quad (10)$$

which may be replaced by

$$\text{Equivalent power ratio} \propto \frac{d\phi}{d\omega}$$

$$\propto \text{Rate of change of phase with frequency.} \quad (11)$$

Of course, this will hold only to the extent that our direct-coupled-cavity filter resembles an infinite uniform periodic structure.

The phase  $\phi$  appearing in (11) and elsewhere above refers to the total phase shift from input to output, whereas the computer program was designed to give the excess phase shift through the filter over the phase shift through a uniform transmission line of the same length. (One of the advantages of plotting the excess phase shift is that it permits a more accurate graphical description of phase change than does a plot of total phase shift. Thus, in Fig. 5 the latter would require an ordinate range of several thousand degrees instead of the several hundred degrees which are needed to plot the excess phase shift.) To obtain  $\phi$  from the plotted (excess) phase shift, one then has to add back  $360L/\lambda_g$  degrees, where  $L$  is the length of the filter and  $\lambda_g$  is the guide wavelength.

#### NUMERICAL RESULTS

Three different filters were investigated. Their circuit parameters are first given:

Filter 1; Number of cavities,  $n=6$ :

Susceptances (see Fig. 1):

$$B_1 = B_7 = 1.77977 \text{ at band-center}$$

$$B_2 = B_6 = 6.40453 \text{ at band-center}$$

$$B_3 = B_5 = 9.54427 \text{ at band-center}$$

$$B_4 = 10.15377 \text{ at band-center.}$$

Spacings (see Fig. 1):

$$\theta_1 = \theta_6 = 147.161^\circ \text{ at band-center}$$

$$\theta_2 = \theta_5 = 165.411^\circ \text{ at band-center}$$

$$\theta_3 = \theta_4 = 168.511^\circ \text{ at band-center.}$$

Over-all length of filter

$$= \frac{962.166}{360} \text{ wavelengths at band-center.}$$

<sup>9</sup> L. Brillouin, "Wave Propagation in Periodic Structures," Dover Publications, New York, N. Y.; 1953.

<sup>10</sup> D. A. Watkins, "Topics in Electromagnetic Theory," John Wiley and Sons, Inc., New York, N. Y.; 1958.



Filter 2;  $n=4$ :

$$\begin{aligned} B_1 &= B_5 = 2.84605 \text{ at band-center.} \\ B_2 &= B_3 = B_4 = 9.90000 \text{ at band-center.} \\ \theta_1 &= \theta_4 = 156.741^\circ \text{ at band-center.} \\ \theta_2 &= \theta_3 = 168.579^\circ \text{ at band-center.} \end{aligned}$$

Over-all length of filter:

$$= \frac{650.640}{360} \text{ wavelengths at band-center.}$$

Filter 3;  $n=3$ :

$$\begin{aligned} B_1 &= B_4 = 0.50000 \text{ at band-center.} \\ B_2 &= B_3 = 1.20000 \text{ at band-center.} \\ \theta_1 &= \theta_3 = 112.500^\circ \text{ at band-center.} \\ \theta_2 &= 120.964^\circ \text{ at band-center.} \end{aligned}$$

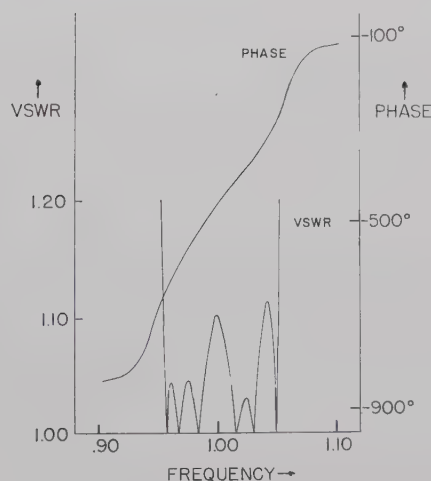


Fig. 3—VSWR and phase vs frequency of the six-cavity filter (Filter 1) over the lowest pass band.

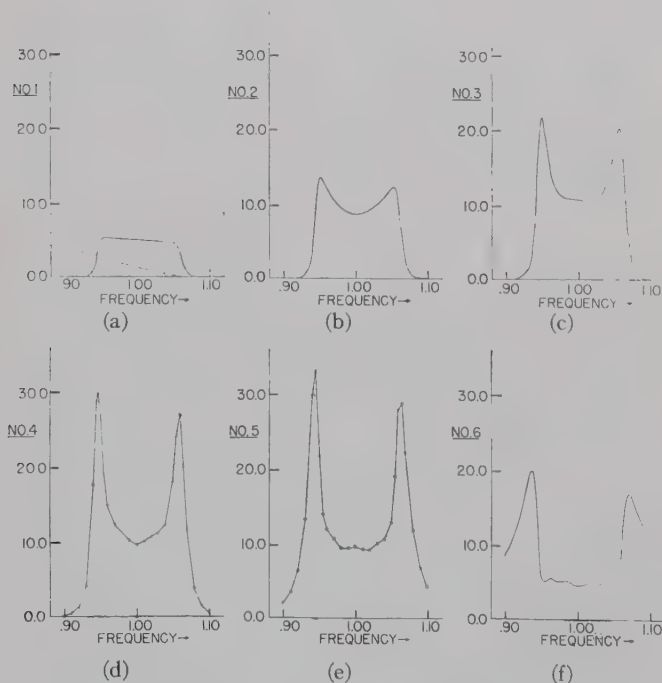


Fig. 4—Equivalent power ratios in the six cavities of Filter 1 over the lowest pass band.

Over-all length of filter

$$= \frac{345.964}{360} \text{ wavelengths at band-center.}$$

## DISCUSSION

### Filter 1

The performance of Filter 1 is dealt with in Figs. 3–6. This is a six-cavity filter, the same one which is described in Fig. 9 of Cohn.<sup>5</sup> It has a 9.5 per cent bandwidth inside which the maximum VSWR is 1.113. This will be called its pass band. Its VSWR and (excess) phase response are plotted in Fig. 3 over and near the pass band. Note that here and throughout the graphs, the frequency axis should be labeled proportional to “reciprocal guide wavelength” in the case of dispersive waveguides.

The equivalent power ratios inside and just beyond the pass band are plotted against frequency for cavities 1 to 6 in Fig. 4(a)–4(f). By “Cavity 1” is meant the

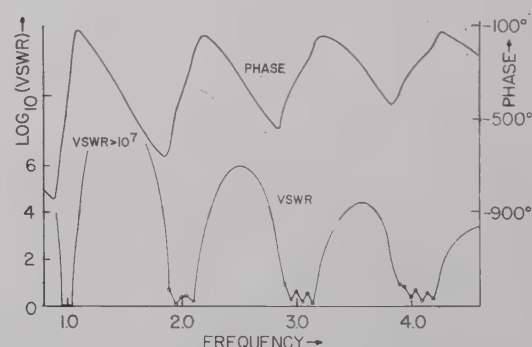


Fig. 5—VSWR and phase vs frequency of the six-cavity filter (Filter 1) up to the fourth harmonic.

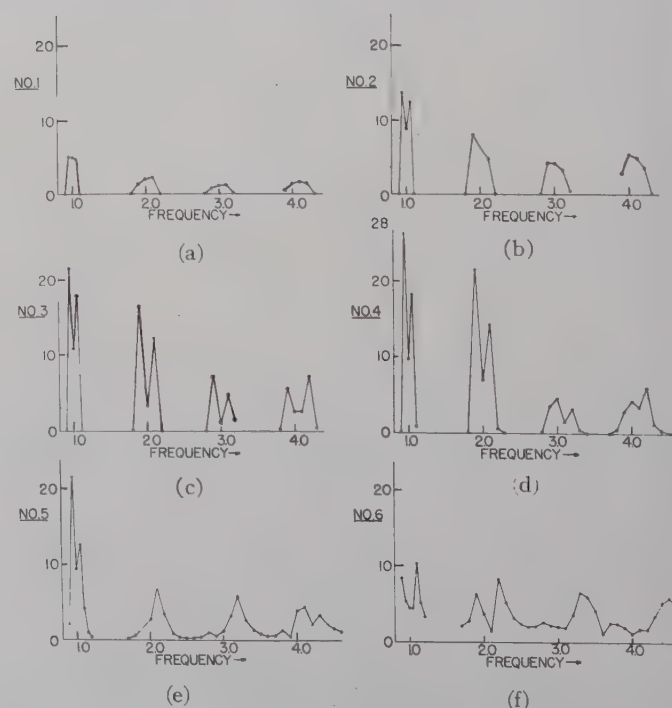


Fig. 6—Equivalent power ratios in the six cavities of Filter 1 up to the fourth harmonic.

cavity nearest the load, while "Cavity 6" is the one nearest the generator. For most of the curves, so many points were computed that a continuous curve is shown. Where only a small number of points were computed, as in Fig. 4(d) and (e), the computed points are shown by circles and joined by straight lines.

The greatest equivalent power ratio inside the pass band occurs in Cavity 4 at each edge of the band, where it reaches the value 20. This is twice as much as the equivalent power ratio in the same cavity at band-center. The greatest equivalent power ratio anywhere occurs in Cavity 5 just outside the lower end of the pass band, where it reaches at least 33.5.

The over-all length of the filter, *i.e.*, the sum of the six cavity lengths, is  $962.166^\circ$  at band-center. An unloaded uniform transmission line of this length increases its electrical length by  $9.62^\circ$  whenever the frequency increases by 1 per cent of the center frequency. This has to be added to the slope of the (excess) phase shift vs frequency curve plotted in Fig. 3 to get the total rate of change of phase with frequency, which, according to (11), should be approximately proportional to the equivalent power ratio in any cavity. It is clear by visual inspection that the slope of the phase plot in Fig. 3 does indeed rise and fall as the equivalent powers in all cavities except the first [Fig. 4(b)–(f)]. More precisely, if the slopes are determined from Fig. 3, and  $9.62^\circ$  per 0.01 change in frequency is added, then the respective slopes of the total phase shift at  $f=0.947$ , 1.00, and 1.06, where they are maximum, minimum, and maximum in turn, are in the ratio 2.2:1:1.8, which is in fair agreement with (11) and Fig. 4.

Figs. 5 and 6 represent the same six-cavity filter, plotted from below the first pass band to beyond the fourth harmonic. The same double humps in the equivalent power ratios are observed, but they get more "blurred" as the frequency and cavity number increase. The (excess) phase vs frequency slope in the graphs sometimes appears negative because, as explained before, it has been computed as a phase shifter; when the phase slope of  $9.62$  degrees per 0.01 increase in frequency is added, the curve always takes on a positive slope, with a staircase appearance.

### Filter 2

This is a four-cavity filter, and is based on another one of Cohn's examples.<sup>6</sup> This one was selected to have  $g_1=g_2=g_3=g_4=1$ , which maximizes the power handling capacity for a given degree of selectivity.<sup>6</sup> Unfortunately, the VSWR inside the pass band is not very good (Fig. 7). Here  $g_0=0.1$  is used to define the filter. (Cohn's filter is defined differently; it corresponds to  $g_0=0.08$ .) The phase vs frequency curve (Fig. 7) is remarkably straight over most of the band, and the equivalent power ratio in most cavities stays relatively constant over the same portion of the band, as would be expected from (11). There are the same two familiar sharp peaks of equivalent power ratio just outside the

band, corresponding to the two kinks in the phase curve. Compare Figs. 7 and 8(a)–(d).

Fig. 4 of Cohn<sup>6</sup> plotted the relative electric field strength against the frequency parameter  $\omega'$  of the prototype filter, taking it from  $\omega'=0$  to  $\omega'=1.1$ . This corresponds approximately to the range  $f=0.97$  to  $f=1.03$  in our frequency scale.<sup>11</sup> The twin peaks of the equivalent power ratio against frequency curves occur at the very edges of the pass band, at approximately  $f=0.95$  and  $f=1.05$ , and so are beyond the frequency range covered in Cohn's Fig. 4.

<sup>11</sup> Dr. Cohn has pointed out to the author that in Fig. 4 in "Design considerations for high power microwave filters" (*op. cit.*), Curves 3 and 4 were inadvertently interchanged. The agreement with Fig. 8 here is then quite close.

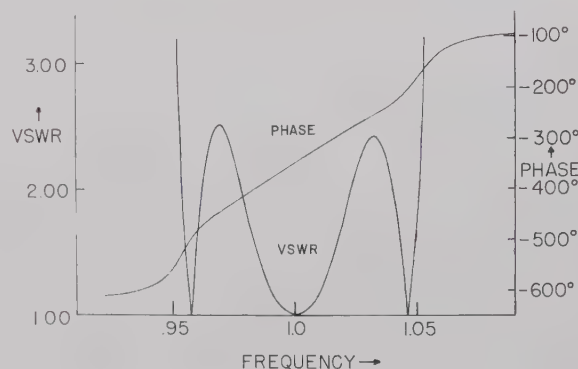


Fig. 7—VSWR and phase vs frequency of the four-cavity filter (Filter 2) over the lowest pass band.

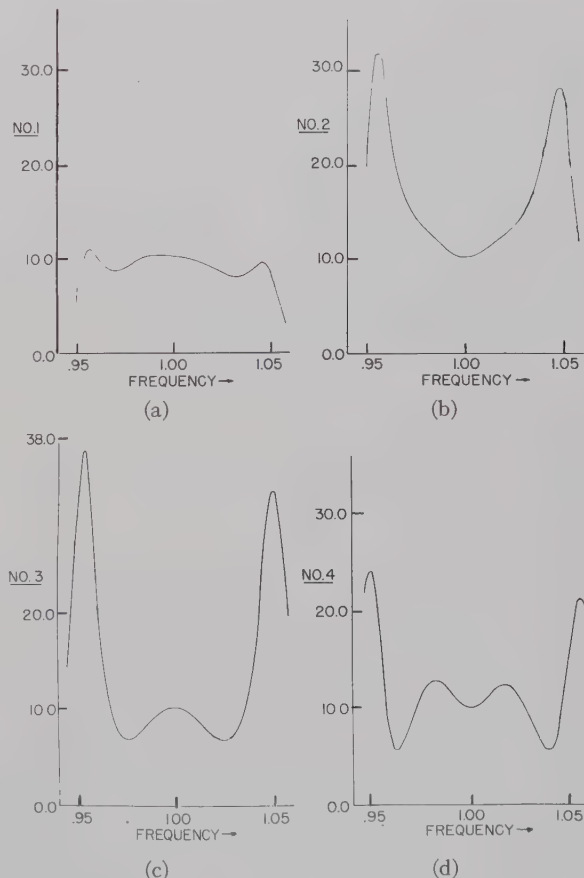


Fig. 8—Equivalent power ratios in the four cavities of Filter 2 over the lowest pass band.



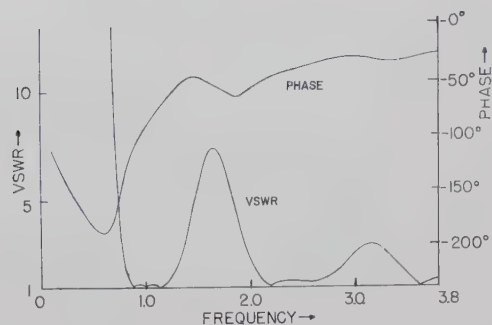


Fig. 9—VSWR and phase vs frequency of the three-cavity filter (Filter 3) up to the third harmonic.

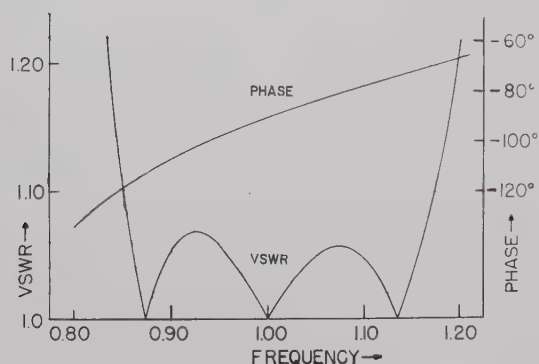
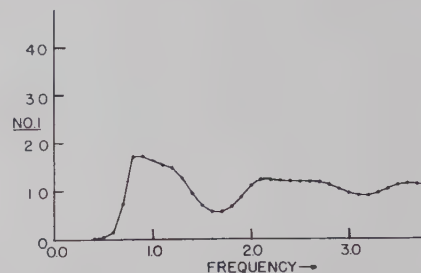


Fig. 10—VSWR and phase vs frequency of the three-cavity filter (Filter 3) over the lowest pass band.

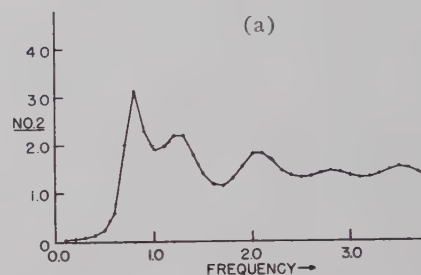
### Filter 3

This filter<sup>12</sup> has three cavities. They are much more strongly coupled than in the previous two examples. The highest VSWR above the pass band is only 7.4 (Fig. 9). It has a 30.6 per cent pass band, inside which the VSWR never exceeds 1.07 (Fig. 10). The phase

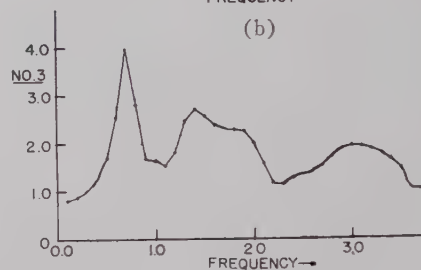
<sup>12</sup> L. Young, "The quarter-wave transformer prototype circuit," IRE TRANS. ON MICROWAVE THEORY AND TECHNIQUES, vol. MTT-8, pp. 483-489; September, 1960.



(a)



(b)



(c)

Fig. 11—Equivalent power ratios in the three cavities of Filter 3 up to the third harmonic.

plots are also given in Figs. 9 and 10. The equivalent power ratios in each cavity are plotted beyond the third harmonic in Fig. 11(a)–11(c). The general behavior is as noted in the previous two examples.

### ACKNOWLEDGMENT

The author is very grateful to A. C. Robertson for performing numerical work with so much care, and to W. M. Etchison for his constant help and advice on computer programming.

# Mismatch Errors in Microwave Phase Shift Measurements\*

G. E. SCHAFER†, SENIOR MEMBER, IRE

**Summary**—The phase difference between the incident and transmitted waves at the input and output ports, respectively, of a two-arm waveguide junction in a reflection free system is a characteristic of the waveguide junction and is defined as the “phase shift.” The difference between the phase shift in a reflection free system and the “change of phase” observed in a system which is not reflection free will be termed mismatch error. The mismatch error depends not only on the reflections present in the system but also on the choice of the wave used as the reference wave in a phase measurement. Similar considerations hold for the measurements of variation of phase shift and the observed change of phase in adjustable components.

A formal scattering matrix analysis is used to derive expressions for phase relationships of the wave amplitudes for a two-arm waveguide junction in a system with reflections. The results of this analysis are used to evaluate mismatch error for different choices of reference waves. Two techniques of variation of phase shift measurements are analyzed. Graphs of the limits of mismatch error in a commonly used method of measurement are presented.

## INTRODUCTION

THE phase shift through a waveguide component at a single frequency is the phase difference under matched conditions between corresponding incident and transmitted field quantities at the input and output ports, respectively, ignoring multiples of  $2\pi$  radians.<sup>1</sup> From this definition, it is seen that the phase shift through a waveguide component is a characteristic of the component. However, if the component is inserted in a system which has reflections, two interactions take place which cause errors in measurements of phase shift. It will be shown that the phase difference between the emergent wave from the output port (transmitted wave) and the wave incident at the input port (incident wave) depends only on the reflection coefficient of the equivalent load attached to the junction and the characteristics of the junction. However, the phase of the incident wave with respect to some independent reference such as the component of the incident wave supplied by the generator depends on the reflection coefficients of both the load and the generator, and the characteristics of the junction. Consequently, the phase of the emergent wave with respect to an independent reference depends on the reflection coefficients of the load and generator and characteristics of the junction. The difference between the phase shift and the phase change

observed will be termed a mismatch error. Care must be exercised to determine which wave is being used as a reference in evaluating these mismatch errors. Similar considerations hold for measurements of variation of phase shift and the observed change of phase in adjustable components such as microwave phase shifters or attenuators.

A scattering matrix analysis is used to derive the phase relationship among various wave amplitudes in a two-arm waveguide junction inserted in a system with reflections. Mismatch errors are evaluated for two choices of reference waves. Two commonly used methods of measuring variations of phase shift in adjustable components are analyzed for mismatch error. Limits of mismatch error are calculated for the first method, a two channel arrangement, and presented in two graphs. One graph presents limits of error for lossless components and is valid for low loss phase shifters. The limits of mismatch error for a lossless phase shifter are slightly larger than those which would be encountered in a low loss component such as a commercial phase shifter, or in an attenuator when one or both of the settings is less than 20 db. The other graph is for components which have at least 20 db loss at both settings. This graph is presented since such measurements have smaller limits of mismatch error.

The second method which is treated uses a short circuit and slotted line to measure the phase shift or variation of phase shift of low-loss components. The error is evaluated and it is found to depend to the first order only on the mismatches of the component and not on the mismatches of the generator.

## THEORY

A two-arm waveguide junction may be represented as in Fig. 1. The phase of the emergent wave from arm 2

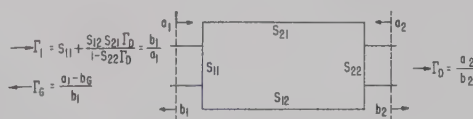


Fig. 1—A two-arm waveguide junction representation.

(the transmitted wave) with respect to the other waves associated with the junction may be derived by the use of the scattering matrix,  $S$ . In terms of this matrix,

$$b = Sa \quad (1)$$

where  $b$  is a column matrix of the emergent wave ampli-

\* Received by the PGMTT, May 10, 1960; revised manuscript received, July 13, 1960.

† Radio Standards Lab., National Bureau of Standards, Boulder, Colo.

<sup>1</sup> "IRE standards on antennas and waveguides: waveguide and waveguide component measurements, 1959," *PROC. IRE*, vol. 47, pp. 568-582; April, 1959.



tudes,  $a$  is a column matrix of the incident wave amplitudes, and  $S$  is the scattering matrix of the junction. It can readily be shown from (1) and Fig. 1 that the output wave is related to the component of the input wave supplied by the generator  $b_G$  by

$$\frac{b_2}{b_G} = \frac{S_{21}}{(1 - \Gamma_1 \Gamma_G)(1 - S_{22} \Gamma_D)} \quad (2)$$

where the  $S$ 's are elements of the scattering matrix associated with the two arm junction, and  $\Gamma_G$  and  $\Gamma_D$  are the equivalent generator and detector reflection coefficients, respectively, and  $\Gamma_1$  is the reflection coefficient of the equivalent load attached to the generator.  $\Gamma_1$  may be expressed as

$$\Gamma_1 = S_{11} + \frac{S_{12} S_{21} \Gamma_D}{1 - S_{22} \Gamma_D} \quad (3)$$

The argument of (2) is the phase difference between the emergent wave,  $b_2$ , and  $b_G$ , which is the wave that would be delivered to a reflectionless load.  $b_G$  is independent of the reflections of the system and therefore is termed the independent wave.

Eq. (2) may be written in the form

$$\frac{b_2}{b_G} = \frac{b_2}{a_1} \cdot \frac{a_1}{b_G} \quad (4)$$

where

$$\frac{b_2}{a_1} = \frac{S_{21}}{1 - S_{22} \Gamma_D} \quad (5)$$

and

$$\frac{a_1}{b_G} = \frac{1}{(1 - \Gamma_1 \Gamma_G)} \quad (6)$$

The argument of  $b_2/a_1$  is the phase difference between the transmitted wave and the incident wave. The argument of  $a_1/b_G$  is the phase difference between the incident wave and the independent generator wave,  $b_G$ . When  $\Gamma_D = \Gamma_G = 0$ , the phase difference of (6) reduces to zero and both (2) and (5) reduce to

$$\frac{b_2}{a_1} = S_{21} = |S_{21}| e^{j\phi_{21}} \quad (7)$$

where  $\phi_{21}$  is, by definition, the phase shift through the waveguide component.

#### EVALUATION OF MISMATCH ERROR

*Case I. The Reference Wave is the Independent Wave,  $b_G$*

In techniques where the independent wave is used as the reference wave, the mismatch error for a phase shift measurement may be obtained by rewriting (2) in the form

$$\frac{b_2}{b_G} = |S_{21}| e^{j\phi_{21}} |E_a| e^{j\epsilon_a}, \quad (8)$$

where

$$|E_a| e^{j\epsilon_a} = \frac{1}{(1 - \Gamma_1 \Gamma_G)(1 - S_{22} \Gamma_D)} \quad (9)$$

The difference between the measured change of phase and the phase shift of the component is just  $\epsilon_a$ , the argument of (9). For differential phase shifters or attenuators, using front superscripts  $i$  and  $f$  to denote initial and final settings, respectively, the change of phase of  $b_2$  with respect to the independent wave may be obtained from an expression derived from (2), which is

$$\frac{^f b_2}{^i b_2} = \frac{^f S_{21}}{^i S_{21}} \frac{(1 - ^i \Gamma_1 \Gamma_G)(1 - ^i S_{22} \Gamma_D)}{(1 - ^f \Gamma_1 \Gamma_G)(1 - ^f S_{22} \Gamma_D)}, \quad (10)$$

where the argument of (10) is the change in phase of the emergent wave,  $b_2$ , with respect to the independent wave when the setting of the junction is changed. For  $\Gamma_D = \Gamma_G = 0$ , this reduces to

$$\frac{^f b_2}{^i b_2} = \frac{^f S_{21}}{^i S_{22}} = \frac{|^f S_{21}|}{|^i S_{21}|} e^{j(^f \phi_{21} - ^i \phi_{21})}, \quad (11)$$

where  $^f \phi_{21} - ^i \phi_{21}$  is the variation of phase shift when the setting of the junction is changed. For  $\Gamma_G$  and  $\Gamma_D$  not zero, (10) may be written in the form

$$\frac{|^f b_2|}{|^i b_2|} e^{j(^f \psi_2 - ^i \psi_2)} = \frac{|^f S_{21}|}{|^i S_{21}|} e^{j(^f \phi_{21} - ^i \phi_{21})} |E_b| e^{j\epsilon_b}, \quad (12)$$

where  $^f \psi_2 - ^i \psi_2$  is the change in phase of the emergent wave for  $\Gamma_D$  and  $\Gamma_G$  not zero,  $^f \phi_{21} - ^i \phi_{21}$  is the variation of phase shift of the component, and

$$E_b = |E_b| e^{j\epsilon_b} = \frac{(1 - ^i \Gamma_1 \Gamma_G)(1 - ^i S_{22} \Gamma_D)}{(1 - ^f \Gamma_1 \Gamma_G)(1 - ^f S_{22} \Gamma_D)} \quad (13)$$

From (12) it can be seen that the mismatch error in this case is the argument of (13).

*Case II. The Reference Wave is the Incident Wave at the Input,  $a_1$*

In techniques where the incident wave is used as the reference wave, (5) may be written in the form

$$\frac{b_2}{a_1} = |S_{21}| e^{j\phi_{21}} |E_c| e^{j\epsilon_c} \quad (14)$$

where  $^f \phi_{21}$  is the phase shift of the component and

$$|E_c| e^{j\epsilon_c} = \frac{1}{1 - S_{22} \Gamma_D} \quad (15)$$

It can be seen that the argument of (15) is the mismatch error when the incident wave is used as a reference. For adjustable components, the change in phase of the emergent wave may be written, when the incident input wave is used as a reference wave, as

$$\frac{^f b_2}{^i b_2} = \frac{^f S_{21}}{^i S_{21}} \frac{1 - ^i S_{22} \Gamma_D}{1 - ^f S_{22} \Gamma_D} \quad (16)$$

or as

$$\frac{{}^f b_2}{{}^i b_2} = \frac{|{}^f S_{21}|}{|{}^i S_{21}|} e^{j({}^f \phi_{21} - {}^i \phi_{21})} |E_d| e^{j\epsilon_d} \quad (17)$$

where

$$|E_d| e^{j\epsilon_d} = \frac{1 - {}^i S_{22} \Gamma_D}{1 - {}^f S_{22} \Gamma_D} \quad (18)$$

and  $\epsilon_d$  is the mismatch error in this case.

#### APPLICATION I

A two-channel method of measuring variation of phase shift is illustrated in Fig. 2. Usually there is considerable isolation between the component under test and power dividing network. Under these circumstances, a portion of the energy of the oscillator traverses a separate isolated path and behaves as an independent reference wave for the change of phase measurements.

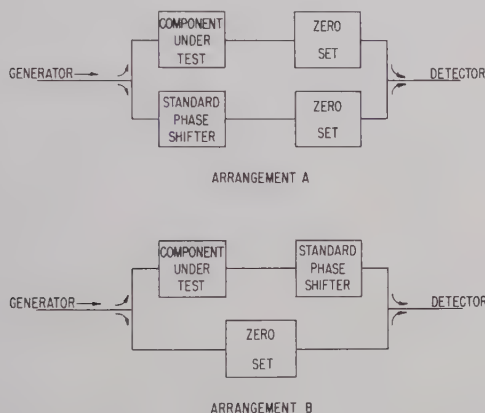


Fig. 2—Arrangement of equipment for a two-path method of measuring phase shift.

Without this isolation, the equipment may be adjusted to use the incident wave as a reference. The present discussion assumes this isolation to be infinite. Since the independent wave is used as a reference, the mismatch error is given by (13). If the magnitudes of the terms other than  $|E|$  and unity in (13) are small compared to unity then to a good approximation,

$$|E| e^{j\epsilon} = 1 - {}^i \Gamma_1 \Gamma_G - {}^i S_{22} \Gamma_D + {}^f \Gamma_1 \Gamma_G + {}^f S_{22} \Gamma_D, \quad (19)$$

and the mismatch error,  $\epsilon$ , may be written approximately as

$\epsilon$  = argument of

$$[1 - {}^i \Gamma_1 \Gamma_G - {}^i S_{22} \Gamma_D + {}^f \Gamma_1 \Gamma_G + {}^f S_{22} \Gamma_D]. \quad (20)$$

However, it is inconvenient or sometimes difficult to evaluate the phases of the scattering and reflection coefficients, while limits of their magnitudes are more readily determined from estimates of maximum VSWR. Therefore, limits of error (maximum error) for arbitrary

phases of these coefficients are evaluated here. One may represent (19) in graphical form as shown in Fig. 3. Allowing the phases of the coefficients to take on appropriate values, the maximum error,  $\lim \epsilon$ , will occur when the resultant is  $90^\circ$  out of phase with the variables, as shown in Fig. 4. Under these conditions

$\sin(\lim \epsilon)$

$$= |{}^i \Gamma_1 \Gamma_G| + |{}^i S_{22} \Gamma_D| + |{}^f \Gamma_1 \Gamma_G| + |{}^f S_{22} \Gamma_D|, \quad (21)$$

which for small angles may be written,

$\lim \epsilon$

$$= |{}^i \Gamma_1 \Gamma_G| + |{}^i S_{22} \Gamma_G| + |{}^f \Gamma_1 \Gamma_G| + |{}^f S_{22} \Gamma_D|. \quad (22)$$

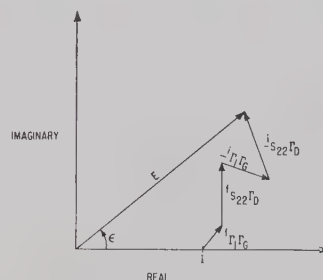


Fig. 3—Representation of (19).

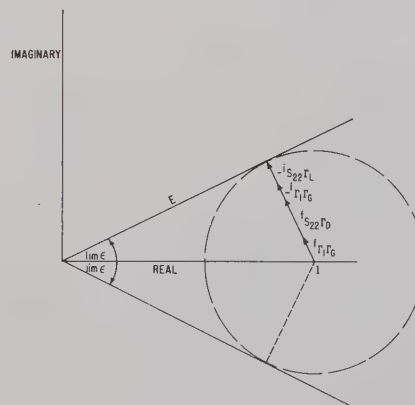


Fig. 4—Representation of (19) for maximum  $\epsilon$ .

A conservative estimate of the limits of mismatch error may be quickly obtained by using the manufacturers' specifications for the magnitudes of the scattering coefficients. It should be noted, however, that for a specific measurement, determining the value of the magnitude of the scattering coefficients will usually result in smaller limits of error since manufacturers generally specify only the maximum value over the entire operating range. It should be emphasized that the limits of error calculated from (22) are maximum errors based on the assumption that the phases of the scattering coefficients change an arbitrary amount. Limits to these phase changes can frequently be determined, and for precise measurements, it is then desirable to use these limits and determine the smaller limits of error by use of (13).



## GRAPHICAL PRESENTATION OF RESULTS

The graphs are constructed to present a limit of mismatch error in variation of phase shift measurements as a function of the mismatches of the generator, detector, and phase shifter. The following assumptions were made to simplify the presentation and they introduce only a small loss of generality. It is assumed that: 1) the equivalent generator and detector reflection coefficients are of equal magnitude,  $|\Gamma_G| = |\Gamma_D|$ ; 2) the input and output voltage standing-wave ratio (VSWR) of the phase shifter are equal, and therefore  $|S_{11}| = |S_{22}|$ ; and 3) the detector reflection coefficient and  $S_{11}$  combine to give maximum magnitude of  $\Gamma_1$ .

The results for a lossless phase shifter are presented in Fig. 5, and for a lossy one in Fig. 6. The limits of error are plotted against the input or output VSWR

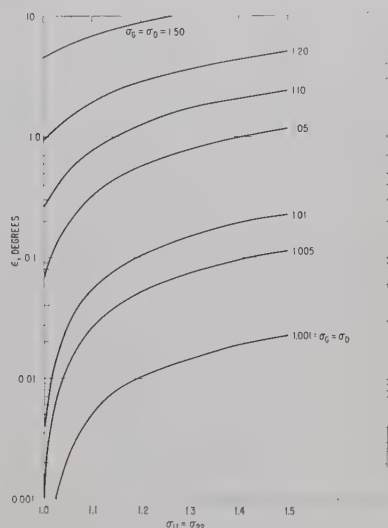


Fig. 5—Limit of mismatch error for lossless phase shifters.

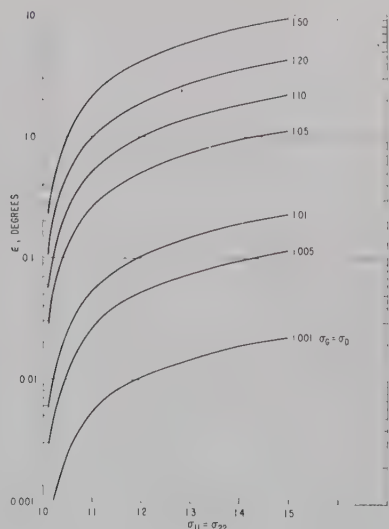


Fig. 6—Limit of mismatch error for attenuators with initial and final settings greater than 20 db.

( $\sigma_{11}$  or  $\sigma_{22}$ ) of the phase shifter or attenuator. Fig. 5 gives limits of error for a lossless phase shifter and conservative limits of error for phase shifters with less than 20 db loss or attenuators with one or both settings at less than 20 db loss. Fig. 6 gives limits of error for attenuators when both settings are at least 20 db or phase shifters with 20 db or more of insertion loss.

As an example, consider a phase shifter with 0.5 db insertion loss and maximum input and output VSWR of 1.35 placed in a waveguide system with maximum VSWR looking towards the generator and detector of 1.05. The conservative limit of error as given by Fig. 5 is  $0.90^\circ$ . However, if this component has 20 db or more loss at both settings, the limit of error as given by Fig. 6 is  $0.84^\circ$ . The difference between the limits of error for the lossless and high loss cases becomes more pronounced as the ratio of  $|\Gamma_D|$  to  $|S_{11}|$  becomes larger and therefore both graphs are presented.

The graphs may also be used to estimate the maximum permissible VSWR of the equivalent generator and detector to attain a given accuracy of variation of phase shift with a calibrated phase shifter. One case of interest is a microwave phase shifter of maximum VSWR of 1.35 which is calibrated to  $2^\circ$  accuracy. To utilize this accuracy, an estimate from Fig. 5 indicates that it should be used in a system where the VSWR looking towards the generator and detector are 1.10, or less. Another case of interest is the comparison of the variation of phase shift of two components within  $0.1^\circ$  in a two channel method. This would be satisfied if the limit of mismatch error for each component was  $0.05^\circ$ . If one of the components is a microwave phase shifter with maximum VSWR of 1.35, the maximum VSWR of the equivalent generator and detector for  $0.05^\circ$  limit is 1.004. If the other component is an attenuator with maximum VSWR of 1.15, the maximum VSWR of the equivalent generator and detector for  $0.05^\circ$  limit is 1.006.

It may be useful here to emphasize the meaning of the limits of error presented in the graphs. These are maximum errors due to mismatches, since it was assumed that the phase changes of all coefficients were arbitrary. If one has knowledge of the limits of phase changes of the coefficients, or actual values, it is desirable for critical work to turn to (11) and evaluate closer limits of mismatch error, or actual mismatch error.

## APPLICATION II

A method which has been used to measure the variation of phase shift of a low-loss reciprocal waveguide component by terminating it with a calibrated sliding short circuit and using a slotted section as a detector is illustrated in Fig. 7. A minimum of the input standing wave pattern is used as a reference to position the probe. When the component under test is adjusted to a

new setting, the minimum of the input standing wave pattern is restored to the reference plane of the probe by moving the calibrated short circuit. Since the wave travels through the component in both directions to form this pattern, twice the phase shift of the component is assumed to be equal to the change of phase of the reflection coefficient of the attached short circuit.

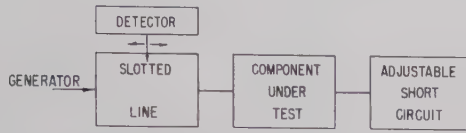


Fig. 7—Arrangement of equipment for a short circuit method of measuring phase shift of low-loss components.

Neglecting any errors caused by probe loading, the minimum of the input standing wave pattern occurs when

$$\arg \frac{b_1}{a_1} = (2n + 1)\pi, \quad (23)$$

where  $n$  is an integer. The minimum of the pattern is restored to the initial position by adjustment of the short circuit and this condition may be expressed by

$$\arg \frac{f b_1}{f a_1} = \arg \frac{i b_1}{i a_1}, \quad (24)$$

or

$$\arg f \Gamma_1 = \arg i \Gamma_1 \quad (25)$$

where  $\Gamma_1$  is the input reflection coefficient of the component when arm 2 is terminated with a sliding short circuit with reflection coefficient  $\Gamma_s$ . Substitution of an expression for  $\Gamma_1$  in terms of the scattering coefficients of the component and the short circuit allows the adjustment conditions to be written as

$$\begin{aligned} \arg \left( f S_{11} + \frac{f S_{21}^2 f \Gamma_s}{1 - f S_{22} f \Gamma_s} \right) \\ = \arg \left( i S_{11} + \frac{i S_{21}^2 i \Gamma_s}{1 - i S_{22} i \Gamma_s} \right), \end{aligned} \quad (26)$$

when reciprocity in the form,  $S_{21} = S_{12}$ , has been assumed. For  $|S_{22} \Gamma_s| \ll 1$ , this may be written approximately as

$$\begin{aligned} \arg (f S_{11} + f S_{21}^2 f \Gamma_s + f S_{21}^2 f S_{22} f \Gamma_s^2) \\ = \arg (i S_{11} + i S_{21}^2 i \Gamma_s + i S_{21}^2 i S_{22} i \Gamma_s^2). \end{aligned} \quad (27)$$

The measured variation of phase shift is based on the assumption that  $S_{11} = S_{22} = 0$  and that the arguments of  $f S_{21}^2 f \Gamma_s$  and  $i S_{21}^2 i \Gamma_s$  are equal, which leads to

$$f \phi_{21} - i \phi_{21} = \frac{1}{2} (f \psi_s - i \psi_s) \quad (28)$$

where  $i \psi_s$  and  $f \psi_s$  are the initial and final phases, respectively, of the reflection coefficient of the sliding short circuit,  $\Gamma_s$ .

It is apparent, however, that the actual change of phase can differ from this ideal when  $S_{11}$  and  $S_{22}$  are not zero, or

$$(f \phi_{21} - i \phi_{21}) - \frac{1}{2} (f \psi_s - i \psi_s) = \epsilon_e, \quad (29)$$

where  $\epsilon_e$  is the mismatch error in this method. Eq. (29) can be shown to be equivalent to

$$2\epsilon_e = \arg \frac{f S_{21}^2 f \Gamma_s}{i S_{21}^2 i \Gamma_s} = \arg f S_{21}^2 f \Gamma_s - \arg i S_{21}^2 i \Gamma_s. \quad (30)$$

The difference between these two arguments,  $2\epsilon_e$ , can be seen from Fig. 8, a graphical representation of (27) which describes the actual adjustment of conditions for the general case. The limits of this difference, assuming all phases of the reflection coefficients are possible, may be obtained from

$$\begin{aligned} \sin (\lim \epsilon_e) &= \frac{1}{2} [\sin (\lim \epsilon_1) + \sin (\lim \epsilon_2)] \\ &= \frac{1}{2} \frac{|f S_{11}| + |f S_{21}^2 f S_{22} f \Gamma_s^2|}{|f S_{21}^2 f \Gamma_s|} \\ &\quad + \frac{1}{2} \frac{|i S_{11}| + |i S_{21}^2 i S_{22} i \Gamma_s^2|}{|i S_{21}^2 i \Gamma_s|} \end{aligned} \quad (31)$$

where  $\lim \epsilon_e$  is the limit of error, and  $\lim \epsilon_1$  and  $\lim \epsilon_2$  are limits of  $\epsilon_1$  and  $\epsilon_2$  as shown in Fig. 8. A readily calculated approximation for the limit of error may be found by assuming  $|S_{21}| = 1$ ,  $|\Gamma_s| = 1$ , and  $|S_{11}|$  and  $|S_{22}|$  do not change with adjustment. This approximate limit of error may be obtained from

$$\sin (\lim \epsilon_e) \approx |S_{22}| + |S_{11}|. \quad (32)$$

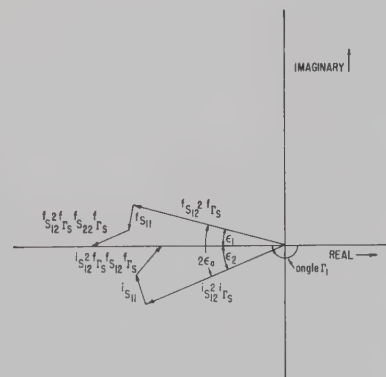


Fig. 8—Representation of (27).



If the input and output VSWR of the component are equal and the error is small, the limit of mismatch error may be written as

$$\lim \epsilon_e = 2 |S_{11}| \text{ radians} \quad (33)$$

which can be readily shown to be equivalent to a result for lossless components quoted by Magid.<sup>2</sup> It may be useful here to emphasize the meaning of the limits of error obtained by (33). These are maximum errors due to mismatches, since it was assumed that the phase changes of all coefficients were arbitrary.

<sup>2</sup> M. Magid, "Precision microwave phase shift measurements," IRE TRANS. ON INSTRUMENTATION, vol. I-7, pp. 321-331; December, 1958.

For the same phase shifter considered in Application I (VSWR < 1.35), the limits of error are  $\pm 17^\circ$ . It is of interest to note that the mismatch error in a variation of phase shift measurement in this method is independent of the reflection coefficient of the generator.

Additional errors in this method such as those caused by probe loading in the slotted line are not within the scope of this analysis, but should be taken into account, if they are appreciable compared to the mismatch error.

#### ACKNOWLEDGMENT

The author extends thanks to R. W. Beatty for constructive criticism of this analysis, and to O. L. Patty and W. A. Downing for performing the necessary calculations to evaluate the limits of error.

## A Note on the Optimum Source Conductance of Crystal Mixers\*

R. J. MOHR<sup>†</sup>, MEMBER, IRE, AND S. OKWIT<sup>‡</sup>, MEMBER, IRE

**Summary**—This paper describes an accurate and convenient technique for measuring the match of a crystal mixer. Use is made of the fact that with a proper RF drive level, the fundamental conductance of a mixer crystal may be made equal to the optimum source conductance of the crystal for mixer operation. The required drive level depends on certain crystal parameters and on the image frequency termination of the mixer. Design curves are given which simplify the determination of the proper RF drive level for a wide range of crystal parameters and their condition of image frequency termination.

#### INTRODUCTION

THE DESIGN of a crystal mixer may conveniently be broken down into three parts:

- 1) design of a signal coupling mechanism which will provide the optimum source conductance for minimum available conversion loss,
- 2) design of a local-oscillator coupling mechanism that has negligible effect on the signal admittance,
- 3) design of an RF bypass circuit that will not allow the RF power to couple to the IF load circuit.

This paper deals with certain considerations of the design of the signal coupling mechanism. In order to achieve a minimum noise figure crystal mixer receiver, it is necessary to design the mixer for minimum available conversion loss. From linear network theory, applicable to a crystal mixer, there is an optimum source conductance for minimum available conversion loss. In the practical design of a crystal mixer, it is usually assumed that this optimum conductance is equal to the fundamental component of the conductance of the crystal for a high-level RF signal, of the same magnitude as the local-oscillator drive, but in the absence of this local-oscillator drive. Under this assumption, the crystal mount is then designed to be matched to the line at this high level of RF signal.<sup>1</sup> This generally gives a good approximation to the optimum match condition for the broadband mixer<sup>2,3</sup> (image frequency termination equal

\* Received by the PGMTT, April 29, 1960; revised manuscript received, July 18, 1960.

<sup>†</sup> Microwave Dynamics Corp., Plainview, L. I., N. Y. Formerly with FXR Inc., Woodside, N. Y.

<sup>‡</sup> Airborne Instruments Lab., Melville, L. I., N. Y.

<sup>1</sup> R. V. Pound, "Microwave Mixers," Rad. Lab. Series, McGraw-Hill Book Co., Inc., New York, N. Y., vol. 16, p. 122; 1945.

<sup>2</sup> H. C. Torrey and C. A. Whitmer, "Crystal Rectifiers," Rad. Lab Series, McGraw-Hill Book Co., Inc., New York, N. Y., vol. 15, pp. 111-178; 1948.

<sup>3</sup> Operation in this condition is discussed by Torrey and Whitmer, *Ibid.* Data cited there show that the conversion loss ( $L_0$ ) for this condition differs from the optimum conversion loss ( $L_2$ ) in the broadband condition by less than 0.2 db.

to the signal frequency termination). However, the question arises as to how accurate this technique is in approximating the optimum match condition for narrow-band mixers (image frequency termination short-circuited or open-circuited).

It is the purpose of this paper to investigate the accuracy of this measurement method for the three mixer cases of general interest:

- 1) short-circuited image frequency termination,
- 2) image frequency termination = signal frequency termination,
- 3) open-circuited image frequency termination;

and to show how, from a knowledge of the dc characteristics of the crystal, a modification in the RF drive level can be made to improve the accuracy. Only single-ended mixers will be discussed. However, application to balanced mixers should be clear.

The interrelationship of the high-level crystal conductance and the optimum mixer source conductance may not be immediately apparent. For this reason, mixer theory will be briefly reviewed and equivalent networks will be presented which will show this relationship quite clearly.

#### REVIEW OF CRYSTAL MIXER THEORY

A simple mixer circuit is shown in Fig. 1. The RF choke serves as a low-impedance path for both dc and the IF frequency. Hence, as viewed from the IF terminals, the crystal is effectively across  $BB'$ . The RF bypass assures that no signal power will be lost to the IF circuit and, as viewed from the RF terminals, effectively places the crystal across  $AA'$ . The local oscillator is represented by the current source  $i_0 = I_0 \cos \omega_0 t$ , and admittance  $Y_0$ . In a practical mixer circuit, the local oscillator is very loosely coupled to the crystal ( $Y_0 \ll Y_r$ , where  $Y_r$  = signal generator admittance), and its effect on the conversion loss and impedance relationships can be neglected. The area indicated as "crystal" is meant to include only the active region of the crystal, that is, the vicinity of the point contact. All the passive parts of the crystal (whisker, ceramic and contacts) are implicit in the RF transformation network. Consequently, all admittances shown are referred to this region.

It has been shown<sup>2,4,5</sup> that a crystal mixer can be accurately represented, at the active region of the crystal, by the three-port network shown in Fig. 2. The conductances of the network can be obtained from an analysis of the current that will flow as a result of a small

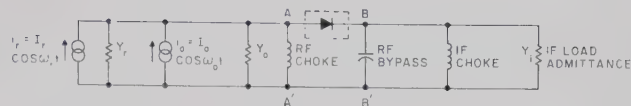


Fig. 1—Equivalent circuit of simple mixer.

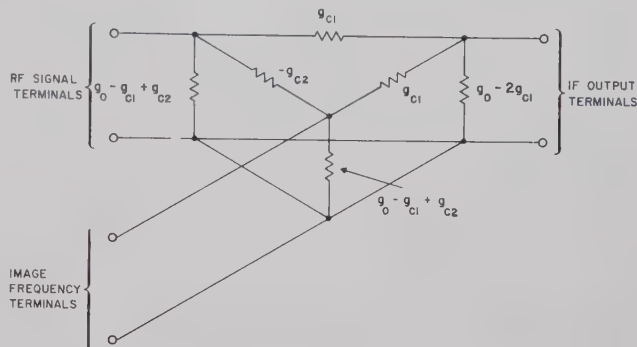


Fig. 2—Equivalent network of crystal for mixer calculations.

signal voltage being applied to the crystal, when the crystal is excited by a high-level local oscillator signal. Except for the fact that frequency translations implicitly occur, the laws of linear network theory apply to the network. An analysis of the network will yield, among other parameters, the available conversion loss, and optimum source conductance for minimum available conversion loss, for any arbitrary image frequency termination. Any deviation of the source conductance from its optimum value will cause a degradation in conversion loss by approximately the mismatch loss.

From Fig. 2, it can be seen that the image frequency termination will affect the optimum source conductance and conversion loss. The conditions of image termination of general interest are:

- Case 1) image frequency terminals shorted (narrow-band case),
- Case 2) image frequency termination equal to signal frequency termination (broadband case),
- Case 3) image frequency terminals open-circuited (narrow-band case).

For mixer crystals with small back conductance, it has been shown<sup>6</sup> that the open-circuited image condition (Case 3) will always yield the greatest conversion efficiency. It should be noted that, in a properly designed mixer, the over-all improvement in receiver performance obtained by using an open-circuited image frequency termination in preference to a matched image frequency termination is not large, usually about 0.5 to 1.0 db decrease in over-all noise figure. However, in cases where a preselector must be used for purposes other than noise figure considerations, improper location of the preselector relative to the mixer can increase

<sup>4</sup> L. C. Peterson and F. B. Llewellyn, "The performance of mixers in terms of linear network theory," *PROC. IRE*, vol. 33, pp. 458-476; July, 1945.

<sup>5</sup> E. W. Herold, R. R. Bush, and W. R. Ferris, "Conversion loss of diode mixers having image frequency impedance," *PROC. IRE*, vol. 33, pp. 603-609; September, 1945.

<sup>6</sup> P. D. Strum, "Some aspects of mixer crystal performance," *PROC. IRE*, vol. 41, pp. 875-889; July, 1953.



over-all receiver noise figure by as much as 4.0 to 5.0 db over that which would be obtained if the preselector were properly placed. This degradation is primarily due to:

- 1) increased conversion loss,
- 2) increased IF noise figure resulting from the effect of a radically changed IF output impedance.

The optimum source conductance for each case of image frequency termination may be expressed in terms of the conductances of the network of Fig. 2. These are:

Case 1

$$g_{r1} = \sqrt{g_0^2 - g_{c1}^2} \quad (1)$$

(Image short-circuited),

Case 2

$$g_{r2} = \sqrt{(g_0 + g_{c2}) \left( g_0 + g_{c2} - \frac{2g_{c1}^2}{g_0} \right)} \quad (2)$$

(Image matched),

Case 3

$$g_{r3} = \sqrt{g_0^2 - g_{c2}^2} \sqrt{\frac{2g_{c1}^2(g_{c2} - g_0) - g_0(g_{c2}^2 - g_0^2)}{g_0(g_0^2 - g_{c1}^2)}} \quad (3)$$

(Image open-circuited),

where

$$g_0 = \frac{1}{2\pi} \int_0^{2\pi} g d\omega_0 t, \quad (4)$$

$$g_{cn} = \frac{1}{2\pi} \int_0^{2\pi} g \cos 2n\omega_0 t d\omega_0 t \quad (5)$$

and  $g$  = instantaneous small-signal conductance.

These conductances,  $g_0$ ,  $g_{c1}$  and  $g_{c2}$ , are found from an analysis of the current flow resulting from the application of a low-level signal to a crystal driven by the local oscillator, and, as discussed in the next section, may conveniently be expressed in terms of the parameters of the crystal law.

#### IMPORTANT MIXER PARAMETERS IN TERMS OF THE CRYSTAL LAW

The  $E$ - $I$  characteristics of a crystal can be very closely approximated by:<sup>6</sup>

$$i_f = Ke^x; \quad (e > 0) \quad (6)$$

$$i_b = g_b e; \quad (e < 0), \quad (7)$$

where  $i_f$  is instantaneous forward current,  $i_b$  is the instantaneous back current,  $e$  is the applied voltage,  $k$  is a proportionality constant,  $x$  is the approximate value of  $d \log i_f / d \log e$  of the crystal, and  $g_b$  is the nearly constant

back conductance. (The method of obtaining these parameters from the dc characteristic of a crystal is illustrated in the Appendix.)

The instantaneous small-signal conductance is:

$$g = \frac{di}{de} = Kxe^{x-1}; \quad (e > 0) \quad (8)$$

$$g = g_b; \quad (e < 0). \quad (9)$$

Assuming a local-oscillator voltage of the form  $e = E_0 \cos \omega_0 t$ , and substituting  $g$  from (8) and (9) into (4) and (5), we get

$$g_0 = A \left[ \frac{\left( \frac{x-2}{2} \right)!}{\left( \frac{x-1}{2} \right)!} \right] + \frac{g_b}{2} \quad (10)$$

$$g_{c1} = A \left[ \frac{\left( \frac{x-1}{2} \right)!}{\left( \frac{x}{2} \right)!} \right] + \frac{g_b}{\pi} \quad (11)$$

$$g_{c2} = A \left[ \frac{2 \left( \frac{x}{2} \right)!}{\left( \frac{x+1}{2} \right)!} - \frac{\left( \frac{x-2}{2} \right)!}{\left( \frac{x-1}{2} \right)!} \right] \quad (12)$$

where

$$A = \frac{KxE_0^{x-1}}{2\sqrt{\pi}}.$$

Other quantities of interest are the fundamental component of the high RF level conductance,  $g_1$  (which is the ratio of the fundamental component of the crystal current to the applied voltage, and is the conductance which is used to approximate the optimum source conductance required for minimum  $L_c$ ) and the rectified current  $I_a$ <sup>7</sup>:

$$g_1 = g_0 - g_{c2} \quad (13)$$

$$I_a = \frac{KF_0^x}{2\sqrt{\pi}} \frac{\left( \frac{x-1}{2} \right)!}{\left( \frac{x}{2} \right)!} - \frac{g_b E_0}{\pi}. \quad (14)$$

#### APPLICATION TO MATCHING TECHNIQUE

Based on Figs. 1 and 2, the equivalent circuit of Fig. 3 is obtained. As in Fig. 1, the passive parts of the crystal structure are implicit in the various transformers

<sup>7</sup> S. Okwit, "Theoretical Analysis of High- $Q$  Mixer Receiver Design," M.S. thesis, Adelphi College, Garden City, N. Y.; 1957.

shown. Physically, the transformers for the signal and image frequencies are identical. However, in general, the RF matching network is frequency-sensitive and the representation of Fig. 3 shows this explicitly. The characteristic admittance,  $g_r$ , of the input transmission line is assumed to be the same at the signal frequency,  $\omega_s$ , and at the image frequency,  $\omega_k = 2\omega_0 - \omega_s$ .

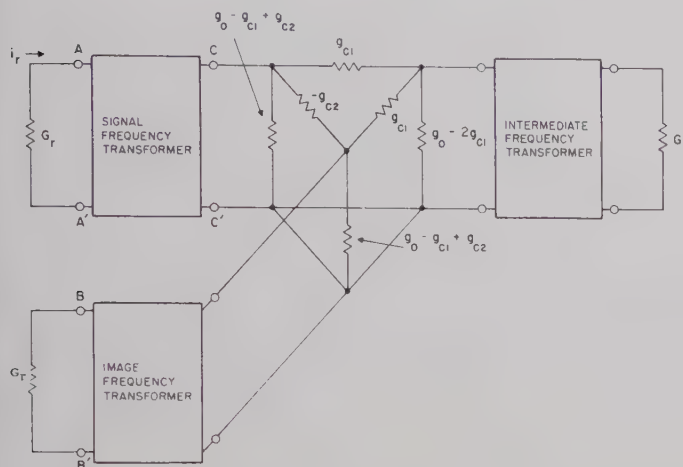


Fig. 3—Equivalent circuit of mixer.

For minimum conversion loss, the conductance seen looking toward the generator at terminals  $CC'$  should be equal to the optimum source conductance for the mixer [(1)–(3)]. A convenient way to obtain this optimum match condition in practice is first to place a conductance at the active region of the crystal (terminal  $CC'$ , Fig. 3) which is equal to the optimum source conductance and then to adjust the input transformation network to obtain optimum power transfer to the conductance. This corresponds to a conjugate match at terminal  $CC'$ , and if the signal frequency transformer is lossless then there will also be a condition of match at terminals  $AA'$ . Hence, slotted-line measurements in the input transmission line can accurately record the degree of match of the crystal mixer. These data can then be used to “broadband” match the crystal mount by the use of conventional microwave broadband matching techniques.<sup>8</sup>

A convenient method of effectively placing the optimum conductance at the active region of the crystal is to drive the crystal with a predetermined high level of RF, such that its fundamental conductance  $g_1$  (13), is equal to the optimum source conductance of the mixer for the particular case of interest [(1)–(3)]. The level of the drive is indicated in practice by the amount of rectified current. In the VSWR measurement, it is only necessary that the probe in the slotted section be suf-

ficiently narrow-band that the second- and higher-order harmonics of the rectified current be rejected adequately.

Let us now discuss how the foregoing is applied to the design of a crystal mixer. Consider the following. It is desired to design a broad-band mixer (Case 2) using a 1N21E crystal. The drive level to be used for optimum sensitivity, as recommended by the manufacturer, is 0.6 ma. It is necessary for the designer to make measurements of the  $E$ - $I$  characteristics of several crystal samples, in order to obtain the average crystal law parameters. Utilizing the techniques described in the Appendix, we find the average crystal law parameters of the 1N21E crystal to be:

$$X = 4$$

$$K = 0.4$$

$$g_b = 0.2 \text{ millimhos.}$$

It now remains to determine at what level of RF drive (rectified current) the crystal mount should be matched to the line.

The procedure is as follows. From the parameters of the crystal law the optimum source conductance,  $g_{r2}$ , is determined. A value of rectified current is then found at which  $g_1$  is equal to  $g_{r2}$ . This will then be the level of RF drive at which the crystal mount should be matched to the line.

From (10)–(13),

$$g_0 = 0.340E_0^3 + 10^{-4} \quad (15)$$

$$g_{c1} = 0.300E_0^3 - 0.637 \times 10^{-4} \quad (16)$$

$$g_{c2} = 0.204E_0^3 \quad (17)$$

$$g_1 = 0.136E_0^3 + 10^{-4}. \quad (18)$$

The value of  $E_0$ , as determined from (14), with a crystal drive of 0.6 ma is  $E_0 = 0.307$  volts. Use of this value of  $E_0$  in (15)–(17) yields

$$g_0 = 9.92 \text{ millimhos} \quad (19)$$

$$g_{c1} = 8.62 \text{ millimhos} \quad (20)$$

$$g_{c2} = 5.90 \text{ millimhos.} \quad (21)$$

Substituting (19)–(21) into (2), we get

$$g_{r2} = 3.68 \text{ millimhos.} \quad (22)$$

The level of rectified current needed to make the fundamental conductance of the crystal equal to the optimum source conductance (22) can now be found. Eq. (18) is solved yielding  $E_0 = 0.298$  volts, at which value  $g_1 = g_{r2} = 3.68$  millimhos.

From (14),  $I_a = 0.53$  ma, which is the required value of crystal drive for correct matching as compared to the usual 0.6-ma drive which would be used by the standard method. If on-off square-wave modulated RF is used in the measurement, the average current, as read on a milliammeter, should be half this value.

<sup>8</sup> G. L. Ragan, “Microwave Transmission Circuits,” Rad. Lab. Series, McGraw-Hill Book Co., Inc., vol. 9; 1948.



A similar procedure applied to the short-circuited and open-circuited image frequency conditions yields a crystal drive of 0.81 ma and 0.42 ma, respectively, for correct matching.

It is of interest to see what mismatches would exist if the mixer were matched to the line at a signal level equal to the operating local-oscillator level. For the 1N21E crystal utilized in the previous example, (18) yields  $g_1=4$  millimhos at 0.6 ma drive. In the broad-band case, the mixer would have been mismatched by  $4/3.68=1.09:1$ ; and in the narrow-band conditions  $4.92/4=1.23:1$  for Case 1 and  $4/3.01=1.33:1$  for Case 3. These mismatches are, in themselves, small and produce little degradation in conversion loss. However, when this mismatch is considered together with the usual crystal impedance spread and accuracy of adjustment of match over a sizeable band, it is recognized that the combination VSWR may be significantly greater than that which would be obtained by matching with the correct drive level.

#### GENERAL DESIGN CURVES

By making certain simplifying approximations, we may obtain a set of design curves which will greatly simplify the procedure described above.

For  $g_b \ll g_0$ , as in most high-performance crystals, it can be shown that

$$\frac{I_{an}}{I_{a0}} \simeq \left( \frac{g_{rn}}{g_1} \right)^{x/x-1}, \quad (23)$$

where

$I_{an}$  = rectified crystal current at which fundamental conductance  $= g_{rn} (n=1, 2, 3)$ ,

$I_{a0}$  = rectified crystal current at which crystal will be operated in practice,

$g_{rn}$  = optimum source conductance for case  $n$  ( $n=1, 2, 3$ ),

$g_1$  = fundamental conductance at drive level  $I_{a0}$ .

By use of the above equations and the calculated values of  $g_{rn}$  for a wide range of  $x$  and  $g'_0$ , the curves of Figs. 4-6 were obtained. These curves cover most of the high-performance crystals available today.

The curves are plotted with  $g'_0$  as a parameter, which is the average small-signal conductance normalized to the average small-signal conductance in the forward direction.  $g'_0$  is [from (10)]

$$g'_0 = \frac{g_0}{g_0 - g_b/2} \simeq 1 + \frac{g_b}{2g_0}. \quad (24)$$

Applying these curves to the previous example, we get the following approximate values:

Case 1  $I_{a1} = 1.3 \times 0.6 = 0.780$  ma

Case 2  $I_{a2} = 0.88 \times 0.6 = 0.528$  ma

Case 3  $I_{a3} = 0.67 \times 0.6 = 0.402$  ma,

which compare favorably with the exact values in the example.

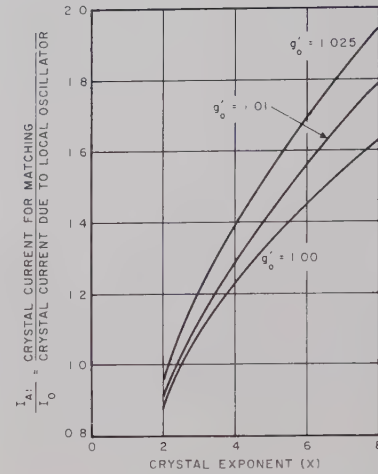


Fig. 4—Normalized crystal drive current vs crystal exponent for Case 1 (short-circuit-image).

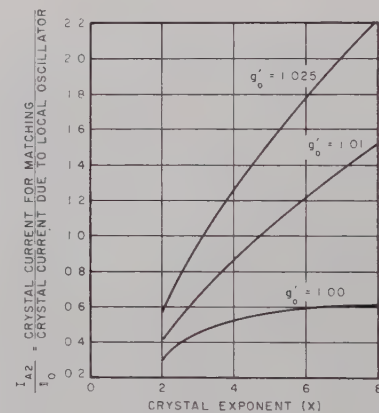


Fig. 5—Normalized crystal drive current vs crystal exponent for Case 2 (matched image).

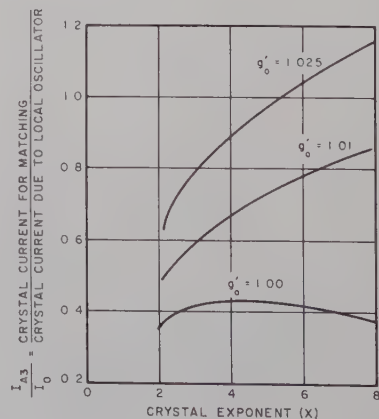


Fig. 6—Normalized crystal drive current vs crystal exponent for Case 3 (open-circuited image).

## CONCLUSIONS

From a knowledge of the dc characteristics of a mixer crystal, a drive level may be found at which the crystal impedance is equal to the optimum source impedance of the mixer. The optimum drive level has been calculated for a wide range of crystal parameters for the three important cases of image frequency termination. The resultant design data are presented in Figs. 4-6.

Although very little experimental verification is available, the design data presented here are based on generally accepted mixer theory, that is, the validity of the equivalent network of the mixer and the validity of the relation of the various crystal conductances to the dc characteristics of the crystal.

## APPENDIX

## DETERMINATION OF PARAMETERS OF CRYSTAL LAW

Inspection of the  $E$ - $I$  characteristics of a mixer crystal plotted on logarithmic coordinates reveals that the crystal law may be approximated over a large portion of the current range by

$$i_f = ke^x \quad (e > 0) \quad (25)$$

$$i_b = g_b e \quad (e < 0), \quad (26)$$

where

$i_f$  = instantaneous forward current

$i_b$  = instantaneous back current

$e$  = instantaneous voltage

$x$  = nearly constant slope =  $(d \log i) / d \log e$

$g_b$  = nearly constant back conductance

$k$  = proportionality constant.

Fig. 7, shows the  $E$ - $I$  crystal characteristics of a typical 1N21E crystal plotted on logarithmic coordinates. From Fig. 7, it is seen that over any 10 to 1 range in current (in the region between 0.05 ma and 5 ma) the  $E$ - $I$  curve can be approximated by a straight line. This, fortunately, is the region of most interest in crystal mixer operation.

Determination of  $x$ 

The average crystal slope is

$$x = \frac{d \log i}{d \log e} = \frac{\log \frac{i_1}{i_2}}{\log \frac{e_1}{e_2}}$$

where  $i_1 > i_2$ ,  $e_1 > e_2$ .

By use of a 10 to 1 current range,

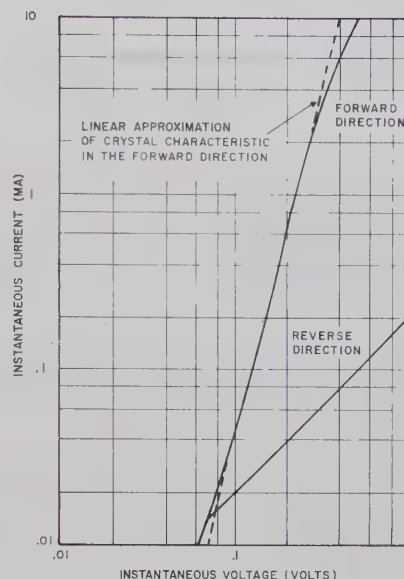


Fig. 7— $E$ - $I$  characteristics of 1N21E crystal.

$$x = \frac{1}{\log \frac{e_1}{e_2}} \quad (27)$$

Application of (27) to the 1N21E crystal plotted in Fig. 7 (where the 10 to 1 current range is 0.1 to 1.0 ma) yields:

$$X = 4.$$

Determination of  $K$ 

Setting  $e = 1$  volt in (25) yields  $i_f = K$ . Hence, by extending the straight-line approximation of the curve to  $e = 1$  volt,  $K$  is determined graphically as the current at the intercept of the 1 volt axis. Application of the above to Fig. 7 yields:

$$K = 0.4.$$

Determination of  $g_b$ 

Setting  $e = 1$  volt in (26) yields  $i_b = g_b$ . For the crystal characteristics plotted in Fig. 7,

$$g_b = 0.2 \text{ millimhos.}$$

In actual operation, the equivalent parameters of the crystal law may be modified by 1) the effect of dc impedance in the crystal circuit which will cause a bias, and 2) the effect of RF impedance in series with the crystal at harmonics of the local-oscillator frequency which will cause the applied local-oscillator voltage to be nonsinusoidal. These effects are usually small and in a direction to cancel each other. They have been neglected in this paper.



# Microwave Switching with Low-Pressure Arc Discharge\*

R. M. HILL† AND S. K. ICHIKI†

**Summary**—The characteristics of a low-pressure, hot cathode arc discharge have been studied and applied to microwave switching applications. The combination of rapid plasma build-up, low ignition voltage, and fairly rapid plasma decay, offers promise for the development of broad-band, high-power microwave switches which can be closed in tenths of microseconds and opened in a few microseconds or less. Experimental results on some particular switches are reported.

## INTRODUCTION

GAS discharge plasmas have long been used to control, attenuate and switch microwave power. TR and ATR tubes use plasmas produced primarily by the microwave power itself. Plasmas produced by hot or cold cathode glow discharges have been used for low power attenuators<sup>1</sup> and switches.<sup>2</sup> RF excited plasmas have been used to develop a phase shifter<sup>3</sup> and Faraday rotator.<sup>4</sup> A magnetically-controlled switch which uses a microwave induced plasma has recently been discussed.<sup>5</sup> The glow discharge control devices tend to be somewhat unstable and are usually restricted to low power applications. Even the ever useful TR can have disadvantages for low power switching or crystal protection, and is always faced with spike leakage problems at high power.

The properties of low pressure arc discharges do not seem to have been exploited for microwave use. A study of some of these properties and their application to switching microwaves will be described.

## PROPAGATION IN PLASMAS

The physical quantity which allows a gas discharge plasma to be used as a microwave switching element is the electron density, or number of electrons, per cubic centimeter. This can be seen from the simplified expression for the microwave index of refraction of a

plasma. This is given by

$$N = \sqrt{1 - \left(\frac{f_p}{f}\right)^2},$$

where  $f_p$  is the plasma frequency ( $f_p \cong 9000 \sqrt{n_e} \text{ sec}^{-1}$ , where  $n_e$  is electron density per cubic centimeter), and  $f$  is the frequency of the wave being propagated. When the ratio  $f_p/f$  is greater than or equal to one, the index of refraction is 0 or imaginary, and propagation in the medium is forbidden. A careful study of microwave propagation in plasmas should include both source and sink terms for the electron density, the effect of electron density gradients, and nonlinear effects. However, a qualitative picture of what can be expected may be obtained by examining the transmission characteristics of an infinite slab of plasma which is of uniform density throughout the slab and has no dc electric field. If we assume that we have a finite slab of thickness  $d$  and a loss term which may be expressed by a collision frequency,  $\nu$ , the expressions for the power transmission and reflection coefficients for normal incidence are given by<sup>6</sup>

$$T = \frac{\text{Power Transmitted}}{\text{Power Incident}} = \left[ \frac{4\gamma e^{(i\omega/c)\gamma d}}{(1+\gamma)^2 - (1-\gamma)^2 e^{(i2\omega/c)\gamma d}} \right]^2$$

$$R = \frac{\text{Power Reflected}}{\text{Power Incident}} = \left[ \frac{(1+\gamma)(1-\gamma)(1 - e^{(i2\omega/c)\gamma d})}{(1+\gamma)^2 - (1-\gamma)^2 e^{(i2\omega/c)\gamma d}} \right]^2,$$

where  $\gamma = \sqrt{1 - \omega_p^2/(\omega(\omega + i\nu))}$ , and  $\omega_p = 2\pi f_p$ . Figs. 1 and 2 give numerical results for these coefficients under the assumption that the thickness of the slab is equal to a free-space wavelength. The transmission and reflection coefficients are plotted against the plasma frequency with the ratio of the collision frequency to the radian frequency of the signal as a parameter. Fig. 1 shows that the transmission coefficient falls very rapidly for densities greater than the plasma density when the loss frequency is of the order of 1/10 or less of the radian frequency. Under the same conditions Fig. 2 shows that virtually all of the incident signal is reflected from the plasma slab. These calculations suggest seeking a low pressure source of plasma for switching purposes.

\* Received by the PGMTT, June 10, 1960; revised manuscript received, July 18, 1960. This work was performed under Air Force Contract No. AF 30(602)-1886.

† Microwave Physics Lab., Sylvania Electric Products, Inc., Mountain View, Calif.

<sup>1</sup> E. M. Bradley and D. H. Pringle, "The theory and design of gas-discharge microwave attenuators," *J. Brit. IRE*, vol. 15, pp. 11-24; January, 1955.

<sup>2</sup> L. Goldstein and N. L. Cohen, "Behavior of gas-discharge plasma in high-frequency electromagnetic fields," *Elec. Comm.*, vol. 28, pp. 305-321; December, 1951.

<sup>3</sup> D. H. Pringle and E. M. Bradley, "Some new microwave control valves employing the negative glow discharge," *J. Electronics*, vol. 1, pp. 389-404; January, 1956.

<sup>4</sup> L. Goldstein, M. A. Lampert and J. F. Heney, "Magneto-optics of an electron gas with guided microwaves," *Elec. Commun.*, vol. 28, pp. 233-234; September, 1951.

<sup>5</sup> S. J. Tetenbaum and R. M. Hill, "High power, magnetic field controlled microwave gas discharge switches," *IRE TRANS. ON MICROWAVE THEORY AND TECHNIQUES*, vol. MTT-7, pp. 73-83; January, 1959.

<sup>6</sup> E. Barrett, private communication.

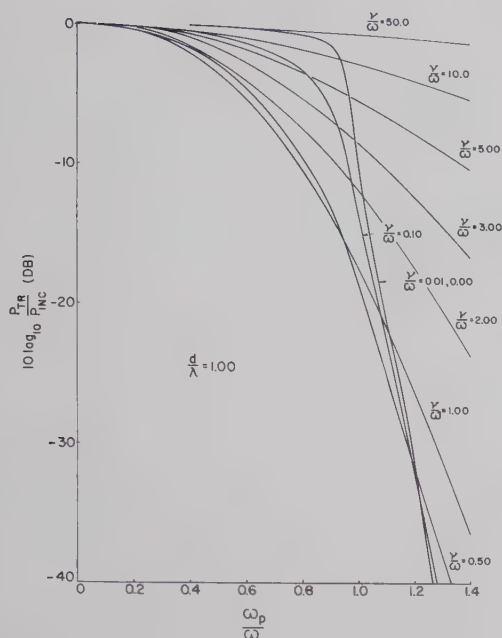


Fig. 1—Layer attenuation vs electron density.

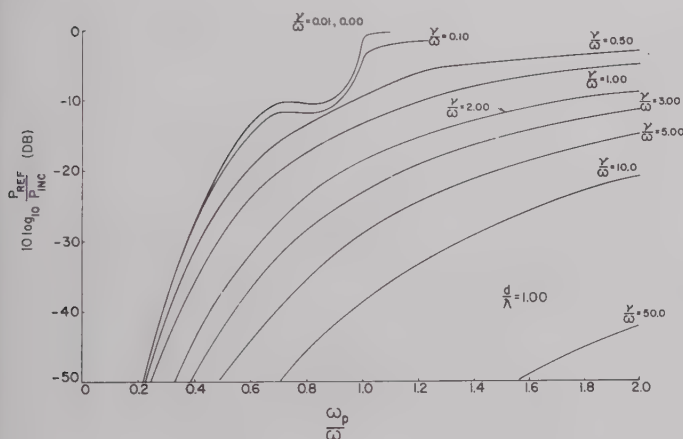


Fig. 2—Layer reflected power vs electron density.

In order to use a gaseous microwave switch with relatively high powers, the question of microwave breakdown of the gas in the switch needs consideration. Brown has shown that,<sup>7</sup> as a function of pressure, there is a minimum in the power required for microwave breakdown which is approximately at the point where the ratio of  $\nu/\omega = 1$  ( $\nu$ , the collision frequency, is directly proportional to pressure). Since the above considerations of reflection and transmission require  $\nu/\omega$  to be less than one, it is evident that the pressure should be kept as low as is practical for high-power applications.

#### LOW-PRESSURE ARC DISCHARGE

The arc discharge is characterized by high current, primarily of electrons, and relatively low voltage drop across the discharge, particularly if a hot cathode is

used. This general type of discharge is used in fluorescent lighting fixtures and also in thyratrons. Typical densities in the positive column of the discharge are of the order of  $10^{12}$ – $10^{13}$  electrons and ions per cubic centimeter, which should be sufficient for microwave switching up to frequencies of 30 kMc. Peak discharge currents of one to hundreds of amperes can be carried by such discharges.

Careful study of the mechanisms operating in hydrogen thyratrons<sup>8</sup> of the type used for magnetron modulators has clarified many features of this discharge and make it a very attractive possibility for use as a microwave switch. The ignition of the discharge, or the build-up of electron density, can take place in a triode structure with a grid providing the trigger for the ignition. Build-up of electron density to its equilibrium value is very rapid, being accomplished in ten to a hundred millimicroseconds. This time is primarily a function of the pressure of the gas and of the applied grid and anode voltages.

The grid, of course, loses any control of the discharge after the initial breakdown, and only after the density has again fallen below some fairly low value can the grid again exert any influence on the tube. The decay of the electron density after removal of the anode voltage is influenced by two things. Firstly, if the anode is allowed to reverse itself for a small period of time, much of the density will be removed from the tube by this sweeping voltage. The remainder decays in a time determined by the geometry of the tube and the ambipolar diffusion coefficient, which is for practical purposes equivalent to twice the positive ion diffusion coefficient. Typical decay or recovery times are of the order of one to tens of microseconds. It would appear, therefore, because of the rapid ignition, high equilibrium density and fairly rapid decay of this density, that the low pressure, grid initiated, arc discharge could be applied to microwave switching problems.

#### EXPERIMENTAL RESULTS

##### Construction and Operation

Several tubes have been constructed in which the positive column of a low pressure arc discharge is contained in a section of X-band waveguide. These were designed for switching pulsed signals and are fired only during the time that the signal to be switched is present. Tubes to switch CW power could be designed but an average discharge power of 40 to 100 watts would have to be dissipated in the tube. Also, CW switching is restricted to relatively low microwave power levels, probably in the tens of watts region, because the power required to maintain an existing discharge is considerably less than that required for the initial breakdown. The rate of electron loss which governs the power required for break-

<sup>7</sup> S. C. Brown, "Handbuch de Physik," Julian Springer, Berlin, Ger., vol. 22; 1955.

<sup>8</sup> Edgerton-Germeshausen and Greer, Inc., "Research Study on Hydrogen Thyratrons," Final Rept. Contract DA 36-039-sc-15372; 1953.



down is the diffusion rate of free electrons. For existing plasmas, the space-charge forces between electrons and ions give rise to the much slower ambipolar diffusion rate; *i.e.*, equal currents of ions and electrons leave the plasma, governed primarily by the rate of ion motion.

Fig. 3 is a drawing of a typical tube. The waveguide section itself is used as the grid and the narrow walls are covered with a wire mesh which serves both as a grid and as a waveguide wall. The cathode and anode are mounted on opposite sides of the waveguide in separate housings, and waveguide pressure windows seal off the waveguide portion of the tube. The tube can also be constructed such that the anode and cathode are mounted on the broad wall of the waveguide, or on opposite sides of a coaxial line. The tube parts were constructed of copper, and a simple oxide-coated tungsten coil was used as a cathode. A pulse-forming network provided the pulse energy for the tube. The circuit was fed by 0-1000-volt, 0-50-ma power supply. The trigger voltage necessary to fire the tube varied between 10 and 100 volts, depending upon the gas pressure. The trigger rise time should be of the order of  $10^{-8}$  seconds and should last for about  $3/10$  microsecond. The type of pulse-forming network depends on the length of the signal to be switched. It is also clear that if low to medium power CW signals are to be switched, a pulse-forming network is unnecessary.

#### Insertion Loss

The tube can be constructed to have essentially waveguide bandwidth in the unfired state. Fig. 4 is a plot of typical VSWR presented by the tube. The unfired insertion loss can be of the order of 1/10 db or less throughout the band. The insertion loss of the fired tube was tested against a calibrated waveguide attenuator. Fig. 5 shows typical traces of the transmitted signal, both fired and unfired, indicating an insertion loss in excess of 67 db. The tube was fired approximately 0.5 microsecond before the beginning of the magnetron pulse. The complete absence of any spike leakage should be noted. This occurs because the electron density is already high enough to produce a very small transmission coefficient by the time the magnetron power is applied. As expected, the gas pressure has a fairly profound effect on the transmitted energy, although over the range of 0.1 to nearly 1 mm of Hg the transmission coefficient is essentially constant. Below these points spike leakage energy appears, and at greatly different pressures the insertion loss deteriorates markedly. At pressures in excess of a few mm of Hg, high-voltage breakdown takes place and results in a continuous glow discharge through the tube. Most of the measurements were made with neon since it has both a relatively low ionization potential, which should keep the power required to run the discharge low, and a low collision frequency, so that the microwave power dissipated in the discharge is low.

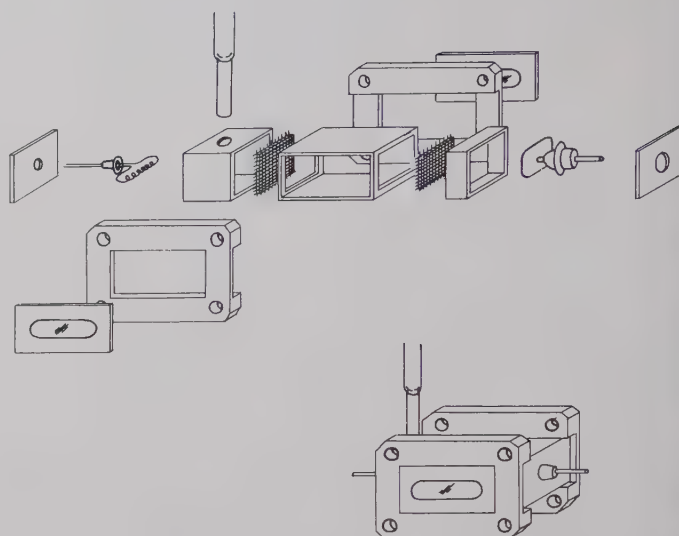


Fig. 3—Pulsed arc discharge switch tube.

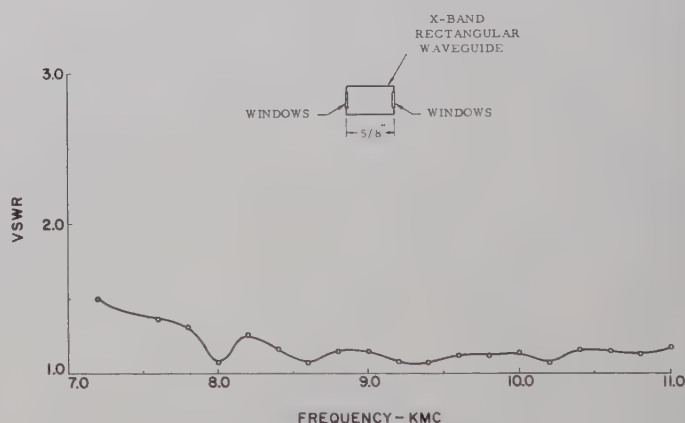


Fig. 4—VSWR of switch tubes.

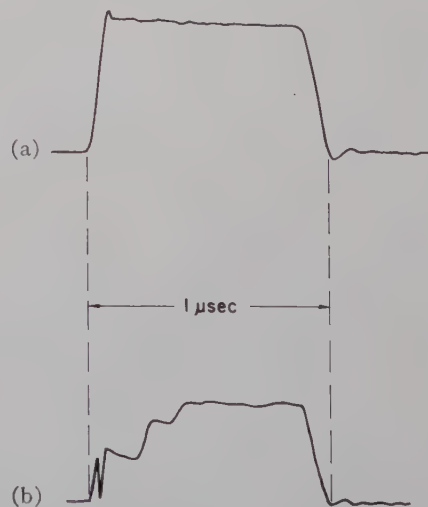


Fig. 5—Typical transmitted waveform. (a) Switch tube fired: no attenuation added at detector. (b) Switch tube unfires: 67-db attenuation added at detector.

### Breakdown Power

A discharge can be initiated by the microwave power itself, as in ordinary TR tubes. When this happens, control is lost and the device is no longer switchable. The theory of microwave breakdown in a gas has been treated extensively by Brown.<sup>7</sup> The exact treatment of this problem is fairly complex, but in essence the breakdown power can be expressed as

$$P_{bl} \sim \frac{u_i D_-}{\Lambda^2}$$

where  $u_i$  is the ionization potential,  $\Lambda$  is the geometrical diffusion length of the lowest diffusion mode, and  $D_-$  is the free electron diffusion coefficient, which is inversely proportional to pressure.

The measurement of breakdown power is quite simple. The power level was slowly increased until the transmitted pulse shape began to change. This took the form of a rapid change of attenuation at the end of the pulse. Fig. 6 shows breakdown data taken for neon and hydrogen plotted against  $1/p$ . As expected breakdown for hydrogen occurs at higher powers, even though the ionization energy of neon is 21.6 electron volts while hydrogen is 15.7 electron volts. The diffusion coefficient for hydrogen is considerably greater than that for neon. At neon pressures less than 150 microns, the points deviate from this line toward higher breakdown powers. This is expected since the electron mean free path is now of the order of the switch tube dimensions and electron losses increase more rapidly. From these data it appears possible to obtain switches capable of controlling quite high peak pulse powers. Although the choice of gases may be limited, variations of the pressure,  $p$ , or the diffusion length,  $\Lambda$ , should allow switching of peak pulse powers in the hundreds of kilowatts range. Since the diffusion length appears squared, minimizing it rather than the pressure may be the most profitable way to insure good high peak power characteristics.

It should be noted here that at high peak powers there is some tendency to clean up even noble gases. One hopes, therefore, to operate with as high a pressure as possible or, perhaps, with a small gas reservoir.

### Arc Loss

Figs. 1 and 2 indicate that for plasma densities in the order of  $10^{13}$  or  $10^{14}$  electrons per cc and  $\nu/\omega \ll 1$ , the expected arc loss should be very small. This is indeed true when the incident power is too low to cause extra ionization in the plasma. Fig. 7 is a plot of arc loss vs power when the arc loss is defined by

$$\text{Arc Loss in db} = 10 \log \frac{P_{\text{Incident}} - P_{\text{Reflected}}}{P_{\text{Incident}}}$$

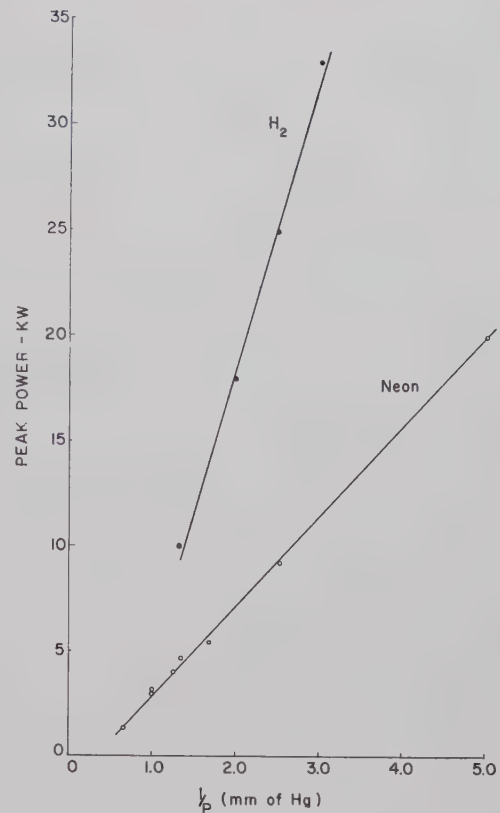


Fig. 6—Breakdown of power vs reciprocal pressure.

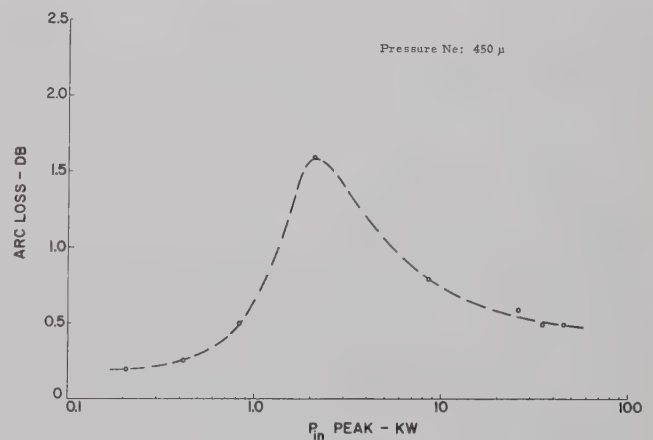


Fig. 7—Arc loss vs input power.

The transmitted power is assumed to be negligible. Both the low and high power ends of this curve show that the arc loss is indeed quite low. However, there is a maximum in the medium power range where a larger percentage of the energy of the power is being dissipated by the plasma. The increase in arc loss in the middle power ranges is probably due to increasing the density close to the microwave window. If an attempt is made to run the arc closer to the window, this curve will probably flatten out.



### Electron Density

An estimate of the minimum electron density which was achieved during the arc can be obtained by measuring the recovery time of the tube as a function of the frequency of the signal being transmitted. A microwave source at milliwatt power levels in the range of 15 to 21 kMc was used to probe the afterglow of the pulse discharge. If one assumes that recombination and attachment losses are negligible and that diffusion takes place in the lower diffusion mode, which should be true for times later than several microseconds, then the density should decay as a simple exponential with the period of the exponential being determined by the ambipolar diffusion coefficient for the gas used in the tube and the geometry of the structure. A semilog plot, of the recovery time of the tube as a function of frequency, should give a straight line plot, the intercept of which is a measure of the zero time electron density. Fig. 8 shows such a plot. The calculated recovery period for this particular structure was  $58 \mu\text{sec}$  in close agreement with the measured period of  $56 \mu\text{sec}$  and the zero time intercept was approximately 31 kMc. This gives an initial electron density in the lowest diffusion mode of approximately  $1 \times 10^{13}$  electrons per cubic centimeter. It is expected that the actual density during the discharge is somewhat higher, since the density which decays by higher-order diffusion modes could not be measured in this way.

### Recovery Time

The recovery time in this measurement was defined as that time required to reach the 3-db attenuation point after the end of the discharge pulse. The measurement was made during the interpulse recovery time of the switch by monitoring the transmission of a low level signal in the afterglow of the discharge. Fig. 9 shows recovery time data for neon and hydrogen. The neon recovery is considerably faster than that shown in Fig. 8 due to voltage overshoot by the discharge network and consequent cleanup of the plasma during this overshoot period. The recovery time is no longer governed entirely by the geometrical diffusion length  $\Lambda$ , but by a modified diffusion length,  $\Lambda_{DC}$ , due to the presence of an electric field.

For single mode diffusion the electron decay is exponential.

$$N = N_0 e^{-t/\tau},$$

where  $\tau = \Lambda^2/D_a$  and  $\Lambda^2$  is lowest mode diffusion length of the structure.  $D_a$  is ambipolar diffusion coefficient of the gas being used and  $p$  is the pressure. In the presence of an electric field  $\Lambda$  is modified to  $\Lambda_{DC}$

$$\frac{1}{\Lambda_{DC}^2} = \frac{1}{\Lambda^2} + \left( \frac{\mu E}{2D_a} \right)^2,$$

where  $\mu$  is the electron mobility in the gas and  $E$  is the electric field strength. For example, if  $E = 16$  volts/cm,  $\Lambda = \frac{1}{4}$  cm and  $D_a/\mu = 0.6$  ev, the decay time  $\tau$  should be

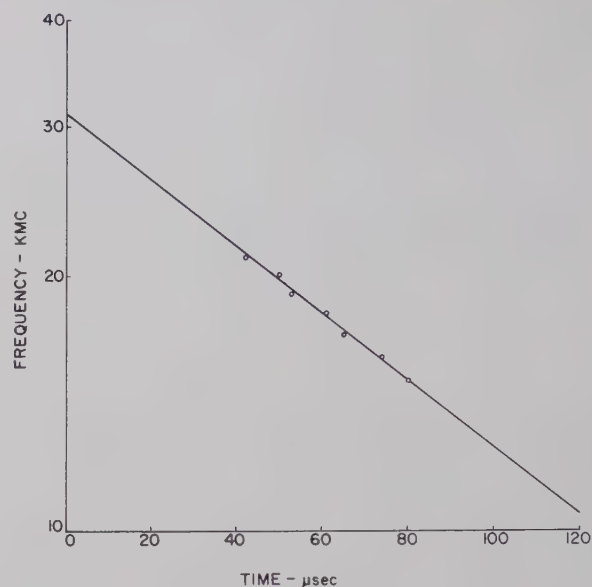


Fig. 8—Recovery time vs frequency (pressure = 0.15 mm Hg of neon).

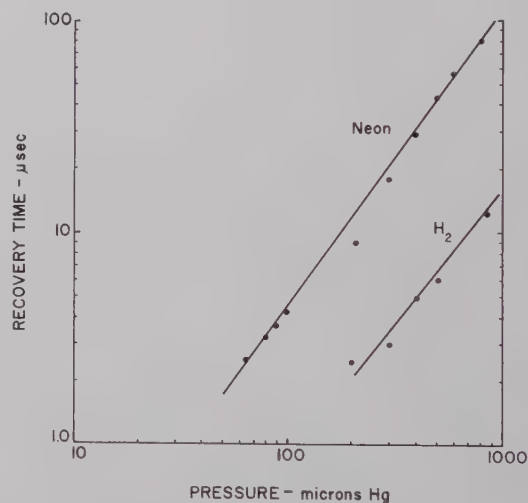


Fig. 9—Recovery time vs gas pressure.

ten times faster than without an electric field. This indicates that a moderate voltage overshoot is a desirable design feature.

Recent data for a hydrogen gas fill show a recovery time less than that for neon. Other data, not shown, indicate that the recovery time can be reduced below  $1 \mu\text{sec}$ .

### Noise

Only a tentative result on the noise measurement will be reported here, since an extensive measurement on the noise output of the switch tube was not undertaken.<sup>9</sup>

A reference noise source of a known output ( $\sim 16$  decibel per megacycle) was used in series with the switch tube. An X-band superheterodyne receiver with a 10-Mc IF bandwidth and a balanced crystal mixer

<sup>9</sup> R. M. Hill and S. K. Ichiki, "Microwave noise from low pressure axes," *J. Appl. Phys.*, vol. 31, p. 735; April, 1960.

was used to detect the noise. Between pulses there was no discernible noise, as expected. Initially, only a very sharp spike of  $-70$  dbm amplitude and a duration of a fraction of a tenth of a microsecond was detected approximately  $0.05 \mu\text{sec}$  after the switch tube was triggered. The sharp spike appeared to be generated by the ionization process of the discharge, and may be due to traveling space potential as described by Westberg.<sup>10</sup>

At first no other noise could be detected, indicating that the switch tube noise was at least 10 db below the noise tube. As the tube aged, noise became discernible in other parts of the pulse and increased monotonically until the cathode ceased functioning. The increased noise generation appears to be due to deposition of cathode material around the tube and on the grid. Sec-

ondary electron emission from the grid and other parts of the tube can take place by positive ion bombardment. It may be possible that thermionic emission from the grid may occur. These and the unstable cathode emission probably contributed to the noise output of the tube.

### CONCLUSION

Low-pressure, hot cathode arc discharges offer considerable promise for the development of rapid, broadband microwave switches and control devices. Plasma densities of the order of  $10^{13}$  per cubic centimeter can be achieved in fractions of a microsecond and dissipated in a few microseconds or less. The power level at which microwave capture of the switch occurs may be adjusted by controlling gas pressure and geometry. Switching action for switching a pulsed source is provided by a low level trigger (10–100 volts) which discharges a storage condenser through the switch tube.

<sup>10</sup> R. G. Westberg, "Nature and role of ionizing potential space waves in glow to arc transitions," *Phys. Rev.*, vol. 114, pp. 1–17; April, 1959.

## Characteristic Impedances of Broadside-Coupled Strip Transmission Lines\*

SEYMOUR B. COHN†, FELLOW, IRE

**Summary**—Formulas are given for the even- and odd-mode characteristic impedances of shielded coupled strip-transmission-line configurations that are especially useful when close coupling is desired. Applications may be made to wideband coupled-strip-line filters, 3-db directional couplers, and many other components. The cross sections considered are thin broadside-coupled strips either parallel or perpendicular to the ground planes. Modification of the formulas for thick strips is discussed. The derivations are outlined, with particular attention given to the underlying assumption that restricts the use of the formulas to cases of close coupling.

### I. INTRODUCTION

**C**OUPLING effects between parallel transmission lines have applications in the design of many components, such as filters,<sup>1,2</sup> directional cou-

plers,<sup>1,3,4</sup> baluns,<sup>5</sup> and differential-phase-shift networks. Three useful coupled-strip-line configurations are shown in Fig. 1. The coplanar-strip cross section of Fig. 1(a) was analyzed previously and design data are conveniently available,<sup>7</sup> while the broadside-coupled strip-line cross sections of Fig. 1(b) and 1(c) are treated in this paper. In all three cases, the theory applies to strips of zero thickness, which may be approximated by metal-foil conductors sandwiched between dielectric plates filling the cross section. If air dielectric is desired, the strips must be given a moderate thickness to provide

\* Received by the PGMTT, June 23, 1960. The work described in this paper was performed at Stanford Res. Inst. with the support of the USASRD.

† Rantec Corp., Calabasas, Calif. Formerly at Stanford Res. Inst., Menlo Park, Calif.

<sup>1</sup> E. M. T. Jones and J. T. Bolljahn, "Coupled-strip-transmission-line filters and directional couplers," *IRE TRANS. ON MICROWAVE THEORY AND TECHNIQUES*, vol. MTT-4, pp. 75–81; April, 1956.

<sup>2</sup> S. B. Cohn, "Parallel-coupled transmission-line-resonator filters," *IRE TRANS. ON MICROWAVE THEORY AND TECHNIQUES*, vol. MTT-6, pp. 224–231; April, 1958.

<sup>3</sup> J. K. Shimizu, "Strip-line 3-db directional couplers," 1957 IRE WESCON CONVENTION RECORD, pt. 1, pp. 4–15.

<sup>4</sup> J. K. Shimizu and E. M. T. Jones, "Coupled-transmission-line directional couplers," *IRE TRANS. ON MICROWAVE THEORY AND TECHNIQUES*, vol. MTT-6, pp. 403–410; October, 1958.

<sup>5</sup> E. M. T. Jones and J. K. Shimizu, "A wide-band strip-line balun," *IRE TRANS. ON MICROWAVE THEORY AND TECHNIQUES*, vol. MTT-7, pp. 128–134; January, 1959.

<sup>6</sup> B. M. Schiffman, "A new class of broad-band microwave 90 degree phase shifters," *IRE TRANS. ON MICROWAVE THEORY AND TECHNIQUES*, vol. MTT-6, pp. 232–237; April, 1958.

<sup>7</sup> S. B. Cohn, "Shielded coupled-strip transmission lines," *IRE TRANS. ON MICROWAVE THEORY AND TECHNIQUES*, vol. MTT-3, pp. 29–38; October, 1955.



mechanical strength. In this case, adequate computational accuracy may be obtained by suitably modifying the zero-thickness formulas.

The coplanar configuration of Fig. 1(a) is particularly well suited to photo-etched strip-line circuits, but cannot be used where very close coupling is required. For example, in directional couplers having couplings greater than about  $-8$  db, the spacing between the strips becomes prohibitively small. However, closer coupling may be obtained with a reasonable spacing if thick strips are used in the arrangement of Fig. 1(a). This is clear if one considers that a sizable parallel-plate capacitance is added to the fringing capacitance between the two strips. To achieve close coupling with thin strips, a broadside coupling arrangement as in Fig. 1(b) and 1(c) is necessary. Both of these configurations have been used successfully in directional couplers having midband couplings as great as  $-2.7$  db.<sup>3</sup>

The details of the analysis of the two broadside-coupled strip configurations are not given here, since they involve a fairly routine application of the well-known Schwartz-Christoffel transformation method. However, the specific transformation geometries are described in Section IV, where they reveal a simplifying approximation that was made in each derivation. It is believed that the error in computed values of characteristic impedance due to these approximations will not be greater than about 0.1 per cent in close-coupling applications. The error increases as the coupling is decreased, but is not likely to exceed 1 per cent in any practical application for which a broadside-coupled strip arrangement would be preferred over a coplanar arrangement. The advantage gained by these approximations is that the elliptic functions necessary in exact solutions are avoided, thus simplifying the use of the formulas, as well as their derivation. However, the reader will be interested to know that rigorous solutions valid for all values of the parameters have recently been carried out by Hachemeister.<sup>8</sup>

## II. FORMULAS FOR BROADSIDE-COUPLED STRIPS PARALLEL TO GROUND PLANES

Two orthogonal TEM modes can propagate on a pair of parallel-coupled transmission lines. These are the *even* mode, for which the respective voltages and currents on the two conductors are equal and of the same sign, and the *odd* mode, for which the respective voltages and currents are equal but of opposite sign. All other voltage, current, and field conditions on the conductors can be expressed as a linear combination of these two modes and, therefore, the complete performance of the coupled conductors in a circuit may be com-

puted in terms of the characteristic impedances and propagation constants of these modes. It will be assumed that losses are small and that the cross sections are uniformly filled with a medium of relative dielectric constant  $\epsilon_r$ , so that the characteristic impedances are essentially real, the attenuation is small, and the phase velocities are equal to  $c/\sqrt{\epsilon_r}$ , where  $c$  is the velocity of light in free space.

The following formulas give the even-mode characteristic impedance,  $Z_{oe}$ , and the odd-mode characteristic impedance,  $Z_{oo}$ , of each conductor with respect to ground for the cross section of Fig. 2. These formulas hold for any ratio of  $w/b$  and  $s/b$ , as long as  $w/s$  is greater than about 0.35:

$$Z_{oe} = \frac{188.3}{\sqrt{\epsilon_r}} \frac{K(k')}{K(k)} \quad (1)$$

$$Z_{oo} = \frac{296.1}{\sqrt{\epsilon_r} \frac{b}{s} \tanh^{-1} k} \quad (2)$$

where

$k$  = a parameter,

$k' = \sqrt{1 - k^2}$ ,

$K(k)$  and  $K(k')$  = complete elliptic integrals of the first kind.

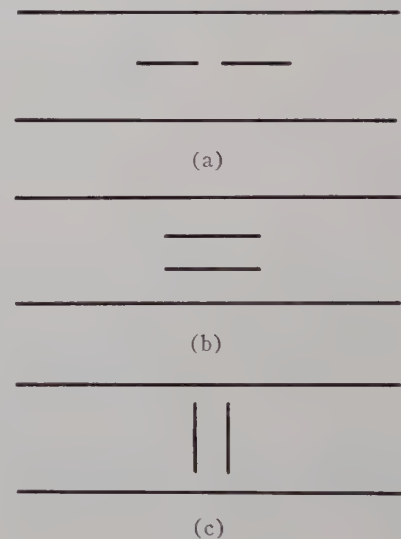


Fig. 1—Three useful configurations of very thin coupled strips between parallel ground planes.

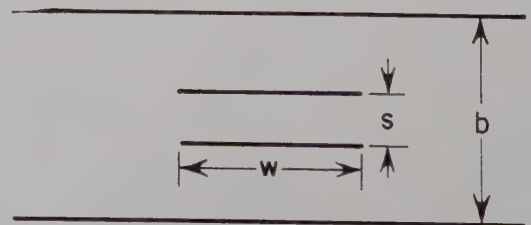


Fig. 2—Cross-section dimensions of broadside-coupled strips parallel to the ground planes.

<sup>8</sup> C. A. Hachemeister, "The Impedances and Fields of Some TEM-Mode Transmission Lines," Microwave Res. Inst., Polytechnic Inst. of Brooklyn, N. Y., Res. Rept. No. R-623-57, PIB-551, Contract No. AF 19(604)-2031, ASTIA Doc. No. AD-160802; April 16, 1958.

The ratio  $w/b$  is given by

$$\frac{w}{b} = \frac{2}{\pi} \left\{ \tanh^{-1} \sqrt{\frac{k \frac{b}{s} - 1}{\frac{1}{k} \frac{b}{s} - 1}} - \frac{s}{b} \tanh^{-1} \left[ \frac{1}{k} \sqrt{\frac{k \frac{b}{s} - 1}{\frac{1}{k} \frac{b}{s} - 1}} \right] \right\}. \quad (3)$$

The quantity  $K(k')/K(k)$  has been tabulated vs  $k$  by Oberhettinger and Magnus.<sup>9</sup> With the aid of their table, a cross section may be designed in a straightforward process to have the desired characteristic impedances  $Z_{oe}$  and  $Z_{oo}$ , as follows. First, from (1), solve for  $K(k')/K(k)$ . Next determine  $k$  from the above-mentioned table.<sup>10</sup> Then, obtain  $b/s$  from (2). Finally, calculate  $w/b$  from (3).

#### A. Simplification for $(w/b)/(1-s/b) \geq 0.35$

If, in addition to the condition  $w/s \geq 0.35$ , one imposes the condition

$$\frac{w/b}{1-s/b} \geq 0.35,$$

the fringing fields at opposite edges of the strips will be sufficiently isolated that fringing capacitances can be specified that are essentially independent of the strip width. Then, the characteristic impedances are given by

$$Z_{oe} = \frac{188.3/\sqrt{\epsilon_r}}{\frac{w/b}{1-s/b} + \frac{C_{fe}'}{\epsilon}} \quad (4)$$

and

$$Z_{oo} = \frac{188.3/\sqrt{\epsilon_r}}{\frac{w/b}{1-s/b} + \frac{w}{s} + \frac{C_{fo}'}{\epsilon}}, \quad (5)$$

where the fringing capacitance,  $C_{fe}'$ , is the capacitance per unit length that must be added at each edge of each strip to the parallel-plate capacitance so that the total capacitance to ground for the even-mode field distribution will be correct.  $C_{fo}'$  is the corresponding quantity for the odd mode, and  $\epsilon$  is the absolute dielectric con-

<sup>9</sup> F. Oberhettinger and W. Magnus, "Anwendung der Elliptischen Functionen in Physik und Technik," Springer-Verlag, Berlin, Germany; 1949.

<sup>10</sup> For  $k$  small, one may use

$$\frac{K(k')}{K(k)} = \frac{2}{\pi} \log_e \frac{4}{k}.$$

The error in this formula increases with  $k$ , being about  $\frac{1}{4}$  per cent for  $k=0.2$ , and 1 per cent for  $k=0.3$ .

stant, equal to  $8.85 \epsilon_r$  mmf per meter. The fringing capacitances are functions only of  $s/b$ , and are given by

$$\frac{C_{fe}'}{\epsilon} = 0.4413 + \frac{1}{\pi} \left[ \log_e \left( \frac{1}{1-s/b} \right) + \frac{s/b}{1-s/b} \log_e \frac{b}{s} \right] \quad (6)$$

$$\frac{C_{fo}'}{\epsilon} = \frac{b/s}{\pi} \left[ \log_e \left( \frac{1}{1-s/b} \right) + \frac{s/b}{1-s/b} \log_e \frac{b}{s} \right]. \quad (7)$$

Eqs. (6) and (7) are plotted vs  $s/b$  in Fig. 3.

#### B. Effect of a Small Thickness of the Strips

When foil strips are used in the cross section of Fig. 2, the strip thickness of about 0.0015 inch is usually not great enough to affect seriously the zero-thickness values of  $C_{fe}'/\epsilon$  and  $C_{fo}'/\epsilon$ , but it can have an appreciable effect on the parallel-plate capacitance between the strips in the odd-mode case, depending on how the dimension  $s$  is defined. In the usual case of  $s/b < 0.5$ ,  $s$  should be taken to be the spacing between the strips, as in Fig. 4; then (1)–(3) or (4)–(7) may be used with good accuracy. For greater strip thickness, the fringing capacitances will be larger than the values given by (6) and (7) and Fig. 3. The parallel-plate capacitance between each strip and its adjacent ground plane will also be increased. A paper on thickness corrections that

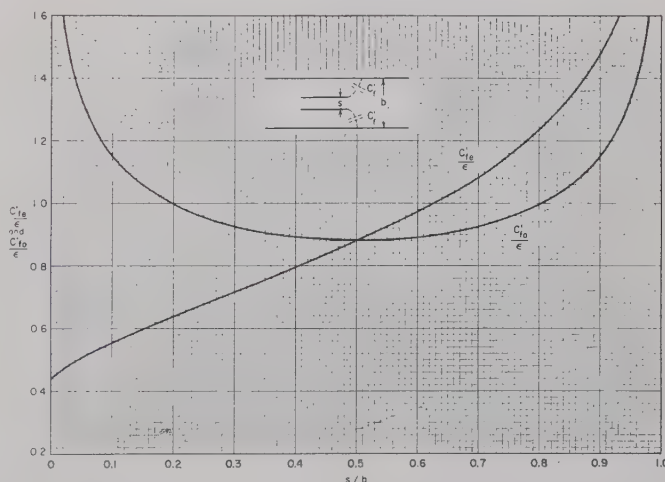


Fig. 3—Even- and odd-mode fringing capacitances for broadside-coupled very thin strips parallel to the ground planes.

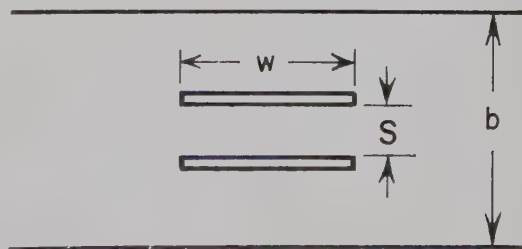


Fig. 4—Thick strips in the broadside-coupled parallel arrangement.



applies to this and numerous other practical configurations is published in this issue.<sup>11</sup>

### III. FORMULAS FOR BROADSIDE-COUPLED STRIPS PERPENDICULAR TO GROUND PLANES

The even- and odd-mode characteristic impedances of the cross section of Fig. 5 are given by these formulas:

$$Z_{oe} = \frac{188.3}{\sqrt{\epsilon_r}} \frac{K(k)}{K(k')} \quad (8)$$

$$Z_{oo} = \frac{296.1/\sqrt{\epsilon_r}}{\frac{b}{s} \cos^{-1} k + \log_e \frac{1}{k}} \quad (9)$$

where  $k$  is a parameter and  $k'$ ,  $K(k)$ , and  $K(k')$  are as defined in Section II. The ratio  $w/b$  is given by

$$\frac{w}{b} = \frac{2}{\pi} \left\{ \tan^{-1} \left[ \frac{k'}{k} \sqrt{\frac{1 - \frac{k}{k'} \frac{s}{b}}{1 + \frac{k'}{k} \frac{s}{b}}} \right] - \frac{s}{b} \tanh^{-1} \left[ \sqrt{\frac{1 - \frac{k}{k'} \frac{s}{b}}{1 + \frac{k'}{k} \frac{s}{b}}} \right] \right\} \quad (10)$$

The inverse cosine and tangent functions in (9) and (10) are evaluated in radians between 0 and  $\pi/2$ . As in the case of broadside strips parallel to the ground planes, the dimension ratios may be determined in a straightforward manner for given values of  $Z_{oe}$  and  $Z_{oo}$ . With the aid of the table of  $K(k)/K(k')$  vs  $k$  in Oberhettinger and Magnus,<sup>9</sup> the parameter  $k$  is determined from (8). Then  $b/s$  is obtained from (9), and finally  $w/b$  from (10).

Eqs. (8)–(10) are accurate for all values of  $w/b$  and  $s/b$ , as long as  $w/s$  is greater than about 1.0. As  $s/b$  is made small compared to 1.0, the formulas remain accurate for smaller values of  $w/s$ . This range of validity covers all practical cases except that of very loose coupling.

#### A. Effect of a Small Thickness of the Strips

In the case of foil strips, the effect of strip thickness can be neglected if  $s$  is defined to be the spacing between the strips, as shown in Fig. 6. For thicker strips the formulas should be used with discretion. A companion paper on thickness corrections, referred to in Section II, will enable an improvement in accuracy in the case of thick strips.<sup>11</sup>

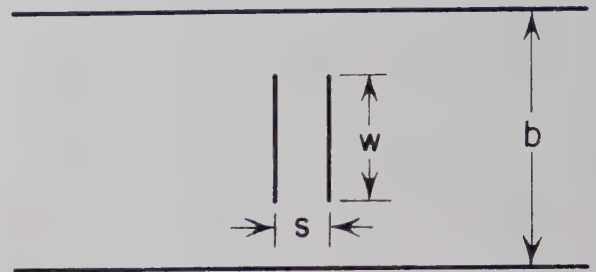


Fig. 5—Cross-section dimensions of broadside-coupled strips perpendicular to the ground planes.

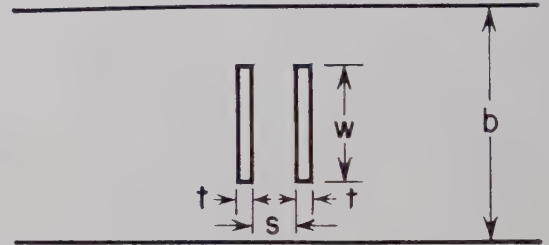


Fig. 6—Thick strips in the broadside-coupled, perpendicular arrangement.

### IV. COMMENTS ON THE DERIVATIONS

The formulas in this paper were derived by the Schwartz-Christoffel conformal-transformation method.<sup>12,13</sup> This method enables one to evaluate the capacitance and characteristic impedance between straight-sided conductors when the problem can be reduced to two dimensions, as in the cross-section plane of a transmission line. By means of one or more transformations in the complex plane, the boundary of the cross section is transformed into a simpler boundary for which the solution is known. Then because of the special properties of the conformal transformation, the capacitance and characteristic impedance of the original boundary are equal to the respective quantities of the transformed boundary.

Fig. 7(a) shows the cross section of broadside-coupled strips parallel to the ground planes. Vertical and horizontal planes of symmetry are indicated, and because of this symmetry the solution can be obtained from the geometry of Fig. 7(b), which is the upper right-hand quarter of the complete cross section. The boundary in Fig. 7(b) consists of half of the upper ground plane, the two sides of half of the upper strip, two vertical magnetic-wall segments, and a horizontal plane which is a magnetic wall for the even-mode case and an electric wall for the odd-mode case. In addition, the open end of the boundary is assumed to be closed at infinity. An exact solution of Fig. 7(b) requires elliptic functions. In order to avoid these functions, it is necessary to reduce the number of right-angle corners in the boundary. One way of doing this is shown in Fig. 7(c), where the lower

<sup>12</sup> W. R. Smythe, "Static and Dynamic Electricity," McGraw-Hill Book Co., Inc., New York, N. Y., 1st ed., p. 80 ff.; 1939.

<sup>13</sup> E. Weber, "Electromagnetic Fields," vol. 1, John Wiley and Sons, Inc., New York, N. Y., p. 325 ff.; 1950.

<sup>11</sup> S. B. Cohn, "Thickness corrections for capacitive obstacles and strip conductors," this issue, p. 638.

vertical segment of magnetic wall is shifted to minus infinity. The new boundary is not exactly equivalent to Fig. 7(a) but the approximation is excellent in the usual case of  $w > s$ . In that case it is clear that for the even mode very little electric-field energy penetrates into the region on the left of the  $x=0$  plane in the lower left-hand part of Fig. 7(c), while for the odd mode, the electric field is virtually uniform in that region. Thus very good accuracy is obtained in the even-mode case by evaluating the total capacitance between the conductors of Fig. 7(c) and assuming it to be equal to the capacitance of Fig. 7(b), and in the odd-mode case by calculating the total capacitance minus the parallel-plate capacitance between  $x=0$  and  $x=-\infty$ . This procedure has been followed in the derivation of (1)–(3), and no further approximations were made. Experience with other geometries of strip conductors indicates that an accuracy of the order of 1 per cent should ensue for  $w/s$  as low as 0.35, and of the order of 0.1 per cent for  $w/s$  greater than 1.0.

A similar approximation was made in the analysis of broadside-coupled strips perpendicular to the ground planes. The cross section is shown with its symmetry planes in Fig. 8(a), and the exact quarter model is shown in Fig. 8(b). As in the previous case, elliptic functions are needed in the solution of Fig. 8(b), but are avoided in the solution of Fig. 8(c), which is the geometry that was used in the derivation of (8)–(10). The total even-mode capacitance in Fig. 8(c) is assumed equal to the even-mode capacitance in Fig. 8(b), while the total odd-mode capacitance minus the parallel plate capacitance from  $y=0$  to  $y=-\infty$  is assumed equal to the odd-mode capacitance in Fig. 8(b). The considerations about accuracy are the same as in the previous case, but it is believed that  $w/s$  should not be made smaller than 1.0 unless further evidence justifies a lower limit.

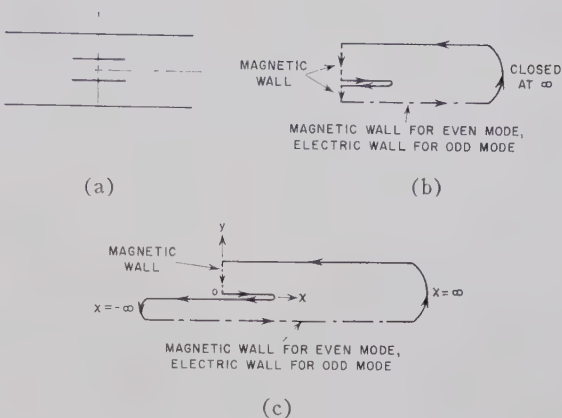


Fig. 7—Boundaries considered for the broadside-coupled parallel case.

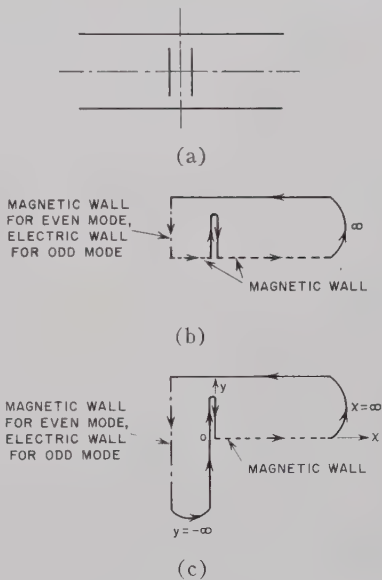


Fig. 8—Boundaries considered for the broadside-coupled perpendicular case.



# Thickness Corrections for Capacitive Obstacles and Strip Conductors\*

SEYMOUR B. COHN†, FELLOW, IRE

**Summary**—Capacitive thickness corrections are derived exactly for two basic geometries involving pairs of semi-infinite plates. In one arrangement the pair of plates are coplanar, while in the other they are parallel to each other. In each case the total capacitance per unit length between the pair of plates is infinite, but the incremental increase of capacitance when the thickness is increased from zero to a value  $t$  is finite. These capacitance increments are evaluated, and it is shown how they may be used as approximate thickness corrections in a great variety of more complicated geometries involving capacitive obstacles in waveguide, coaxial line, and artificial dielectric media. They may also be applied to coupled-strip-line conductors. As examples, the corrections are applied in detail to a waveguide iris, and to three useful coupled-strip-line cross sections.

## I. INTRODUCTION

SOLUTIONS for many capacitive-obstacle and strip-transmission-line cross sections are available only in the case of zero-thickness conductors. If the conductors are sufficiently thin, as in the usual photo-etched strip-line circuit, the accuracy of the solution will be good, but in numerous practical microwave structures finite thickness has a large effect. Except in a few simple cases, exact solutions for the parameters of cross sections containing thick edges are very difficult to achieve. In order to alleviate this problem, two basic thick-edge cross sections are considered in this paper, and the increase in capacitance due to finite thickness is given for each case. These capacitance increments may be applied as corrections to a wide variety of practical structures for which the zero-thickness solutions are either available or obtainable.

The two basic cross sections treated in this paper are shown in Fig. 1. One consists of a pair of semi-infinite thick plates in a coplanar arrangement [Fig. 1(a)], while the other consists of a pair of semi-infinite thick plates in a parallel arrangement [Fig. 1(c)]. In each case, an electric wall may be inserted in the plane of symmetry, thus creating the unsymmetrical equivalents shown in Fig. 1(b) and 1(d). The total capacitance between the semi-infinite conductors are  $C_1'(t/s)$  and  $C_2'(t/s)$  farads per unit length, respectively, in which the *prime* mark indicates that the capacitance is computed for one unit of length of the cylindrical conductors. Because the plates are semi-infinite,  $C_1'(t/s)$  and  $C_2'(t/s)$  are infinite. However, the incremental increase in capacitance when  $t$  is increased from zero with  $s$  held constant is a finite quantity. This increment of ca-

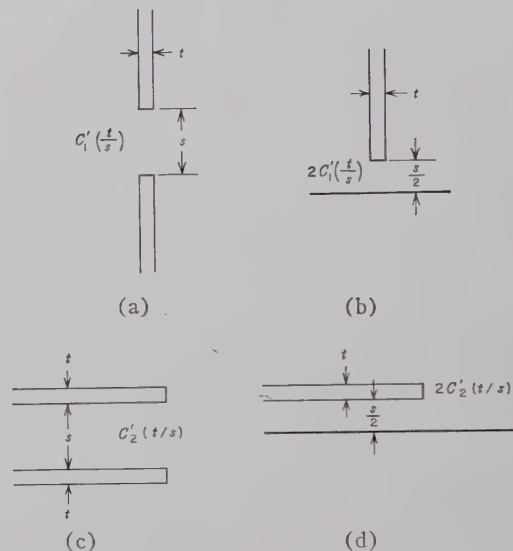


Fig. 1—Basic semi-infinite plate cross sections. (a) and (b) Coplanar arrangement and unsymmetrical equivalent. (c) and (d) Parallel arrangement and unsymmetrical equivalent.

pacitance is defined in each case as follows:

$$\Delta C_{1,2}'(t/s) = C_{1,2}'(t/s) - C_{1,2}'(0). \quad (1)$$

If one considers the field-distribution patterns for  $t=0$  and for  $t>0$ , one realizes that they differ mainly near the plate edges, with negligible difference far from the edges. Thus the increments  $\Delta C_1'(t/s)$  and  $\Delta C_2'(t/s)$  arise from field distortions close to the edges, and their values would be affected only very slightly if additional structural surfaces were present at locations relatively distant. Consequently the capacitance increments derived for Fig. 1(a) and 1(c) may be used as thickness corrections in the case of more complex cross sections for which zero-thickness solutions can be obtained.

Fig. 2 shows a number of practical configurations to which the capacitive increment for the coplanar-plate case may be applied as a thickness correction. Solutions valid for zero thickness are already available for most of these,<sup>1-4</sup> and are feasible to obtain for the others. In the coaxial-line cases, the total correction is  $2\pi r_e \cdot \Delta C_1'(t/s)$ , where  $r_e$  is a judiciously chosen radius between that of

\* Received by the PGM-TT, June 23, 1960; revised manuscript received, July 18, 1960. The research reported in this paper was performed at Stanford Res. Inst., with support partly by USASRD and partly by the AF Cambridge Res. Center.

† Rantec Corp., Calabasas, Calif.

<sup>1</sup> N. Marcuvitz, "Waveguide Handbook," McGraw-Hill Book Co., Inc., New York, N. Y., pp. 218-221; 1951.

<sup>2</sup> *Ibid.*, pp. 229-238.

<sup>3</sup> S. B. Cohn, "Shielded coupled-strip transmission line," IRE TRANS. ON MICROWAVE THEORY AND TECHNIQUES, vol. MTT-3, pp. 29-38; October, 1955.

<sup>4</sup> S. B. Cohn, "Analysis of the metal-strip delay structure for microwave lenses," *J. Appl. Phys.*, vol. 20, pp. 251-262; March, 1949. Also, "Addendum," p. 1011; October, 1949.

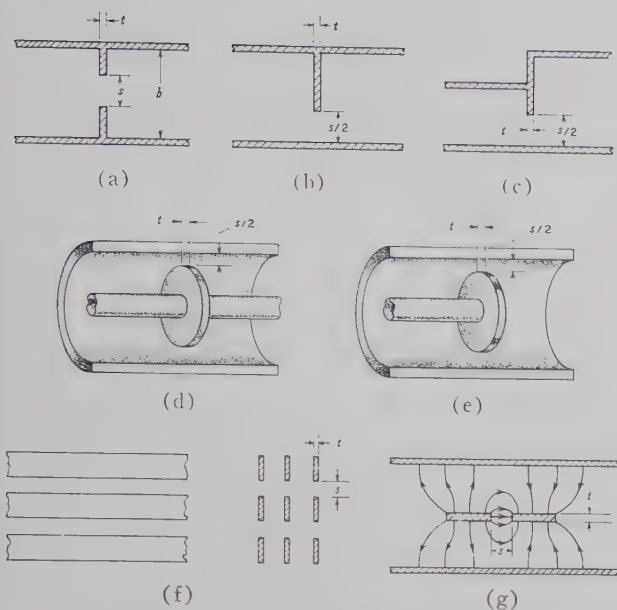


Fig. 2—Practical cases where the coplanar plate thickness correction may be applied. (a)–(e) Examples of capacitive obstacles of moderate thickness in waveguide and coaxial line. (f) Metal strip artificial dielectric medium. (g) Coplanar coupled strip line in odd mode.

the disk and that of the outer conductor. In order for the correction to apply accurately to the cases in Fig. 2, it is necessary that  $s/\lambda_g$  and  $s/r$  be sufficiently small compared to unity ( $\lambda_g$  is the guide wavelength and  $r$  is the distance from the center point of the symmetrical configuration to the nearest extraneous surface). Fortunately, these requirements are not very stringent. On the basis of a study of the waveguide iris of Fig. 2(a) (see Section IV), it is believed that the correction will usually yield good results for  $s/\lambda_g$  as large as  $1/4$ , and  $s/r$  at least as large as  $1/2$ .

Fig. 3 shows situations in which the capacitive increment for the parallel-plate case may be applied. Formulas for the odd- and even-mode characteristic impedances of the coupled-strip lines in Fig. 3(a) and 3(b) have recently been given in another paper, assuming zero thickness.<sup>5</sup> As shown in Section V, the capacitive increment for the parallel-plate case may be used to compute a thickness correction for the odd mode. Fig. 3(c) shows a strip conductor over a ground plane, for which the same correction term is applicable. Fig. 3(d) shows an example of a coaxial cavity containing a capacitive disk closely spaced from an end wall. Here, also, an effective radius  $r_e$  must be judiciously chosen, yielding a total thickness correction  $\Delta C = 2\pi r_e \cdot 2\Delta C_1'(t/s)$ . This problem has been considered in detail by the author, and has resulted in formulas for the resonant frequency and unloaded  $Q$  of coaxial cavities of the type shown in Fig. 3(d). The minimum allowable distance from the edges to the nearest extraneous surface in the configurations of Fig. 3 cannot be determined

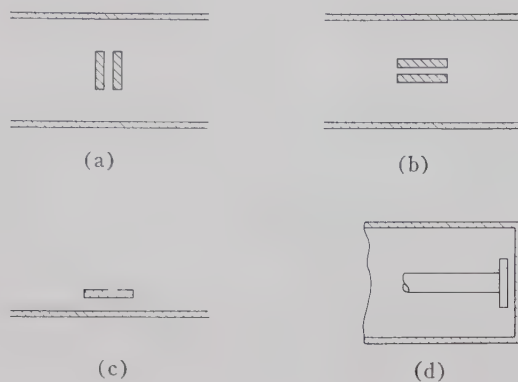


Fig. 3—Practical cases where the parallel-plate thickness correction may be applied.

precisely. However, it is expected that good results will usually be obtained for  $(s+2t)/r$  as large as  $1/2$ , and for  $(s+2t)/\lambda_g$  as large as  $1/4$ .

## II. THICKNESS-CORRECTION TERM FOR COPLANAR PLATES

As derived in Appendix I, the incremental capacitance per unit length is as follows for the coplanar plates of Fig. 1(a):

$$\Delta C_1'(t/s) = \frac{2\epsilon}{\pi} \ln \left[ \frac{E(k) - (1/2)k'^2 K(k)}{\sqrt{k}} \right] \quad (2)$$

where the parameters  $k$  and  $k'$  are solved from the following equations as functions of  $t/s$ :

$$\frac{t}{s} = \frac{\frac{1+k^2}{2} K(k') - E(k')}{2 \left[ E(k) - \frac{k'^2}{2} K(k) \right]} \quad (3)$$

$$k' = \sqrt{1 - k^2}. \quad (4)$$

The units of  $\Delta C_1'(t/s)$  are the same as those of the permittivity  $\epsilon$ , which for free space has the value  $8.85(10)^{-12}$  farads per meter,  $0.0885 \mu\text{f}$  per cm, or  $0.225 \mu\text{f}$  per inch.  $K(k)$  and  $E(k)$  are complete elliptic integrals of the first and second kinds, respectively.

Eqs. (2)–(4) have been computed, and the resulting curve is given in Fig. 4. The procedure used was first to select values of  $k$ , and then to calculate the corresponding values of  $\Delta C_1'$  and  $t/s$ . The quantity plotted is  $[\Delta C_1'(t/s) - \epsilon t/s]/\epsilon$ , in which the term  $\epsilon t/s$  is the parallel-plate capacitance per unit length neglecting fringing. By subtracting this parallel-plate term from  $\Delta C_1'$ , the curve is made to approach a constant value as  $t/s$  is made large enough so that the fringing fields on the two sides of the configuration become independent. It is seen that this occurs for  $t/s \geq 1$ . The limiting value of  $\Delta C_1'$  for  $t/s \geq 1$  is of interest. With the aid of limiting values of the elliptic integrals, one may show this to be

<sup>5</sup> S. B. Cohn, "Characteristic impedances of broadside-coupled strip transmission lines," IRE TRANS. ON MICROWAVE THEORY AND TECHNIQUES, this issue, p. 633.



$$\frac{\Delta C_1'}{\epsilon} = \frac{t}{s} + \frac{2}{\pi} \left( 1 + \ln \frac{\pi}{8} \right) = \frac{t}{s} + 0.0415. \quad (5)$$

The curve approaches zero as  $t/s$  goes to zero. For  $t/s < 0.001$  the correction is very small, so that parameter values for zero-thickness cases may be used with high accuracy. For  $t/s > 0.5$ , the correction is essentially constant, so that data for isolated step discontinuities may be applied accurately. The range  $0.001 < t/s < 0.5$  is, therefore, the region of interest for which the thickness correction presented here is needed. Most practical capacitive-iris structures fall within this range.

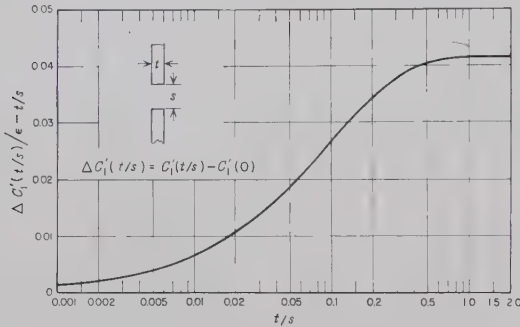


Fig. 4—Plot of coplanar capacitance correction.

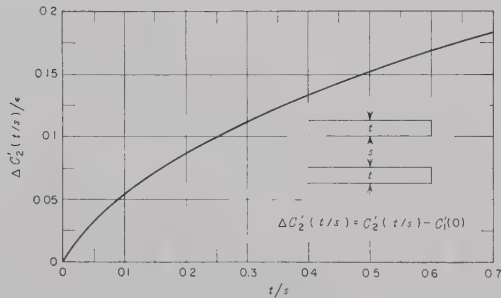


Fig. 5—Plot of parallel-plate capacitance correction.

### III. THICKNESS-CORRECTION TERM FOR PARALLEL PLATES

The following formula is derived in Appendix II for the incremental capacitance per unit length of the parallel plates of Fig. 1(c).

$$\Delta C_2'(t/s) = \frac{\epsilon}{2\pi} \left[ \left( 1 + \frac{t}{s} \right) \ln \left( 1 + \frac{t}{s} \right) - \frac{t}{s} \ln \frac{t}{s} \right]. \quad (6)$$

Eq. (6) is plotted in Fig. 5.

### IV. EXAMPLE OF THICK CAPACITIVE IRIS IN WAVEGUIDE

The manner in which the thickness correction may be applied to practical configurations will be illustrated by the example of a thick capacitive iris in waveguide. (This case has also been treated by Marcuvitz by dif-

ferent methods.<sup>6</sup>) Fig. 6(a) shows a longitudinal  $E$ -plane section through a rectangular waveguide containing a zero-thickness, perfectly conducting, symmetrical capacitive iris. It is assumed that only the  $TE_{10}$  mode is propagating. In the limiting case of  $b/\lambda_g \rightarrow 0$ , the equivalent normalized susceptance of the iris<sup>1</sup> is

$$\frac{B}{Y_0} = \frac{4b}{\lambda_g} \ln \csc \left( \frac{\pi s}{2b} \right), \quad (7)$$

where  $B$  is the susceptance of the iris,  $Y_0$  is the characteristic admittance of the waveguide,  $\lambda_g$  is the guide wavelength, and  $b$  and  $s$  are dimensions defined in Fig. 6(a).

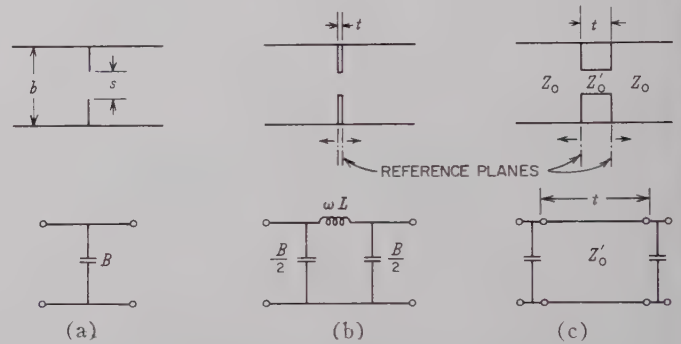


Fig. 6—Capacitive obstacle in rectangular waveguide for (a) very thin, (b) moderately thick, and (c) very thick cases.

In applying the capacitive thickness correction, it is necessary to employ an equivalence theorem between  $E$ -plane structures in  $TE_{10}$ -mode rectangular waveguide and in TEM-mode parallel-plane transmission line. If the structure has the same boundary in all longitudinal  $E$ -plane sections in both cases, then the normalized element values of the waveguide equivalent circuit are identical to those of the parallel-plane equivalent circuit, if  $\lambda_g$  of the  $TE_{10}$  mode is used in place of  $\lambda$  of the TEM mode.<sup>7</sup> The normalized susceptance increment due to thickness may therefore be evaluated in terms of  $\Delta C_1'$  as follows. Assume a parallel-plane TEM-mode transmission line with  $E$ -plane dimension  $b$  and  $H$ -plane dimension  $a$ . The characteristic admittance is  $Y_0 = (a/b) \sqrt{\epsilon/\mu}$  mhos, where  $\epsilon$  and  $\mu$  are the permittivity and permeability of the filling medium in mks units. The susceptance increment is  $\Delta B = a\omega\Delta C_1' = 2\pi a\Delta C_1'/\lambda \sqrt{\epsilon\mu}$ . Hence, the normalized susceptance increment due to thickness is

$$\frac{\Delta B}{Y_0} = \frac{2\pi b}{\lambda} \cdot \frac{\Delta C_1'}{\epsilon}.$$

<sup>6</sup> Marcuvitz, *op. cit.*, pp. 248–255 and 404–406.

<sup>7</sup> C. G. Montgomery, R. H. Dicke, and E. M. Purcell, "Principles of Microwave Circuits," McGraw-Hill Book Co., Inc., New York, N. Y., p. 172; 1948.

By virtue of the equivalence theorem, the corresponding quantity in rectangular waveguide is

$$\frac{\Delta B}{Y_0} = \frac{2\pi b}{\lambda_g} \frac{\Delta C_1'}{\epsilon}, \quad (8)$$

where  $\Delta C_1'/\epsilon$  is obtained as a function of  $t/s$  from (2)–(4), or from the graph in Fig. 5.

In addition to the increase in capacitive susceptance, thickness also requires a series inductive reactance to be added to the equivalent circuit, as shown in Fig. 6(b). This reactance represents the magnetic-field energy in the gap region of the thick iris. In the parallel-plane case, the inductance of this region is simply  $L = \mu t s / a$ , while the characteristic impedance is  $Z_0 = \sqrt{\mu/\epsilon}(b/a)$ . Therefore, the normalized reactance is  $\omega L/Z_0 = 2\pi t s / \lambda b$ . In waveguide, this becomes,

$$\frac{\omega L}{Z_0} = \frac{2\pi t s}{\lambda_g b}. \quad (9)$$

An interesting check on the thickness correction may be obtained in the very thick iris case of Fig. 6(c). If  $t/\lambda_g \ll 1$  and  $t/s \geq 1$ , the total shunt susceptance is obtained by adding (7) and (8), with the aid of (5):

$$\frac{B}{Y_0} = \frac{4b}{\lambda_g} \left[ \ln \csc \left( \frac{\pi s}{2b} \right) + \frac{\pi t}{2s} + 1 + \ln \frac{\pi}{8} \right]. \quad (10)$$

In the limit  $s/b \rightarrow 0$ , this reduces to

$$\frac{B}{Y_0} = \frac{4b}{\lambda_g} \left( \ln \frac{b}{4s} + 1 + \frac{\pi t}{2s} \right). \quad (11)$$

The total susceptance for this case may also be evaluated by adding the parallel-plate capacitance to two times the step discontinuity capacitance. The normalized shunt susceptance appropriate to the parallel-plate capacitance is  $(2\pi t/\lambda_g)(b/s)$ , while the normalized step discontinuity susceptance<sup>8</sup> in the limit  $s/b \rightarrow 0$  is  $(2b/\lambda_g)[\ln(b/4s) + 1]$ . The total shunt susceptance is, therefore,

$$\begin{aligned} \frac{B}{Y_0} &= 2 \left( \frac{2b}{\lambda_g} \right) \left( \ln \frac{b}{4s} + 1 \right) + \frac{2\pi t b}{\lambda_g s} \\ &= \frac{4b}{\lambda_g} \left( \ln \frac{b}{4s} + 1 + \frac{\pi}{2} \frac{t}{s} \right). \end{aligned} \quad (12)$$

This agrees exactly with (11), which was obtained by adding the thickness correction to the zero-thickness value. It should be remembered that this exact agreement assumes  $s/b \ll 1$ . However, more detailed calculations have indicated close agreement for  $s/b \leq 0.25$ , and fair agreement for  $s/b$  at least as large as 0.6.

<sup>8</sup> *Ibid.*, pp. 307–310.

## V. EXAMPLES OF THICK COUPLED STRIPS

### A. Coplanar-Coupled Strip Line

The coplanar-coupled strip transmission line of Fig. 7 will now be considered. The odd- and even-mode characteristic impedances of one strip to ground are related to the odd- and even-mode capacitances per unit length of one strip to ground by, respectively,

$$Z_{oo} = \frac{\sqrt{\mu\epsilon}}{C_{oo}'} \quad \text{and} \quad Z_{oe} = \frac{\sqrt{\mu\epsilon}}{C_{oe}'}, \quad (13)$$

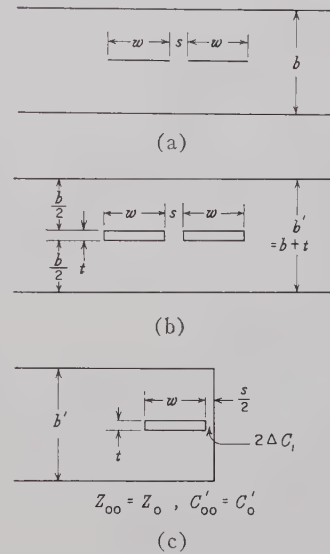


Fig. 7—Coplanar coupled-strip transmission line.

where  $\mu$  and  $\epsilon$  are the permeability and permittivity of the filling medium in mks units. First consider the odd mode. Symmetry permits a vertical electric wall to be inserted between the strips, reducing the cross section to that of Fig. 7(c). The characteristic impedance and capacitance per unit length of Fig. 7(c) are  $Z_{oo}$  and  $C_{oo}'$ , the quantities desired. In general,  $C_{oo}'$  is a function of the dimension ratios  $w/b$ ,  $s/b$ , and  $t/b$ . For  $t/b = 0$  [Fig. 7(a)],

$$C_{oo}' \left( \frac{w}{b}, \frac{s}{b}, \frac{t}{b} \right) = C_{oo}' \left( \frac{w}{b}, \frac{s}{b}, 0 \right), \quad (14)$$

which may be obtained exactly from Cohn.<sup>3</sup> For  $t/b > 0$ ,  $b$  should be increased by  $t$  to  $b' = b + t$ , as shown in Fig. 7(b) and 7(c), so that the proportions above and below the strips will be unchanged. Then the thickness effect at the strip edges adjacent to the gap  $s$  requires the addition of  $2\Delta C_1'(t/s)$  to  $C_{oo}'(w/b, s/b, 0)$ . The gap  $s$  is assumed to be small enough compared to  $b/2$  and  $w$  for  $\Delta C_1'(t/s)$  to apply accurately ( $s < b/4$  and  $s < w/2$  are probably sufficient). At the strip edges remote from the gap, the thickness effect requires the addition of  $2C_f'(t/b') - 2C_f'(0)$ , where  $C_f'(t/b')$  is the fringing



capacitance to ground per unit length from each corner of a semi-infinite plate of thickness  $t$  midway between infinite ground planes of spacing  $b'$ , and  $C_f'(0)$  is the same for  $t=0$ . Values of  $C_f'(t/b')$  may be obtained from (5) or Fig. 3 of Cohn.<sup>9</sup> Hence for  $t>0$ ,

$$C_{oo}'\left(\frac{w}{b'}, \frac{s}{b'}, \frac{t}{b'}\right) = C_{oo}'\left(\frac{w}{b}, \frac{s}{b}, 0\right) + 2\Delta C_1'(t/s) + 2C_f'(t/b') - 2C_f'(0). \quad (15)$$

For the even mode, the two strips are at the same potential, so that  $\Delta C_1'(t/s)$  does not apply. Eq. (18) of Cohn<sup>3</sup> may be used to obtain a good approximation to  $Z_{oe}$  or  $C_{oe}'$ . Or, for  $s/b$  small, another very good approximation is

$$C_{oe}'\left(\frac{w}{b'}, \frac{s}{b'}, \frac{t}{b'}\right) = C_{oe}'\left(\frac{w}{b}, \frac{s}{b}, 0\right) + 2C_f'\left(\frac{t}{b'}\right) - 2C_f'(0), \quad (16)$$

where  $C_{oe}'(w/b, s/b, 0)$  is the even-mode capacitance to ground per unit length for zero-thickness strips, obtainable exactly from Cohn.<sup>3</sup>

### B. Broadside-Coupled Strip Line

Formulas valid for zero thickness have been obtained for the even- and odd-mode characteristic impedances of the two broadside-coupled strip cross sections of Figs. 8(a) and 9(a). The corresponding capacitances per unit length of one strip to ground,  $C_{oo}'(w/b, s/b, 0)$  and  $C_{oe}'(w/b, s/b, 0)$ , are related to these characteristic impedances by (13).

First consider the odd mode in Fig. 8. For  $t>0$ , the proportions above and below the pair of strips may be preserved by increasing the plate spacing to  $b'=b+2t$ . The odd-mode potential distribution permits insertion of an electric wall at ground potential between the strips, reducing the cross section to that of Fig. 8(c). The characteristic impedance of the latter cross section is the quantity desired. This may be obtained from the capacitance per unit length of the odd mode, which is approximately as follows,

$$C_{oo}'\left(\frac{w}{b'}, \frac{s}{b'}, \frac{t}{s}\right) = C_{oo}'\left(\frac{w}{b}, \frac{s}{b}, 0\right) + 4\Delta C_2'\left(\frac{t}{s}\right). \quad (17)$$

<sup>9</sup> S. B. Cohn, "Problems in strip transmission lines," IRE TRANS. ON MICROWAVE THEORY AND TECHNIQUES, vol. MTT-3, pp. 119-126; March, 1955.

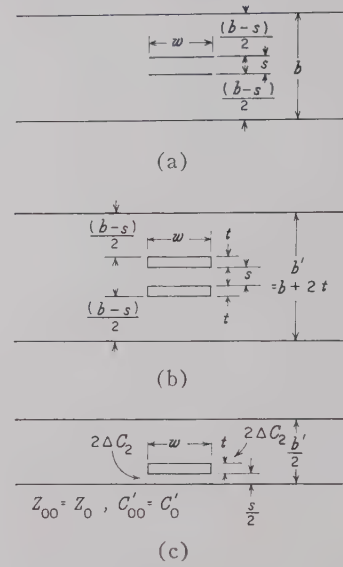


Fig. 8—Broadside coupled-strip transmission line; strips parallel to ground planes.

For the even mode, if  $t \ll s$ , the capacitance per unit length is,

$$C_{oe}'\left(\frac{w}{b'}, \frac{s}{b'}, \frac{t}{s}\right) = C_{oe}'\left(\frac{w}{b'}, \frac{s'}{b'}, 0\right), \quad (18)$$

in which  $s' = s + 2t$ . If  $t \gg s$ , then

$$C_{oe}'\left(\frac{w}{b'}, \frac{s}{b'}, \frac{t}{s}\right) = \frac{1}{2} C_o'\left(\frac{w}{b'}, \frac{t'}{w}\right), \quad (19)$$

where  $C_o'(w/b', t'/w)$  is the characteristic impedance of a single strip of width  $w$  and thickness  $t'$  midway between ground planes spaced by  $b' = b + 2t$ .<sup>9,10</sup> Here,  $t' = s + 2t$ . In the usual case of close coupling, (18) and (19) will agree very closely for any values of  $t$  and  $s$ .

Now consider Fig. 9. The odd-mode characteristic impedance of Fig. 9(b) is equal to the characteristic impedance of the reduced cross section shown in Fig. 9(c). The capacitance per unit length of the latter cross section is

$$C_{oo}'\left(\frac{w}{b}, \frac{s}{b}, \frac{t}{s}\right) = C_{oo}'\left(\frac{w}{b}, \frac{s}{b}, 0\right) + 4\Delta C_2'\left(\frac{t}{s}\right). \quad (20)$$

For the even mode, if  $t \ll s$ ,

$$C_{oe}'\left(\frac{w}{b}, \frac{s}{b}, \frac{t}{s}\right) = C_{oe}'\left(\frac{w}{b}, \frac{s'}{b}, 0\right), \quad (21)$$

<sup>10</sup> R. H. T. Bates, "The characteristic impedance of the shielded slab line," IRE TRANS. ON MICROWAVE THEORY AND TECHNIQUES, vol. MTT-4, pp. 28-33; January, 1956.

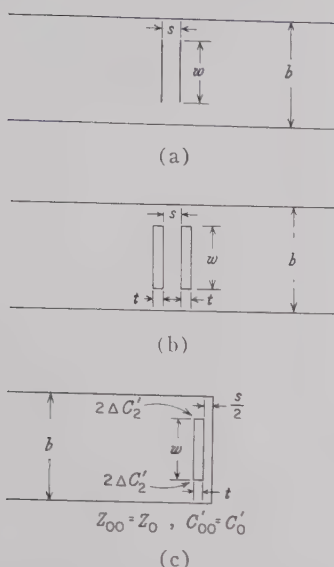


Fig. 9—Broadside coupled-strip transmission line; strips perpendicular to ground planes.

in which  $s' = s + 2t$ . If  $t \gg s$ ,

$$C_{oe}' \left( \frac{w}{b}, \frac{s}{b}, \frac{t}{s} \right) = \frac{1}{2} C_0 \left( \frac{w'}{b}, \frac{t'}{w'} \right) \quad (22)$$

where  $w' = s + 2t$  and  $t' = w$ . Again, there will generally be little difference between (21) and (22) in the usual case of close coupling.

$$z = j \frac{s}{2} \left\{ \frac{u \left[ k'^2 - \frac{2E(k)}{K(k)} \right] - 2zn(u, k) - \frac{cn(u, k)dn(u, k)}{sn(u, k)}}{2E(k) - k'^2K(k)} \right\} - \frac{t}{2} \quad (25)$$

## VI. CONCLUSIONS

Practical geometries containing thick capacitive obstacles or strips can seldom be solved rigorously, although solutions are frequently possible if zero thickness is assumed. The approximate thickness corrections derived in this paper may be applied to many practical cross sections for which zero-thickness solutions are available or can be obtained. The examples treated demonstrate the simplicity of this method.

## APPENDIX I

### DERIVATION OF $\Delta C_1'(t/s)$

The derivation of (2) and (3) is based on a conformal-mapping analysis by Davy<sup>11</sup> of the double-semi-infinite-plate boundary shown in Fig. 10. He obtained the following formula for the capacitance per unit length between the two plates over the regions  $QBCDP$  and  $Q'B'C'D'P'$  of the boundary:

$$C_1' = -\frac{\epsilon}{\pi} \ln [k \operatorname{sn}^2(u_2, k)], \quad (23)$$

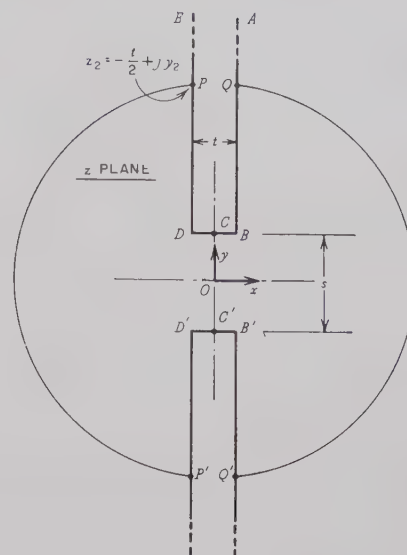


Fig. 10—Coplanar semi-infinite plate boundary in  $z$  plane.

where  $k = 1 - k'^2$  is a real, positive parameter between 0 and 1 that may be solved as a function of  $t/s$  from the following equation:

$$\frac{t}{s} = \frac{K(k') - 2E(k') + k'^2K(k')}{2[2E(k) - k'^2K(k)]} \quad (24)$$

The symbol  $u$  is a complex variable that is a function of  $z = x + jy$ , and  $\operatorname{sn}(u, k)$  is an elliptic function.<sup>11,12</sup> The transformation relating  $z$  and  $u$  is

where  $zn$ ,  $cn$ , and  $dn$  also are elliptic functions.

At point  $P$  between  $D$  and  $E$  on the boundary,  $u$  is negative real, approaching zero as  $y_2$  approaches infinity. The following limiting values are valid for  $u \rightarrow 0$ :

$$\begin{aligned} \operatorname{sn}(u, k) &\rightarrow u & dn(u, k) &\rightarrow 1 \\ cn(u, k) &\rightarrow 1 & zn(u, k) &\rightarrow [1 - E(k)/K(k)]u. \end{aligned} \quad (26)$$

Substituting these in (25) we obtain in the limit  $u \rightarrow 0$ ,

$$y_2 = \frac{s}{2[2E(k) - k'^2K(k)](-u_2)} \quad (27)$$

while (23) reduces to

$$C_1' = \frac{\epsilon}{\pi} \ln \left( \frac{1}{ku_2^2} \right). \quad (28)$$

<sup>11</sup> N. Davy, "The field between equal semi-infinite rectangular electrodes or magnetic pole pieces," *Phil. Mag.*, vol. 35, ser. 7, pp. 819-840; December, 1944.

<sup>12</sup> F. Oberhettinger and W. Magnus, "Anwendung der Elliptischen Funktionen in Physik und Technik," Springer-Verlag, Berlin, Ger., 1949.



Combining (27) and (28) leads (in the limit  $y_2 \rightarrow \infty$ ) to the following:

$$C_1' \left( \frac{t}{s}, \frac{y_2}{s} \right) = \frac{2\epsilon}{\pi} \ln \left[ \frac{2y_2}{s} \cdot \frac{2E(k) - k'^2 K(k)}{\sqrt{k}} \right]. \quad (29)$$

This may be simplified for  $t/s \rightarrow 0$ , since then  $k \rightarrow 1$ ,  $k' \rightarrow 0$ ,  $E(k) \rightarrow 1$ , and  $k'^2 K(k) \rightarrow 0$ . Thus

$$C_1' \left( 0, \frac{y_2}{s} \right) = \frac{2}{\pi} \ln \frac{4y_2}{s}. \quad (30)$$

Now we shall define the capacitance increment  $\Delta C_1'(t/s)$  by

$$\Delta C_1'(t/s) = \lim_{y_2 \rightarrow \infty} \left[ C_1' \left( \frac{t}{s}, \frac{y_2}{s} \right) - C_1' \left( 0, \frac{y_2}{s} \right) \right]. \quad (31)$$

Eq. (2) now follows directly from (29)–(31).

## APPENDIX II

### DERIVATION OF $\Delta C_2'(t/s)$

The derivation of (6) will be outlined to illustrate the method of analysis, but with intermediate steps omitted for brevity.

E. Weber<sup>13</sup> gives the transformation  $z=f(w)$  that relates the  $z$  and  $w$  planes in Fig. 11 such that all the conducting boundaries in the  $z$  plane are transformed into the real axis of the  $w$  plane. The top, bottom, and end of the semi-infinite plate in the  $z$  plane transform into the negative real axis of the  $w$  plane, while the infinite boundary at ground potential in the  $z$  plane transforms into the positive real axis of the  $w$  plane. A minute break in the real axis may be assumed at  $u=0$  to permit the discontinuity in potential.

The electric-field lines above and to the right of the plate in the  $z$  plane become semicircles as  $|z|$  becomes large. Below the plate, the field lines become straight vertical lines as  $x$  recedes to minus infinity. In the  $w$  plane, all electric-field lines are semicircles with center at  $w=0$ .

The capacitance per unit length in the  $w$  plane due to the electric flux contained between field lines of radius  $u_a$  and  $u_b$  is

$$C_{ab}' = \frac{\epsilon}{\pi} \ln \frac{u_b}{u_a}. \quad (32)$$

<sup>13</sup> E. Weber, "Electromagnetic Fields, Vol. 1," John Wiley and Sons, Inc., New York, N. Y., p. 351, (55); 1950. (Note that  $p$  should be related to  $k$  by  $p = 2k^2 - 1 + 2k\sqrt{k^2 - 1}$ .)

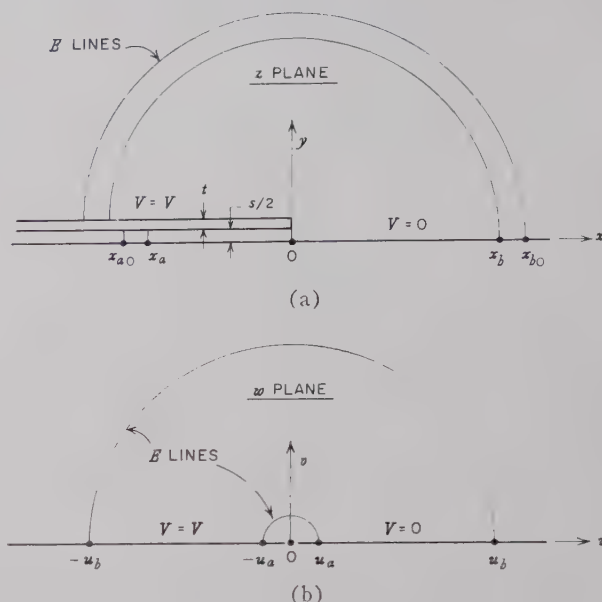


Fig. 11—Transformation between  $z$  and  $w$  planes used in derivation of  $\Delta C_2'(t/s)$ .

Let points  $z_a = x_a + j0$  and  $z_b = x_b + j0$  correspond to  $w_a = u_a + j0$  and  $w_b = u_b + j0$ , respectively. Because of a basic property of conformal transformations, we know that the capacitance per unit length in the  $z$  plane due to the electric flux contained between field lines terminating at  $x_a$  and  $x_b$  is exactly equal to  $C_{ab}'$ . Now, if  $t$  is reduced to zero with  $s$  unchanged, points  $x_a$  and  $x_b$  move to  $x_{a0}$  and  $x_{b0}$ , with the capacitance per unit length still equal to the same value,  $C_{ab}'$ . But in comparing the  $t=0$  and  $t>0$  cases, we must evaluate the capacitances between the same points on the  $x$  axis. Let these points be  $x_{a0}$  and  $x_{b0}$  in both cases. Then for  $t>0$  and  $x$  very large, the electric flux terminating between  $x_b$  and  $x_{b0}$  adds

$$\Delta C_b' = \frac{\epsilon}{\pi} \ln \frac{x_{b0}}{x_b} \quad (33)$$

to  $C_{ab}'$ , while the flux terminating between  $x_a$  and  $x_{a0}$  adds

$$\Delta C_a' = \frac{\epsilon(x_a - x_{a0})}{s/2}. \quad (34)$$

The total difference in capacitance per unit length between the values for  $t>0$  and  $t=0$  is therefore

$$\Delta C_a' + \Delta C_b' = 2\Delta C_2'(t/s), \quad (35)$$

where  $\Delta C_2'(t/s)$  is the thickness-effect increment for the symmetrical parallel-plate configuration. Carrying the above steps out in detail leads to (6).

# Inhomogeneous Quarter-Wave Transformers of Two Sections\*

LEO YOUNG†, SENIOR MEMBER, IRE

**Summary**—An inhomogeneous transformer is defined as one in which the guide wavelength is a function of position; for a homogeneous transformer, the guide wavelength is independent of position.

A previous paper<sup>1</sup> has dealt with inhomogeneous transformers of one section; the existence of an optimum design (which is never homogeneous) was demonstrated. The mathematical tools for inhomogeneous transformers of two or more sections have been presented in another paper.<sup>2</sup> Our purpose here is to apply these results to the solution of the two-section inhomogeneous transformer.

The maximally flat ideal transformer was solved exactly and the design equations verified by subsequent numerical analysis. An approximate procedure to improve the performance over a finite bandwidth (similar to the Tchebycheff response of homogeneous transformers) is also explained.

## INTRODUCTION

THE NEED for inhomogeneous transformers may arise when it is desired to connect two waveguides of different dimensions. Consider, for instance, rectangular waveguide of dimensions  $a \times b$  (Fig. 1). The guide wavelength depends only on the width  $a$ . If two waveguides differing only in their  $b$  dimensions are to be connected, then a homogeneous quarter-wave transformer is possible (but not necessary and probably not optimum<sup>1</sup>). It has been shown on a first-order theory that where a homogeneous transformer is possible, the shortest maximally flat transformer is a quarter-wave transformer.<sup>3</sup> Since a single-section homogeneous quarter-wave transformer can always be improved by an inhomogeneous design,<sup>1</sup> it seems likely that an inhomogeneous quarter-wave transformer of more than one section will likewise improve the best electrical performance when a maximum transformer length is specified. This result, however, remains to be confirmed.

If two waveguides differing in the  $a$  dimension (Fig. 1), as well as possibly the  $b$  dimension, are to be connected, then a homogeneous transformer is not possible at all, and again it may be suspected that an inhomogeneous quarter-wave transformer will yield the best performance when the transformer is to be kept below a

certain length. Such a discussion then provides the motivation for the following investigation.

## MATHEMATICAL SUMMARY

In this section, some definitions and formulas will be summarized which have been proved elsewhere,<sup>1,2</sup> and which are needed to derive the design equations of a two-section quarter-wave transformer. Such a transformer is shown in Fig. 2. The two sections are generally of unequal electrical lengths  $\theta_1$  and  $\theta_2$ , which become equal only at center frequency, when

$$\theta_1 = \theta_2 = \frac{\pi}{2} \quad (1)$$

The four characteristic impedances from input to output are denoted by  $Z_0$ ,  $Z_1$ ,  $Z_2$ , and  $Z_3$ . The log ratios of the three steps are defined<sup>2</sup> by

$$\alpha_i = \frac{1}{2} \ln \frac{Z_i}{Z_{i-1}} \quad (i = 1, 2, 3) \quad (2)$$

The spin matrix exponentials,<sup>2</sup> which will be needed to express transformation matrices, are

$$\begin{aligned} E_1(x) &= \exp(\sigma_1 x) \\ E_2(x) &= \exp(\sigma_2 x) \\ E_3(x) &= \exp(\sigma_3 x) \end{aligned} \quad (3)$$

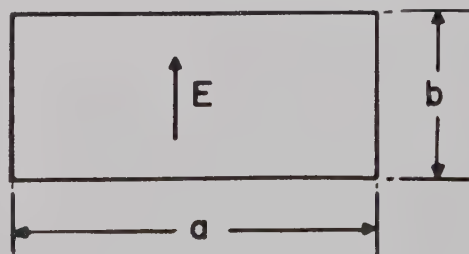


Fig. 1—Waveguide cross section.

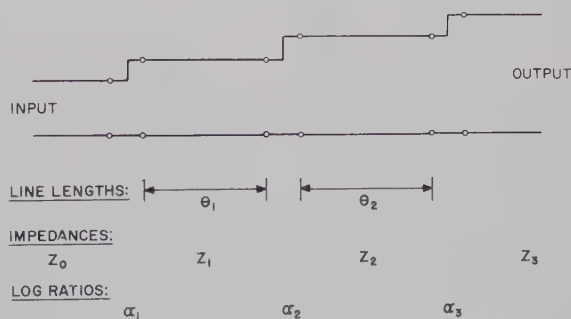


Fig. 2—Two section transformer parameters.

\* Received by the PGMTT, March 2, 1960; revised manuscript received, July 19, 1960. This paper is based on part of a dissertation for the D.Eng. degree at The Johns Hopkins Univ., Baltimore, Md., 1959.

† Stanford Res. Inst., Menlo Park, Calif. Formerly with Electronics Div., Westinghouse Electric Corp., Baltimore 3, Md.

<sup>1</sup> L. Young, "Optimum quarter-wave transformers," 1960 IRE INTERNATIONAL CONVENTION RECORD, pt. 3, pp. 123-129. Also, IRE TRANS. ON MICROWAVE THEORY AND TECHNIQUES, vol. MTT-8, pp. 478-483; September, 1960.

<sup>2</sup> L. Young, "Spin matrix exponentials and transmission matrices," to be published in *Quart. Appl. Math.*

<sup>3</sup> H. J. Riblet, "A general theorem on an optimum stepped impedance transformer," IRE TRANS. ON MICROWAVE THEORY AND TECHNIQUES, vol. MTT-8, pp. 169-170; March, 1960.



where  $\sigma_1$ ,  $\sigma_2$ , and  $\sigma_3$  are the three Pauli spin matrices

$$\begin{aligned}\sigma_1 &= \begin{pmatrix} 0 & 1 \\ 1 & 0 \end{pmatrix} \\ \sigma_2 &= j \begin{pmatrix} 0 & -1 \\ 1 & 0 \end{pmatrix} \\ \sigma_3 &= \begin{pmatrix} 1 & 0 \\ 0 & -1 \end{pmatrix}.\end{aligned}\quad (4)$$

The transfer matrix,<sup>2,4</sup> of each impedance step is then the first spin matrix exponential of the log ratio of that impedance step,

$$E_1(\alpha), \quad (5)$$

and the transfer matrix of each section of line is given by the third spin matrix exponential of that line length times  $\sqrt{-1}$ ,

$$E_3(j\theta). \quad (6)$$

The over-all transfer matrix of the two-section transformer is given in terms of the two line lengths  $\theta_1$ ,  $\theta_2$ , and the three log ratios  $\alpha_1$ ,  $\alpha_2$  and  $\alpha_3$ , by the product

$$\mathbf{T} = E_1(\alpha_1)E_3(j\theta_1)E_1(\alpha_2)E_3(j\theta_2)E_1(\alpha_3). \quad (7)$$

At center frequency

$$E_3(j\theta_i) = E_3\left(j\frac{\pi}{2}\right) = \sigma_3, \quad (8)$$

and in that case (7) reduces to

$$\mathbf{T}_{(\theta_i=\pi/2)} = E_1(\alpha_1 - \alpha_2 + \alpha_3) \quad (9)$$

by means of (8) of Young.<sup>2</sup>

Writing

$$\mathbf{T} = \begin{pmatrix} T_{11} & T_{12} \\ T_{21} & T_{22} \end{pmatrix}, \quad (10)$$

the diagonal part<sup>2</sup> of  $\mathbf{T}$  is then denoted by

$$\text{Di}(\mathbf{T}) = \begin{pmatrix} T_{11} & 0 \\ 0 & T_{22} \end{pmatrix} \quad (11)$$

and the antidiagonal part<sup>2</sup> of  $\mathbf{T}$  by

$$\text{Ag}(\mathbf{T}) = \begin{pmatrix} 0 & T_{12} \\ T_{21} & 0 \end{pmatrix}. \quad (12)$$

The condition for a match is

$$\text{Ag}(\mathbf{T}) = 0. \quad (13)$$

Therefore, for a match at center frequency, (9) yields

$$\alpha_1 - \alpha_2 + \alpha_3 = 0. \quad (14)$$

Denote the free space (or medium) wavelength by  $\lambda$  and define the differential operator<sup>1</sup>

$$D = \lambda \frac{d}{d\lambda}. \quad (15)$$

The condition for perfect match, as well as zero slope of the frequency response curve at center frequency, is given by (13) combined with

$$\text{Ag}(D\mathbf{T}) = 0. \quad (16)$$

From (7) and (8), with (5), (7) and (8) of Young,<sup>2</sup>

$$\begin{aligned}D\mathbf{T} &= \sigma_1 \mathbf{T} D\alpha_1 - \sigma_1 \mathbf{T} D\alpha_2 + \sigma_1 \mathbf{T} D\alpha_3 \\ &\quad + j\sigma_3 E_1(-\alpha_1)\sigma_3 E_1(\alpha_2)\sigma_3 E_1(\alpha_3) D\theta_1 \\ &\quad + j\sigma_3 E_1(-\alpha_1)\sigma_3 E_1(-\alpha_2)\sigma_3 E_1(\alpha_3) D\theta_2\end{aligned} \quad (17)$$

$$\begin{aligned}\therefore D\mathbf{T} &= \sigma_1 \mathbf{T} D(\alpha_1 - \alpha_2 + \alpha_3) \\ &\quad + \text{terms in } I, \sigma_3, \text{ and } \sigma_2.\end{aligned} \quad (18)$$

To satisfy (16), first note that

$$\text{Ag}(I) = \text{Ag}(\sigma_3) \equiv 0. \quad (19)$$

This leaves the coefficients of  $\sigma_1$  and  $\sigma_2$  in (18) to be separately equated to zero. [It will be seen from (2) of Young<sup>2</sup> that  $\sigma_2$  terms are generated in (17).] The coefficient of  $\sigma_1$  is immediately evident from (18). For it to be zero, it is required that

$$D(\alpha_1 - \alpha_2 + \alpha_3) = 0. \quad (20)$$

[This equation does not follow from (14), since the  $\alpha$ 's are not independent of frequency, as they would be in a homogeneous transformer.]

It can be shown<sup>1,5</sup> that

$$D\alpha_i = \frac{1}{2}(t_i^2 - t_{i-1}^2), \quad (21)$$

where

$$t = \frac{\lambda_g}{\lambda}, \quad (22)$$

$\lambda_g$  being the guide wavelength. In general, each section will have its own value  $t_i$ , which is a function of frequency.

It can also be shown<sup>1</sup> that

$$D\theta_i = -t_i^2 \theta_i. \quad (23)$$

From (20) and (21),

$$t_1^2 - t_2^2 = \frac{1}{2}(t_0^2 - t_3^2). \quad (24)$$

The output to input impedance ratio is

$$R = \frac{Z_3}{Z_0}, \quad (25)$$

<sup>4</sup> L. Young, "Analysis of a transmission cavity wavemeter," IRE TRANS. ON MICROWAVE THEORY AND TECHNIQUES, vol. MTT-8, pp. 436-439; July, 1960.

<sup>5</sup> L. Young, "Design of Microwave Stepped Transformers with Applications to Filters," D.Eng. dissertation, The Johns Hopkins Univ., Baltimore, Md.; April, 1959.

and the  $\alpha$ 's are therefore related by

$$\alpha_1 + \alpha_2 + \alpha_3 = \frac{1}{2} \ln R. \quad (26)$$

Eqs. (14) and (24) are necessary but not sufficient conditions for a maximally flat transformer. The other conditions derive from the coefficient of  $\sigma_2$  in (18) being zero. This yields

$$Ag[E_1(-\alpha_1 - \alpha_2 + \alpha_3)D\theta_1 + E_1(-\alpha_1 + \alpha_2 + \alpha_3)D\theta_2] = 0, \quad (27)$$

after using (2) and (8) of Young.<sup>2</sup> Therefore, from (23) and (1), at center frequency

$$t_1^2 \sinh(-\alpha_1 - \alpha_2 + \alpha_3) + t_2^2 \sinh(-\alpha_1 + \alpha_2 + \alpha_3) = 0. \quad (28)$$

Using (14), this reduces to

$$\frac{\sinh 2\alpha_1}{\sinh 2\alpha_3} = \left(\frac{t_2}{t_1}\right)^2. \quad (29)$$

Eqs. (14), (24) and (29), together with the identity (26), are the complete solution of the maximally flat two-section inhomogeneous transformer problem. When the input and output waveguides are specified,  $t_0$ ,  $t_3$ , and  $R$  are known. It is easy to see that there always exists a solution for  $t_1$ ,  $t_2$ ,  $\alpha_1$ ,  $\alpha_2$ , and  $\alpha_3$ . Moreover, this solution is not unique, since there is only one constraining equation (24) on the two parameters  $t_1$  and  $t_2$ .

Each solution will exhibit "maximally flat" behavior in the sense that the reflection coefficient against frequency curve will have a double zero at center frequency. However, some solutions will be flatter than others, and if the one-section transformer may be taken for a guide,<sup>1</sup> we should sometimes expect one solution to be the "flattest maximally flat." We might expect significant differences only as cutoff is approached, or for large values of  $R$ , or both.

Instead of finding the optimum solution, as was done for the single-section transformer, this extra one degree of freedom may serve another useful purpose. In rectangular waveguide, the smaller the H-plane steps, the more nearly ideal is the transformer. The parameters  $t_1$  and  $t_2$  may therefore be selected so as to make none of the individual H-plane steps too large. This will reduce first order corrections which might be necessary for nonideal junctions.<sup>1</sup>

Eqs. (14) and (29) may be expressed in terms of the characteristic impedances  $Z_0$ ,  $Z_1$ ,  $Z_2$ , and  $Z_3$ , instead of the log ratios  $\alpha_1$ ,  $\alpha_2$  and  $\alpha_3$ . They become

$$\left(\frac{Z_2}{Z_1}\right)^2 = R, \quad (30)$$

and

$$\left(\frac{Z_1}{Z_0}\right)^2 = \frac{t_1^2 + t_2^2 R^{1/2}}{t_1^2 + t_2^2 R^{-1/2}}, \quad (31)$$

respectively, where  $R$  is given by (25).

#### NUMERICAL RESULTS FOR MAXIMALLY FLAT TRANSFORMERS

To test the theory, several two-section transformers designed by these equations were analyzed. In each case, a maximally flat response, in the sense of a double zero of the reflection coefficient at center frequency, was obtained.

Let  $a$ ,  $b$  again denote guide width and height, respectively (Fig. 1). The suffix numbering is as shown in Fig. 2.

##### Example 1

Design wavelength,

$$\begin{aligned} \lambda_0 &= 9.1 \text{ inches,} \\ a_0 &= 8 \text{ inches,} & b_0 &= 2 \text{ inches} \\ a_3 &= 5 \text{ inches,} & b_3 &= 3 \text{ inches.} \end{aligned}$$

Selecting either  $a_1$  or  $a_2$  determines the design uniquely. A plot of VSWR against wavelength of five cases is shown in Fig. 3. For example, the dimensions of the transformer with the flattest curve in Fig. 3, are

$$\begin{aligned} a_1 &= 8.000 \text{ inches,} & b_1 &= 3.462 \text{ inches} \\ a_2 &= 5.341 \text{ inches,} & b_2 &= 3.210 \text{ inches.} \end{aligned}$$

There is little change in performance when  $a_1$  is reduced from 8 inches to about 6 or 6.5 inches (Fig. 3). The choice of  $a_1$  will then depend more on practical considerations concerning the departure of the H-plane steps from ideal transformers. The extent to which H-plane steps in rectangular waveguide depart from ideal transformers has already been discussed elsewhere.<sup>1</sup> Unfortunately, each of the transformers in Fig. 3 involves at least one junction which is too far from ideal for a physical model to be expected to follow the ideal transformer theory. An alternative approach would be to use two intermediate transformers of two sections each, and spaced a quarter wave apart, which would reduce the steps to where each transformer is essentially ideal.

##### Example 2

Design wavelength,

$$\begin{aligned} \lambda_0 &= 1.390 \text{ inches} \\ a_0 &= 0.900 \text{ inch,} & b_0 &= 0.400 \text{ inch,} \\ a_1 &= 0.850 \text{ inch,} & b_1 &= 0.429 \text{ inch,} \\ a_2 &= 0.771 \text{ inch,} & b_2 &= 0.417 \text{ inch,} \\ a_3 &= 0.750 \text{ inch,} & b_3 &= 0.400 \text{ inch,} \end{aligned}$$



which conform to the design equations. The VSWR against wavelength response is shown in Fig. 4.

### NUMERICAL RESULTS ON BROAD-BANDING

Usually one is concerned with obtaining the best possible performance over a prescribed frequency band, rather than maximally flat response. For the homogeneous transformer, this problem has been solved analytically,<sup>6,7</sup> and the author has made up numerical tables<sup>8</sup> for this case.

Since no exact solution has been found for the inhomogeneous transformer, it seemed worthwhile to try to modify the exact maximally flat solution, using the homogeneous transformer tables as a guide. This attempt turned out to be very successful.

The central idea was to find from the homogeneous transformer tables how much a homogeneous maximally flat transformer had to be modified to give the required bandwidth. This was treated as an additive "correction" to the log ratios,  $\alpha$ , or as a multiplicative correction to the impedances,  $Z$ . Returning to the inhomogeneous transformer, each guide width  $a$  was kept constant, and the "correction" to each  $Z$  was absorbed in the height  $b$  of the guide.

#### Example 3

Modifying the transformer with the flattest response curve in Fig. 3, Example 1, for a 30 per cent bandwidth (in reciprocal guide wavelength) yields, with  $a_1$  and  $a_2$  kept the same,

$$\begin{aligned} a_0 &= 8.000 \text{ inches}, & b_0 &= 2.000 \text{ inches}, \\ a_1 &= 8.000 \text{ inches}, & b_1 &= 3.512 \text{ inches}, \\ a_2 &= 5.341 \text{ inches}, & b_2 &= 3.167 \text{ inches}, \\ a_3 &= 5.000 \text{ inches}, & b_3 &= 3.000 \text{ inches}. \end{aligned}$$

The VSWR against wavelength response is shown in Fig. 5. The parent maximally flat case (lowest curve in Fig. 3) is reproduced for comparison (broken line).

In this case  $R=4.761$  and from the tables,<sup>8</sup> a 30 per cent bandwidth transformer yields a maximum VSWR of 1.05. This agrees with the computed value for this inhomogeneous transformer (1.051 in Fig. 5). It is harder to predict the frequency bandwidth, because the guides are not uniformly dispersive. Now  $(d\lambda_g/\lambda_g)/(d\lambda/\lambda) = (\lambda_g/\lambda)^2$ . For the 8-inch guide, this quantity is 1.48, and for the 5-inch guide 5.88, both at  $\lambda_0=9.1$  inches. The arithmetic mean is 3.68. We might therefore expect

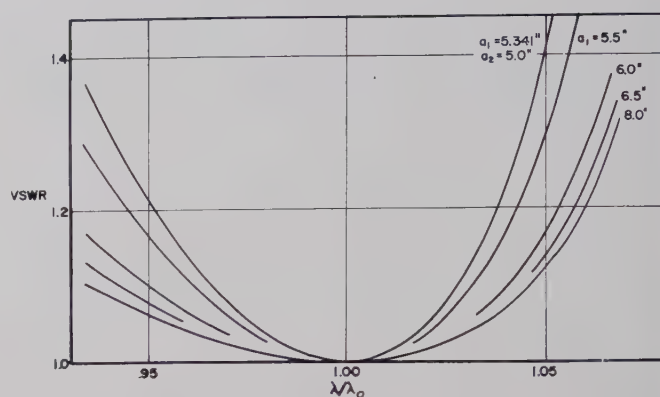


Fig. 3—VSWR vs wavelength of several two-section maximally flat transformers, all from 8×2 inches to 5×3 inches (Example 1).

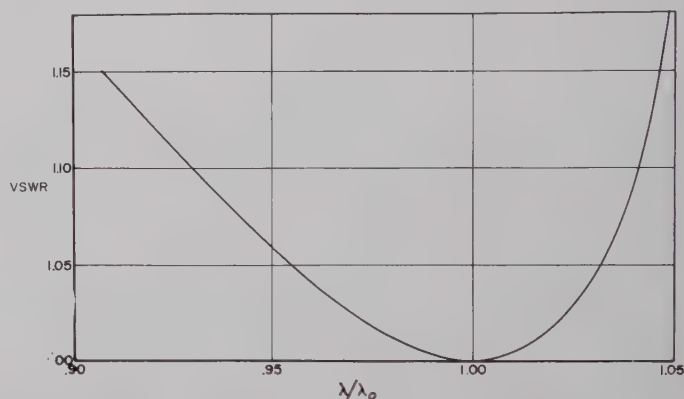


Fig. 4—VSWR vs wavelength of two-section maximally flat transformer 0.9×0.4 inch to 0.75×0.4 inch (Example 2).

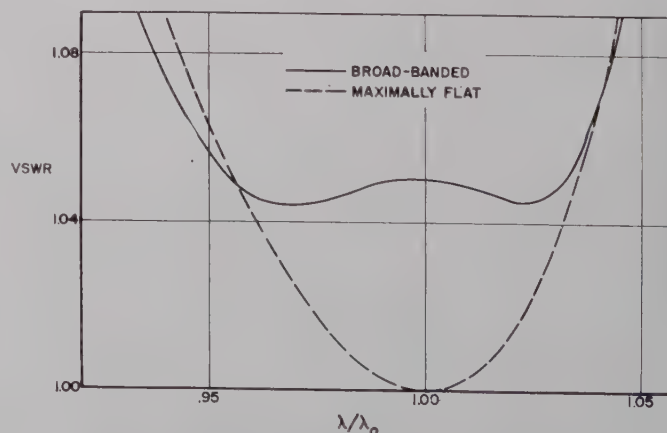


Fig. 5—VSWR vs wavelength of broad-banded and maximally flat transformers (Example 3).

<sup>6</sup> H. J. Riblet, "General synthesis of quarter-wave impedance transformers," IRE TRANS. ON MICROWAVE THEORY AND TECHNIQUES, vol. MTT-5, pp. 36-43; January, 1957.

<sup>7</sup> S. B. Cohn, "Optimum design of stepped transmission-line transformers," IRE TRANS. ON MICROWAVE THEORY AND TECHNIQUES, vol. MTT-3, pp. 16-21; April, 1955.

<sup>8</sup> Leo Young, "Tables for cascaded homogeneous quarter-wave transformers," IRE TRANS. ON MICROWAVE THEORY AND TECHNIQUES, vol. MTT-7, pp. 233-237, April, 1959; and vol. MTT-8, pp. 243-244, March, 1960.

a bandwidth in the order of  $30/3.68 \approx 8$  per cent. The computed bandwidth for maximum  $VSWR = 1.051$  (Fig. 5) is in very close agreement, being 7.8 per cent.

#### Example 4

This is Example 2 modified as described above for a 62 per cent bandwidth (in reciprocal guide wavelength). The  $a$ 's were again kept the same and the new dimensions are:

$$\begin{aligned} a_0 &= 0.900 \text{ inch}, & b_0 &= 0.400 \text{ inch}, \\ a_1 &= 0.850 \text{ inch}, & b_1 &= 0.437 \text{ inch}, \\ a_2 &= 0.771 \text{ inch}, & b_2 &= 0.409 \text{ inch}, \\ a_3 &= 0.750 \text{ inch}, & b_3 &= 0.400 \text{ inch}. \end{aligned}$$

The VSWR against wavelength response is shown in Fig. 6, with the original maximally flat case (Fig. 4) reproduced for comparison (broken line).

In this case  $R = 2.027$ , and for a bandwidth of 62 per cent, the tables give a maximum VSWR of 1.09 for the homogeneous transformer. Our inhomogeneous transformer (Fig. 6) is in close agreement with its maximum VSWR of 1.084. The arithmetic mean value of  $(d\lambda_g/\lambda_g)/(d\lambda/\lambda) = (\lambda_g/\lambda)^2$  is now  $(2.47 + 7.04)/2 = 4.75$ , and therefore we might expect a (frequency) bandwidth in the order of  $62/4.75 = 13$  per cent. The computed bandwidth for maximum  $VSWR = 1.084$  is given by Fig. 6 as 12 per cent, which again is in excellent agreement.

#### DISCUSSION

Inhomogeneous transformers are commonly required when a nonstandard waveguide has to be connected to a component in standard waveguide, or in similar applications calling for small steps. Then a first-order theory is usually adequate. An example of an inhomogeneous transformer of large  $R$  and wide band occurred in connection with the design of a diplexing filter,<sup>9</sup> using waveguide sections which were cut off in the lower frequency band and transmitted, but were nearly cut off in the upper band. A transformer had to be built from an 8-inch  $\times$  2-inch waveguide to a waveguide of 5 inches  $\times$  3 inches, which was approaching cutoff for the upper band of 1250 to 1350 Mc. At that time, no theory was available for inhomogeneous transformers, and a combination  $E$ -plane (homogeneous) transformer and a double linear taper were used. A view of the filter is reproduced in Fig. 7. This filter involves no less than ten transformers, five homogeneous and five inhomogeneous. The inhomogeneous ones were all double linear tapers, but could now be designed systematically as quarter-wave transformers, thereby reducing their length and improving their performance. The measured

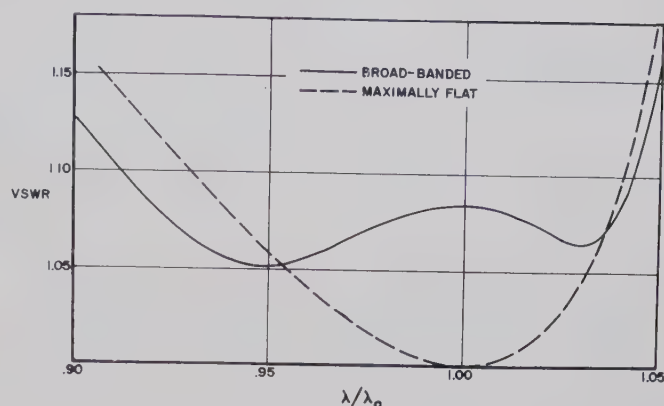


Fig. 6—VSWR vs wavelength of broad-banded and maximally flat transformers (Example 4).

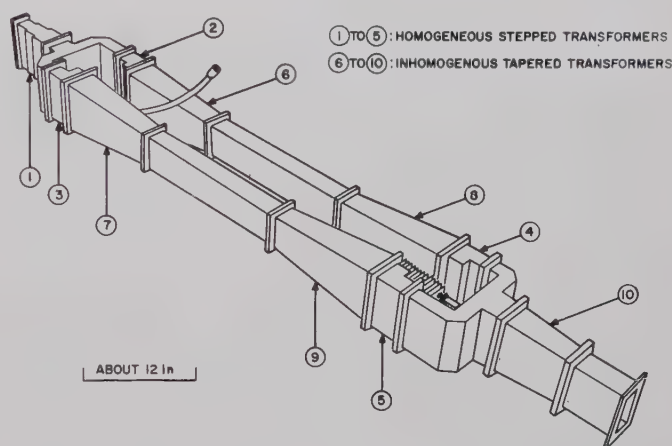


Fig. 7—Waveguide diplexing filter.

performance<sup>9</sup> of a maximum VSWR of 1.22 in a length of over two feet could be greatly improved with only a two-section ideal transformer (Example 1). As already mentioned, the ideal transformer assumption would not be expected to hold for the large steps involved, but a cascade of two transformers, each of two sections and themselves separated by a quarter-wave section (making a total of five sections), should also give substantially improved performance and would still be shorter than the original design. With the smaller steps involved, it would be possible to make first-order corrections for the transformers not being ideal.

#### ACKNOWLEDGMENT

The author owes much to the teaching and encouragement of Dr. W. H. Huggins of The Johns Hopkins University. The help of Dr. Ferdinand Hamburger, Jr. and Dr. C. F. Miller, also of The Johns Hopkins University, is gratefully acknowledged.

W. M. Etchison and A. C. Robertson helped with most of the computations.

This work was made possible by the financial support of the Westinghouse Electric Corporation's B. G. Lamme Graduate Scholarship for 1958–1959.

<sup>9</sup> L. Young and J. Q. Owen, "A high power diplexing filter," IRE TRANS. ON MICROWAVE THEORY AND TECHNIQUES, vol. MTT-7, pp. 384–387; July, 1959.



# Errors in Dielectric Measurements Due to a Sample Insertion Hole in a Cavity\*

A. J. ESTIN†, MEMBER, IRE, AND H. E. BUSSEY†, SENIOR MEMBER, IRE

**Summary**—The measurement of complex permittivities of isotropic media at microwave frequencies is performed with high precision by means of cylindrical cavity resonators. However, a hole in the cavity wall, for inserting the sample causes a frequency pulling of the resonator, which in turn introduces an error in the measured dielectric constant. These effects are measured, and with perturbation theory as a guide, correction factors are developed.

## INTRODUCTION

THE cavity resonator has assumed a prominent role in the microwave determination of dielectric parameters of materials.<sup>1,2</sup> Among the more useful of the resonant modes, particularly at 10 cm and longer wavelengths, are the cylindrical  $TM_{0m0}$  family. One sample geometry conformable to this mode is a concentric post equal in height to that of the cavity. In order to introduce such a sample into the cavity, without removing the lid each time, it is convenient to have a centered hole in one endplate. If the sample is made somewhat longer than the height of the cavity, then this hole will in addition provide concentric alignment. The redistribution of fields due to this hole, however, results in a frequency-pulling, which in turn produces an error in the measured value of the dielectric constant of the material of the post.

The hole causes a departure from the geometrically simple shape of an idealized cavity, and the exact solution becomes exceedingly difficult. Accordingly, a solution is usually attempted in terms of some approximate perturbation or variational method.<sup>3,4</sup> With certain of these mathematical techniques, the limits of error or order of magnitude of error can be predicted.<sup>4</sup> Nevertheless, even with these, and particularly with perturbation methods, an experimental check of the predicted results is of vital importance. This paper provides experimental data of a high quality suitable both for direct empirical use and for experimental verifica-

tion of any theoretical approach to the problem. Furthermore, a perturbation development is presented in this paper, and is intended as a general guide to show the expected functional dependence.

## INSTRUMENTATION

A cavity was fabricated which resonated in the  $TM_{010}$  mode at 509 Mc and reresonated in the  $TM_{020}$  mode at 1168 Mc. This cavity (Fig. 1) was made with an axial hole in one endplate, which in turn opened outward into a tube of the same diameter. Construction was such as to permit either the insertion of various sizes of metal tubular sample guides, or the use of a solid plug

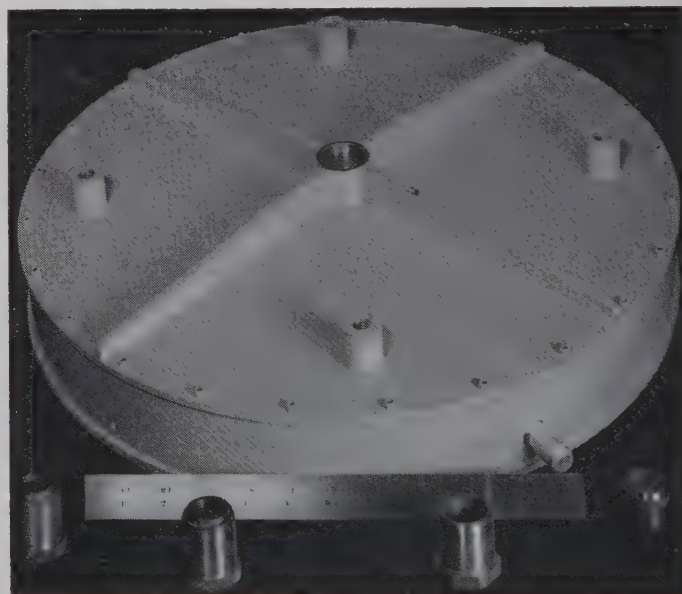


Fig. 1— $TM_{0m0}$ -mode cavity with axial hole. The tubular sample guides and the plug are shown. The diameter is 17.8 inches and the height is 2.25 inches.

to enclose the sample for closely approximating the closed ("perfect") cavity. Samples of various materials were carefully machined to a right cylindrical shape to fit under the solid plug with a clearance of no more than 0.002 inch. Additional cylinders were made from the same materials to permit extension of the dielectric post out through the hole and tube in the cases where the hole pulling was to be examined. Three sizes of tubes were employed in order to examine the dependence of error on hole size. In this way a direct comparison was made between the true resonant frequencies and di-

\* Received by the PGM-TT, May 27, 1960; revised manuscript received, July 22, 1960.

† National Bureau of Standards, Boulder, Colo.

<sup>1</sup> G. Birnbaum and J. Franeau, "Measurement of the dielectric constant and loss of solids and liquids by a cavity perturbation method," *J. Appl. Phys.*, vol. 20, pp. 817-818; August, 1949.

<sup>2</sup> F. Horner, *et al.*, "Resonance methods of dielectric measurement at centimeter wavelengths," *J. IEE*, vol. 93, pt. III, pp. 55-57; January, 1946.

<sup>3</sup> H. A. Bethe and J. Schwinger, "Perturbation Theory of Resonant Cavities," NDRC, Rept. No. D1-117; March, 1943. Their development is for a hole in a thin wall; the problem considered in this paper is where the cavity wall is so thick that the hole is in fact an "infinitely long" tube.

<sup>4</sup> P. M. Morse and H. Feshbach, "Methods of Theoretical Physics," McGraw-Hill Book Co., Inc., New York, N. Y., vol. 2; 1953. (See especially ch. 9.)

electric constant as measured with the plug closing the cavity, and the pulled resonant frequencies and apparent dielectric constant obtained with a hole and long tube extension.

Possible sources of experimental inaccuracy were thoroughly investigated to determine the limitations of the investigation. It was found that the effects of iris pulling, of imperfect closing of the plug, and of cavity and sample asymmetries were negligible. The most serious systematic error present was the tolerance of 0 to -0.002 inch on the length of the post. However, within the tolerances held, this error could not affect the hole pulling results by more than 5 per cent at a dielectric constant of eight, and the effect rapidly diminished for lower values. The remaining limitations, such as imperfect frequency resolution of the cavity and inexact frequency measurements were random and are indicated by the dispersion of the results.

Under the assumption that the  $Q$  of the cavity is high and that the loss tangent of the dielectric material is small, the real part of the dielectric constant is readily determined from a calculation involving only the frequency shift, the physical dimensions of the system, and a knowledge of the mode of oscillation involved. Exact solution of the boundary value problem yields the following for the real part of the dielectric constant,<sup>2</sup>

$$\frac{\sqrt{\kappa} ka J_1(\sqrt{\kappa} ka)}{J_0(\sqrt{\kappa} ka)} = \frac{J_1(ka) - \frac{J_0(kb)}{Y_0(kb)} Y_1(ka)}{J_0(ka) - \frac{J_0(kb)}{Y_0(kb)} Y_0(ka)} ka, \quad (1)$$

where  $a$  is the sample radius,  $b$  is the cavity radius,  $k$  is the wave number of the cavity resonated with sample,  $\kappa$  is the real part of the relative dielectric constant, and  $J_n$  and  $Y_n$  are Bessel functions of order  $n$  of the first and second kinds. A numerical solution of this equation (along with other relations for the imaginary part of the dielectric constant) has been programmed for high-speed digital computation. All experimental results in this paper were calculated by this method.

The measurement at 1100 Mc was made by means of an improved cavity  $Q$ -meter technique.<sup>5</sup> However, the lack of a conveniently swept oscillator source at 500 Mc necessitated a different technique. In brief, a stable, continuously tunable, CW signal generator provided the signal; a portion of this signal was mixed with an arbitrary fixed frequency (usually 500 Mc) derived from the National Bureau of Standards' 100-kc primary standard, and the difference was then directly measured to an accuracy of  $\pm 1$  kc.

## THEORY

The theoretical evaluation of the effect of the hole upon the dielectric constant necessitates two steps. First, an expression is required for the frequency pulling of a cavity by a dielectric-filled hole. Second, this expression must be substituted into one for the error in dielectric constant as a function of errors in resonant frequencies.

The frequency pulling of the hole may be calculated by applying the Adiabatic Invariance Theorem (Boltzmann-Ehrenfest Principle).<sup>6</sup> This states that for an oscillating electromagnetic system, the relative frequency pulling is equal to the relative energy change of the system due to changing its configuration. One thinks of the hole as being created by pulling a disk section of the cavity wall the size of the hole to infinity against the electromagnetic stress on the surface,  $(\epsilon E^2 - \mu H^2)/2$ , while the dielectric column follows, filling the hole like a liquid. The energy change is obtained from the work performed. It will now be assumed, as in perturbation theory, that the frequency changes as a result of inserting the dielectric post and creating the hole are small compared with the empty resonant frequency of the cavity. This is insured by requiring that

$$b^2/m^2 \gg a^2\kappa \quad (2)$$

where  $m$  is the radial index of the  $TM_{0m0}$  mode of the cavity and  $a$  is the radius of the hole, identical to the sample radius. Eq. (2) insures that the wave in the dielectric-filled tube is evanescent, and that the dielectric perturbation is small.

In order to calculate the work of removing the disk to infinity, it is necessary to estimate the fields against which this work is done. The circularly symmetric  $TM$  mode in the cavity insures that only  $TM_{0j}$  modes will be excited in the tube. We shall approximate the electric field in the tube by the  $TM_{01}$  mode only:

$$E = AJ_0\left(\frac{\rho_{01}r}{a}\right)e^{-i\gamma z}, \quad (3)$$

where  $A$  is the amplitude factor,  $z$  is the distance into the tube as measured outward from the interface between the cavity and the tube, and  $\gamma$  is the propagation constant in the tube of the  $TM_{01}$  mode.

For conditions where the tube is far below cutoff,  $\gamma \approx -j\rho_{01}/a$ . We rather arbitrarily equate the integrated square of the unperturbed cavity field at the interface to the integrated square of the tube field at the interface. Thus the amplitude factor in (3) is given by

$$A = E_0/J_1(\rho_{01}) \quad (4)$$

where  $E_0$  is the amplitude factor of the electric field in the cavity.

<sup>5</sup> C. G. Montgomery, "Technique of Microwave Measurements," M.I.T. Rad. Lab. Ser., McGraw-Hill Book Co., Inc., New York, N. Y., vol. 8, sec. 6.29; 1948.

<sup>6</sup> W. R. MacLean, "The resonator action theorem," *Quart. Appl. Math.*, vol. 2, pp. 329-335; January, 1945. See also J. Bernier, "Sur les cavités électromagnétiques," *L'Onde Elect.*, vol. 26, pp. 305-317; August-September, 1946.



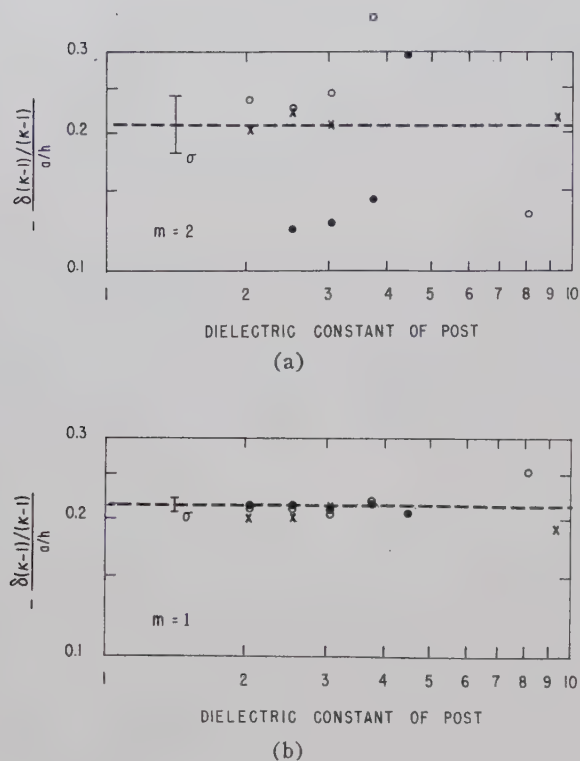
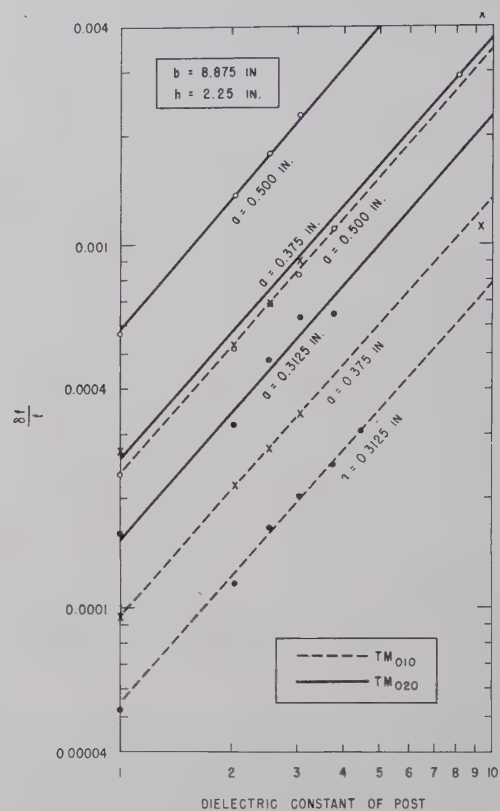
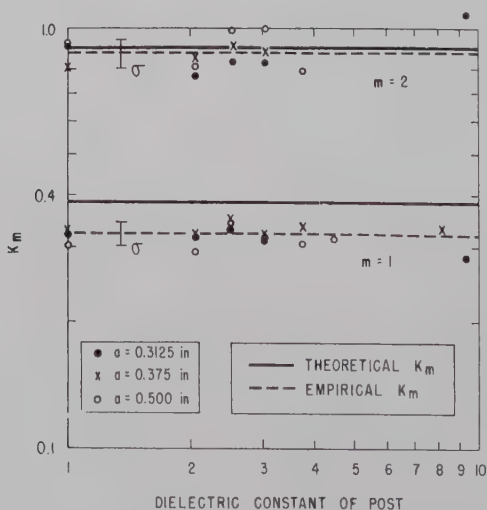


Fig. 2—Experimental points showing that

$$\frac{\delta(\kappa-1)/(\kappa-1)}{a/h}$$

is nearly constant. (a) TM<sub>010</sub> mode at 509 Mc, (b) TM<sub>020</sub> mode at 1168 Mc.

- $a = 0.3125$  inch
- ×  $a = 0.375$  inch
- $a = 0.500$  inch.

Fig. 3—Experimental frequency shift due to an axial hole of radius  $a$ , with various dielectric materials in the cavity and extending out through the hole.Fig. 4—The fit of the experimental data to the constant  $K_m$  defined by (8).

Combining (3) and (4) into the Adiabatic Invariance Theorem, we arrive at an expression for the frequency pulling:

$$\frac{\delta f}{f} = \frac{a^3 \kappa}{4b^2 h \rho_{01} J_1^2(\rho_{0m})} \quad (5)$$

where  $h$  is the height of the cavity and  $\rho_{0m}$  is the  $m$ th root of  $J_0$ , corresponding to the  $TM_{0m0}$  mode in the cavity, and where  $h$  is 2.25 inches.

The first-order perturbation relation for dielectric constant in terms of frequency shift<sup>1,3</sup> is

$$\kappa - 1 = 2J_1^2(\rho_{0m}) \frac{b^2}{a^2} \left( \frac{f_e}{f_s} - 1 \right), \quad (6)$$

where  $f_s$  is the resonant frequency with the sample inserted, and  $f_e$  is the resonant frequency of the empty cavity. The error in  $(\kappa - 1)$  due to errors in  $f_s$  and  $f_e$  is easily obtained from (6), and with the expression for the error in frequency, (5), this error in dielectric constant is finally:

$$\frac{\delta(\kappa - 1)}{\kappa - 1} = - \frac{a}{2\rho_{01}h} \frac{f_e}{f_s} \approx - \frac{1}{2\rho_{01}} \frac{a}{h}. \quad (7)$$

#### RESULTS AND DISCUSSION

A series of direct measurements was made on materials of relative dielectric constants between 1 and 10. Ratios of  $a/h$  up to 0.22 were investigated. In no case did the value of  $m^2 a^2 \kappa / b^2$  exceed 0.11.

If the experimental values of

$$\frac{\delta(\kappa - 1)}{(\kappa - 1)} \bigg/ \frac{a}{h}$$

are plotted as a function of  $\kappa$  (Fig. 2), (7) predicts that the curve will be a constant function with value equal to  $1/2\rho_{01} = 0.208$ , independent of  $\kappa$  and of the radial

index of the mode of oscillation within the  $TM_{0m0}$  family. Experimentally, this value was found to be 0.21 for the  $TM_{010}$  mode and 0.2 for the  $TM_{020}$  mode.

The experimental behavior of the normalized frequency shift was next investigated. If a log-log plot is made of  $\delta f/f$  against  $\kappa$ , as in Fig. 3, a dependence on some power of  $\kappa$  higher than unity is indicated, *i.e.*,  $\kappa^{1+\Delta}$ . From the slope,  $\Delta$  was found to be about 0.16. The approximate theory developed herein accounts only for  $\Delta = 0$ . However, a strict first-order perturbation theory<sup>7</sup> indicates that  $\Delta$  is greater than zero.

Therefore, we shall empirically modify (5) to

$$\frac{\delta f}{f} = K_m \frac{a^3 \kappa^{1+\Delta}}{b^2 h}, \quad (8)$$

where  $\Delta = 0.16$  and  $K_m$  is a function only of  $m$ , the radial mode index. The theory (5) gives  $K_1 = 0.386$  and  $K_2 = 0.897$ . Experimentally the values of  $K_1$  and  $K_2$  are found to be 0.32 and 0.87, respectively. Fig. 4 shows the experimental data that determined  $K_m$ .

It is interesting to note that although the simple equation (5) departs significantly from the experimental equation (8), this causes no discernible error in (7) which depends on (5). [It may be seen that (7) is well supported by the experimental data in Fig. 2.] This has not been investigated in detail, but it would seem that (6) also departs from experiment, and that when (5) and (6) are combined to obtain (7) there is a cancelling of errors.

#### ACKNOWLEDGMENT

The authors are indebted to Dr. George Birnbaum for his early leadership in problems of cavity dielectric measurements, out of which this investigation arose.

<sup>7</sup> D. M. Kerns and H. E. Bussey, manuscript in preparation.

## Correction

D. S. Lerner and H. A. Wheeler, authors of "Measurement of Bandwidth of Microwave Resonator by Phase Shift of Signal Modulation," which appeared on pages 343-345 of the May, 1960, issue of these TRANSACTIONS, have brought the following to the attention of the *Editor*.

Reference [8], which appears on page 345, should read:

F. H. James, "A method for the measurement of high  $Q$ -factors," *Proc. IEE*, vol. 106, pt. B, pp. 489-492; September, 1959. (Recent proposal of the subject method.)



# A Pre-TR Tube for High Mean Power Duplexing\*

D. W. DOWNTON† AND P. D. LOMER‡

**Summary**—A gas discharge tube for transmit-receive switching capable of handling average power levels up to at least 25 kw at 3000 Mc is described. The discharge is excited in the annular space between two concentric silica tubes and recovery time is controlled by the dimensions and gas pressure. In this way, a tube with constant characteristics during life has been achieved. The tube is mounted in a thick resonant iris, and sparking is avoided by using accurately ground silica mounted in a precision-bore hole.

The arc loss of the tube in this form of mount is less than 0.1 db at 5 Mw peak 10 kw average, and the recovery time is about 100  $\mu$ sec to 3 db. The attenuation is about 30 db, and the insertion loss is less than 0.1 db.

Performance of this form of tube is discussed for average power levels of up to 50 kw in a phase-shift duplexer and 25 kw in a balanced duplexer, and the expected performance during life is also considered. Lives in excess of 10,000 hours are deduced from extrapolated data obtained with radioactive krypton in tubes operating at 10 kw average.

## INTRODUCTION

AT power levels below 50-kw peak at 10,000 Mc and 500-kw peak at 3000 Mc, transmit-receive switching can be adequately achieved with conventional narrow-band and broad-band TR cells. Above this level, the complex requirements of the TR cell are difficult to maintain, and Smullin and Montgomery<sup>1</sup> and, more recently, Hawkins<sup>2</sup> have discussed the advantages of performing the switching with a pre-TR cell which is used in conjunction with a TR cell or pulsed attenuator. The first requirement of a pre-TR cell is that it should have a low loss during transmission and reception; that is, its arc loss and insertion loss should be low. Secondly, the recovery time should be adequate. Longer recovery times can be tolerated at very high power levels for long-range radars, since short-range information is normally not required for that application. A recovery time of 100  $\mu$ sec to 3 db was aimed at in this work. The leakage of the device is less important and an attenuation of 30 db is sufficient.

Several forms of pre-TR cells have been developed. The first, described by Smullin and Montgomery,<sup>1</sup> consisted essentially of a quarter wavelength section of waveguide sealed at the ends with low  $Q$  windows and filled with a mixture of argon and water vapor. Detuning of the cell caused by sputtering of metal from the cell body onto the glass window and the rapid clean-up of water vapor were major problems with this type of

device. These problems were avoided by Parker,<sup>3</sup> who used a silica tube containing silica wool and filled with rare gas. In this case, recovery time was controlled by diffusion of ions and electrons to the surface of the silica wool where surface recombination takes place. Sparking was avoided by using accurately ground silica so that good contact was ensured between tube and mount. This type of tube has since been developed for handling powers up to 3 Mw peak, 3 kw average at 3000 Mc. Alternate approaches by Dutt<sup>4</sup> and by Gould, Edwards, and Reingold,<sup>5</sup> relied on the same physical processes for achieving rapid de-ionization of the discharge. The main disadvantages of these developments were associated with the complicated structures used to support the discharge tube. Glass-to-metal seals were an integral part of these structures, so that relatively low melting-point glass had to be used.

The high melting point of silica, coupled with its very low loss, make it the most attractive material for use at very high power levels. However, it has been found that sputtering of the silica wool can occur at 4 kw average with the particular tube described by Parker. This results in more rapid gas clean-up and eventual fusing of the silica wool. The properties of silica wool in reducing recovery time can be achieved in a much more controlled manner by confining the discharge to the annular space between two concentric silica tubes. This approach was first applied by Lomer and O'Brien<sup>6</sup> to a microwave pulsed attenuator but is equally applicable to a pre-TR tube. Thus the advantages of controlling recovery time by diffusion and surface recombination are maintained, and very high power operation is possible from this new type of tube.

## DESCRIPTION OF PRE-TR MOUNT AND TUBE

Fig. 1 shows the complete pre-TR unit. The mount, which was first examined by Speake,<sup>7</sup> contains two tubes and is for use with a short slot hybrid. The two waveguide sections are recessed in the mount. In each section there are two thick resonant slots which are perpendicular to the electric field. The iris size is adjusted for resonance at any given frequency, the length of the iris being given for a range of frequencies in Fig. 2,

\* A. B. Parker, "A new form of X-band pre-TR cell," *Proc. IEE*, vol. 105B, Suppl. No. 10, pp. 488-491; May, 1958.

† Services Electronics Res. Lab., Baldock, Herts., England.

‡ L. D. Smullin and C. G. Montgomery, "Microwave Duplexers," Mass. Inst. Tech. Rad. Lab. Ser., McGraw-Hill Book Co., Inc., New York, N. Y., vol. 14; 1948.

<sup>2</sup> P. O. Hawkins, "Active microwave duplexing systems," *Proc. IEE*, vol. 105B, Suppl. No. 10, pp. 505-507; May, 1958.

<sup>3</sup> G. D. Speake, unpublished work.

\* Received by the PGMTT, October, 1959; revised manuscript received, August 15, 1960.

† Services Electronics Res. Lab., Baldock, Herts., England.

‡ L. D. Smullin and C. G. Montgomery, "Microwave Duplexers," Mass. Inst. Tech. Rad. Lab. Ser., McGraw-Hill Book Co., Inc., New York, N. Y., vol. 14; 1948.

<sup>2</sup> P. O. Hawkins, "Active microwave duplexing systems," *Proc. IEE*, vol. 105B, Suppl. No. 10, pp. 505-507; May, 1958.

<sup>3</sup> G. D. Speake, unpublished work.

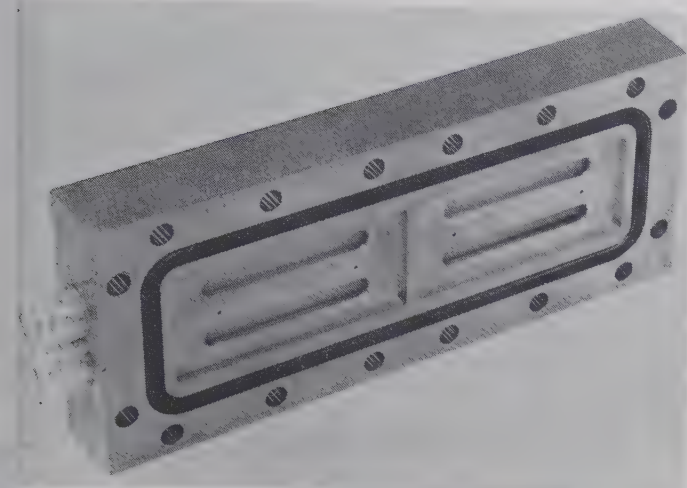


Fig. 1—Pre-TR mount and tubes.

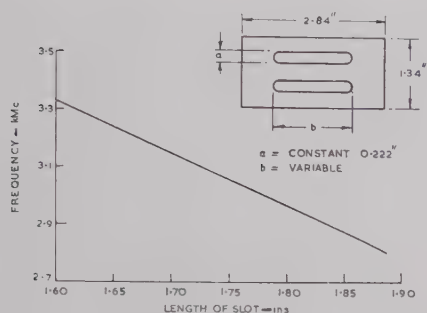


Fig. 2—Resonant frequency as a function of the length of slot.

assuming the height to remain constant. The height of the iris is adjusted to give a large contact area between tube and mount, and this is illustrated in Fig. 3. The loaded  $Q$ -factor of both sections of the mount is 2.3.

The discharge tube consists essentially of a silica envelope containing a rare gas. The length of the discharge is accurately defined by the slots in the mount. The discharge does not extend along the tube since it is not coupled to the field. Thus there is little radiation loss from the ends of the tube and negligible coupling between the adjacent waveguides. The discharge acts as a short circuit in reflecting the power, but there is a leakage between discharge and mount. This leakage is about 30 db down on the incident power. The tubes are heated by the discharge, but there is efficient cooling because of the large contact area between tubes and the mount. A further advantage of this type of mount is the relative ease of construction.

The discharge tube which is shown in Fig. 4 consists of two concentric tubes of silica with an annular gap of 0.030 inch between them. Precision-bore silica tubing, ground externally to a fine tolerance, is used so that reproducible resonant frequencies are achieved. A close fit between tube and mount is ensured by accurate control of the outer dimension. The space between the tubes is filled with krypton at a pressure of 60 mm Hg, and about 10 microcuries of tritium is added to ensure

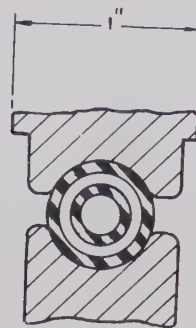


Fig. 3—Cross section of tube in mount.

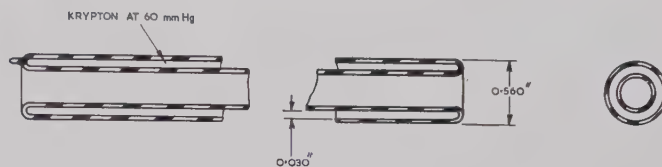


Fig. 4—Pre-TR tube.

immediate ionization on applying the microwave field. Since the inner tube is left open to the atmosphere, the discharge only occurs in the krypton-filled annular space between the outer tube and the insert.

The choice of gas pressure and annular space was based on a series of experiments, the results of which are shown in Figs. 5 through 9. It was apparent from previous work that the recovery time of tubes without inserts decreased with increasing pressure as shown in Fig. 5, so that high pressure of krypton is necessary to achieve short enough recovery times. However, it was found by more detailed examination of these tubes, filled at a pressure of 60 mm Hg, that the recovery time increases alarmingly with the mean power as shown in Fig. 6. This increase in recovery time with mean power indicates that the effective gas density in the discharge region decreases with increasing power level because of the establishment of temperature and hence gas density differentials along the tube. Thus the performance of the tube at high power levels corresponds to a movement along the recovery time/pressure curves to lower pressures.

In tubes with inserts, de-ionization at lower pressures is a function of both recombination and diffusion losses, so that recovery time is fairly constant as a function of pressure. Thus, although the gas density in the working region of the tube decreases as the average power is increased, the recovery time remains fairly constant. In Fig. 7 recovery time at a high average power (10 kw) is given as a function of pressure for tubes containing various sizes of insert. It is apparent that the smallest annular gap should be used, since the recovery time is then least and there is also least variation with pressure. Since recovery time is almost independent of pressure in a tube with a small gap, the choice of pressure must



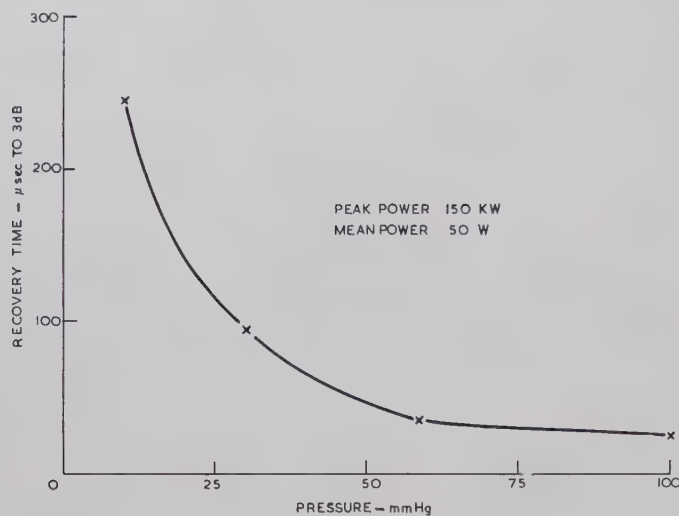


Fig. 5—Recovery time—pressure characteristic for a tube without insert.

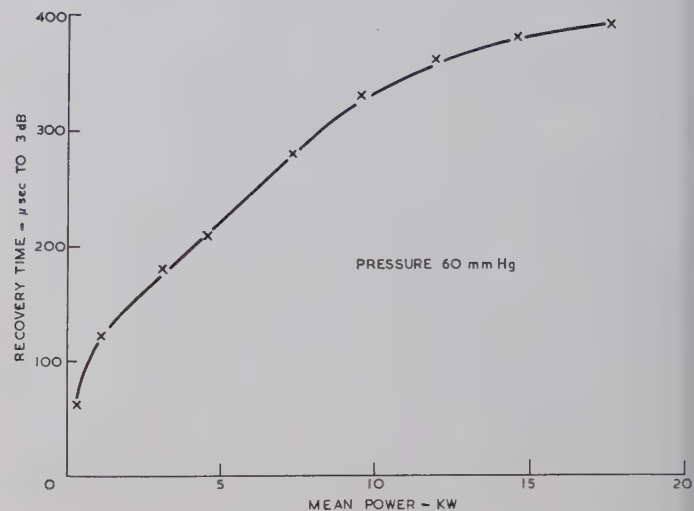


Fig. 6—Recovery time against mean power for a tube without insert.

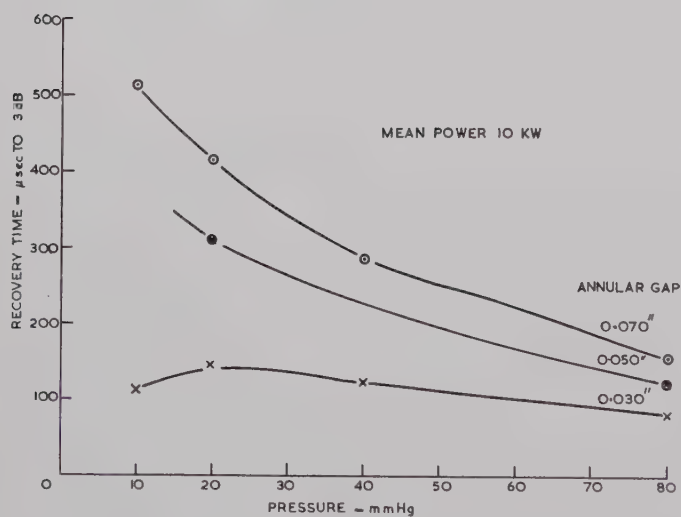


Fig. 7—Recovery time—pressure characteristic for three sizes of annular gap.

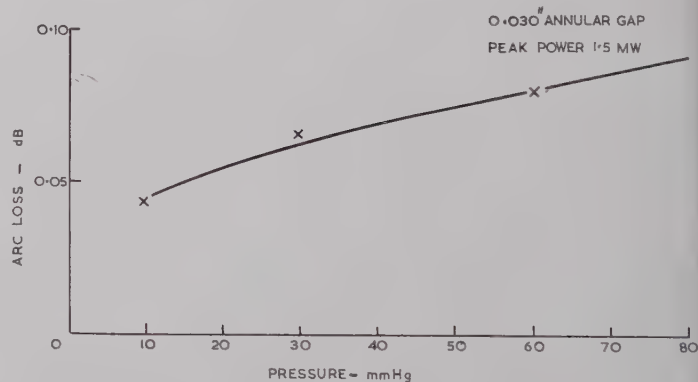


Fig. 8—Arc loss as a function of pressure.

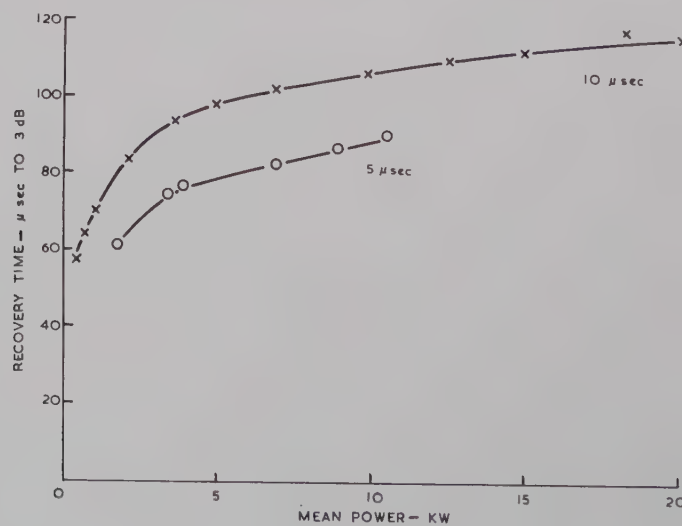


Fig. 9—Recovery time as a function of mean power at two different pulse lengths.

be governed by other factors. Although it is desirable to use as high a pressure as possible, because end of life is determined by clean-up of gas, the arc loss increases with pressure so that a compromise must be made between these considerations. The variation of arc loss with pressure at 1.5 Mw is given in Fig. 8, and it reaches a value of nearly 0.1 db at 60 mm Hg. This will represent a dissipation of nearly 100 w in each tube when working at 10-Mw peak, 20-kw average, so that any increase in pressure above 60 mm Hg is unwarranted. Should life tests prove that the rate of clean-up is small and hence the life very long, it may be desirable to reduce the pressure.

Braden<sup>8</sup> in an independent investigation has achieved much shorter recovery times than those quoted above by reducing the annular gap and also the gas pressure and hence increasing the electron diffusion losses. Braden proposes a tube filled with argon at a pressure of 4 mm Hg. Although the initial performance of such a tube will be good, its life at very high power levels will be very short because of gas clean-up. For example, tubes filled with krypton at a pressure of 10 mm Hg have failed after 400 hours operation at 5 Mw peak, 10 kw average, in a balanced duplexer. This life problem may to some extent be avoided if a gas reservoir can be tolerated.

#### PERFORMANCE OF THE PRE-TR TUBES AND MOUNT

The performance of the pre-TR tubes containing krypton at a pressure of 60 mm Hg and having an annular gap of 0.030 inch was measured in a mount which was attached to a short-slot hybrid<sup>9</sup> as in a balanced duplexer. Data obtained at 5 Mw, 10 kw is quoted in Table I.

TABLE I

Power Level	5 Mw peak, 10 kw average, 10 $\mu$ sec pulse
Arc Loss	0.05 db
Recovery Time	95 $\mu$ sec to 6 db 110 $\mu$ sec to 3 db 135 $\mu$ sec to 1 db
Leakage Power	5 kw peak, 10 w average ( <i>i.e.</i> , 30 db attenuation)
Position of Short	0.06 cm from the face of the tube
Discharge Initiation Power	<10 kw.

The only properties which are influenced appreciably by the power level are arc loss and recovery time. The recovery time, which is shown in Fig. 9, is virtually independent of average power from 5 kw up to 20 kw, as expected from the recovery time/pressure curves,

but does change with pulse length. All high power measurements of recovery time were made using a power multiplication circuit.<sup>10</sup> This circuit is a waveguide loop connected to a power source by a directional coupler. The loop acts as a resonator with an amplification dependent on the  $Q$ -factor of the circuit. The electrical length of the loop is changed by a high-power phase shifter consisting of a 3-db coupler followed by two waveguide plungers, designed to obviate sparking. Any small mismatches in the circuit are cancelled by the use of four dielectric plungers.

Arc loss measurements at low powers were made by replacing the tubes with metal rods and noting the change in power level. This technique is not of high absolute accuracy, and additional measurements were made using a power multiplication circuit, developed for life-testing four pairs of tubes. The gain of these circuits depends on insertion losses, so that an average value of the arc loss can be obtained with greater accuracy by replacing the tubes with metal rods. These experiments resulted in estimates for the arc loss of one pair of tubes of 0.05 db at 5 Mw peak, 10 kw average.

#### PERFORMANCE DURING LIFE

The only significant change in the tube anticipated during operation is that of gas pressure. This is expected to decrease steadily as gas is absorbed on the walls of the tube. Some early measurements at  $2\frac{1}{2}$  Mw peak, 3 kw average, with tubes containing silica wool and radioactive krypton<sup>11</sup> indicated clean-up at a rate of approximately  $10^{-4}$  cc at STP/hour. This high rate of clean-up was probably due to sputtering of silica from the silica wool and consequent trapping of gas, and indeed further measurements on similar tubes without silica wool yielded clean-up rates of only  $10^{-5}$  cc at STP/hour. More recently, tests on the new tubes described here have been extended to 5 Mw peak, 10 kw average, using the same radioactive techniques for estimating pressure changes and again low clean-up rates of about  $2 \times 10^{-5}$  cc at STP/hour have been recorded despite the increase in average power. These tests have now been extended with eight tubes being simultaneously tested in the power multiplication circuit shown in Fig. 10. Tubes filled at a pressure of 60 mm Hg have been on test at 5 Mw peak, 10 kw average, for 4100 hours with a gas clean-up of about 8 per cent. Hence, a life well in excess of 10,000 hours should be obtained.

There has been little change in performance during life as expected from the small variation of arc loss and recovery time with pressure. Recovery time has slightly increased and arc loss decreased.

<sup>8</sup> R. S. Braden, "A new concept in microwave gas switching elements," IRE TRANS. ON ELECTRON DEVICES, vol. ED-7, pp. 54-59; January, 1960.

<sup>9</sup> H. J. Riblet, "The short-slot hybrid junction," PROC. IRE, vol. 40, pp. 180-184; February, 1952.

<sup>10</sup> L. Milosevic and R. Vautey, "The travelling wave resonator and its application to high power microwave testing," *Onde Elect.*, vol. 37, pp. 290-294; March, 1957.

<sup>11</sup> D. W. Downton, "Measurement of clean-up in gas discharge tubes using radioactive krypton," *Proc. IEE*, vol. 105B, Suppl. No. 10, pp. 485-487; May, 1958.



# APPLICATION TO BALANCED AND PHASE-SHIFT DUPLEXERS

## Balanced Duplexer

The performance of the tubes in a balanced duplexer has been examined using a circuit of two short-slot hybrids<sup>9</sup> and the pre-TR mount as illustrated in Fig. 11. The low-level performance is given in Fig. 12, showing that the duplexer has a bandwidth of about 14 per cent. The bandwidth is limited by that of the hybrid junction in this particular duplexer, but the most important limitation is caused by the rather high  $Q$ -factor of the mount. Reflections from the mount during reception constitute a loss in power which becomes significant at frequencies more than a few per cent from the center

frequency. This is illustrated in Fig. 12; the insertion loss of the duplexer increases rapidly at 2700 Mc and 3100 Mc, and this is entirely caused by reflection losses from the mount.

The performance at high power levels has already been described in detail. The only feature peculiar to the balanced duplexer is that further receiver isolation is provided by the second hybrid so that a total isolation of 50 db exists between transmitter and receiver. Thus for a duplexer operating at 10 Mw peak, 20 kw average, the power incident on the receiver arm is 100 w peak, 200 mw average. A standard TR cell is needed to protect the mixer crystal from this power level. Alternatively, if a traveling-wave tube is used in the receiver system, it may be necessary to include a simple gas discharge tube for protection.

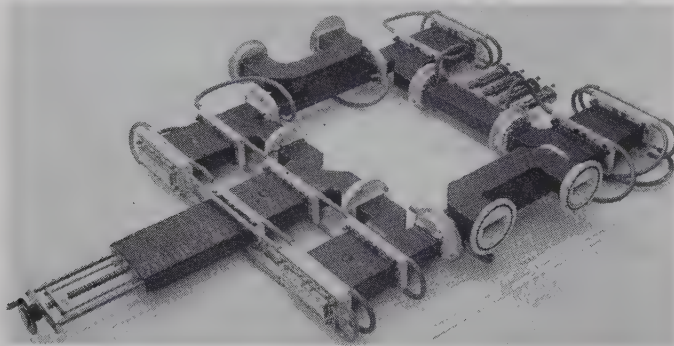


Fig. 10—Power multiplication circuit used for life-testing four pairs of tubes.

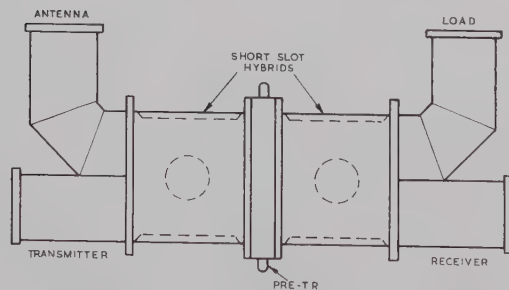


Fig. 11—Balanced duplexer (using short-slot hybrids).

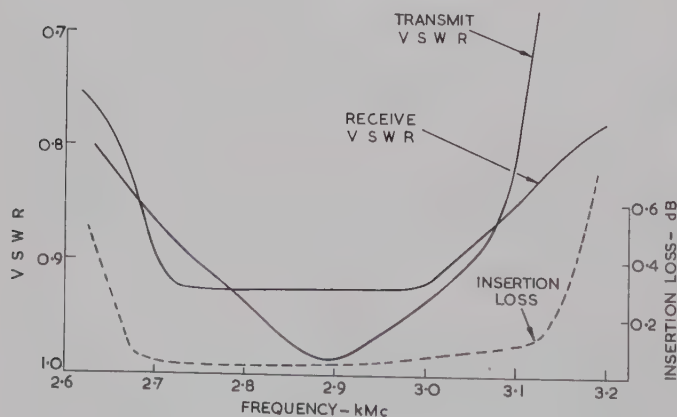


Fig. 12—Balanced duplexer characteristics.

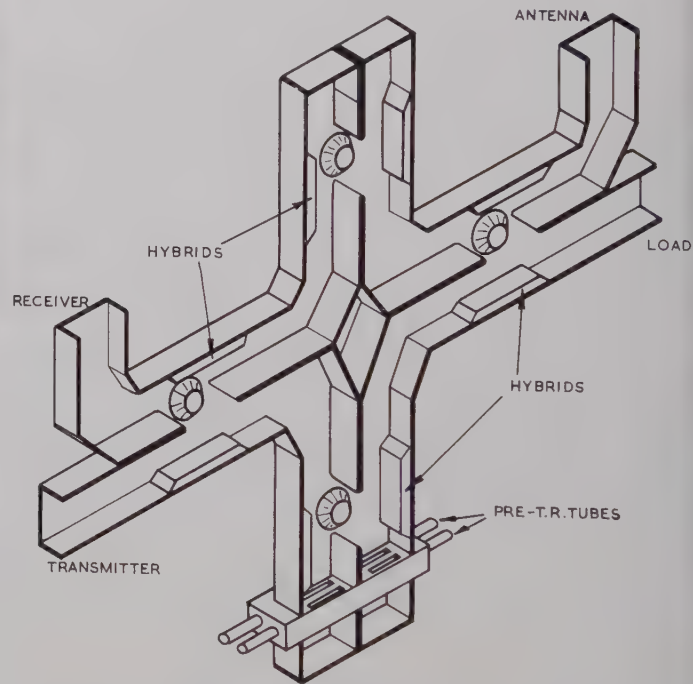


Fig. 13—Phase-shift duplexer (using short-slot hybrids).

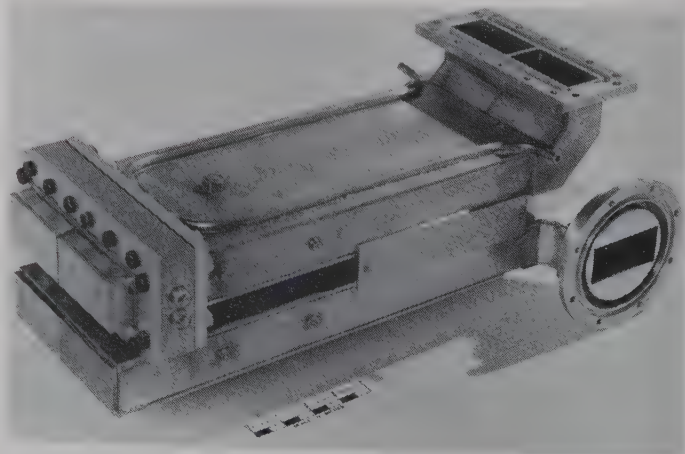


Fig. 14—Phase-shift duplexer using short-slot and binomial-slot hybrids.

### *Phase-Shift Duplexer*

The circuits examined for a phase-shift duplexer have been described by Lomer and O'Brien<sup>12</sup> and are shown in Figs. 13 and 14. The low-level performance of this form of duplexer depends again on the performance of the hybrid junctions and is very similar to that of the balanced duplexer. The insertion loss is about 0.25 db over the frequency band. The high-level performance is favorable since only half the power is incident on the tubes and, in fact, this type of duplexer will handle twice the power of the corresponding balanced duplexer. Since the tubes have been tested in a balanced duplexer at 10 Mw peak, 25 kw average, this corresponds to a phase-shift duplexer operating at 20 Mw peak, 50 kw average.

### POWER HANDLING LIMITATIONS

The majority of the tests on the tube were made with balanced duplexers operating at 10 Mw peak, 25 kw average, or less. Any extensions of peak power levels require pressurization in excess of 45 pounds per square inch, and would require much stronger waveguide components. On the other hand, extensions of average power with relatively low peak power is feasible, provided water cooling is provided.

No serious extension in average power could be examined in these experiments however, since the source of power was a 3 Mw peak, 3 kw average magnetron operating into a power multiplication cir-

cuit in which peak and average power levels are both increased. Thus, a serious study of average power handling above 25 kw requires a source of high average power with low peak power.

There have been no indications of an approaching limit to average power handling. For example, the temperature of the inner wall of the inserts has only reached 280°C at 20 kw average. This temperature could be considerably reduced by air cooling, and undoubtedly the silica tubes could be used at much higher temperatures without affecting the performance. Thus, from this point of view, much higher power levels could be handled.

### CONCLUSIONS

A pre-TR tube capable of handling up to 10 Mw peak, 25 kw average, in a balanced duplexer, and 20 Mw peak, 50 kw average in a phase-shift duplexer, has been developed for 3000 Mc. The properties of the tube are controlled by its dimensions and do not vary greatly with gas pressure. Thus, the performance of the tubes will not change, appreciably during life. Life tests at 5 Mw peak, 10 kw average, have been in progress for 4100 hours and have provided data from which lives in excess of 10,000 hours are obtained by extrapolation.

### ACKNOWLEDGMENT

The tubes were life tested at the Services Valve Test Laboratory under the direction of G. J. Halford, whose constant cooperation is gratefully acknowledged.

The paper is published by permission of the Admiralty.

---

<sup>12</sup> P. D. Lomer and R. M. O'Brien, "A new form of high-power microwave duplexer," IRE TRANS. ON MICROWAVE THEORY AND TECHNIQUES, vol. MTT-6, pp. 264-267; July, 1958.



# Circular Electric Mode Directional Coupler\*

BUNICHI OGUCHI†, SENIOR MEMBER, IRE

**Summary**—This paper describes a circular electric mode directional coupler, composed of two coaxial bifurcations in circular waveguide. The coupling coefficient of the directional coupler depends on the separation between the two bifurcations, and a hybrid junction for the circular electric mode may be obtained at the proper separation. The analysis is carried out in terms of scattering matrix elements characterizing each coaxial bifurcation.

The scattering matrix elements were experimentally determined via the Weissfloch tangent method at 5000-Mc band. For convenience, experiments were carried out in sectoral waveguide instead of circular waveguide. Measured characteristics at 9000-Mc band are in good agreement with values determined by circuit calculations employing parameters of the coaxial bifurcation measured at 5000-Mc band. For the case of a hybrid junction, wide-band matching has been accomplished and verified experimentally. Applications of this directional coupler are outlined.

## INTRODUCTION

THE circular electric mode has received a great deal of attention, especially in connection with millimeter waves, because of its low-loss transmission characteristics. There have been many publications about  $TE_{01}$  mode transducers which transfer power from the dominant mode in rectangular waveguide to the  $TE_{01}$  mode in circular waveguide. With the exception of the mode transducer, however, there has been little information about circular electric mode components whose design is complicated by the fact that even a small discontinuity in circular waveguide easily gives rise to spurious modes.

This paper describes a symmetrical directional coupler involving the circular electric mode, composed essentially of two coaxial bifurcations in a circular waveguide. (Cf. Figs. 1 and 4.) Consider a circular waveguide in which the  $TE_{01}$  and  $TE_{02}$  modes can propagate, but the  $TE_{03}$  mode is beyond cutoff. A coaxial bifurcation is located at the special surface on which  $E_\phi = 0$  for the  $TE_{02}$  mode. In this bifurcated region, only one of the two circular electric modes can propagate in the small circular waveguide and the coaxial waveguide, respectively.<sup>1</sup>

Suppose two separate coaxial bifurcations to be located in a circular waveguide. If a circular electric

mode is incident into the circular waveguide region from one of the bifurcated regions, the  $TE_{01}$  and  $TE_{02}$  modes are simultaneously excited in the circular waveguide region. These  $TE_{01}$  and  $TE_{02}$  modes have differing phase velocities. Because of this difference, the phase relation between the two modes changes along the waveguide, and the two modes interfere with one another. In the second bifurcated region, they excite respective circular electric modes whose amplitudes are changed by the phase difference between the  $TE_{01}$  and  $TE_{02}$  modes at the second bifurcation. Therefore, a wide variety of transfer coefficients between the two four-ports may be obtained by changing the separation between the bifurcations. In particular, a hybrid junction may be obtained at the proper separation. These characteristics are very similar to those of the short-slot hybrid junction in rectangular waveguide.<sup>2</sup>

The circuit parameter of a bifurcation in a circular waveguide was determined, experimentally, through the Weissfloch tangent method at 5000-Mc band. A directional coupler has been constructed at 9000-Mc band in sectoral waveguide, instead of circular waveguide, for the sake of experimental convenience. Measured characteristics of this directional coupler are in good agreement with values determined by circuit calculations employing parameters of the coaxial bifurcation measured at 5000-Mc band. For a hybrid junction, wide-band matching has been accomplished and verified experimentally.

Hybrid junctions may be employed to realize a branching filter for a  $TE_{01}$  mode transmission system. A  $TE_{01}$ - $TE_{02}$  mode transducer in a circular waveguide may be constructed by utilizing this directional coupler.

## COAXIAL BIFURCATION OF A CIRCULAR ELECTRIC MODE WAVEGUIDE

### A. General Characteristics

We shall consider characteristics of a coaxial bifurcation of a circular waveguide by a circular cylindrical partition of zero thickness. In region I, shown in Fig. 1, a cylinder partitions a circular waveguide into a small circular waveguide and a coaxial waveguide. Each waveguide has its own circular electric mode. The ratio of the diameter  $D_1$  of the cylindrical partition to the diameter  $D_2$  of the circular waveguide is chosen such that  $D_1/D_2 = x_{01}'/x_{02}'$ , where  $x_{01}'$  and  $x_{02}'$  are, respectively, the first and second nonzero roots of

\* Received by the PGMTT, May 20, 1960; revised manuscript received, August 22, 1960. The work described in this report was performed at the Microwave Res. Inst., Polytechnic Institute of Brooklyn, Brooklyn, N. Y., under Contract No. DA-36-039 sc-78001 sponsored by the USASRD.

† Electrical Communication Lab., Nippon Telegraph and Telephone Public Corp., Tokyo, Japan.

<sup>1</sup> Inherent in the construction of this junction is circular symmetry; thus, the  $TE_{01}$  mode excites only  $TE_{0n}$  mode ( $n=1, 2, \dots$ ), and the junction may be represented by a four-port circuit. But this picture changes if another mode is employed in this junction.

A similar consideration can be employed for the  $TM_{0n}$  modes in such a bifurcated waveguide, but here we will only deal with the  $TE_{0n}$  modes.

<sup>2</sup> H. J. Riblet, "The short-slot hybrid junction," *Proc. IRE*, vol. 40, pp. 180-184; February, 1952.

$J_0'(x)=0$ . This special location of the cylindrical partition coincides with a surface  $E_\phi=0$  for the  $TE_{02}$  mode in the circular waveguide. Region II is a circular waveguide in which both the  $TE_{01}$  and  $TE_{02}$  modes can propagate, and the  $TE_{03}$  mode is beyond cutoff.

Suppose the  $TE_{02}$  mode to be incident from the circular waveguide on the left in Fig. 1. This mode can propagate towards the right in region I without any disturbance by the partition because of the special choice of the diameter of the cylindrical partition. The incident power is divided between the lowest cutoff circular electric mode in the smaller circular waveguide, and the lowest cutoff coaxial circular electric mode in the coaxial waveguide in region I. This power ratio is easily calculated from the field distribution of the circular  $TE_{02}$  mode. On the other hand, if the  $TE_{01}$  mode is incident from the left, a small amount of power is reflected from the end of the partition; the remainder is divided between the two modes mentioned above. Even in this case, no other mode is generated far from the edge of the bifurcation except these three modes, because the whole construction is circularly symmetric. The reflected power remains only in the same circular  $TE_{01}$  mode, and no  $TE_{02}$  mode is generated in region II. The latter is easily seen to follow from reciprocity and the fact that the incident  $TE_{02}$  mode suffers no reflection.

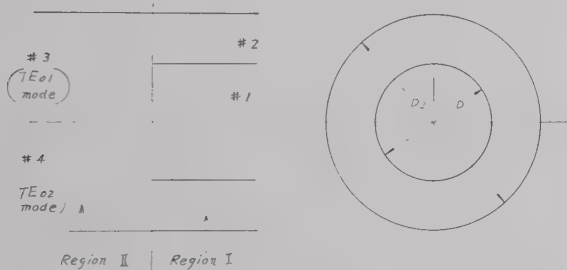


Fig. 1—Coaxial bifurcation of a circular waveguide.

Let us express these relations more clearly by using scattering matrix notation. We label the  $TE_{01}$  mode port of the small circular waveguide on the right port no. 1, the right coaxial mode port no. 2, the large circular  $TE_{01}$  mode port on the left no. 3, and the circular  $TE_{02}$  mode port on the left no. 4, as shown in Fig. 1. All metallic walls are assumed to be perfectly conducting. The important points are that, as demonstrated in the preceding paragraph,  $s_{34}=s_{44}=0$ , where  $s_{ij}$  are the scattering matrix elements. Because of this fact and the unitary condition on the scattering matrix, all magnitudes of the scattering coefficients may be expressed rigorously in terms of the two parameters  $|s_{14}/s_{24}|=k$  and  $|s_{33}|=r$ , where  $k$  is an amplitude ratio of transmission coefficients of the  $TE_{02}$  mode between two coaxial waveguides, and  $r$  is a magnitude of a reflection coefficient of the  $TE_{01}$  mode in a large circular

waveguide. The expressions are as follows:

$$\begin{aligned} |s_{11}| &= \frac{r}{1+k^2}, & |s_{12}| &= \frac{kr}{1+k^2}, & |s_{13}| &= \frac{\sqrt{1-r^2}}{\sqrt{1+k^2}}, \\ |s_{14}| &= \frac{k}{\sqrt{1+k^2}}, & |s_{22}| &= \frac{k^2r}{1+k^2}, & |s_{23}| &= \frac{k\sqrt{1-r^2}}{\sqrt{1+k^2}}, \\ |s_{24}| &= \frac{1}{\sqrt{1+k^2}}, & |s_{33}| &= r, & |s_{34}| &= |s_{44}| = 0. \end{aligned} \quad (1)$$

Also, we may get the following relations among the phasors of the scattering coefficients by the same considerations. Denote the phase angle of  $s_{ij}$  by  $\phi_{ij}$ , then

$$\begin{aligned} \phi_{11} &= \phi_{22} = \phi_{12} \pm 2m\pi, \\ \phi_{13} &= \phi_{23}, \\ \phi_{14} &= \phi_{24} \pm \pi, \text{ and} \\ \phi_{11} + \phi_{33} &= 2\phi_{13} \pm (2m' + 1)\pi, \end{aligned} \quad (2)$$

where  $m$  and  $m'$  are integers.

The value of  $k$ , computed from the field configuration of the  $TE_{02}$  mode, is 1.077. Also, the value of  $\phi_{14}$  is easily determined because no field disturbance of the  $TE_{02}$  mode occurs at the end of the bifurcation. Upon choosing the boundary plane between regions I and II as the reference plane for all ports,  $\phi_{14}$  becomes 0. Therefore, if we could obtain the values of  $r$ ,  $\phi_{33}$  and  $\phi_{13}$  by some means, the whole scattering matrix characterizing this bifurcation would be determined by (1) and (2).

### B. Measured Parameters

As indicated in the previous section, the problem of obtaining the scattering matrix of the bifurcation is reduced to the problem of getting the values of  $r$ ,  $\phi_{33}$  and  $\phi_{13}$ . We have decided to measure these values experimentally. The Weissfloch tangent method for the  $TE_{01}$  mode has been employed for the analysis of a resonance type measurement. The measurements have been carried out in a circular waveguide of 5.758 inches ID at 5000-Mc band of frequencies. A conducting cylindrical partition of 3.145-inch mean diameter and 0.005-inch thickness is supported concentrically inside the circular waveguide by a polyfoam annulus of 1-inch length. A polyfoam pill box of the same length is inserted in a corresponding position inside the cylindrical partition, in order to keep the same phase constant in both the inside and outside regions of the partition cylinder. The circular waveguide is closed at both ends by movable plungers to form a resonant cavity, as shown in Fig. 2.

The cavity is equipped with exciting and detecting magnetic probes. A mode absorbing filter for  $TE_{0n}$  mode composed of polyfoam and radial resistive cards is used to eliminate effects of the spurious modes. In the frequency range of interest many spurious resonances may occur, since the operating frequency is so high that the  $TE_{02}$  mode can also propagate.



The usual Weissfloch tangent method may be applied to the measurement of one discontinuity. In our case, however, as shown in Fig. 2, the discontinuity of interest for the  $TE_{01}$  mode occurs twice, at both ends of the bifurcated region consisting of circular and coaxial waveguides, isolated from each other. Although different amplitudes of respective modes are excited in both waveguides by the incident  $TE_{01}$  mode, these two waves suffer the same amount of phase shift at the end of the bifurcation, as shown in (2), and have the same phase velocity in the respective waveguides; moreover, the  $TE_{01}$  mode does not couple to the  $TE_{02}$  mode at the discontinuities, located at both ends of the bifurcated region. Thus, these two waves may be considered as one normal mode in the two waveguides, and for the purpose of determining the three parameters,  $r$ ,  $\phi_{33}$ , and  $\phi_{13}$ , the bifurcated region may be represented by one equivalent line connected between the discontinuities. Then, the Weissfloch tangent method gives us the characteristics of the whole circuit, comprising the two symmetrically placed discontinuities and a length of waveguide. Since this circuit has a symmetrical character, with respect to the central plane of this region, these over-all characteristics may yield only two independent parameters.

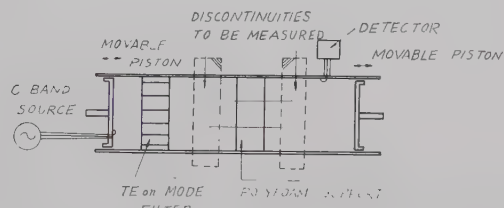


Fig. 2—Measuring cavity.

It is necessary, however, to have three independent parameters in order to determine the three parameters,  $r$ ,  $\phi_{33}$ , and  $\phi_{13}$ . Some further measurement is required. If we measure the circuit again, changing only the length of the bifurcated region, we again obtain two parameters. Then, we may determine the desired circuit parameters from the four values and the known changed length of the bifurcated region. Actually, we have employed three cylindrical partitions of different lengths, nominally 2 inches,  $2\frac{1}{2}$  inches, and 3 inches. (Actual lengths are 2.032 inches, 2.513 inches, and 3.044 inches, respectively.)

The equations relating the desired parameters of the bifurcation to these measured parameters may be conveniently determined by expressing every portion of the circuit in the form of a scattering transfer matrix, because the bifurcated region may be expressed by one line for this purpose, as mentioned before.

Even though polyfoam has a dielectric constant similar to that of air, it is better to treat it as a distinct portion, and thereby compensate for any effect caused by polyfoam. We have measured the dielectric con-

stant of polyfoam by the Weissfloch tangent method in the same circular waveguide for the  $TE_{02}$  mode. This constant has been 1.027, which has been employed to compensate for the polyfoam effect.

We have measured the various coaxial bifurcations with different lengths by the above method at four different frequencies within 5000-Mc band. The scattering transfer matrix elements of the bifurcation may be calculated from the measured values by compensating for the polyfoam effect. In this calculation, each element is expressed in a form  $T_{ij} = T_{ij0} + t_{ij}$ , where  $T_{ij0}$  is an element obtained by neglecting the effect of polyfoam. The  $t_{ij}$  may be determined by a successive approximation method to first order in  $\epsilon - 1$ , where  $\epsilon$  is a relative dielectric constant of polyfoam.

The parameters of the coaxial bifurcation for the  $TE_{01}$  mode may be obtained from the calculated matrix elements. Frequency characteristics of  $r$ ,  $\phi_{33}$  and  $\phi_{13}$  are shown in Fig. 3. In this figure, 9000-Mc band frequency is also indicated as the abscissa for convenience in later application, where  $a = \frac{1}{2}D_2$ .

These parameters are expected to have a character similar to the analogous parameters for an  $H$ -plane  $0^\circ = Y$  junction of a wide rectangular waveguide, because the field configurations for both cases are similar.<sup>3</sup>

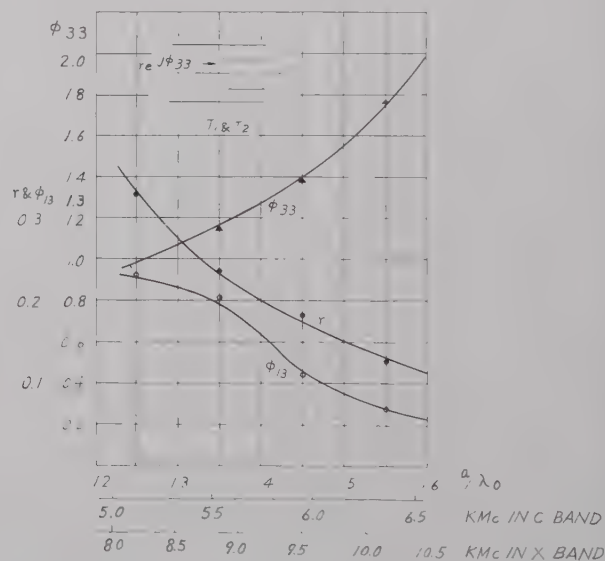


Fig. 3—Frequency characteristics of  $r$ ,  $\phi_{33}$ , and  $\phi_{13}$ . All reference planes are on the boundary plane of the bifurcation.

## CIRCULAR ELECTRIC MODE DIRECTIONAL COUPLER

### A. General Characteristics

Let us consider the characteristics of a circular electric mode directional coupler composed of the above mentioned bifurcations, which are located symmetrically along an axis, as shown in Fig. 4. If the separation  $L$  is sufficiently large to neglect the interaction

<sup>3</sup> N. Marcuvitz, "Waveguide Handbook," Mass. Inst. Tech., Rad. Lab. Ser., McGraw-Hill Book Co., Inc., New York, N. Y., vol. 10, p. 383; 1951.

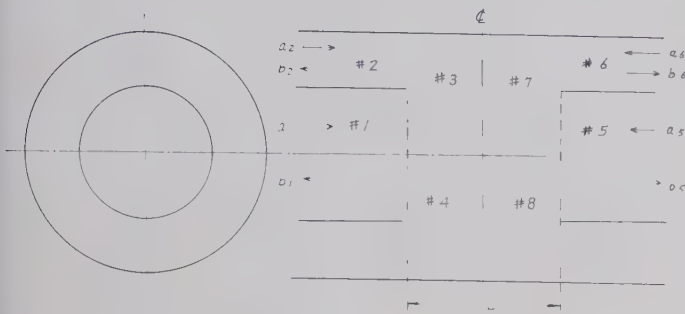


Fig. 4—Circular electric mode directional coupler.

effect caused by cutoff between the two bifurcations, relations between the incident, reflected, and transmitted waves are easily expressed in terms of the scattering matrix elements of each bifurcation, and phase delays engendered by the separation. When the concealed ports are eliminated, the scattering matrix for the over-all coupler network, shown in Fig. 4, are as follows:

$$\begin{pmatrix} b_1 \\ b_2 \\ b_5 \\ b_6 \end{pmatrix} = S \begin{pmatrix} a_1 \\ a_2 \\ a_5 \\ a_6 \end{pmatrix} \quad S = \begin{pmatrix} S_{11} & S_{12} & S_{15} & S_{16} \\ S_{21} & S_{22} & S_{25} & S_{26} \\ S_{51} & S_{52} & S_{55} & S_{56} \\ S_{61} & S_{62} & S_{65} & S_{66} \end{pmatrix} \quad (3)$$

$$S_{11} = S_{55} = s_{11} + \frac{s_{13}^2 s_{33}}{\eta} e^{-j2\theta_3} = \frac{r e^{j\phi_{11}}}{1+k^2} \frac{1 - e^{-j2(\theta_3 - \phi_{33})}}{\eta}$$

$$S_{12} = S_{56} = s_{12} + \frac{s_{13} s_{23} s_{33}}{\eta} e^{-j2\theta_3} = k S_{11}$$

$$S_{22} = S_{66} = s_{22} + \frac{s_{23}^2 s_{33}}{\eta} e^{-j2\theta_3} = k^2 S_{11}$$

$$S_{15} = \frac{s_{13}^2}{\eta} e^{-j\theta_3} + s_{14}^2 e^{-j\theta_4} = \frac{e^{-j\theta_4}}{1+k^2} \left[ \frac{1-r^2}{\eta} e^{-j\Theta} + k^2 \right] \quad (4)$$

$$S_{16} = S_{25} = \frac{s_{13} s_{23}}{\eta} e^{-j\theta_3} + s_{14} s_{24} e^{-j\theta_4}$$

$$= \frac{k e^{-j\theta_4}}{1+k^2} \left[ \frac{1-r^2}{\eta} e^{-j\Theta} - 1 \right]$$

$$S_{26} = \frac{s_{23}^2}{\eta} e^{-j\theta_3} + s_{24}^2 e^{-j\theta_4} = \frac{e^{-j\theta_4}}{1+k^2} \left[ \frac{k^2(1-r^2)}{\eta} e^{-j\Theta} + 1 \right]$$

$$\eta = 1 - s_{33}^2 e^{-j2\theta_3} = 1 - r^2 e^{-j2(\theta_3 - \phi_{33})}$$

$$\theta_3 = \beta_3 L, \quad \theta_4 = \beta_4 L$$

$$\Theta = \theta_3 - \theta_4 - 2\phi_{13}, \quad (5)$$

where

$a_1, a_2, a_5, a_6$  = the incident wave phasors in the circular and coaxial waveguides, respectively, (Fig. 4)

$b_1, b_2, b_5, b_6$  = the reflected wave phasors in the circular and coaxial waveguides, respectively, (Fig. 4)

$\beta_3$  = the propagation constant of the  $TE_{01}$  mode in the larger circular waveguide, and

$\beta_4$  = the propagation constant of the  $TE_{02}$  mode in the larger circular waveguide.

It is evident that there is a simple relation between  $S_{11}$ ,  $S_{12}$ , and  $S_{22}$ , and that these three values are almost the same because  $k$  is very close to unity. The magnitudes of these values are always small because  $r$  is small. On the other hand, the magnitudes of  $S_{15}$ ,  $S_{16}$  and  $S_{26}$  vary widely between 0 and 1, depending upon the phase difference  $\Theta$ .

There are two conditions for no reflection and infinite directivity. One is that  $\theta_3 - \phi_{33} = n\pi$  ( $n$ : integer), and the other is that  $r$  is cancelled by employing some additional matching element which has no effect on the  $TE_{02}$  mode. The former condition is rather complicated in design, because  $\theta_3$  is also linearly dependent on  $\Theta$ , which is fixed mainly by the specified transfer coefficient. Moreover, this method may be frequency sensitive, because, although the variation of  $\phi_{33}$  tends to compensate for the variation of  $\theta_3$ ,  $\theta_3$  changes quickly with frequency. As we will explain later, the latter condition may be expected to yield wide-band characteristics.

For either of the above ideal conditions, we have the following relations from (3), (4) and (5):

$$S_{11} = S_{12} = S_{22} = S_{55} = S_{56} = S_{66} = 0,$$

$$S_{15} = \frac{e^{-j\theta_4}}{1+k^2} [k^2 + e^{-j\Theta}],$$

$$S_{16} = S_{25} = \frac{-k e^{-j\theta_4}}{1+k^2} [1 - e^{-j\Theta}],$$

$$S_{26} = \frac{e^{-j\theta_4}}{1+k^2} [1 + k^2 e^{-j\Theta}]. \quad (6)$$

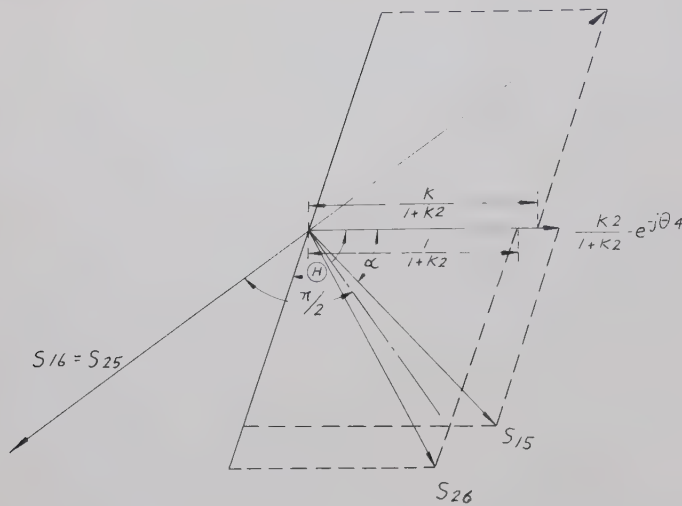
A vector diagram of  $S_{15}$ ,  $S_{16}$ ,  $S_{25}$  and  $S_{26}$  is shown in Fig. 5. As illustrated in this figure, the magnitudes of  $S_{15}$  and  $S_{26}$  are the same. The phase angles between  $S_{16}$  (or  $S_{25}$ ),  $S_{15}$  and  $S_{26}$  are not  $\pi/2$ , as in the analogous rectangular waveguide short-slot junction, but  $\pi/2 \pm (\Theta/2 - \alpha)$  respectively, where

$$\alpha = \sin^{-1} \frac{\sin \Theta}{\sqrt{1 + 2k^2 \cos \Theta + k^4}}.$$

However, as  $k$  is very close to unity (actually 1.077),  $(\Theta/2 - \alpha)$  is a small quantity. The magnitudes of  $S_{15}$ ,  $S_{16}$ ,  $S_{25}$  and  $S_{26}$  are widely changed by  $\Theta$ . If  $\Theta$  becomes  $2n\pi$  ( $n$ : integer),  $S_{16} = S_{25} = 0$  and  $|S_{15}| = |S_{26}| = 1$ . Nevertheless,  $S_{15}$  and  $S_{26}$  may not vanish completely, even though a very small minimum value of 0.0745 ( $-22.6$  db) occurs at  $\Theta = (2n+1)\pi$ . If  $\Theta$  is chosen to be

$$\Theta = (2n+1)\pi \mp \cos^{-1} \frac{(k^2 - 1)^2}{4k^2} = 90.32^\circ, 269.68^\circ, \dots,$$



Fig. 5—Vector diagram of  $S_{15}$ ,  $S_{16}$ ,  $S_{25}$  and  $S_{26}$ .

then

$$|S_{15}| = |S_{16}| = |S_{25}| = |S_{26}| = \frac{1}{\sqrt{2}},$$

and the coupler becomes a 3-db hybrid coupler.

### B. Measured Characteristics

Experiments on this directional coupler have been carried out at 9000-Mc band within sectoral waveguide instead of circular waveguide. The principle is not changed by using sectoral waveguide, and then a very simple rectangular to sectoral waveguide taper operates as a required mode transducer. Furthermore, it is not necessary to worry about spurious modes in such a transducer, if the sector angle is chosen properly. The experimental setup is composed of  $H$ -plane branched waveguides, rectangular to sectoral taper waveguides and a directional coupler portion as is illustrated in Fig. 6. The sector angle is chosen as  $22.5^\circ$  in order to render the mode equivalent to the circular  $TE_{11}$  mode nonexistent in the sectoral guide. Rectangular waveguides at both ends have the conventional dimension of 0.9 inch  $\times$  0.4 inch so that ordinary components for the 9000-Mc band may be employed. Other dimensions are shown in Fig. 6. The taper waveguides, which have been made by electroforming, are rather long to reduce reflection. The directional coupler portion has been constructed by assembling brass blocks and an interchangeable partition plate of 0.005-inch thickness between them. This permits us to change the dimensions of the coupling region very easily, during experiments.

Frequency characteristics of the measured magnitudes of the transfer coefficients for the directional coupler are shown in Fig. 7. We have measured the transfer coefficient  $S_{12}$  between adjoining ports instead of the reflection coefficients  $S_{11}$  and  $S_{22}$ , because they are proportional, as shown in (4). Calculated values which are obtained from (4) and (5) using values of the parameters,  $r$ ,  $\phi_{33}$  and  $\phi_{13}$ , measured at 5000-Mc band

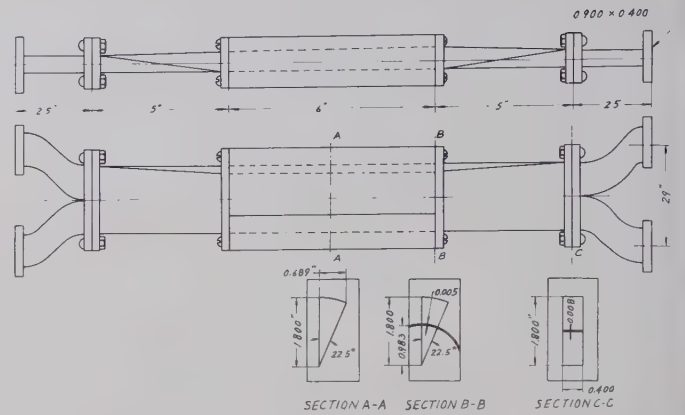


Fig. 6—Experimental setup of the directional coupler.

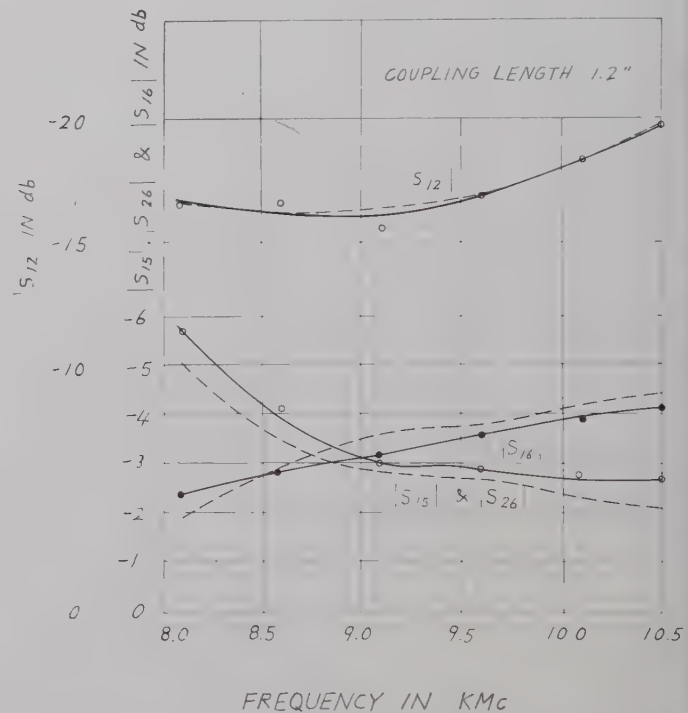


Fig. 7—Frequency characteristics of transfer coefficients for the directional coupler.

— measured curve,  
 - - - - - calculated curve.

in Fig. 3, are also shown on the same graphs. The magnitudes of the same transfer coefficients vs the coupling length are shown in Fig. 8. The measured values, in both cases, are in good agreement with calculated ones. The fact that the difference between measured and calculated values increases as the coupling length becomes short is thought to be a result of cutoff mode interaction between bifurcations, which is neglected in the calculation.  $|S_{15}|$  and  $|S_{26}|$  are, in general, not distinguishable in these figures, unless the reflection coefficient becomes quite large or  $|S_{15}|$  becomes very small.

As illustrated in Fig. 7, the variations of  $|S_{15}|$  and  $|S_{16}|$  with frequency are rather small. This is attributed to the fact that variations of  $(\theta_3 - \theta_4)$  and  $\phi_{13}$  have

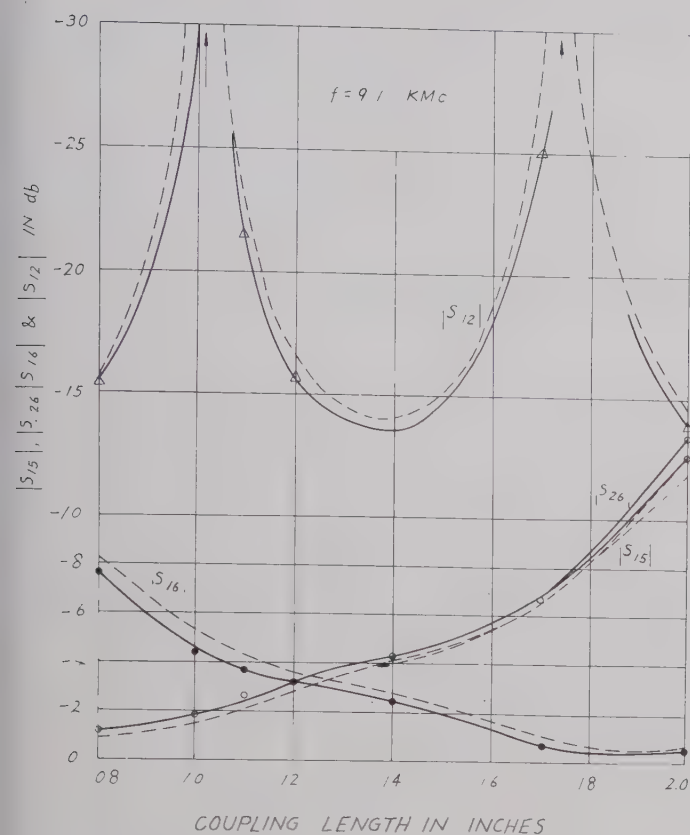


Fig. 8—Transfer coefficients vs coupling length characteristics.  
— measured curve,  
--- calculated curve.

the same trend with frequency, as shown in Fig. 3. Then the variation of  $\Theta$  becomes small. Thus, we may expect a wide-band component if we utilize these characteristics properly.

As mentioned before, there are two methods for reducing the reflection coefficient. The method which cancels  $S_{33}$  by some matching element is better than the other in all respects. The  $TE_{01}$  mode admittance characteristics of the bifurcation, seen from the circular waveguide and referred to the boundary plane, may be obtained from Fig. 3 and have been replotted on a Smith chart, as shown on curve 1 in Fig. 9. In transforming admittances along the guide by rotation about the center of a Smith chart, a given physical length of guide represents more rotation on the chart at higher frequencies than it does at lower ones. Therefore, if the admittances represented by curve 1 are transformed properly along the guide towards the generator, the admittances at all frequencies may fall near the curve of unity conductance on the chart. These transformed characteristics are shown on curve 2 in Fig. 9, in which the physical length of the guide of 0.365 inch is selected, and higher order mode effect, caused by the bifurcation, is assumed to be neglected. These characteristics show that the addition of a shunt susceptance element placed at this referred position gives wide-band matching, if the susceptance has smaller value at higher fre-

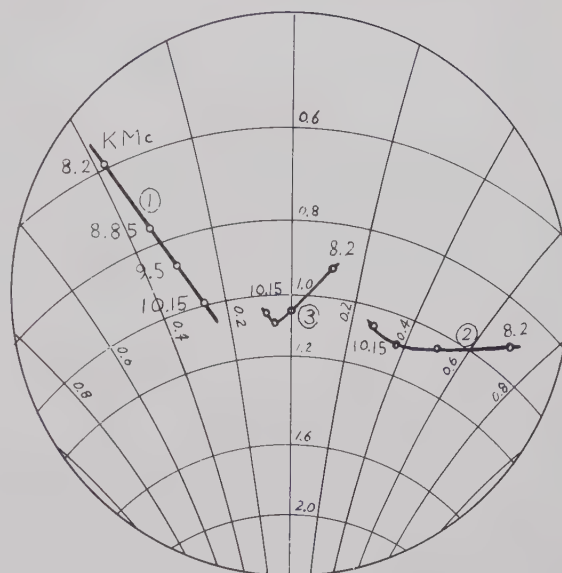


Fig. 9— $TE_{01}$  mode admittance characteristics of the coaxial bifurcation, seen from the circular waveguide.  
① refers to the boundary plane,  
② refers to the plane 0.365 inch apart from the boundary plane, and  
③ refers to the addition of a strip of 0.04 inch width.

quencies than at lower ones. An inductive susceptance has this character.<sup>4</sup> Thus, a thin-strip matching element (same thickness as the partition) with finite width in the axial direction, located on the same cylindrical surface as the bifurcation, may be used for the matching element, because the strip has an inductive susceptance for the  $TE_{01}$  mode and no appreciable effect on the  $TE_{02}$  mode. The susceptance may be calculated approximately.<sup>5</sup> With the addition of a strip of 0.04-inch width at that position, the input admittances of the bifurcation move into the area around the center on the chart, as shown on curve 3 in Fig. 9. This figure explains the possibility of wide-band matching.

Actually, it was necessary to determine, experimentally, the optimum position for the matching element, because the effective length between the edge of the bifurcation and a matching element might be influenced by the higher modes generated in the vicinity of bifurcation. The optimum length found was considerably shorter than the calculated one, and was 0.286 inch. The matching strips actually used were of the same dimension as the calculated ones.

Another important point is that a matching element causes a phase shift of the transmitted wave in the  $TE_{01}$  mode. Suppose a shunt susceptance of  $B/Y_0$  would cancel reflections completely; then the additional phase shift of the transmitted wave caused by the shunt element is given by  $\tan^{-1}(-B/2Y_0)$ . Thus,

<sup>4</sup> The usual short-slot hybrid junction has a character similar to this coupler. Therefore, it would probably be better to use an inductive element in that case also rather than the capacitive one, which has been commonly used. (See footnote 2.)

<sup>5</sup> Marcuvitz, *op. cit.*, p. 257.



if inductive matching elements are employed, it is necessary to make the coupling length longer, in order to get the same transfer coefficient as previously obtained without a matching element.

The measured magnitudes of the transfer coefficient for a directional coupler are shown in Fig. 10. The coupling length has been chosen with an aim towards obtaining a hybrid junction. It is evident in this figure that, with the inductive matching elements, the magnitude of  $|S_{12}|$  becomes quite small in a wide frequency region. Since the taper waveguides, bends, and terminations at the output ports have small reflections, these effects upon  $|S_{12}|$  may not be negligible, if  $|S_{12}|$  becomes very small. [It has been confirmed that the VSWR of the terminations are less than 1.03 (return loss = 36.6 db) in the entire frequency region of interest.] Nevertheless, it is clear that wide-band match has been obtained, and that the inductive matching elements were quite suitable for this purpose. Also, we were able to get a 3-db hybrid coupler at the center frequency with dimensions of the coupling region as shown in the upper right of Fig. 10. The transfer coefficients  $S_{15}$ ,  $S_{26}$  and  $S_{16}$  also have fairly wide-band character. The calculated values shown in the same figure are obtained from (6), taking into account the phase shift caused by matching elements, which is determined by the calculated susceptance value. The calculated and measured values are in very good agreement with one another.

#### APPLICATIONS

Finally, some applications of this directional coupler are described briefly.

These couplers may be used as the important elements of a branching filter for the  $TE_{01}$  mode, together with two rejection filters, which are coupled inner and outer waveguides between two couplers, respectively.<sup>6</sup> In this case the coupler in a semicircular waveguide may be employed conveniently.

Another application is a  $TE_{01}$ - $TE_{02}$  mode transducer. If we choose the ratio of  $|S_{15}|$  to  $|S_{16}|$  equal to  $k$ , and the phase shift between  $S_{15}$  and  $S_{16}$  equal to  $\pi$ , then the output waves have the same field configuration as that of  $TE_{02}$  mode. The required conditions may be at-

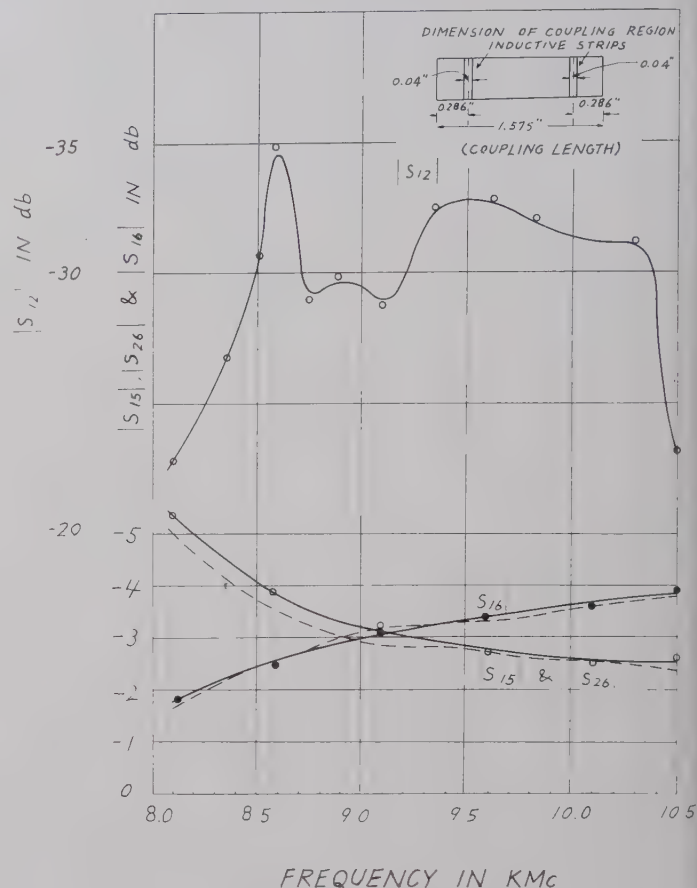


Fig. 10—Frequency characteristics of transfer coefficients for a hybrid junction with inductive matching elements.  
— measured curve,  
- - - - - calculated curve.

tained by a proper coupling length for the coupler

$$\left( \Theta = \cos^{-1} \frac{k^2 - 1}{2k^2} = 86.0^\circ \right)$$

and the phase shifter. The  $TE_{01}$  mode incident in a smaller circular input waveguide is transferred to the  $TE_{02}$  mode in a larger circular output waveguide.

#### ACKNOWLEDGMENT

The author wishes to express his sincere gratitude to Drs. L. B. Felsen and W. K. Kahn for their valuable suggestions, stimulating discussions, and revisions of the manuscript. The author also thanks the staff members of the Electrophysics Group of MRI for their encouragement.

<sup>6</sup> W. D. Lewis and L. C. Tillotson, "A non-reflecting filter for microwaves," *Bell Sys. Tech. J.*, vol. 27, pp. 83-95; January, 1948.

# Correspondence

## An Equivalent Circuit of the Internal Cavity Reflex Klystron-Amplifier

The experimental results of microwave amplification by the reflex klystron 2K25 have been reported.<sup>1-4</sup> An equivalent circuit of the 2K25 amplifier was developed and checked with the experimental results.

The fundamental circuit arrangement of the 2K25 internal cavity reflex klystron amplifier is shown in Fig. 1. The tube is mounted in the middle of the waveguide. The center conductor of the coaxial output line is extended and terminated by a variable reactor. Microwave signals are fed into the left opening of the waveguide and taken out of the right.

An equivalent circuit of the 2K25 reflex klystron amplifier is shown in Fig. 2. The letters A, B, C, . . . , in Fig. 1 correspond to the letters A, B, C, . . . , in Fig. 2. In this case, losses in the cavity resonator and transmission lines are neglected. In Fig. 2,

- $l_{1,2,3}$  = line-lengths of the coaxial lines,
- $\lambda_{1,2,3}$  = wavelengths on the lines,
- $Z_{01,2,3}$  = characteristic impedances of the lines
- $Z_{g1,2}$  = driving point impedances across the terminals FH,  $Z_{g1}$  for the input side and  $Z_{g2}$  for the output side,
- $X_s$  = a reactance of the variable reactor.

The equivalent parallel resistance  $R_{sh}$  and the parallel reactance  $X_{sh}$  of the external circuit impedance across the grids of the reflex klystron 2K25 are given by elementary analysis of the equivalent circuit shown in Fig. 2, as follows:

$$R_{sh} = Z^2 / R_{CD}(\omega M)^2, \quad (1)$$

$$X_{sh} = -Z^2 / [\omega C_P Z^2 + (X_{CD} + \omega L_s)(\omega M)^2 - \omega^2 L_s L_P - X_{CD} \omega L_P - \omega L_P R_{CD}^2] \quad (2)$$

where

$$Z^2 = \{(\omega M)^2 - \omega^2 L_s L_P - X_{CD} \omega L_P\}^2 + \omega^2 L_P^2 R_{CD}^2. \quad (3)$$

Here,  $R_{CD}$  and  $X_{CD}$  are equivalent series resistance and reactance of the right-hand side of the network across the terminals CD in Fig. 2, and are given by either analysis or Smith Chart. Apparently these are functions of  $X_s$ . Thus, the values of  $R_{sh}$  and  $X_{sh}$  can be adjusted by changing  $X_s$ , the reactance of the variable reactor.

\* Received by the PGMTT, May 27, 1960; revised manuscript received, July 27, 1960.

<sup>1</sup> K. Ishii, "Microwave amplifier," Japanese Patent No. 24710; August 13, 1958.

<sup>2</sup> K. Ishii, "X-band receiving amplifier," *Electronics*, vol. 28, pp. 202-210; April, 1955.

<sup>3</sup> K. Ishii, "One-way circuit by the use of a hybrid T for the reflex klystron amplifier," *Proc. IRE*, vol. 45, p. 687; May, 1957.

<sup>4</sup> K. Ishii, "Impedance adjustment effects on reflex klystron amplifier noise," *Microwave J.*, vol. 2, pp. 43-46; November, 1959.

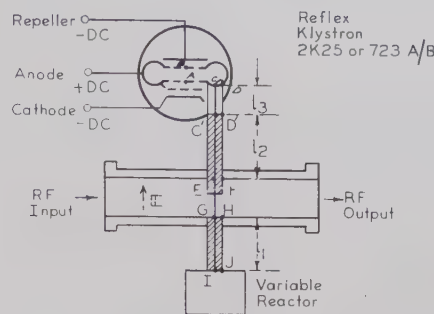


Fig. 1—Fundamental circuit of internal cavity reflex klystron amplifier.

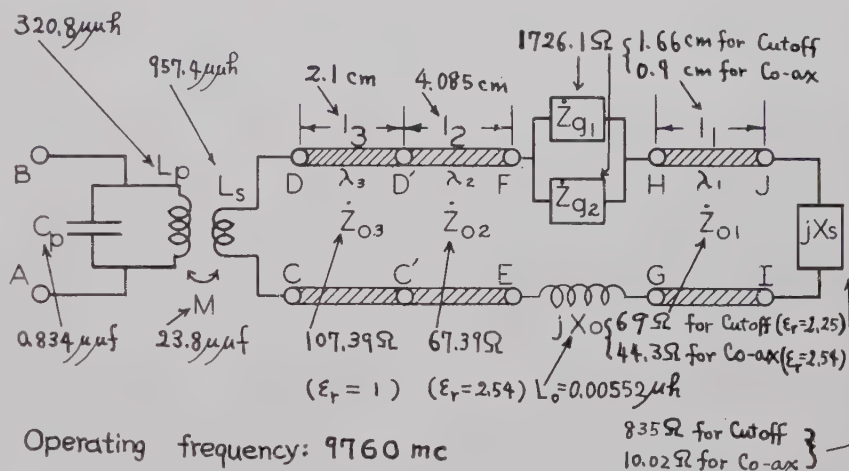


Fig. 2—Equivalent circuit of internal cavity reflex klystron amplifier.

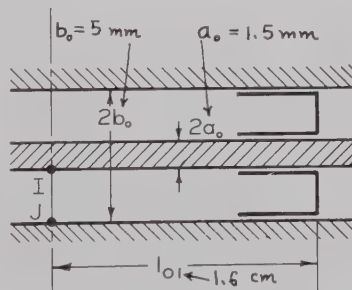


Fig. 3—Coaxial variable reactor.

The value of  $X_s$  for the coaxial variable reactor shown in Fig. 3 is given simply by

$$X_s = Z_{00} \tan(2\pi l_{01}/\lambda), \quad (4)$$

where  $Z_{00}$  is a characteristic impedance of

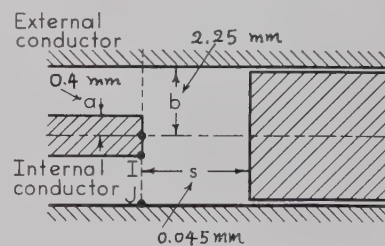


Fig. 4—Cutoff variable reactor.

the coaxial line. On the other hand, the value of  $X_s$  for the cutoff variable reactor, which was newly designed for this amplifier circuit, shown in Fig. 4, is given by the following equation:

$$X_s = \frac{\sqrt{\mu/\epsilon}}{16\pi a b s} \frac{\lambda}{\lambda} \frac{\{I_0(\sigma b) - I_0(\sigma a)\} \{a K_1(\sigma a) - b K_1(\sigma b)\} - \{K_0(\sigma b) - K_0(\sigma a)\} \{b I_1(\sigma b) - a I_1(\sigma a)\}}{I_1(\sigma b) K_1(\sigma a) - I_1(\sigma a) K_1(\sigma b)} \quad (5)$$



TABLE I  
OUTPUT IMPEDANCE ACROSS THE GRID  
OF THE REFLEX KLYSTRON

Reactor	$R_{sh}$	$X_{sh}$	$R_{sh} \cos \phi$
Cutoff	$2.99 \times 10^5 \Omega$	$-3.91 \times 10^3 \Omega$	$3.91 \times 10^3 \Omega$
Coaxial	$2.75 \times 10^5 \Omega$	$-19.01 \times 10^3 \Omega$	$1.89 \times 10^3 \Omega$

TABLE II  
GAIN MEASURED AND CALCULATED

Reactor	Gain (db) Measured	Anode Voltage $V_0$	Repeller $-V_r$	$I_0$ (ma)	$N$	$\beta$	Gain (db) Calculated
Cutoff	23.2	280	88	7.7	10.75	0.525	22.71
Coaxial	28.0	304	268	2.5	6.75	0.55	29.1

$$\text{Note: } \beta = \sin \frac{3170 dg}{2\lambda\sqrt{V_0}} \bigg/ \frac{3170 dg}{2\lambda\sqrt{V_0}}, \quad N = 4fl \bigg/ \sqrt{\frac{m}{2e} V_0/(V_0 + V_r)}$$

$$l = 3.44 \times 10^{-3} \text{ m,} \\ \text{Gap-distance } d_g = 0.61 \times 10^{-3} \text{ m.}$$

where  $I_s'$  and  $K_s'$  are the modified Bessel functions and

$$\sigma = \sqrt{\left(\frac{\pi}{4s}\right)^2 - \left(\frac{2\pi}{\lambda}\right)^2}. \quad (6)$$

This cutoff reactor gives the same positive reactance for extremely small distance of the shorting plunger setting in comparison with the coaxial reactor. The cutoff reactor is mechanically simpler than the coaxial type.

The numerical circuit constants used to obtain the values of  $R_{sh}$  and  $X_{sh}$  are shown in Figs. 2-4. The dimensions are based on measurement of the actual circuit used. The constants of the klystron cavity  $C_P$ ,  $L_P$ ,  $L_s$ , and  $M$  were calculated by Fujisawa's method.<sup>5,6</sup> The impedance  $Z_{01}$  and  $Z_{02}$  in Fig. 2 were calculated by Tanaka's method.<sup>7</sup> The reactance of the antenna,  $X_0$ , was calculated assuming it was a uniform cylindrical conductor. The computed results of  $R_{sh}$  and  $X_{sh}$  are given in Table I, where  $\cos \phi$  is the power factor of the circuit. These values were checked by the experiment in the following way.

The gain of the reflex klystron amplifier can be calculated by the following equation<sup>8</sup> based on the regenerative action of the electron beam.

$$A = \frac{V_0}{V_0 - I_0 \beta^2 R_{sh} \pi N \cos \phi} \quad (7)$$

where

$A$  = gain,

$V_0$  = anode voltage,

$I_0$  = effective electron beam current,

$\beta$  = beam coupling coefficient,

$N$  = number of electron transit time cycles in the repeller space.

The calculated results are listed in Table II with some measured data such as anode and repeller voltage, effective current, and dimensions of the tube. As shown in this table, the calculated gains are in good agreement with the measured gains.

KORYU ISHII  
Dept. of Elec. Engrg.  
Marquette University  
Milwaukee, Wis.

### Some Comments on the Method of Kyhl\*

The purpose of this letter is not to criticize the philosophy of Kyhl's<sup>1</sup> method nor even to engage in a debate as to whether his method is, or is not, more useful than ours.<sup>2,3</sup> We find his proposals both interesting and meaningful. First, we would like to call attention to two errors in his letter and then to show the close relation of his method to ours.

Let us consider his method. He proposes that a " $\Gamma$ " =  $1/\Gamma$  be used when  $|\Gamma| > 1$ . This, he claims, will produce his "double SMITH- HTIMS chart." This is in error because, if  $|\Gamma| > 1$ , the original point in the extended Standard Smith chart<sup>4</sup> is without the unit circle, and the inversion type operation (with or without the minus sign) within the unit circle; hence, the "HTIMS" part of the chart will coincide with the regular Smith chart.

\* Received by the PGM-TT, June 16, 1960.

<sup>1</sup> R. L. Kyhl, "Plotting impedance with negative resistive components," IRE TRANS. ON MICROWAVE THEORY AND TECHNIQUES, vol. MTT-8, p. 337; May, 1960.

<sup>2</sup> D. J. R. Stock and L. J. Kaplan, "An extension of the reflection coefficient chart to include active networks," IRE TRANS. ON MICROWAVE THEORY AND TECHNIQUES, vol. MTT-7, pp. 298-299; April, 1959.

<sup>3</sup> L. J. Kaplan and D. J. R. Stock, "The representation of impedances with negative real parts in the projective chart," IRE TRANS. ON MICROWAVE THEORY AND TECHNIQUES, vol. MTT-7, p. 475; October, 1959.

To obtain Kyhl's "double SMITH- HTIMS chart," we suggest the following construction. An inversion in the unit circle, followed by a symmetry<sup>4</sup> (reflection) with respect to the line  $\Gamma = 1$ . This can be written analytically as " $\Gamma$ " =  $-\Gamma^*/2$ , where  $\Gamma^* = 1/\Gamma$ .

We next consider the statement that our method is not analytic. By this statement, we presume that Kyhl means that the modified  $\beta$  and the modified  $\beta^{-1}$  transformations, or the Darboux transformation<sup>5</sup> as shown in footnote 2, is presented in its natural graphical form. The following is the transformation in analytic form:

$$[\Gamma_1 = 1/\Gamma^*, \ln [O\Gamma', AB] = 2 \ln [O\Gamma_1, AB],$$

$$\Gamma' = \frac{2\Gamma_1}{1 + |\Gamma_1|^2} = \frac{2\Gamma}{1 + |\Gamma|^2}$$

where  $A$  and  $B$  are the two points on the unit circle, intersected by the straight line, connecting the center ( $O$ ) and the inverse point ( $\Gamma_1$ ). The brackets indicate the cross ratio of the four points in question. The final analytic form shows the invariance of the final point with respect to inversion in the unit circle, which was proven geometrically.<sup>2</sup> It is noted that the above equation is essentially the same as that stated by Deschamps<sup>6</sup> for the  $\beta$  transformation.

In comparing our results with Kyhl's, we shall use his method with our modification. It is conceded that there are other ways to correct the proposed method. The first step of inversion is the same in both procedures. The difference occurs in the second step. Our transformation (which is of course the Deschamps<sup>7</sup>  $\beta$  and  $\beta^{-1}$  transformation) is best considered as finding the non-Euclidean bisector of a line segment.<sup>8,9</sup> The second step in Kyhl's procedure, the reflection, is an involution.<sup>9</sup> The inversion<sup>9</sup> (also an involution), followed by the reflection, is a graphical way of performing a nonloxodromic bilinear transformation. The unit circle is the isometric circle of the equivalent bilinear transformation, which is " $\Gamma$ " =  $(2\Gamma - 1)/\Gamma$ . This result also could have been obtained analytically, instead of using the geometrical interpretation. In summary, it is noted that Kyhl's and our results are quite similar in form, both analytically and geometrically, but differ mostly in the final presentation.

L. J. KAPLAN  
D. J. R. STOCK  
Elec. Engrg. Dept.  
New York University  
New York, N. Y.

<sup>4</sup> R. Deaux, "Introduction to the Geometry of Complex Numbers," F. Ungar Publishing Co., New York, N. Y.; 1956.

<sup>5</sup> E. F. Bolinder, "Theory of noisy two-port networks," Tech. Rep. 344, and personal correspondence, M.I.T. Res. Lab. for Electronics, Cambridge, Mass.

<sup>6</sup> G. A. Deschamps, "A Hyperbolic Protractor for Microwave Impedance Measurement," Fed. Telecommun. Lab., Nutley, N. J., 1953.

<sup>7</sup> G. A. Deschamps, "Determination of reflection coefficients and insertion loss at a wave-guide junction," J. Appl. Phys., vol. 24, pp. 1046-1050; August, 1953.

<sup>8</sup> L. J. Kaplan and D. J. R. Stock, "Non-Euclidean Geometric Representations for Microwave Networks," New York University, College of Engrg., Tech. Note 400-3, pt. 2; October, 1959.

<sup>9</sup> E. F. Bolinder, "Impedance and Power Transformations by the Isometric Circle Method and Non-Euclidean Hyperbolic Geometry," M.I.T. Res. Lab. for Electronics, Cambridge, Mass., Tech. Rept. 312; June, 1957.

<sup>5</sup> K. Fujisawa, "The precise L.C.R. parallel equivalent circuits of re-entrant cavity resonators," J. Inst. Elec. Commun. Engrs. Japan, vol. 36, pp. 151-158; April, 1953.

<sup>6</sup> K. Fujisawa, "The precise L.C.R. parallel equivalent circuits of re-entrant cavity resonators (Supplement)," J. Inst. Elec. Commun. Engrs. Japan, vol. 36, pp. 389-392; July, 1953.

<sup>7</sup> S. Tanaka, "A broad band coaxial to wave-guide junction," J. Inst. Elec. Commun. Engrs. Japan, vol. 37, pp. 172-176; March, 1954.

<sup>8</sup> T. Okabe, "Microwave Amplification by the Use of Reflex Klystrons," Rept. of Microwave Res. Committee in Japan, Tokyo; June-July, 1952.

Reply by R. L. Kyhl

I have no disagreement with the comments of L. J. Kaplan and D. J. R. Stock. I was thinking of plotting the two parts of the chart from different origins. My chief interest was in the type of graphical display chosen.

While the issue was at the press, a similar use of a double chart was published elsewhere.<sup>10</sup>

<sup>10</sup> R. M. Steere, "Novel applications of the Smith chart," *Microwave J.*, vol. 3, pp. 97-100; March, 1960.

## Scattering Matrix for an N-Port Power-Divider Junction\*

### INTRODUCTION

During the course of an investigation of a data-processing technique yielding effectively reduced sidelobes and beamwidth for a microwave radar antenna, the need arose for multiport power dividers. In order to avoid an undesirable decrease in the signal-to-noise ratio, it was necessary that these dividers waste no power. Consequently, a scattering matrix was sought which would have the obvious requirement that there be no wave reflected in the input port and which would allow the power to be divided into arbitrary but fixed relative parts.

It should be noted that there now exist two methods<sup>1</sup> for synthesizing an  $n$ -port junction at a single frequency directly from the normalized scattering matrix, without use of the associated impedance matrix.

### THE SCATTERING MATRIX

A reciprocal, lossless junction can be represented by a symmetric, unitary scattering matrix  $S'$ . It is sufficient to consider a real matrix first without losing generality, because the matrix  $S'$  for the general case (including phase shifts) can be derived from the real case by a simple transformation.<sup>2</sup>

The purpose of this paper is to find the scattering matrix for an  $n$ -port junction, such that when a wave is fed into, say, port one, there will be no reflected wave in that port, and such that the amplitude of the wave transmitted to port  $k$  is equal to a given  $x_k$ . Analytically expressed, this requires that

$$x_k = \sum_i S_{ki} \delta_{i1} = S_{k1}, \quad (1)$$

where the  $x_k$  are subject to the restriction

$$x_1 = 0 \quad \text{and} \quad \sum_{k=2}^n x_k^2 = 1. \quad (2)$$

Symmetry requires that

$$S_{ij} = S_{ji}, \quad (3)$$

and unitarity, which reduces to orthogonality for the real case considered here, requires that

$$\sum_{k=1}^n (\tilde{S})_{ik} S_{kj} = \sum_{k=1}^n S_{ik} S_{kj} = \delta_{ij} \quad (4)$$

[where use has been made of (3)].

the matrix  $S$  satisfying (1), (3), and (4) may be obtained as follows:

$$\left. \begin{aligned} A. S_{11} &= 0, \\ B. S_{kk} &= x_k^2 - 1 \quad \text{for } k > 1, \\ C. S_{ij} &= S_{ji} = x_i x_j \quad \text{for } i \neq j, i > 1, j > 1, \\ D. S_{1i} &= S_{i1} = x_i \quad \text{for } i > 1. \end{aligned} \right\} \quad (5)$$

To prove that (5) is the required solution, it is only necessary to verify that it satisfies (1), (3), and (4). From  $A$  and  $D$ , it is evident that (1) is satisfied, and from  $C$  and  $D$  it is evident that (3) is satisfied. To verify that (4) is also satisfied, it is necessary to consider separately various possible values of  $i$  and  $j$ , because of the special nature of the various  $S_{ij}$ .

1)  $i=j=1$ .

Using (2) and the rules given in (5),

$$\sum_{k=1}^n S_{1k} S_{k1} = \sum_{k=2}^n x_k^2 = 1,$$

which satisfies (4).

2)  $i=j \neq 1$ .

Proceeding as above,

$$\begin{aligned} \sum_{k=1}^n S_{ik} S_{ki} &= S_{i1}^2 + S_{ii}^2 + \sum_{k \neq 1, i} S_{ik} S_{ki} \\ &= x_i^2 + (x_i^2 - 1)^2 + x_i^2 \sum_{k \neq i} x_k^2. \end{aligned}$$

According to (2), the above sum on  $k$  is  $(1 - x_i^2)$  and hence the right side reduces to one as required.

3)  $i \neq j$ .

$$\begin{aligned} \sum_{k=1}^n S_{ik} S_{kj} &= S_{i1} S_{1j} + S_{ii} S_{ij} + S_{ij} S_{jj} \\ &\quad + \sum_{k \neq 1, i, j} S_{ik} S_{kj}. \end{aligned} \quad (6)$$

It is necessary to consider separately the case  $i=1$  (or  $j=1$ ) and  $i \neq 1 \neq j$ .

a)  $i=1$ .

For this case, the above expression reduces to

$$\sum_{k=1}^n S_{1k} S_{kj} = x_j (x_j^2 - 1) + x_j \sum_{k \neq j} x_k^2 = 0.$$

The case  $j=1$  is essentially the same as that above and therefore (4) is satisfied in both of these cases.

b)  $i \neq 1 \neq j$ .

For this case, (6) becomes

$$\begin{aligned} \sum_{k=1}^n S_{ik} S_{kj} &= x_i x_j + x_i x_j (x_i^2 + x_j^2 - 2) \\ &\quad + x_i x_j \sum_{k \neq i, j} x_k^2. \end{aligned}$$

When use is made of (2), the above equation reduces to zero as required.

### CONCLUSION

It has been shown that it is theoretically possible to provide a junction which will divide an input wave into many output waves of arbitrary but fixed relative amplitudes. The arbitrariness of the power division

means that one may choose any ratios for the output waves and have no reflected wave in the input port. Once such a divider is constructed, however, the ratio of the output waves is fixed.

O. R. PRICE

Hughes Res. Labs.

A Division of Hughes Aircraft Co.

Malibu, Calif.

M. LEICHTER

Ground Systems Group

A Division of Hughes Aircraft Co.

Fullerton, Calif.

## Lossy Resonant Slot Coupling\*

The paper by Allen and Kino<sup>1</sup> suggests a novel method of combating troublesome cut-off oscillations in periodic slow-wave structures. The idea is to couple loss periodically into the system through slots which are resonant at the center of the (narrow) oscillation range. The high  $Q$  of the slots will effectively decouple the loss in the operating range of the pass band.

To develop this idea, we start with Allen and Kino's (13) for the voltage  $\phi(x)$  along the slot in terms of the tangential  $\hat{H}$  field along the slot. With respect to their Fig. 2 coordinates, shown in Fig. 1 below, we can

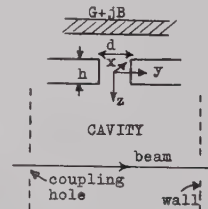


Fig. 1—A lossy slot in a cavity wall. Voltage  $\phi(x)$  exists across the slot gap,  $d$ .

write the transmission line equation for the slot voltage as

$$(\partial^2/\partial x^2 + k^2)\phi(x) = -j\omega L_0 [(I_c \bar{H}_{cx})_+ - \hat{H}_{x-}] \quad (1)$$

where the tangential magnetic field is  $(I_c \bar{H}_{cx})_+$  on the  $+z$ - or cavity side of the slot and is  $\hat{H}_{x-}$  on the  $-z$ -side. Eq. (1) can be derived rigorously for a TEM slot mode. The caret denotes a total field, and we have split the cavity field into an amplitude  $I_c$  and a vector field pattern  $\bar{H}_c$  for equivalent circuit purposes; this notation differs from that of Allen and Kino.  $L_0$  is the slot inductance per unit length in the  $x$ -direction.

Let us introduce the lossy susceptance  $G+jB$  by saying that the average voltage

\* Received by the PGM-TT, July 20, 1960.

<sup>1</sup> M. A. Allen and G. S. Kino, "On the theory of strongly coupled cavity chains," *IRE TRANS. ON MICROWAVE THEORY AND TECHNIQUES*, vol. MTT-8, pp. 362-372, May, 1960.

\* Received by the PGM-TT, July 15, 1960.

<sup>1</sup> D. C. Youla, "Direct single frequency synthesis from a prescribed scattering matrix," *IRE TRANS. ON CIRCUIT THEORY*, vol. CT-6, pp. 340-344; December, 1959.

<sup>2</sup> "Reference Data for Radio Engineers," American Book-Stratford Press, Inc., New York, N. Y., 4th ed.; 1956.



across the gap,  $\phi(x)/d$ , produces  $\hat{H}_{xz}$  according to

$$\hat{H}_{xz}d = \phi(x)(G + jB) \quad (2)$$

so that (1) may be written as

$$\begin{aligned} (\partial^2/\partial x^2 + \kappa^2)\phi(x) &= -j\omega L_0 I_c \bar{H}_{cz} \\ \kappa^2 &= k^2 - j\omega \frac{L_0}{d} (G + jB) \\ &\cong k^2 - j\omega (L_0/d)G. \end{aligned} \quad (3)$$

(Note that  $L_0/d$  is well-behaved as  $d$  approaches zero because  $L_0 \cong (\mu d/h)$ . It will turn out that we will need very little conductance  $G$  for our purposes; hence  $\omega(L_0/d)G \ll k^2$ , and since  $B$  is presumed on the order of  $G$ , we have neglected  $\omega(L_0/d)B$  above.

Eq. (3) is our transmission line equation for slot voltage  $\phi(x)$ , with a loss term representing decay of a wave traveling along the slot  $x$ -axis. The equation says that all power flowing into the slot from the cavity is absorbed by  $G$ . To prove this, merely multiply (3) by  $\phi(x)^*$  and integrate from  $x = -l/2$  to  $+l/2$ . By integration of the first term by parts we obtain

power from cavity

$$\begin{aligned} &= 1/2 \operatorname{Re} I_c^* \bar{H}_{cz} \int_{-l/2}^{+l/2} \phi(x) dx \\ &= 1/2 (G/d) \int_{-l/2}^{+l/2} |\phi(x)|^2 dx \quad (4) \\ &= \text{power into } G, \text{ consistent with (2).} \end{aligned}$$

We shall use the first expression for power flow rather than the second.

Webster's solution (15) of the reference reduces, for the case of  $I_c \bar{H}_{cz}$  constant over the long narrow slot, to

$$\begin{aligned} \phi(x) &= +j\omega L_0 I_c \bar{H}_{cz} \frac{2 \sin \kappa l/2}{\kappa^2 \sin \kappa l} \\ &\cdot [\cos \kappa x - \cos \kappa l/2] \end{aligned} \quad (5)$$

which correctly reduces to zero at the ends of the slot,  $x = \pm l/2$ .

With slot voltage  $\phi(x)$  known in terms of  $I_c$  from (5), we now want to determine cavity mode amplitude  $I_c$  in terms of  $\phi(x)$ . Suppose the unwanted oscillations occur near the  $\pi$ -cutoff frequency of the first pass band of a cavity chain with hole coupling from one cavity to the next. In such a "cold" structure of  $\pi$ -phase shift, the magnetic field will be purely normal and the electric field purely tangential to the cavity coupling holes. We conveniently define the cavity  $\pi$ -mode patterns  $\bar{E}_c$  and  $\bar{H}_c$  as

$$\nabla \times \bar{E}_c = k_\pi \bar{H}_c \quad (6a)$$

$$\nabla \times \bar{H}_c = k_\pi \bar{E}_c \quad (6b)$$

$$\int_v \bar{E}_c^2 dv = \int_v \bar{H}_c^2 dv = \tau,$$

cavity volume (normalization) (6c)

with

$$\bar{E}_c \cdot \bar{n} = 0 \text{ on coupling holes,}$$

$$\bar{E}_c \times \bar{n} = 0 \text{ on the "lossy" slot surface and metal walls.}$$

In a frequency range near the  $\pi$ -cutoff, we expand the fields of Maxwell's equations,

but not their curls, in the one- $\pi$  mode, as

$$\nabla \times \hat{E} = -j\omega \mu (I_c \bar{H}_c), \quad (7a)$$

$$\nabla \times \hat{H} = \hat{J} + j\omega \epsilon (V_c \bar{E}_c). \quad (7b)$$

The interaction of the beam current density  $\hat{J}$  with the circuit near the cutoff causes the unwanted oscillations. Eqs. (7a) and (7b) neglect the irrotational field, which is weak compared to the one strongly-excited solenoidal  $\pi$ -mode.

To evaluate  $V_c$  and  $I_c$  of (7) we dot-multiply (7a) by  $\bar{H}_c$ ; (7b) by  $\bar{E}_c$ ; integrate both equations over the cavity volume, and integrate the curl  $\hat{E}$  and curl  $\hat{H}$  terms by parts, viz.,

$$\begin{aligned} &\int_v \bar{H}_c \cdot \nabla \times \hat{E} dv \\ &= \int_v \hat{E} \cdot \nabla \times \bar{H}_c dv + \int_{\text{slot}} \hat{E} \times \bar{H}_c \cdot \bar{n} ds \\ &= \int_v V_c \bar{E}_c \cdot (k_\pi \bar{E}_c) dv + \int_{\text{slot}} \hat{E} \times \bar{H}_c \cdot \bar{n} ds. \end{aligned} \quad (8)$$

We obtain the equations for amplitudes  $V_c$  and  $I_c$  as

$$\begin{aligned} k_\pi V_c &= - (1/\tau) \int_{\text{slot}} \bar{i}_y \phi(x) \times \bar{i}_x H_{cz} \\ &\cdot (-\bar{i}_z) ds - j\omega \mu I_c \end{aligned} \quad (9a)$$

$$k_\pi I_c = j\omega \epsilon V_c + k_\pi \Delta I \quad (9b)$$

with

$$\begin{aligned} k_\pi \Delta I &\triangleq (1/k_\pi \tau) \left[ \int_v \hat{J} \cdot \bar{E}_c dv \right. \\ &\left. + \int_{\text{coupling holes}} \bar{E}_c \times \hat{H} \cdot \bar{n} ds \right]. \end{aligned}$$

Note that the last integral in  $k_\pi \Delta I$  represents the cavity hole coupling to its neighbors by means of tangential  $\hat{H}$  on the hole surfaces. Thus we do not consider resonant slot coupling between cavities, effected by tangential  $\hat{E}$  on the slot surfaces. Next, we will compare the power flow through the coupling holes with that dissipated across the slot in such a way that  $k_\pi \Delta I$  will be irrelevant in (9). But first we derive the equivalent circuit.

If we divide both parts of (9) by  $k_\pi^2$  and define equivalent circuit quantities as

$$V_c' \triangleq V_c/k_\pi \text{ (volt)} \quad L_c \triangleq \mu/k_\pi$$

$$I_c' \triangleq I_c/k_\pi' \text{ (ampere)} \quad C_c \triangleq \epsilon/k_\pi \quad (10a)$$

$Z_s$ , slot impedance

$$\begin{aligned} &= +j\omega \frac{L_0}{k_\pi} \frac{H_{cz}^2}{\tau} \frac{2 \sin \kappa l/2}{\kappa^3 \sin \kappa l} \\ &\cdot \left[ 2 \sin \frac{\kappa l}{2} - \kappa l \cos \frac{\kappa l}{2} \right] \end{aligned} \quad (10b)$$

$$\kappa \cong k - j\omega \frac{L_0}{2k} \frac{G}{d}, \quad (10c)$$

from (3) for small loss, then (9) and (10) give us

$$V_c' = -Z_s I_c' - j\omega L_c I_c' \quad (11a)$$

$$I_c' = j\omega C_c V_c' + \Delta I/k_\pi, \quad (11b)$$

which has the equivalent circuit representation shown in Fig. 2 below. It may be verified that the time average stored energies and the power flow into  $\operatorname{Re}(Z_s)$  of the circuit are equal to the actual ones times the dimensionless factor  $(k_\pi^2 \tau)^{-1}$ . Closer examination would reveal that the power flow  $\frac{1}{2} \operatorname{Re} V_c' (\Delta I/k_\pi)^*$  represents flow into the beam and across the coupling holes by the same factor of proportionality.

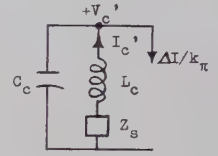


Fig. 2—Equivalent circuit for the cavity excited by the slot.  $Z_s$  is the slot impedance. The effect of the beam current and coupling to adjacent cavities is represented by  $\Delta I/k_\pi$ .

Now we note the fact that the electromagnetic power flowing into the cavity across a coupling hole (through which the beam may be flowing) is proportional to the product of amplitude of electric field  $V_c$ , and  $I_c^*$ , which is proportional to  $V_c^*$  in (11a). Therefore the electromagnetic power flow in the chain is proportional to  $|V_c'|^2$  in the equivalent circuit. Since the power dissipated into  $\operatorname{Re}(Z_s)$  is also proportional to  $|V_c'|^2$ , we see that the significant parameter for comparison of power input to a cavity with power dissipated is

$$P_d'/|V_c'|^2 = \frac{1}{2} \frac{\operatorname{Re} Z_s}{|Z_s + j\omega L_c|^2}, \quad (12)$$

$P_d'$  being the equivalent circuit power dissipation across the lossy slot. We shall call the ratio of (12) the relative power dissipation.

We now show that as conductance  $G$  of the lossy material goes to zero, the relative power dissipation tends to concentrate in a narrow frequency range about the slot resonant frequency. Let us define the loss parameter  $\alpha$  as  $(\omega L_0 G/2dk)$  from (10c). For small loss,  $|Z_s| \ll \omega L_c$  in (12) and  $\operatorname{Re}(Z_s)$  varies rapidly about  $kl = \pi$ , the first half-wavelength resonance of the slot, so we write  $P_d'/|V_c'|^2$  as

$$\begin{aligned} P_d'/|V_c'|^2 &= \frac{1}{2} \frac{1}{(\omega L_c)^2} \frac{\omega L_0}{k_\pi} \frac{H_{cz}^2 \tau^3}{\tau} \frac{2}{(kl)^3} R_s' \end{aligned} \quad (13a)$$

$$R_s' = \operatorname{Re} \frac{j \sin \kappa l/2}{\sin \kappa l} [2 \sin \kappa l/2 - \kappa l \cos \kappa l/2] \quad (13b)$$

$$\kappa l = kl - j\alpha l \quad \alpha = \frac{\omega L_0}{2k} \left( \frac{G}{d} \right).$$

Plots of  $R_s'$  as a function of the slot length  $kl$ , in radians, appear on Fig. 3 for various losses  $\alpha l$ . Because  $|Z_s| \ll \omega L_c$  in the range of  $R_s'$  shown, the equivalent circuit current  $I_c'$  in Fig. 2 remains constant for fixed  $|V_c'|$  but as  $\alpha l$  decreases,  $G$  decreases and  $\operatorname{Re}(Z_s)$  increases, hence the relative power dissipation at  $\pi$  increases with decreasing  $\alpha l$  on Fig. 3. Note that in describing the behavior of these parameters we have not involved the resonant properties of the Fig. 2 circuit;

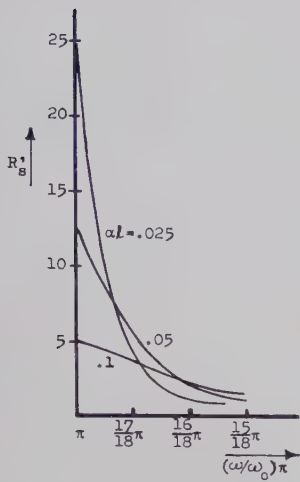


Fig. 3—Relative power dissipation measured by  $R_s'$  vs frequency  $\omega$ , for various values of the loss parameter  $\alpha l$ .

hence, the Fig. 3 behavior in no way contradicts the behavior of  $Q$  with loss and frequency.

A properly designed lossy slot will not have the relative power dissipation so large at the slot resonant frequency  $\omega_0$  that sufficient power will dissipate within the pass band to interfere with operation there. Nor should it be so small that sufficient residual power remains to start oscillation. One design procedure is the following:

1) Decide from a calculation of power flow across the coupling holes how much relative power  $P_d/|V_c|^2$  is to be dissipated per cavity. Convert this to the equivalent circuit relative dissipation by

$$\begin{aligned} P_d'/|V_c'|^2 &= (P_d/k_\pi^2\tau)(k_\pi^2/|V_c|^2) \\ &= (P_d/|V_c|^2)(1/k_\pi\tau). \end{aligned} \quad (14)$$

( $V_c$  is the amplitude of electric field in volts/meter.)

2) Choose a loss parameter

$$\alpha l = (\omega\mu l/2k)(L_0/\mu)(G/d)$$

from Fig. 3 for the desired power dissipation bandwidth about the half-wavelength frequency  $\omega_0$  of the slot. This expression involves two parameters:  $(L_0/\mu)$ , the slot transmission line inductance/unit length along the long axis divided by  $\mu$ , and  $(G/d)$ , the ratio of the lossy surface conductance presented to the slot divided by the gap length in Fig. 1.

3) From the known parameters  $k_\pi$ ;  $H_{cx}$  at the slot;  $\omega\mu$ ;  $l$ , the slot length; and  $\tau$ , the cavity volume, choose  $(L_0/\mu) \cong (d/h)$  from (10b) and (12) for sufficient relative power dissipation at frequency  $\omega_0$ .

4) Return to the expression for  $\alpha l$  in 2) and, with  $L_0/\mu$  now known, determine  $G/d$ . We shall see next that the relative power dissipation at  $\omega_0$  tends to be unduly large unless  $L_0/\mu \cong d/h$  of the slot is designed rather small.

Some numerical results now follow. Suppose we have the parameters

$$\begin{aligned} &\left\{ \begin{array}{l} k_\pi = 75 \sim 3.6 \text{ kmc} \\ H_{cx} = 1.1^2 \\ l = 4.15 \times 10^{-2} \text{ meter} \\ \tau = 12.2 \times 10^{-5} \text{ meter}^3 \end{array} \right. \\ &\text{cavity} \\ &\left\{ \begin{array}{l} \text{radius } 1/4 \text{ inch} \\ \text{current } 50 \text{ amperes} \\ \text{voltage } 100 \text{ kv.} \end{array} \right. \\ &\text{beam} \end{aligned}$$

We estimate from the gain per cavity of the small-signal growing wave, which exists for synchronism of the slow space charge mode with the "cold" circuit near the  $\pi$ -cutoff, a value of  $P_{\text{flow}}/|V_c|^2$  of  $6.8 \times 10^{-7}$ . Let us dissipate this amount of relative power through the slot, so that  $P_d/|V_c|^2$  has this value. We choose  $\alpha l = 0.025$  in Fig. 3 so that the slot dissipation will be effective over  $10^\circ$  or so, corresponding to  $\Delta f = 0.2$  kMc. From (14) we get  $P_d'/|V_c'|^2 = 7.5 \times 10^{-5}$ . Then, from (13) we find  $(L_0/\mu) \cong d/h$  to be about 0.052. This value is impractically small but we can insert a lossy slot into every fifth cavity of the chain and dissipate five times the relative power in that cavity. Then  $d/h$  becomes about 0.26. From (13b) for  $a$  we get a value of  $G/d$  of about  $1 \times 10^{-2}$ . For a  $3/2$ -inch-wide slot,  $G = 10^{-5}$  mho per unit surface area.

Despite the critical nature of the relative power dissipation and the loss bandwidth upon  $G$ , the idea of lossy slot coupling for combating undesirable cutoff oscillations looks promising.

R. M. BEVENSEE

E.E. Dept.

University of California  
Berkeley

### Authors' Comment\*

The idea suggested by Bevensee for coupling energy out of a periodic system by a means which is effective only over a narrow pass band is one of many possibilities which have been considered in this Laboratory. Another alternative, described by Rynn,<sup>3</sup> for instance, involves the use of another propagating structure which is itself lossy and which is coupled to the main structure. In this case, conditions are arranged for the phase velocities of the two structures to be equal over only the narrow oscillation pass band.

A note of caution should be introduced. It will be realized from our analysis that a long slot is capable of presenting a large impedance over a wide frequency band. Consequently, if additional slots are cut into every fifth cavity of the system, as Bevensee suggests, there is the strong possibility that new stop bands will be introduced in the region of  $\pi/5$ ,  $2\pi/5$ ,  $3\pi/5$ , and  $4\pi/5$  phase shift between cavities, and cutoff oscillations may occur at the corresponding frequencies. The introduction of extra resonant elements in an already complicated propagating system can sometimes hinder rather than help.

G. S. KINO

M. A. ALLEN

Microwave Lab.

Stanford University

Stanford, Calif.

\* N. Rynn, "On the periodic coupling of propagating structures," IRE TRANS. ON ELECTRON DEVICES, vol. ED-6, pp. 325-329; July, 1959.

### Broad-Band Hybrid Junctions\*

A coaxial version of the wide-band stripline magic T described by E. M. T. Jones in the March, 1960 issue of these TRANSACTIONS was developed jointly at the Mullard Research Laboratories and the Laboratories of the General Electric Company, England, some years ago. It has proved a powerful component in the design of broad-band receiver circuits and has the advantage of small size and geometrical symmetry in addition to wide frequency coverage.

In particular, the circuit has been used in broad-band balanced mixers, balanced modulators, single side-band modulators, limiters and isolating power splitters. In each case, the property of a  $180^\circ$  hybrid, by which isolation is independent of the value of two balanced terminating impedances, gives the device advantages over the more usual broad-band  $90^\circ$  hybrid circuits. Mullard balanced mixers type L361 (S-band) and L360 (X-band) are examples of the commercial application of the circuit.

Devices have been successfully operated in the frequency range 1.0–11.5 kMc, and for many applications it has proved convenient to divide this range into five overlapping bands.

The simplest embodiment of the hybrid is used, in which one arm contains a shorted coupled line filter section and the other three arms are simple lines for which  $\theta = \pi/2$  at midband. In this case, one set of conditions for satisfactory operation is

$$Z_1 = Z_2 = 0.71Z$$

and

$$Z_{oo} = Z_{oe} = 1.33Z,$$

whence

$$\theta = \beta = \frac{\pi}{2}$$

at midband, where

$\theta$  = the electrical length of the three similar arms,

$\beta + \pi$  = the electrical length of the filter section,

$Z$  = the characteristic impedance of the three similar arms,

$Z_{oo}$  = the characteristic impedance of the unbalanced mode,

$Z_{oe}$  = the characteristic impedance of the balanced mode,

$Z_1 = Z_2$  = the hybrid terminating impedances.

Circuits with open-coupled line sections and other systems of compensation have not justified the additional mechanical complexity. Moreover, the basic circuit has the advantage of superior isolation symmetry between the various terminals. If an attempt is made to recover this symmetry by compensating all three remaining arms, instead of one as described, extremely broad-band isolation characteristics can be obtained, but the input match of the device suffers.

Typical theoretical and experimental performance figures for the basic circuit over

\*  $\bar{H}_c$  is easily estimated from the formula for  $\bar{H}_c$  of the TM<sub>010</sub> mode of a closed cylindrical cavity, satisfying (6). It is  $i\phi \sqrt{3.7J_1(k_1r)}$ , where  $k_1 = 2.4/(\text{cavity radius})$ .

\* Received by the PGCTT, August 8, 1960.



the octave range  $60^\circ < \theta < 120^\circ$  are shown in Table I.

TABLE I

	Theoretical	Experimental
Isolation	>22 db	>18 db
Input Match	<1.5:1	<1.4:1

The performance figures observed from the four possible input terminals are similar over this frequency range.

S. J. ROBINSON  
For Director  
Mullard Res. Labs.  
Cross Oak Lane  
Salfords, near Redhill  
Surrey, England

## BIBLIOGRAPHY

- [1] General Electric Co. and E. M. Hicken, British Patent Application no. 20725/54.
- [2] Mullard Ltd., S. J. Robinson, and N. E. Goddard, British Patent Application no. 770317.
- [3] A. B. McNaughton, "A new broad-band coaxial hybrid ring," *Proc. of the Internatl. Congress on Ultra High Frequency Circuits and Antennas*, Paris, France, October, 1957.

## Lightweight Y-Junction Strip-Line Circulator\*

In a recent issue, the practical realization of a Y-junction strip-line circulator was described<sup>1</sup> which used disks of yttrium iron garnet located at the junction of the Y, magnetically biased above resonance at approximately 2200 gauss. By using a material with a lower saturation magnetization (magnesium, manganese, aluminum ferrite,  $4\pi M_s = 600$ ) we have reduced the bias field required to approximately 190 gauss for frequencies in the 2-kMc range and to approximately 800 gauss for frequencies in the 1-kMc range, thus reducing considerably the weight of the circulator. If the circulator is to be operated as a switch, the reduced field requirements permit faster switching times or, for a given switching time, a considerable reduction in power supply requirements.

Fig. 1 shows the results of a circulator operating at a fixed magnetic bias of 190 gauss. Although no attempt was made to determine the optimum ferrite diameter for this frequency range, it is felt that the performance of the circulator would be improved if a more optimum diameter were used.

Below 1400 Mc, the performance of the circulator was degraded at these low biasing fields, but by reversing the polarity of the magnetic field and biasing above resonance, good circulator action could again be obtained. Reversing the biasing field and biasing above resonance does not change the direction of circulation, as may be seen by referring to the equation below given by

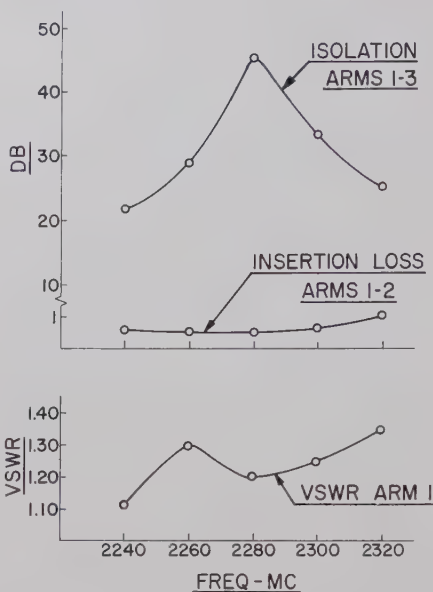


Fig. 1—Circulator characteristics with fixed dc magnetic bias;  $H_{DC} = 190$  gauss.

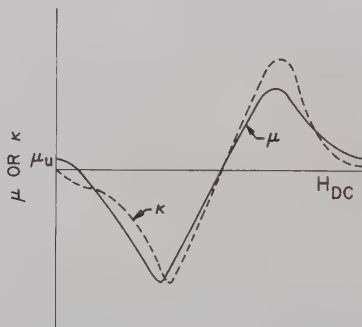


Fig. 2—Typical variations of real components of tensor permeability as a function of dc magnetic field.

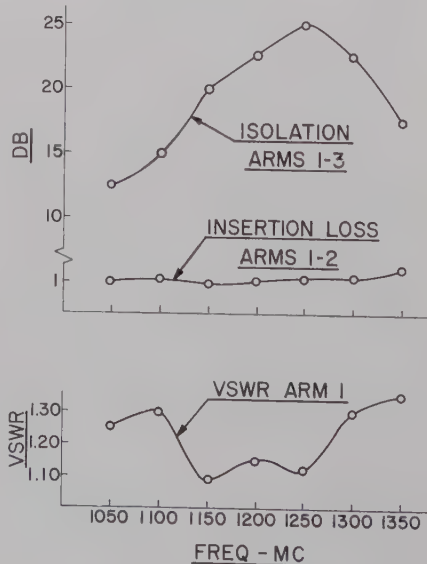


Fig. 3—Circulator characteristics with fixed dc magnetic bias;  $H_{DC} = 820$  gauss.

Auld<sup>2</sup> for the change in the  $a$ th eigenvalue ( $\delta s_a$ ) of the scattering matrix of the symmetrical Y-junction due to the application of the magnetic biasing field. The magnetic biasing field splits the reciprocity degeneracy of the eigenvalues to give circulator action:

$$\delta s_a = -j \frac{b}{2\omega\mu_u^2} \sum_{p=-\infty}^{\infty} A_{-p}^{(-a)} A_p^{(a)} \cdot \left\{ (\mu - \mu_u) \int_0^R f_p^{(-a)} \cdot f_p^{(a)} r dr + j\kappa \int_0^R k \cdot f_p^{(-a)} \times f_p^{(a)} r dr \right\} a \neq 0$$

where  $\mu$  and  $\kappa$  are the components of the permeability tensor and the other symbols are as defined by Auld.<sup>2</sup>

A typical variation of  $\mu$  and  $\kappa$  as a function of magnetic field is shown in Fig. 2. The magnetic biasing field is adjusted to make  $\mu - \mu_u = 0$  either above or below resonance. Since  $\kappa$  reverses sign above resonance, there is a reversal in the direction of circulation, but by reversing the biasing field, the direction of circulation remains the same. Fig. 3 shows the characteristics of a circulator biased above resonance but still only requiring a magnetic field of 820 gauss. Here again it is felt that the performance would be improved if ferrites of optimum diameter were used. Thus by using a material with a lower saturation magnetization than yttrium iron garnet, bias field requirements are reduced with a consequent reduction in weight of the circulator.

L. FREIBERG  
Electromagnetic Systems  
Lockheed Missiles and Space Div.  
Sunnyvale, Calif.

\* B. A. Auld, "The synthesis of symmetrical waveguide circulators" IRE TRANS. ON MICROWAVE THEORY AND TECHNIQUES, vol. MTT-7, pp. 238-246; April 1959.

## A Novel Broad-Band Balun\*

Broad-band baluns have recently become the subject of renewed interest, particularly those suitable to couple spiral or planar log periodic antennas to the commonly used coaxial lines.<sup>1-3</sup>

To make such a balun capable of operating over the frequency band of 1000-4000 Mc and to take advantage of the strip transmission line techniques, the broad-band

\* Received by the PGMTT, September 6, 1960.

<sup>1</sup> R. Bawer and J. J. Wolfe, "A printed circuit balun for use with spiral antennas," IRE TRANS. ON MICROWAVE THEORY AND TECHNIQUES, vol. MTT-8, pp. 319-325; May, 1960.

<sup>2</sup> E. M. T. Jones and J. K. Shimizu, "A wide-band stripline balun," IRE TRANS. ON MICROWAVE THEORY AND TECHNIQUES, vol. MMT-7, pp. 128-134; January, 1959.

<sup>3</sup> J. W. McLaughlin, D. A. Dunn, and R. W. Grow, "A wide-band balun," IRE TRANS. ON MICROWAVE THEORY AND TECHNIQUES, vol. MTT-6, pp. 314-316; July, 1958.

\* Received by the PGMTT, August 15, 1960.

<sup>1</sup> U. Milano, J. H. Saunders, and L. Davis, Jr., "A Y-junction strip-line circulator," IRE TRANS. ON MICROWAVE THEORY AND TECHNIQUES, vol. MTT-8, pp. 346-351; May, 1960.

phase difference circuit of Schiffman<sup>4</sup> was utilized. In this balun the 50-ohm coaxial input is transformed to strip transmission line at 50 ohms, which then splits into two 100-ohm lines in parallel. By an application of two 90° phase difference circuits (Schiffman Type A), two outputs with approximately 180° phase difference over a broad frequency band are obtained. These are connected to opposite sides of a 200-ohm twin wire balanced transmission line. Since the two 100-ohm striplines are thus effectively placed in series, a match is obtained at the junction.

The center conductor of the strip transmission line is laid out as shown in Fig. 1. The ratio  $Z_{oe}$  to  $Z_{oo}$  for the coupled sections is taken as 3 with a  $Z_o$  of 100 ohms. This gives  $Z_{oe} = 173 \Omega$  and  $Z_{oo} = 57.7 \Omega$ . The lengths of the coupled sections and the difference in path length are made such as to give a center frequency of 2750 Mc. The photograph of Fig. 2 shows the balun assembled.

Measurements of the characteristics of the junction were made by the method described by Wentworth and Barthel.<sup>5</sup> The VSWR of the junction as determined by this method is shown in Fig. 3. This indicates a reasonably matched structure from 750 to 4750 Mc, a range of greater than 6 to 1.

<sup>4</sup> B. M. Schiffman, "A new class of broad-band microwave 90° phase shifters," IRE TRANS. ON MICROWAVE THEORY AND TECHNIQUES, vol. MTT-6, pp. 232-237; April, 1958.

<sup>5</sup> F. L. Wentworth and D. R. Barthel, "A simplified calibration of two-port transmission line devices," IRE TRANS. ON MICROWAVE THEORY AND TECHNIQUES, vol. MTT-4, pp. 173-175; July, 1956.

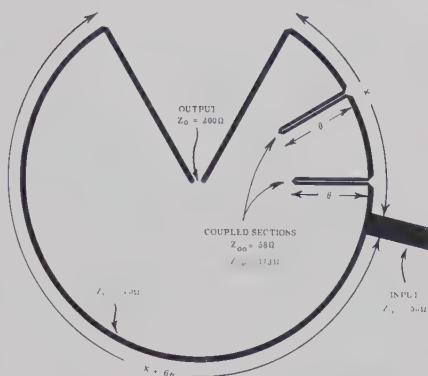


Fig. 1—Center conductor configuration of differential phase-shift balun.

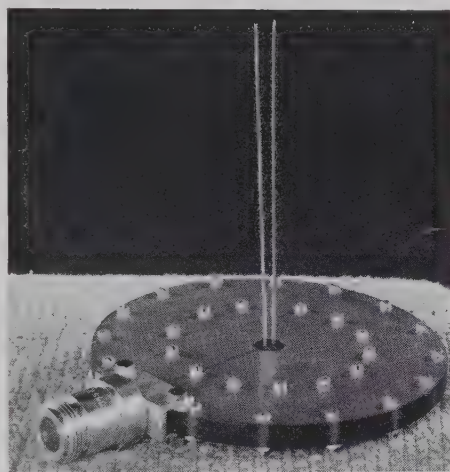


Fig. 2.

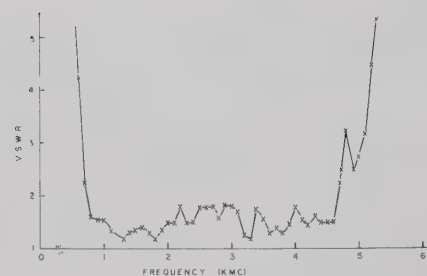


Fig. 3—Differential phase-shift balun VSWR vs frequency.

Simple tests also indicate that radiation from the balanced line only becomes apparent at the extremes of this range.

This particular configuration for a balun arose from a requirement for the balun to be mounted on the rear of the flat reflector of a broad-band antenna with a minimum rearward projection while still allowing relatively easy changes of reflector spacing.

Although this model of the balun was designed for a balanced output of 200 ohms, other output impedances could be obtained by suitable tapers either within the balun structure or on the unbalanced input line. Somewhat larger bandwidths or lower VSWR's could be obtained by taking advantage of the more complex combination of coupled sections as indicated by Schiffman. This balun uses only the simplest configuration.

J. H. CRAVEN  
Radio and Electr. Engrg. Division  
Natl. Res. Council  
Ottawa, Canada



# Contributors

A. E. Barrington was born on March 22, 1921, in Vienna, Austria. He received the B.S. and Ph.D. degrees from the University of London, England, in 1947 and 1950, respectively.



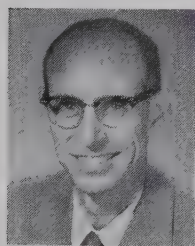
A. E. BARRINGTON

From 1950 to 1952, he was a tube design engineer at Machlett Laboratories, Inc., and from 1952 to 1955 a senior scientific officer with the British Admiralty engaged in microwave tube research. He then joined the Electrical Engineering Department at Queen Mary College, University of London, as Harwell Research Fellow and lecturer where he participated in a linear accelerator project sponsored by the Atomic Energy Authority. He is now a Research Fellow on the Cambridge Electron Accelerator and lecturer in applied physics at Harvard University.

Dr. Barrington is an associate member of the Institution of Electrical Engineers.



Howard E. Bussey (SM'56) was born in Yankton, S. D., on September 14, 1917. He attended Yankton College and George Washington University, Washington, D. C., receiving from the latter the B.A. degree in mathematics in 1943, and the M.S. degree in physics in 1951. He continued his studies at the University of Maryland, College Park, and the University of Colorado, Boulder.



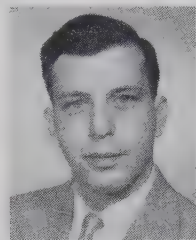
H. E. BUSSEY

His military service included meteorological studies at Massachusetts Institute of Technology, Cambridge, Mass., and duties as a forecasting and a radar-weather officer.

In 1946, Mr. Bussey joined the Central Radio Propagation Laboratory of the National Bureau of Standards, Washington, D. C., to do tropospheric propagation research. In 1951 he transferred to the Radio Standards Division of the same Laboratory to do microwave physics research. He has been the project leader for microwave dielectric and magnetic measurements since 1956.

He is a member of the American Physical Society, American Meteorological Society, RESA, Commission I of the International Scientific Radio Union, and Sigma Pi Sigma.

Seymour B. Cohn (S'41-A'44-M'46-SM'51-F'59) was born in Stamford, Conn., on October 21, 1920. He received the B.E. degree in electrical engineering from Yale University, New Haven Conn., in 1942, the M.S. degree in communication engineering, and the Ph.D. degree in engineering sciences and applied physics from Harvard University, Cambridge, Mass., in 1946 and 1948.



S. B. COHN

From 1942 to 1945 he was employed as a special research associate by the Radio Research Laboratory of Harvard University, and also represented that laboratory as a technical observer with the U. S. Army Air Force in the Mediterranean theater of operations. He worked at Sperry Gyroscope Company, Great Neck, N. Y., from 1948 to 1953, where he held the position of research engineer in the microwave instruments and components department. From 1953-1960, he was with the Stanford Research Institute, Menlo Park, Calif., as head of the Microwave Group and, since 1957, as manager of the Electromagnetics Laboratory. In July, 1960, he joined Rantec Corporation, Calabasas, Calif., as Vice President and Technical Director.

Dr. Cohn is a member of Tau Beta Pi and Sigma Xi. He is currently serving on the PGMTT Administrative Committee.



R. Lawrence Comstock (S'55) was born in Butte, Mont. on August 9, 1932. After serving two years in the U.S.A.F. he received the B.S. and M.S. degrees in electrical engineering in 1956 and 1957, respectively, from the University of California, Berkeley.

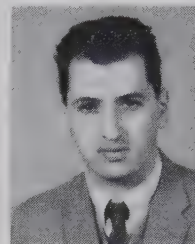


R. L. COMSTOCK

While at the University of California, he served as a teaching and research assistant. In 1957, he joined the Bell Telephone Laboratories, Murray Hill, N. J., where his work was concerned with ferrite device development. He now holds an appointment as research assistant in the W. W. Hansen Microwave Laboratory at Stanford University, Stanford, Calif., where he is studying for the Ph.D.

Mr. Comstock is a member of Tau Beta Pi, Eta Kappa Nu, and Sigma Xi.

J. Dekleva was born on January 4, 1925, in Ljubljana, Yugoslavia. He graduated in 1949 from the University of Ljubljana.



J. DEKLEVA

In 1951 he joined the J. Stefan Institute in Ljubljana as a member of the scientific staff and became head of the laboratory for mass spectrometry. In 1956 he received the D.Sc. degree for an investigation of the properties of a non-magnetic RF mass spectrometer. Since 1956 he has been a research fellow in physics on the Cambridge Electron Accelerator at Harvard University where he has been concerned primarily with the design of the synchrotron RF system.



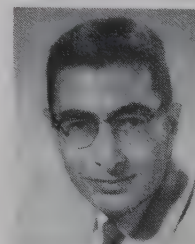
D. W. Downton was born in Birmingham, England, on May 10, 1921. After service in the Royal Air Force from 1941 to 1946, he rejoined the General Post Office, where he was engaged on single side-band and carrier telephony. He completed studies for the City and Guilds Certificate in Telecommunications, and then joined the Admiralty in 1949. Since 1951 he has been at the Services Electronics Research Laboratory, Baldock, England, and has lately been concerned with gas discharge tubes for use with high power microwave duplexers.



D. W. DOWNTON



Arthur J. Estin (S'49-A'50-M'54) was born in New York, N. Y., on February 15, 1927. He received the B.E.E. degree from Cooper Union, New York, N. Y., in 1949 and the M.S. degree in physics from the University of Colorado, Boulder, in 1958.



A. J. ESTIN

Mr. Estin has been associated with the National Bureau of Standards since 1948. From 1950 to 1954, he was on the

staff of the Cheyenne Mountain Field Station in Colorado Springs, Colo., engaged in problems of tropospheric propagation of VHF. In 1955 he transferred to the Radio Standards Division of the NBS Boulder Laboratories where he has been engaged in problems of microwave physics. He was in charge of microwave noise research and is presently investigating problems of microwave-plasma interactions.

He is a member of the American Physical Society, RESA, and Tau Beta Pi.



Clifford E. Fay (A'26-SM'45-F'56) was born on December 2, 1903, in St. Louis, Mo. He received the B.S. degree and the M.S. degree in electrical engineering, both from Washington University, St. Louis, Mo.



C. E. FAY

In 1927 he joined Bell Telephone Laboratories, Murray Hill, N. J., where he was engaged in the development of high-power electron tubes until 1955. More recently, he has been concerned with the development of microwave ferrite devices.

Mr. Fay is a member of Sigma Xi and Tau Beta Pi.



Robert M. Hill was born in New York, N. Y., on September 20, 1926. He received the B.A. degree in physics from Cornell University, Ithaca, N. Y., in 1949, and the Ph.D. degree in physics from Duke University, Durham, N. C., in 1953. His dissertation was done in the field of microwave spectrum of oxygen.



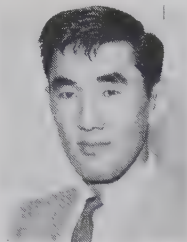
R. M. HILL

He joined Sylvania Electric Products, Inc., Mountain View, Calif., in 1953, and has been doing research in plasma and solid-state physics since then.

Dr. Hill is a member of Sigma Xi and the American Physical Society.



Stephen K. Ichiki was born in Sacramento, Calif., on September 11, 1924. He received the A.B. degree in physics from the University of California, Berkeley, in 1950, and the M.S. degree in physics from Stanford University, Stanford, Calif., in 1959.



S. K. ICHIKI

From 1950 to 1956, he was at the U. S. Naval Radiological Defense Laboratory, San Francisco, Calif., working in radiochemistry, autoradiography and aerosol research. He joined Sylvania Electric Products, Inc., Mountain View, Calif., in 1956, and has been doing work in gaseous electronics.

Mr. Ichiki is a member of the American Physical Society.



P. D. Lomer was born in Cornwall, England, on May 17, 1928. He received the B.S. degree in physics in 1948, and the M.S. degree in 1950, both from the University College of the South West, Exeter.



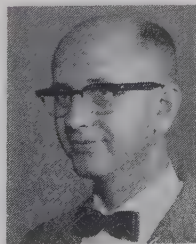
P. D. LOMER

He then joined the Services Electronics Research Laboratory, Baldock, England where he has been studying gas discharge devices with particular reference to microwave duplexers, and more recently, pulsed neutron sources.

Mr. Lomer is an associate member of the Institute of Physics.



George L. Matthaei (S'49-A'52-M'57) was born in Tacoma, Wash. on August 28, 1923. He received the B.S. degree in electrical engineering from the University of Washington, Seattle, Wash., in 1948. He received the Ph.D. degree from Stanford University, Stanford, Calif., in 1952.



G. L. MATTHAEI

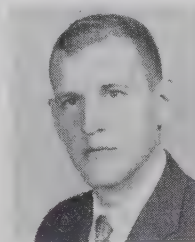
While at Stanford University, he was a research assistant in the Electronics Research Laboratory, where he did research on network synthesis. In 1951, he joined the faculty of the Division of Electrical Engineering of the University of California, Berkeley, where he was an assistant professor. He continued research on network synthesis, and supervised graduate student research in that field. During 1955 to 1958, he was a member of the technical

staff of the Ramo-Wooldridge Corp., Los Angeles, Calif. He was engaged in system analysis and research on microwave components. In September, 1958, Dr. Matthaei joined the staff of Stanford Research Institute, Menlo Park, Calif., where he is assistant head of the Microwave Group in the Electromagnetics Laboratory.

He is a member of Sigma Xi, Tau Beta Pi, and the Tensor Club of Great Britain.



Richard J. Mohr (M'58) was born in New York, N. Y. on April 12, 1930. He received the B.S.E.E. degree from the College of the City of New York, N. Y., in 1952 and the M.S.E.E. degree from the Polytechnic Institute of Brooklyn, Brooklyn, N. Y., in 1957.



R. J. MOHR

From 1952 to 1955, he was employed by the Naval Materiel Laboratory, Brooklyn, N. Y., where he evaluated microwave electron devices for military application. From 1955 to 1958, he was with Airborne Instruments Laboratory, Melville, N. Y., engaged in the design of special-purpose, low-noise receiving equipment. At FXR, Inc., Woodside, N. Y., from 1958 to 1960, he was responsible for the development of microwave components and systems. Since September of 1960, Mr. Mohr has been employed by Microwave Dynamics Corp., Plainview, N. Y., where he heads the microwave development section.



Bunichi Oguchi (SM'58) was born on November 21, 1921, in Nagano Prefecture, Japan. He received the B.S. degree in electrical engineering in 1943, and the D.Eng. degree in 1951, from the University of Tokyo, Japan.



B. OGUCHI

In 1948, he joined the Electrical Communication Laboratory of the Nippon Telegraph and Telephone Public Corp. and has been engaged in research on microwave components, antennas, solid state applications, and low-loss waveguide transmission. From September, 1958, to October, 1959, he was on leave from the laboratory, and was working at the Microwave Research Institute of the Polytechnic Institute of Brooklyn, Brooklyn, N. Y., as a research associate.

Dr. Oguchi is a member of Sigma Xi, the Institute of Electrical Communication Engineers of Japan and the Institute of Electrical Engineers of Japan.



Seymour Okwit (A'55) was born on August 31, 1929, in New York, N. Y. He received the B.S. degree in physics from Brooklyn College, Brooklyn, N. Y., and the M.S. degree in applied mathematics and physics from Adelphi College, Garden City, N. Y., in 1952 and 1958, respectively. He is presently working toward the Ph.D. degree in mathematical physics. From 1952 to 1954, he was in the



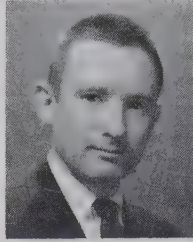
S. OKWIT

armed forces. He was assigned to the detection division of the Chemical and Radiological Laboratories of the Army Chemical Center Edgewood, Md., where he did extensive development work on instrumentation for the detection and analysis of the poisonous "G" nerve gases. Detection instruments upon which he has worked include an infrared scanning system and a system utilizing microwave spectroscopy. From 1954 to 1955, he was associated with the radar department of Arma Corporation, Long Island, N. Y., where he was concerned with boresight studies on monopulse antennas. He joined the Airborne Instruments Laboratory, a division of Cutler-Hammer, Inc., Melville, N. Y., in November, 1955, as an engineer in the Department of Applied Electronics, where he was concerned with the design and development of RF, IF, and microwave components and systems. Since 1958, he has been responsible for, and has performed considerable theoretical and experimental work on solid-state devices such as low-loss circulators, low-level ferrite limiters, and cavity and traveling-wave masers. He is now a group leader in the Applied Electronics Department at AIL,

and is currently directing programs in the development of advanced solid-state devices including masers, parametric amplifiers, and novel ferrite components.



J. R. Rees was born on February 17, 1930, in Peru, Ind. He received the B.A. degree in 1951, the M.S. degree in 1955 and the Ph.D. degree in 1957 from Indiana University, Bloomington.



J. R. REES

He has been working on the Cambridge Electron Accelerator since 1957, where he has primarily studied the design and construction of the Radio Frequency accelerating system.

Dr. Rees is a member of the American Physical Society.



Kenneth W. Robinson (S'45-A'49-M'55) was born on June 30, 1925, in San Diego, Calif. He received the M.S. degree in electrical engineering from the California Institute of Technology, Pasadena, in 1948, and the Ph.D. degree in physics from Princeton University, Princeton, N. J., in 1955.



K. W. ROBINSON

From 1948 to 1952, he was employed at the Radio Corporation of Amer-

ica Laboratories at Princeton, N. J. Since 1955, he has been a research fellow at Harvard University, Cambridge, Mass., on the staff of the Cambridge Electron Accelerator.

Dr. Robinson is a member of the American Physical Society and Sigma Xi.



George E. Schafer (SM'57) was born in Lincoln, Neb., on April 27, 1922. He received the B.A. degree in physics from Macalester College, St. Paul, Minn., in 1943, the M.A. degree in physics from the University of Minnesota, Minneapolis, in 1949, and the Ph.D. degree in physics from the University of Colorado, Boulder, in 1958.



G. E. SCHAFER

He served as a weather officer in the United States Air Force from 1943 to 1946, taught physics from 1948 to 1950, and joined the National Bureau of Standards, Boulder, Colo., in 1951. He is presently engaged in work on microwave attenuation and field strength standards.

Dr. Schafer is a member of the American Physical Society, American Association of Physics Teachers, the Colorado and Wyoming Academy of Science, RESA, and Sigma Xi.



Leo Young (M'54-SM'57), for a photograph and biography, please see page 470 of the July, 1960, issue of these TRANSACTIONS.

### SYMPOSIUM ISSUE

A large group of papers from the 1960 National Symposium held at San Diego, Calif., will appear in the January, 1961, issue of the IRE TRANSACTIONS ON MICROWAVE THEORY AND TECHNIQUES.

# IRE Transactions on Microwave Theory and Techniques

## Index to Volume MTT-8, 1960

### Contents

#### Volume MTT-8, Number 1, January, 1960

Message from the Editor, <i>Donald D. King</i> .....	2
Microwave Prize.....	3
Theoretical Limitations to Ferromagnetic Parametric Amplifier Performance, <i>R. W. Damon and J. R. Eshbach</i> .....	4
An Extension of the Mode Theory to Periodically Distributed Parametric Amplifiers with Losses, <i>K. Kurokawa and J. Hamasaki</i> .....	10
Action of a Progressive Disturbance on a Guided Electromagnetic Wave, <i>J. C. Simon</i> .....	18
Periodic and Guiding Structures at Microwave Frequencies, <i>A. F. Harvey</i> .....	30
Design of Mode Transducers, <i>L. Solymar and C. C. Eaglesfield</i> .....	61
UHF Resonator with Linear Tuning, <i>B. H. Wadia and R. L. Sarda</i> .....	66
Equivalent Circuits for Small Symmetrical Longitudinal Apertures and Obstacles, <i>Arthur A. Oliner</i> .....	72
On the $TE_{no}$ Modes of a Ferrite Slab Loaded Rectangular Waveguide and the Associated Thermodynamic Paradox, <i>A. D. Bresler</i> .....	81
L-Band Ferromagnetic Resonance Experiments at High Peak Power Levels, <i>E. Schlomann, J. Saunders, and M. Sirvetz</i> .....	96
High Power Ferromagnetic Resonance at X-Band in Polycrystalline Garnets and Ferrites, <i>J. J. Green and E. Schlomann</i> .....	100
Microwave Diode Cartridge Impedance, <i>R. V. Garver and J. A. Rosado</i> .....	104
Theory of the Germanium Diode Microwave Switch, <i>R. V. Garver, J. A. Rosado, and E. F. Turner</i> .....	108
Improvement in the Square Law Operation of 1N23B Crystals from 2 to 11 KMC, <i>A. Staniforth and J. H. Craven</i> .....	111
An N-Way Hybrid Power Divider, <i>Ernest J. Wilkinson</i> .....	116
Correspondence.....	119
Higher Order Modes in Coupled Helices, <i>Russell E. Hayes</i> ....	120
The Tetrahedral Junction as a Waveguide Switch, <i>Jerold A. Weiss</i> .....	121
Some Measurements of Travelling-Wave Tube Attenuators at 2000 MC, <i>C. H. Dix</i> .....	123
PGMTT News.....	125
Contributors.....	

#### Volume MTT-8, Number 2, March, 1960

Editorial, <i>Harold M. Barlow</i> .....	131
Broad-Band Coaxial Choked Coupling Design, <i>Howard E. King</i> .....	132
A Study of Multielement Transmission Lines, <i>Hiroshi Kogo</i> ..	136
Measurement of Relative Phase Shift at Microwave Frequencies, <i>C. A. Finnila, L. A. Roberts and C. Susskind</i> .....	143
Resonant Modes in Waveguide Windows, <i>M. P. Forrer and E. T. Jaynes</i> .....	147
Temperature Compensation of Coaxial Cavities, <i>J. R. Cogdell, A. P. Deam and A. W. Straiton</i> .....	151
A Graphical Method for Measuring Dielectric Constants at Microwave Frequencies, <i>Charles B. Sharpe</i> .....	155
Wide-Band Strip-Line Magic-T, <i>E. M. T. Jones</i> .....	160
A General Theorem on an Optimum Stepped Impedance Transformer <i>Henry J. Riblet</i> .....	169
Minimal Positive Polynomials, <i>James E. Eaton</i> .....	171
Complementarity in the Study of Transmission Lines, <i>G. H. Owyang and R. King</i> .....	172
High Resolution Millimeter Wave Fabry-Perot Interferometer <i>William Culshaw</i> .....	182

Boundary Conditions and Ohmic Losses in Conducting Wedges, <i>Robin M. Chisholm</i> .....	189
On the Theory of the Ferrite Resonance Isolator, <i>E. Schlomann</i> .....	199
Analysis of Microwave Measurement Techniques by Means of Signal Flow Graphs, <i>J. K. Hunton</i> .....	206
Stepped Transformers for Partially Filled Transmission Lines, <i>D. J. Sullivan and D. A. Parkes</i> .....	212
Parametric Diodes in a Maser Phase-Locked Frequency Divider, <i>M. L. Stitch, N. O. Robinson and W. Silvey</i> .....	218
Parametric Devices and Masers: An Annotated Bibliography, <i>E. Mount and B. Begg</i> .....	222
Correction to "Tables for Cascaded Homogeneous Quarter-Wave Transformers," <i>Leo Young</i> .....	243
Correspondence.....	
Analysis of Split Coaxial Line Type Balun, <i>Hiroshi Kogo</i> .....	245
Nonreciprocal Attenuation of Ferrite in Single-Ridge Waveguide, <i>T. S. Chen</i> .....	247
A New Automatic Frequency Regulation System, <i>J. R. Singer</i> .....	249
On Some Problems in Designing Microwave Faraday-Rotation Devices, <i>S. J. Lewandowski and J. Konopka</i> .....	249
Equivalence of 0 and -1 Space Harmonics in Helical Antenna Operation, <i>T. S. MacLean and D. A. Watkins</i> .....	251
Application of Perturbation Theory to the Calculation of $\omega$ - $\beta$ Characteristics for Periodic Structures, <i>Murray D. Sirkis</i> ..	251
Ice as a Bending Medium for Waveguide and Tubing, <i>Franklin S. Coale</i> .....	252
On Higher-Order Hybrid Modes of Dielectric Cylinders, <i>S. P. Schlesinger, P. Diamant, and A. Vigants</i> .....	252
A Property of Symmetric Hybrid Waveguide Junctions, <i>J. M. Smith</i> .....	253
Attenuation in a Resonant Ring Circuit, <i>K. Tomiyasu</i> .....	253
Reciprocal Ferrite Phase Shifters, <i>Alvin Clavin</i> .....	254
Contributors.....	255
PGMTT National Symposium Program.....	260
PGMTT Roster.....	261

#### Volume MTT-8, Number 3, May, 1960

Administrative Committee, 1959-1960.....	272
An Analysis of Four-Frequency Nonlinear Reactance Circuits, <i>David K. Adams</i> .....	274
Some Properties of Three Coupled Waves, <i>Laszlo Solymar</i> ....	284
Noise Figures of Reflex Klystron Amplifiers, <i>Koryu Ishii</i> ....	291
On Measurements of Microwave E and H Field Distributions by Using Modulated Scattering Methods, <i>Ming-Kuei Hu</i> ..	295
Analysis of Certain Transmission-Line Networks in the Time Domain, <i>W. J. Getsinger</i> .....	301
Sets of Eigenvectors for Volumes of Revolution, <i>J. van Bladel</i> .....	309
A Printed Circuit Balun for Use with Spiral Antennas, <i>R. Bawer and J. J. Wolfe</i> .....	319
The P-I-N Modulator, an Electrically Controlled Attenuator for MM and Sub-MM Waves, <i>F. C. de Ronde, H. J. G. Meyer, and O. W. Memelink</i> .....	325
Discontinuities in the Center Conductor of Symmetric Strip Transmission Line, <i>H. M. Altschuler and A. A. Oliner</i> .....	328
A Variational Integral for Propagation Constant of Lossy Transmission Lines, <i>Robert E. Collin</i> .....	339
Measurement of Bandwidth of Microwave Resonator by Phase Shift of Signal Modulation, <i>D. S. Lerner and H. A. Wheeler</i> ..	343
A Y-Junction Strip-Line Circulator, <i>U. Milano, J. H. Saunders and L. Davis, Jr.</i> .....	346
A Wide-Band UHF Traveling-Wave Variable Reactance Amplifier, <i>R. C. Honey and E. M. T. Jones</i> .....	351
On the Theory of Strongly Coupled Cavity Chains, <i>M. A. Allen and G. S. Kino</i> .....	362



Microphony in Waveguide, <i>I. Goldstein and S. Soorsoorian</i> . . .	372	A Waveguide Switch Employing the Offset Ring-Switch Junction, <i>R. C. Johnson, A. L. Holliman, and J. S. Hollis</i> . . .	532
Correspondence		Some Limitations on Parametric Amplifier Noise Performance, <i>R. D. Weglein</i> . . .	538
Discussion of Line Width and Gyromagnetic Ratio, <i>Isidore Bady</i> . . .	376	TE Mode Excitation on Dielectric Loaded Parallel Plane and Trough Waveguides, <i>M. Cohn, E. S. Cassedy, and M. A. Kott</i> . . .	545
Plotting Impedances with Negative Resistive Components, <i>R. L. Kyhl</i> . . .	377	A New Semiconductor Microwave Modulator, <i>H. Jacobs, F. A. Brand, M. Benanti, R. Benjamin, and J. Meindl</i> . . .	553
Comments on "The Design of Ridged Waveguide," <i>Richard M. Kurzrok</i> . . .	377	Theory and Measurement of $Q$ in Resonant Ring Circuits, <i>Hellmut Golde</i> . . .	560
Contributors . . .	378	Correspondence	

## Volume MTT-8, Number 4, July, 1960

Report of Advances in Microwave Theory and Techniques in Great Britain—1959, <i>John Brown</i> . . .	382	Ferrite Shape Considerations for UHF High-Power Isolators, <i>Ernest Stern</i> . . .	565
Report of Advances in Microwave Theory and Techniques in Western Europe—1959, <i>Georges Goudet</i> . . .	387	Measurement Technique for Narrow Line Width Ferromagnets, <i>J. I. Masters, B. R. Capone, and P. D. Gianino</i> . . .	565
Report of Advances in Microwave Theory and Techniques in Japan—1959, <i>Kiyoshi Morita</i> . . .	395	Multidiode Switches, <i>Janis Galejs</i> . . .	566
The Design and Measurement of Two Broad-Band Coaxial Phase Shifters, <i>C. F. Augustine and J. Cheal</i> . . .	398	Technique for Polishing Single Crystal Yttrium-Iron-Garnet Spheres, <i>P. D. Gianino, B. R. Capone, E. Kelly, and J. I. Masters</i> . . .	569
A Dielectric Resonator Method of Measuring Inductive Capacities in the Millimeter Range, <i>B. W. Hakki and P. D. Coleman</i> . . .	402	Tunable Two-Mode Cavity with Capacitive Loading, <i>J. D. McGee</i> . . .	569
Summary of Measurement Techniques of Parametric Amplifier and Mixer Noise Figure, <i>R. D. Haun, Jr.</i> . . .	410	Unloaded $Q$ of Single Crystal Yttrium-Iron-Garnet Resonator as a Function of Frequency, <i>P. S. Carter, Jr., and C. Flammer</i> . . .	570
Duplexing Systems at Microwave Frequencies, <i>A. F. Harvey</i> . . .	415	A Note on the Derivation of the Fields in a Radial Line, <i>J. F. Dienst</i> . . .	571
Impedances of an Elliptic Waveguide (For the $H_1$ Mode), <i>G. R. Valenzuela</i> . . .	431	Surface Waves on Symmetrical Three-Layer Sandwiches, <i>J. H. Richmond</i> . . .	572
Analysis of a Transmission Cavity Waveguide, <i>Leo Young</i> . . .	436	Higher-Order Evaluation of Dipole Moments of a Small Circular Disk, <i>Wilhelm H. Eggimann</i> . . .	573
Scattering of a Plane Wave on a Ferrite Cylinder at Normal Incidence, <i>Wilhelm E. Eggimann</i> . . .	440	Properties of Symmetric Hybrid Waveguide Junctions, <i>R. Levy</i> . . .	573
Phase Adjustments Effects on Cascaded Reflex Klystron Amplifiers, <i>Koryu Ishii</i> . . .	445	Contributors . . .	574
TE Modes of the Dielectric Loaded Trough Line, <i>Marvin Cohn</i> . . .	449		
Coupling of Modes in Uniform Composite Waveguides, <i>Luiz C. Bahiana and Louis D. Smullin</i> . . .	454		
Correction to "Design of Linear Double Tapers in Rectangular Waveguides," <i>R. C. Johnson</i> . . .	458		
Correspondence			
The Extended Theory of the Manley-Rowe's Energy Relations in Nonlinear Elements and Nonlinear Lossless Medium, <i>Hiroshi Iwasawa</i> . . .	459		
A Method of Improving Isolation in Multi-Channel Waveguide Systems, <i>Glenn F. Engen</i> . . .	460		
A Microwave Impedance Meter Capable of High Accuracy, <i>R. W. Beatty</i> . . .	461		
On the Noise Temperature of Coupling Networks, <i>E. Bedrosian</i> . . .	463		
A Logarithmic Transmission Line Chart, by <i>A. C. Hudson, Peter I. Somlo</i> . . .	463		
Velocity Sorting Detection in Backward Wave Autodyne Reception, <i>J. K. Pulfer</i> . . .	463		
A Broad-Band Crystal Mount 10.5 KMC to 20 KMC, <i>A. Staniforth</i> . . .	464		
Proposed Parametric Amplifier Utilizing Ferroelectric Substance, <i>Yoshimasa Aoki</i> . . .	465		
A Broad-Band Ferrite Reflective Switch, <i>C. M. Johnson and J. C. Wiltse</i> . . .	466		
Contributors . . .	468		
PGMTT News . . .	471		

## Volume MTT-8, Number 5, September, 1960

Noise Studies on Two-Cavity CW Klystrons, <i>George A. Esperesen</i> . . .	474	Design of Wide-Band (and Narrow-Band) Band-Pass Microwave Filters on the Insertion Loss Basis, <i>George L. Matthaei</i> . . .	580
Optimum Quarter-Wave Transformers, <i>Leo Young</i> . . .	478	Radio-Frequency System of the Cambridge Electron Accelerator, <i>Kenneth W. Robinson</i> . . .	593
The Quarter-Wave Transformer Prototype Circuit, <i>Leo Young</i> . . .	483	Model Studies of a Strongly Coupled Synchrotron RF System, <i>A. E. Barrington, J. Dekleva, and J. R. Rees</i> . . .	597
Broad-Band Ridge Waveguide Ferrite Devices, <i>E. S. Grimes, Jr., D. D. Bartholomew, D. C. Scott, and S. C. Sloan</i> . . .	489	Operation of the Field Displacement Isolator in Rectangular Waveguide, <i>R. L. Comstock and C. E. Fay</i> . . .	605
Radiation Patterns of a Noise-Excited Thin Slot, <i>Nicholas George</i> . . .	493	Peak Internal Fields in Direct-Coupled-Cavity Filters, <i>Leo Young</i> . . .	612
Variational Principles and Mode Coupling in Periodic Structures, <i>T. J. Gobllick, Jr., and R. M. Bevensee</i> . . .	500	Mismatch Errors in Microwave Phase Shift Measurements, <i>G. E. Schafer</i> . . .	617
Determination of the Capacitance, Inductance, and Characteristic Impedance of Rectangular Lines, <i>Tsung-Shan Chen</i> . . .	510	A Note on the Optimum Source Conductance of Crystal Mixers, <i>R. J. Mohr and S. Okwit</i> . . .	622
The Analysis of a Broad-Band Circular Polarizer Including Interface Reflections, <i>S. Adachi and E. M. Kennaugh</i> . . .	520	Microwave Switching with Low-Pressure Arc Discharge, <i>R. M. Hill and S. K. Ickiki</i> . . .	628
Large Signal Analysis of a Parametric Harmonic Generator, <i>Kenneth M. Johnson</i> . . .	525	Characteristic Impedances of Broadside-Coupled Strip Transmission Lines, <i>Seymour B. Cohn</i> . . .	633
		Thickness Corrections for Capacitive Obstacles and Strip Conductors, <i>Seymour B. Cohn</i> . . .	638
		Inhomogeneous Quarter-Wave Transformers of Two Sections, <i>Leo Young</i> . . .	645
		Errors in Dielectric Measurements Due to a Sample Insertion Hole in a Cavity, <i>A. J. Estlin and H. E. Bussey</i> . . .	650
		Correction, <i>D. S. Lerner and H. A. Wheeler</i> . . .	653
		A Pre-TR Tube for High Mean Power Duplexing, <i>D. W. Downton and P. D. Lomer</i> . . .	654
		Circular Electric Mode Directional Coupler, <i>Bunichi Oguchi</i> . . .	660
		Correspondence	
		An Equivalent Circuit of the Internal Cavity Reflex-Klystron Amplifier, <i>Koryu Ishii</i> . . .	667
		Some Comments on the Method of Kyhl, <i>L. J. Kaplan, D. J. R. Stock and R. L. Kyhl</i> . . .	668
		Scattering Matrix for an N-Port Power-Divider Junction, <i>O. R. Price and M. Leichter</i> . . .	669
		Lossy Resonant Slot Coupling, <i>R. M. Bevensee, G. S. Kino, and M. A. Allen</i> . . .	669
		Broad-Band Hybrid Junctions, <i>S. J. Robinson</i> . . .	671
		Lightweight Y-Junction Strip-Line Circulator, <i>L. Freiburg</i> . . .	672
		A Novel Broad-Band Balun, <i>J. H. Craven</i> . . .	672
		Contributors . . .	673
		Notice 1960 National Symposium Issue . . .	676
		Annual Index . . .	676

## Index to Authors

### A

Adachi, S.: Sep 520  
 Adams, D. K.: May 274  
 Allen, M. A.: May 362, Nov 667  
 Altschuler, H. M.: May 328  
 Aoki, Y.: Jul 465  
 Augustine, C. F.: Jul 398

### B

Bady, I.: May 376  
 Bahiana, L. C.: Jul 454  
 Barrington, A. E.: Nov 595  
 Bartholomew, D. D.: Sep 489  
 Bawer, R.: May 319  
 Beatty, R. W.: Jul 461  
 Bedrosian, E.: Jul 463  
 Begg, B.: Mar 222  
 Benanti, M.: Sep 553  
 Benjamin, R.: Sep 553  
 Bevensee, R. M.: Sep 500, Nov 667  
 Brand, F. A.: Sep 553  
 Bresler, A. D.: Jan 81  
 Brown, J.: Jul 382  
 Bussey, H. E.: Nov 648

### C

Capone, B. R.: Sep 565, 569  
 Carter, P. S., Jr.: Sep 570  
 Cassidy, E. S.: Sep 545  
 Cheal, J.: Jul 398  
 Chen, Tsung-Shan: Mar 247, Sep 510  
 Chisholm, R. M.: Mar 189  
 Clavin, A.: Mar 254  
 Coale, F. S.: Mar 252  
 Cogdell, J. R.: Mar 151  
 Cohn, M.: Jul 449, Sep 545  
 Cohn, S. B.: Nov 631, 636  
 Coleman, P. D.: Jul 402  
 Collin, R. E.: May 339  
 Comstock, R. L.: Nov 603  
 Craven, J. H.: Jan 111, Nov 671  
 Culshaw, W.: Mar 182

### D

Damon, R. W.: Jan 4  
 Davis, L., Jr.: May 346  
 Deam, A. P.: Mar 151  
 Dekleva, J.: Nov 595  
 de Ronde, F. C.: May 325  
 Diamant, P.: Mar 252  
 Dienst, J. F.: Sep 571  
 Dix, C. H.: Jan 121  
 Downton, D. W.: Nov 652

### E

Eaglesfield, C. C.: Jan 61  
 Eaton, J. E.: Mar 171  
 Eggimann, W. H.: Jul 440, Sep 573  
 Engen, G. F.: Jul 460  
 Eshbach, J. R.: Jan 4  
 Esperson, G. A.: Sep 474  
 Estin, A. J.: Nov 648

### F

Fay, C. E.: Nov 603  
 Finnilla, C. A.: Mar 143  
 Flammer, C.: Sep 570  
 Forrer, M. P.: Mar 147  
 Freiberg, L.: Nov 670

### G

Galejs, J.: Sep 566  
 Garver, R. V.: Jan 104, 108  
 George, N.: Sep 493  
 Getsinger, W. J.: May 301  
 Gianino, P. D.: Sep 565, 569  
 Golde, H.: Sep 560  
 Goldstein, I.: May 372  
 Goblick, T. J., Jr.: Sep 500  
 Goudet, G.: Jul 387  
 Green, J. J.: Jan 100  
 Grimes, E. S., Jr.: Sep 489

### H

Hakki, B. W.: Jul 402  
 Hamasaki, J.: Jan 10  
 Haun, R. D., Jr.: Jul 410  
 Harvey, A. F.: Jan 30, Jul 415  
 Hayes, R. E.: Jan 119  
 Hill, R. M.: Nov 626  
 Holliman, A. L.: Sep 532  
 Hollis, J. S.: Sep 532  
 Honey, R. C.: May 351  
 Hu, Ming-Kuei: May 295  
 Hunton, J. K.: Mar 206

### I

Ichiki, S. K.: Nov 626  
 Ishii, K.: May 291, Jul 445, Nov 665  
 Iwasawa, H.: Jul 459

### J

Jacobs, H.: Sep 553  
 Jaynes, E. T.: Mar 147  
 Johnson, C. M.: Jul 466  
 Johnson, K. M.: Sep 525  
 Johnson, R. C.: Jul 458, Sep 532

Jones, E. M. T.: Mar 160, May 351

### K

Kaplan, L. J.: Nov 666  
 Kelly, E.: Sep 569  
 Kennaugh, E. M.: Sep 520  
 King, G. S.: Nov 667  
 King, H. E.: Mar 132  
 King, R.: Mar 172  
 Kogo, H.: Mar 136, 245  
 Konopka, J.: Mar 249  
 Kott, M. A.: Sep 545  
 Kurokawa, K.: Jan 10  
 Kurzrok, R. M.: May 377  
 Kyhl, R. L.: May 377, Nov 666

### L

Leichter, M.: Nov 667  
 Lerner, D. S.: May 343, Nov 651  
 Levy, R.: Sep 573  
 Lewandowski, S. J.: Mar 249  
 Lomer, P. D.: Nov 652

### M

MacLean, R. S.: Mar 251  
 Masters, J. I.: Sep 565, 569  
 Matthaei, G. L.: Nov 578  
 McGee, J. D.: Sep 569  
 Meindl, J.: Sep 553  
 Memelink, O. W.: May 325  
 Meyer, H. J. G.: May 325  
 Milano, U.: May 346  
 Mohr, R. J.: Nov 620  
 Morita, K.: Jul 395  
 Mount, E.: Mar 222

### O

Oguchi, B.: Nov 658  
 Okwit, S.: Nov 620  
 Oliner, A. A.: Jan 72, May 328  
 Owyang, G. H.: Mar 172

### P

Parkes, D. A.: Mar 212  
 Price, O. R.: Nov 667  
 Pulfer, J. K.: Jul 463

### R

Rees, J. R.: Nov 595  
 Riblet, H. J.: Mar 169  
 Richmond, J. H.: Sep 572  
 Roberts, L. A.: Mar 143  
 Robinson, K. W.: Nov 591  
 Robinson, N. O.: Mar 218

### S

Sarda, R. L.: Jan 66  
 Saunders, J.: Jan 96  
 Saunders, J. H.: May 346  
 Schafer, G. E.: Nov 615  
 Schlesinger, S. P.: Mar 252  
 Schlomann, E.: Jan 96, 100, Mar 199  
 Scott, D. C.: Sep 489  
 Sharpe, C. B.: Mar 155  
 Silvey, W.: Mar 218  
 Simon, J. C.: Jan 18  
 Singer, J. R.: Mar 249  
 Sirkis, M. D.: Mar 251  
 Sirvetz, M.: Jan 96  
 Sloan, S. C.: Sep 489  
 Smith, J. M.: Mar 253  
 Smullin, L. D.: Jul 454  
 Solymar, L.: Jan 61, May 284  
 Somlo, P. I.: Jul 463  
 Soorsoorian, S.: May 372  
 Staniforth, A.: Jan 111, Jul 464  
 Stern, E.: Sep 565  
 Stitch, M. L.: Mar 218  
 Stock, D. J. R.: Nov 666  
 Straiton, A. W.: Mar 151  
 Sullivan, D. J.: Mar 212  
 Susskind, C.: Mar 143

### T

Tomiyasu, K.: Mar 253  
 Turner, E. F.: Jan 108

### V

Valenzuela, G. R.: Jul 431  
 Van Bladel, J.: May 309  
 Vigants, A.: Mar 252

### W

Wadia, B. H.: Jan 66  
 Watkins, D. A.: Mar 251  
 Weglein, R. D.: Sep 538  
 Weiss, J. A.: Jan 120  
 Wheeler, H. A.: May 343, Nov 651  
 Wilkinson, E. J.: Jan 116  
 Wiltse, J. C.: Jul 466  
 Wolfe, J. J.: May 319

### Y

Young, L.: Mar 243, Jul 436, Sep 478, 483, Nov 610, 643

## Index to Subjects

### A

Accelerator, Cambridge Electron, RF System of: Nov 591  
 Amplifiers:  
     Klystron, Cascaded, Phase Adjustments Effects on: Jul 445  
     Klystron, Noise Figures: May 291  
     Parametric, Ferroelectric: Jul 465

Parametric, Ferromagnetic, Performance Limitations: Jan 4  
 Parametric, Mode Theory in Periodically Distributed: Jan 10  
 Parametric, Noise Figure Measurement: Jul 410  
 Parametric, Noise Performance Limitations: Sep 538

UHF Traveling-Wave Variable Reactance: May 351  
 Antenna Helical, Space Harmonics in: Mar 251  
 Antennas, Spiral, Printed Circuit Balun for: May 319  
 Apertures and Obstacles, Equivalent Circuits for Small: Jan 72



Arc Discharge, Microwave Switching With Low-Pressure: Nov 626  
 Attenuator, P-I-N Modulator for Millimeter Waves: May 325  
 Attenuators, Travelling-Wave Tube: Jan 121  
 Autodyne Reception, Velocity Sorting Detection in Backward Wave: Jul 463

## B

Backward Wave Autodyne Reception, Velocity Sorting Detection in: Jul 463  
 Balun, Broad-Band: Nov 671  
 Balun, Printed Circuit, for Spiral Antennas: May 319  
 Balun, Split Coaxial Line Type: Mar 245  
 Bandwidth Measurement of Microwave Resonator by Phase Shift of Signal Modulation: May 343  
 Bandwidth Measurement of Microwave Resonator by Phase Shift of Signal Modulation, Correction to: Nov 651  
 Bibliography on Parametric Devices and Masers: Mar 222

## C

Cambridge Electron Accelerator, RF System of: Nov 591  
 Capacities, Inductive, Measurement in the Millimeter Range: Jul 402  
 Cavities:  
   Chains, Strongly Coupled: May 362  
   Errors in Dielectric Measurements Due to Insertion Hole in: Nov 648  
   Temperature Compensation of Coaxial: Mar 151  
   Tunable Two-Mode: Sep 569  
   Waveguide, Transmission: Jul 436  
 Circulator, Lightweight Y-Junction Strip-Line: Nov 670  
 Circulator, Y-Junction Strip-Line: May 346  
 Coaxial Choked Coupling Design: Mar 132  
 Coaxial Line Type Balun, Split: Mar 245  
 Coaxial Phase Shifters: Jul 398  
 Conducting Wedges, Boundary Conditions and Losses in: Mar 189  
 Coupled Waves, Properties of Three: May 284  
 Coupler, Circular Electric Mode Directional: Nov 658  
 Crystal Mixers, Optimum Source Conductance of: Nov 620  
 Crystal Mount 10.5 KMC to 20 KMC, Broad-Band: Jul 464  
 Crystals, Operation From 2 to 11 KMC: Jan 111  
 Cylinders, Higher-Order Hybrid Modes of Dielectric: Mar 252

## D

Detection, Velocity Sorting, in Backward Wave Autodyne Reception: Jul 463  
 Dielectric:  
   Constants at Microwave Frequencies, Measuring: Mar 155  
   Cylinders, Higher-Order Hybrid Modes of: Mar 252  
   Loaded Trough Line, TE Modes: Jul 449  
   Measurement Errors Due to Insertion Hole in Cavity: Nov 648  
   Resonator Method of Measuring Inductive Capacities in the Millimeter Range: Jul 402  
 Diode Cartridge Impedance, Microwave: Jan 104  
 Diode Microwave Switch, Germanium: Jan 108

Dipole Moments of a Small Circular Disk: Sep 573  
 Directional Coupler, Circular Electric Mode: Nov 658  
 Divider Junction, Scattering Matrix for an N-Port Power: Nov 667  
 Divider, N-Way Hybrid Power: Jan 116  
 Divider, Parametric Diodes in a Maser Phase-Locked Frequency: Mar 218  
 Duplexing Systems at Microwave Frequencies: Jul 415  
 Duplexing, TR Tube for High Mean Power: Nov 652

## E

Eigenvectors for Volumes of Revolution: May 309  
 Electron Accelerator, RF System of Cambridge: Nov 591  
 Equivalent Circuits for Small Apertures and Obstacles: Jan 72

## F

Faraday-Rotation Devices, Designing: Mar 249  
 Ferrites:  
   Cylinder, Scattering of a Plane Wave on a: Jul 440  
   Devices, Broad-Band Ridge Waveguide: Sep 489  
   High Power Ferromagnetic Resonance in Garnets and: Jan 100  
   Loaded Rectangular Waveguide, Modes of: Jan 81  
   Nonreciprocal Attenuation in Single-Ridge Waveguide: Mar 247  
   Phase Shifters, Reciprocal: Mar 254  
   Reflective Switch: Jul 466  
   Resonance Isolator, Theory of: Mar 199  
   Shape Considerations for UHF High-Power Isolators: Sep 565  
 Ferroelectric, Parametric Amplifier Utilizing: Jul 465  
 Ferromagnetic Parametric Amplifier Performance, Limitations to: Jan 4  
 Ferromagnetic Resonance Experiments at High Power Levels: Jan 96  
 Ferromagnetic Resonance in Garnets and Ferrites, High Power: Jan 100  
 Ferromagnets, Measurement Technique for Narrow Line Width: Sep 565  
 Field Distributions, Measurement by Modulated Scattering Methods: May 295  
 Fields in a Radial Line, Derivation of: Sep 571  
 Filters, Insertion Loss Design of Band-Pass Microwave: Nov 578  
 Filters, Peak Internal Fields in Direct-Coupled-Cavity: Nov 610  
 Frequency Divider, Parametric Diodes in a Maser Phase-Locked: Mar 218  
 Frequency Regulation System, Automatic: Mar 249

## G

Garnets and Ferrites, High Power Ferromagnetic Resonance in: Jan 100  
 Generator, Large Signal Analysis of a Parametric Harmonic: Sep 525  
 Great Britain, Advances in Microwave Theory, 1959: Jul 382  
 Guided Wave, Action of a Progressive Disturbance on: Jan 18  
 Guiding Structures at Microwave Frequencies, Periodic and: Jan 30  
 Gyromagnetic Ratio, Line Width and: May 376

## H

Harmonic Generator, Large Signal Analysis of a Parametric: Sep 525  
 Helical Antenna Operation, Space Harmonics in: Mar 251  
 Helices, Higher Order Modes in Coupled: Jan 119

## I

Ice as a Bending Medium for Waveguide: Mar 252  
 Impedance Meter, Microwave: Jul 461  
 Impedances with Negative Resistive Components, Plotting: May 377  
 Insertion Loss Design of Band-Pass Microwave Filters: Nov 578  
 Interferometer, Millimeter Wave Fabry-Perot: Mar 182  
 Isolation Improvement in Multi-Channel Waveguide: Jul 460  
 Isolators, Ferrite Resonance, Theory of: Mar 199  
 Isolators, Ferrite Shape Considerations for UHF High-Power: Sep 565  
 Isolators, Field Displacement, Operation of: Nov 603

## J

Japan, Advances in Microwave Theory, 1959: Jul 395  
 Junctions, Broad-Band Hybrid: Nov 669  
 Junctions, Tetrahedral, as a Waveguide Switch: Jan 120

## K

Klystrons:  
   Amplifiers, Noise Figures of Reflex: May 291  
   Amplifiers, Phase Adjustments Effects on Cascaded Reflex: Jul 445  
   Equivalent Circuit of the Internal Cavity Reflex: Nov 665  
   Noise Studies on Two-Cavity CW: Sep 474  
 Kyhl, Comments on the Method of: Nov 666

## L

Line Width and Gyromagnetic Ratio: May 376  
 Logarithmic Transmission Line Chart: Jul 463

## M

Magic-T, Wide-Band Strip-Line: Mar 160  
 Manley-Rowe's Energy Relations, Extended Theory of the: Jul 459  
 Maser Phase-Locked Frequency Divider, Parametric Diodes in a: Mar 218  
 Masers, Bibliography on Parametric Devices and: Mar 222  
 Meter, Microwave Impedance: Jul 461  
 Microphony in Waveguide: May 372  
 Microwave Theory, Advances in Great Britain, 1959: Jul 382  
 Microwave Theory, Advances in Japan, 1959: Jul 395  
 Microwave Theory, Advances in Western Europe, 1959: Jul 387  
 Millimeter Range, Dielectric Resonator Method of Measuring Inductive Capacities in the: Jul 402  
 Millimeter Waves, P-I-N Modulator Attenuator for: May 325  
 Mixer Noise Figure, Measurement of: Jul 410  
 Mixers, Optimum Source Conductance of Crystal: Nov 620



## Modes:

- Coupling in Uniform Composite Waveguides: Jul 454
- Dielectric Cylinders, Higher-Order Hybrid: Mar 252
- Dielectric Loaded Trough Line, TE: Jul 449
- Ferrite Loaded Rectangular Waveguide: Jan 81
- Periodically Distributed Parametric Amplifiers: Jan 10
- TE Excitation on Dielectric Loaded Waveguides: Sep 545
- Transducers, Design of: Jan 61
- Waveguide Windows, Resonant: Mar 147
- Modulator Attenuator for Millimeter Waves, P-I-N: May 325
- Modulator, Semiconductor Microwave: Sep 553
- Multidiode Switches: Sep 566

## N

- Negative Resistive Components, Plotting Impedances with: May 377

## Noise:

- Figure, Parametric Amplifier and Mixer: Jul 410
- Figures, Reflex Klystron Amplifiers: May 291
- Performance, Limitations on Parametric Amplifier: Sep 538
- Studies on Two-Cavity CW Klystrons: Sep 474
- Temperature of Coupling Networks: Jul 463
- Nonlinear Reactance Circuits, Four-Frequency: May 274

## P

- Parametric Amplifier:
  - Ferroelectric: Jul 465
  - Ferromagnetic, Performance Limitations: Jan 4
  - Mode Theory in Periodically Distributed: Jan 10
  - Noise Figure Measurement: Jul 410
  - Noise Performance Limitations: Sep 538
- Parametric Devices, Bibliography on: Mar 222
- Parametric Diodes in a Maser Phase-Locked Frequency Divider: Mar 218
- Parametric Harmonic Generator, Large Signal Analysis of a: Sep 525
- Periodic and Guiding Structures at Microwave Frequencies: Jan 30
- Periodic Structures, Calculation of Characteristics for: Mar 251
- Periodic Structures, Variational Principles and Mode Coupling in: Sep 500
- Phase Adjustments Effects on Cascaded Reflex Klystron Amplifiers: Jul 445
- Phase-Locked Frequency Divider, Parametric Diodes In a Maser: Mar 218
- Phase Shift:
  - at Microwave Frequencies, Measurement of: Mar 143
  - Measurements, Mismatch Errors in Microwave: Nov 615
  - of Signal Modulation, Bandwidth Measurement of Microwave Resonator by: May 343
  - of Signal Modulation, Bandwidth Measurement of Microwave Resonator by, Correction to: Nov 651
- Phase Shifters, Coaxial: Jul 398
- Phase Shifters, Reciprocal Ferrite: Mar 254
- Plotting Impedances with Negative Resistive Components: May 377

## Polarizer, Analysis of Broad-Band Circular: Sep 520

- Polynomials, Minimal Positive: Mar 171
- Power-Divider Junction, Scattering Matrix for an N-Port: Nov 667
- Power Divider, N-Way Hybrid: Jan 116
- Printed Circuit Balun for Spiral Antennas: May 319
- Propagation Constant of Lossy Transmission Lines: May 339

## Q

- Q in Resonant Ring Circuits, Theory and Measurement of: Sep 560

## R

- Radiation Patterns of a Noise-Excited Slot: Sep 493
- Reactance Amplifier, UHF Traveling-Wave Variable: May 351
- Reactance Circuits, Four-Frequency Nonlinear: May 274
- Resonant Ring Circuits, Theory and Measurement of Q in: Sep 560
- Resonator:
  - Bandwidth Measurement by Phase Shift of Signal Modulation: May 343
  - Bandwidth Measurement by Phase Shift of Signal Modulation, Correction to: Nov 651
  - Method of Measuring Inductive Capacities in the Millimeter Range, Dielectric: Jul 402
  - Unloaded Q of Yttrium-Iron-Garnet: Sep 570
  - with Linear Tuning, UHF: Jan 66
- Ring Circuit, Attenuation in a Resonant: Mar 253
- Ring Circuits, Theory and Measurement of Q in Resonant: Sep 560

## S

- Scattering Matrix for an N-Port Power-Divider Junction: Nov 667
- Scattering Methods, Measurements Field Distributions by Modulated: May 295
- Scattering of a Plane Wave on a Ferrite Cylinder: Jul 440
- Semiconductor Microwave Modulator: Sep 553
- Signal Flow Graphs, Microwave Measurements by: Mar 206
- Slot Coupling, Lossy Resonant: Nov 667
- Slot, Radiation Patterns of a Noise-Excited: Sep 493
- Strip Transmission Lines:
  - Characteristic Impedance of Broadside-Coupled: Nov 631
  - Circulator, Lightweight Y-Junction: Nov 670
  - Circulator, Y-Junction: May 346
  - Conductors, Thickness Corrections for: Nov 636
  - Discontinuities in: May 328
  - Magic-T, Wide-Band: Mar 160
- Surface Waves on Symmetrical Three-Layer Sandwiches: Sep 572
- Switches:
  - Ferrite Reflective: Jul 466
  - Germanium Diode Microwave: Jan 108
  - Low-Pressure Arc Discharge, Microwave: Nov 626
  - Multidiode: Sep 566
  - Waveguide, Employing Offset Ring-Switch Junction: Sep 532
  - Waveguide, Tetrahedral Junction as: Jan 120
- Synchrotron RF System, Model Studies of a Strongly Coupled: Nov 595

## T

- Tapers, Double, in Rectangular Waveguides, Correction to: Jul 458
- Temperature Compensation of Coaxial Cavities: Mar 151
- Transducers, Design of Mode: Jan 61
- Transformers:
  - Cascaded Quarter-Wave, Correction to: Mar 243
  - Quarter-Wave, Optimum: Sep 478
  - Quarter-Wave Prototype Circuit: Sep 483
  - Quarter-Wave, Two Sections: Nov 643
  - Stepped, for Partially Filled Transmission Lines: Mar 212
  - Stepped Impedance, Optimum: Mar 169
- Transmission Cavity Waveguide: Jul 436
- Transmission Lines:
  - Chart, Logarithmic: Jul 463
  - Complementarity in: Mar 172
  - Determination of Impedance of Rectangular: Sep 510
  - Multielement: Mar 136
  - Network Analysis in Time Domain: May 301
  - Propagation Constant of Lossy: May 339
  - Stepped Transformers for Partially Filled: Mar 212
  - Strip, Broadside Coupled, Characteristic Impedance of: Nov 631
  - Strip, Discontinuities in: May 328
  - Traveling-Wave Tube Attenuators: Jan 121
  - Traveling-Wave Variable Reactance Amplifier, May 351
  - Trough Line, TE Modes of the Dielectric Loaded: Jul 449
  - TR Tube for High Mean Power Duplexing: Nov 652

## V

- Velocity Sorting Detection in Backward Wave Autodyne Reception: Jul 463

## W

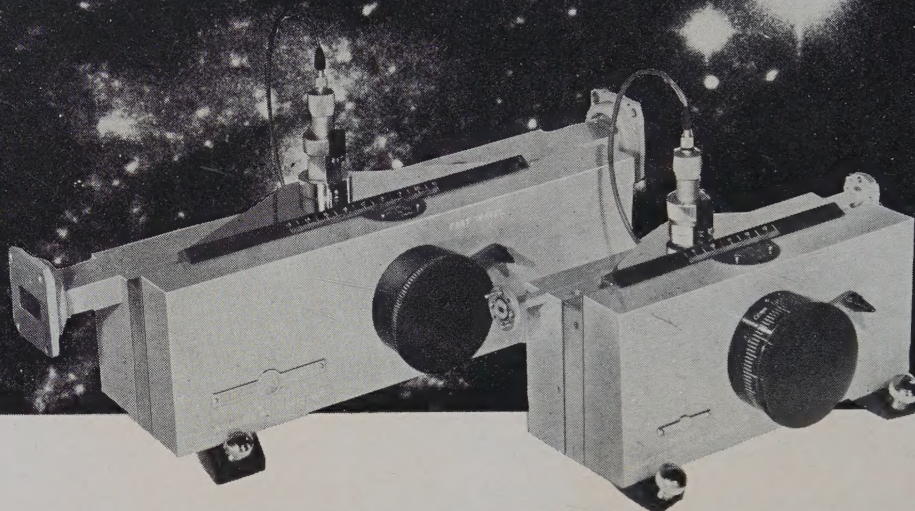
- Waveguides:
  - Coupling of Modes in Uniform Composite: Jul 454
  - Design of Double Tapers in Rectangular, Correction to: Jul 458
  - Elliptic, Impedances of: Jul 431
  - Ferrite Devices, Broad-Band Ridge: Sep 489
  - Ice as a Bending Medium for: Mar 252
  - Improving Isolation in Multi-Channel: Jul 460
  - Junctions, Symmetric Hybrid: Mar 253, Sep 573
  - Microphony in: May 372
  - Modes of a Ferrite Loaded Rectangular: Jan 81
  - Nonreciprocal Attenuation of Ferrite in Single-Ridge: Mar 247
  - Ridge, Design of: May 378
  - Switch Employing Offset Ring-Switch Junction: Sep 532
  - TE Mode Excitation on Dielectric Loaded: Sep 545
  - Transmission Cavity: Jul 436
  - Windows, Resonant Modes in: Mar 147
  - Waves, Properties of Three Coupled: May 284
  - Wedges, Boundary Conditions and Losses in Conducting: Mar 189
  - Western Europe, Advances in Microwave Theory, 1959: Jul 387

## Y

- Yttrium-Iron-Garnet Resonator, Unloaded Q of: Sep 570
- Yttrium-Iron-Garnet Sphere, Polishing: Sep 569



# slotted line performance...?



— here are design parameters uniquely defined

Note how comprehensively D-B parameters cover all requirements of a standing wave detector.

D-B units are designed for unprecedented accuracy, repeatability, and operator convenience. They're built with high-precision parts, under close quality control. Attractively styled and fully guaranteed, they have achieved a tremendous acceptance by the industry.

**Interchangeability with precision.** Any D-B unit will handle adjacent frequency bands by using a different size waveguide block and probe. You can make the change in 30 seconds, with no loss whatever in alignment accuracy.

**Complete range of sizes**—10 models cover from 5.85 KMC to 140 KMC—or you can purchase interchangeable blocks and probes to extend the range of any model, at a saving.

**Uniformity of waveguide surfaces.** D-B provides a high internal surface uniformity by precision machining its millimeter waveguides, and using carefully selected precision waveguide for lower-frequency units. This construction insures a uniform path for measured waves, thus minimizing residual VSWR.

**Slot excitation** is negligible, resulting in minimum RF leakage—another reason why residual VSWR is very low.

**Probe impedance** is properly matched to the waveguide. Uniform probe penetration is pro-

vided by a fast, convenient slope adjustment, made in a few minutes.

**Adequate probe travel** ( $\geq 1\frac{1}{2} \lambda_g$ ) available at all frequencies. Operator can read at least 3 maxima and 3 minima of VSWR.

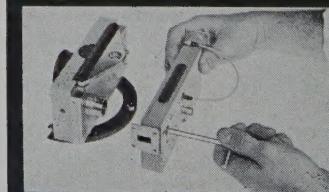
**Efficient mechanical translation.** D-B mechanism functions with exceptional smoothness, giving the unit a definite instrument "feel." Five point kinematic carriage suspension insures excellent linearity of probe motion.

**Vernier readout** on knob periphery permits reading of probe travel to .01mm without mounting of costly accessories.

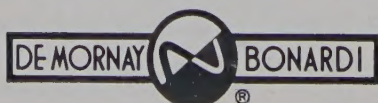
**Continuously variable** drive ratio changes carriage travel from "vernier" to "fast"—a time saver during rapid measurements.

**Direct phase readout.** Phase shift may be measured accurately on the calibrated knob, which reads percentage of  $180^\circ$  directly.

For complete data, see your D-B Catalogue, or request folder DB-825.



Interchangeable waveguide blocks. Each realigns perfectly to probe travel in a few seconds.



780 SOUTH ARROYO PARKWAY • PASADENA, CALIFORNIA



## INSTITUTIONAL LISTINGS

The IRE Professional Group on Microwave Theory and Techniques is grateful for the assistance given by the firms listed below, and invites application for Institutional Listing from other firms interested in the Microwave field.

AIRTRON, INC., A Division of Litton Industries, 200 East Hanover Ave., Morris Plains, N.J.  
Designers and Producers of Complete Line of Microwave Electronic and Aircraft Components

FXR, INC., 25-26 50th Street, Woodside 77, N.Y.  
Precision Microwave Test Equipment, High Power Microwave Electronics, Microwave Components & Instrumentation

HUGHES AIRCRAFT CO., Florence and Teale Sts., Culver City, Calif.  
Res., Dev., Mfg.: Radar Systems and Components, Microwave Devices and Components, Antennas, Tubes

ITT LABORATORIES, 500 Washington Ave., Nutley 10, N.J.  
Line-of-Sight and Over-the-Horizon Microwave Systems; Test Equipment and Components

LITTON INDUSTRIES, Electron Tube Div., 960 Industrial Rd., San Carlos, Calif.  
Magnetron, Klystrons, Carcinotrons, TWT's, Backward Wave Oscillators, Gas Discharge Tubes, Noise Sources

MICROWAVE DEVELOPMENT LABS., INC., 92 Broad St., Babson Park 57, Mass.  
Designers, Developers and Producers of Microwave Components and Assemblies, 400 Mc to 70 kMc

WATKINS-JOHNSON COMPANY, 3333 Hillview Ave., Palo Alto, Calif.  
Res., Dev., Mfr.: Microwave Electron Devices, TWT's, BWO's, Parametric Amplifiers, Microwave Systems

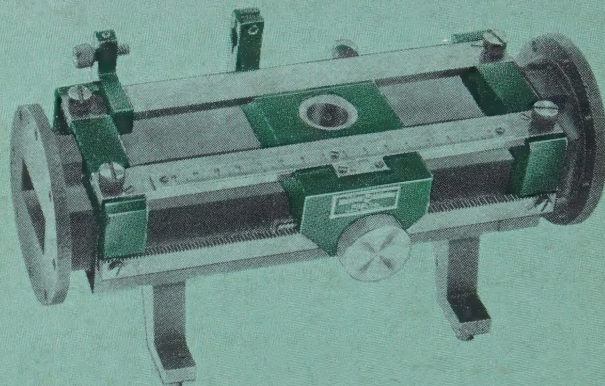
WHEELER LABORATORIES, INC., Great Neck, N.Y.; Antenna Lab., Smithtown, N.Y.  
Consulting Services, Research & Development, Microwave Antennas & Waveguide Components

The charge for an Institutional Listing is \$50.00 per issue or \$210.00 for six consecutive issues. Applications for Institutional Listings and checks (made out to the Institute of Radio Engineers) should be sent to Robert A. Rivers, PGMTT Advertising Editor, Aircom Inc., 354 Main St., Winthrop 52, Mass.



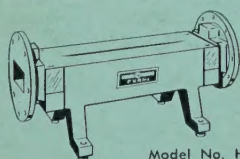
# Interchangeable SLOTTED SECTIONS

convenient and positive

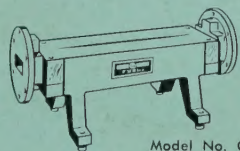


- conveniently interchangeable waveguide sections
- no slope adjustment required
- vernier position scale readable to 0.1 mm.
- dial gauge holder and movable stop
- tapered slots to minimize residual VSWR

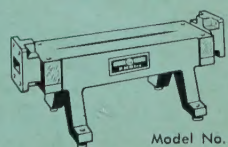
## INTERCHANGEABLE WAVEGUIDE SECTIONS



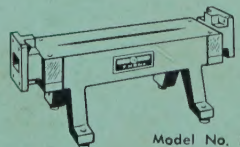
Model No. H115A



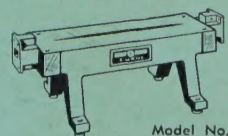
Model No. C115A



Model No. W115A

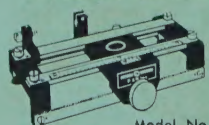


Model No. X115A



Model No. Y115A

## UNIVERSAL CARRIAGE



Model No. Z116A

Like the finest camera with a precisely fitted set of lenses, the FXR Universal Carriage and family of five Interchangeable Slotted Sections are matched to perfection. "Togetherness" with this unrivalled modular waveguide system gains new meaning . . . more rapid interchange of each section without tools or need for alignment, and more dependable performance over the entire frequency range from 3.95 kmc to 18.00 kmc. Another fine FXR "package" with quality and reliability built into it—from the first mark on the drawing board.

## SERIES 115 PRECISION SLOTTED SECTIONS

MODEL NO.	FREQUENCY RANGE (KMC)	WAVEGUIDE DIMENSIONS (Inches)	INSERTION LENGTH	WAVEGUIDE TYPE	FLANGE TYPE
H115A	3.95- 5.85	2 x 1	10 $\frac{3}{8}$ in.	RG-49/U	UG-149A/U
C115A	5.85- 8.20	1 $\frac{1}{2}$ x $\frac{3}{4}$	10 $\frac{3}{8}$ in.	RG-50/U	UG-344/U
W115A	7.05-10.00	1 $\frac{1}{4}$ x $\frac{5}{8}$	10 $\frac{3}{8}$ in.	RG-51/U	UG-51/U
X115A	8.20-12.40	1 x $\frac{1}{2}$	10 $\frac{3}{8}$ in.	RG-52/U	UG-39/U
Y115A	12.40-18.00	0.622 x 0.311 ID	10 $\frac{3}{8}$ in.	RG-91/U	UG-419/U

ACCESSORY: FXR Model No. B200A Tunable Probe.

All units when mounted in Z116A Carriage:

Slope—1.01 max. Irregularity—1.005 max.

Write for Bulletin No. SS115 or contact your local FXR representative.



## FXR, Inc.

Design • Development • Manufacture

25-26 50th STREET

WOODSIDE 77, N. Y.

RA. 1-9000  
TWX: NY 43745